DI Manuel Auer-Berger

Improving the External Quantum Efficiency of Organic Light Emitting Diodes by Enhanced Charge Injection and Improved Light Extraction

DOCTORAL THESIS

For obtaining the academic degree of

Doktor der technischen Wissenschaften

Doctoral Programme of Technical Sciences
Technical Physics

Graz University of Technology

Supervisor:

Prof. Dr. Emil J.W. List-Kratochvil

Institute of Solid State Physics

In cooperation with

JOANNEUM Research Forschungsgesellschaft mbH

Graz, November 2017

Statutory Declaration

I hereby declare that this doctoral thesis has been written independently and without any assistance from third parties. Furthermore, I confirm that no other sources / resources have been used than those specified in the thesis itself and that I have explicitly marked all material which has been quoted literally or by content from the used sources. This thesis has not been used either in whole or part, for a degree at this or any other university or institution. This is to certify that the printed version is equivalent to the submitted electronic one.

Date Signature

Acknowledgement

Even though I know that these sentences mark the last ones that I have to type to declare my thesis as finished, it is still hard to believe it is over, especially with all the typical ups and downs that come with pursuing a PhD. With the last years being a hell of a ride both professionally and personally, I think it is time to thank everyone who accompanied me on this rollercoaster.

First of all, I want to express my deepest gratitude to Emil J.W. List-Kratochvil for providing me with this unique opportunity, his guidance and continuous support even after he accepted the appointment to a full professor at Humbold-Universität zu Berlin.

This work wouldn't be the same if it weren't for the amazing Mirella El Gemayel, Florian Kolb, Birgit Six and Johannes Kofler. Each one of them provided invaluable input, good laughs and moral support when times were especially hard. At this point, I would also like to thank my office colleagues Paul Patter and Alex Blümel for the joyful atmosphere they created. Taking care of my extracurricular education, I owe a special thanks to the 'Quizduell' circle comprising Hannes Holl, Alexander Wheeldon, Karl Popovic and Florian Kolb. Of course, I would like to thank all the other members at Joanneum Research, both past and present, for their collegiality, support and friendship.

At this point I would also like to thank all project partners I had the pleasure of working with during my tenure at NTC Weiz/Joanneum Research. Here, I would especially like to mention Veronika Tretnak, Joachim Krenn as well as Paolo Melgari for their invaluable input, their time and the countless good discussions we had.

Also, I would like to thank Andreas Klug and Roman Trattnig for acquiring the projects Flexibilis and PlasmOLED.

Furthermore, I would also like to express my deepest gratitude to my family for being there and their unconditional support.

The last, but in fact the most important 'THANK YOU!' goes to the most amazing person in my life, my wife, Claudia! She was able to weather even the most intense mood swings and still tried to cheer me up. Thank you for being here! I love you!

Abstract

In recent years, organic light emitting diodes were quite successful in capturing a significant share of the small display market. Thanks to their flexible nature, organic light emitting diodes can be processed on flexible substrates allowing for curved displays. It is this specific property combined with the fact that organic light emitting diodes can be produced over large areas via low-cost solution processes that render them attractive for the lighting market. However, several issues remain before this technology is a viable contender for it. Key issues are amongst others the necessity of solvent resistant charge injection layers as well as the extraction of trapped light within the device. Possible solutions to these issues are presented within this thesis.

The first one is addressed by the introduction of a low-cost solution-processing route of the p-type semiconductor copper (I) thiocyanate. Through the presented method, the formation of unwanted secondary oxides that degrade the performance of the layer is effectively prevented as confirmed by X-Ray photoelectron spectroscopy. Additionally, the presented route effectively planarizes the surface, a necessity for a stable operation of organic light emitting diodes. Of relevance for organic light emitting diodes are the bulk hole mobilities, which, owing to the reduced defect densities, are markedly increased compared to the reference. Combined, these advantages result in a clear efficiency increase of up to 83 % for two different organic light emitting diode stacks, which confirms the effectiveness and universality of the presented approach.

To enhance the generation and extraction of light, this work focused on collective lattice resonances induced by arrays of aluminum nanoparticles. Starting with the confirmation that these collective resonances also exist in the weak cavity of an organic light emitting diode, the impact of important parameters, such as the lattice constant, the particle size and the thickness of the emissive layer of the organic light emitting diode, is assed in a step-by-step manner. Using optimized values, it is clearly demonstrated that the efficiency of a blue-light emitting organic diode can be raised by 35%. This concept is then extended to cover the whole spectral range relevant for illumination application by superimposing two gratings. This way, the efficiency can be raised in a similar fashion to 23%.

Kurzfassung

Organische Leuchtdioden waren in den letzten Jahren sehr erfolgreich darin zunehmend größere Marktanteile im Bereich kleinerer Displays zu beschlagnahmen. , Doch damit nicht genug, denn durch die Möglichkeit sie auf flexible Substrate zu prozessieren, was die Herstellung gekrümmter Displays erlaubt, gepaart mit der Tatsache, dass organische Leuchtdioden über günstige lösungsmittel-basierter Fertigungsprozesse auf große Flächen aufgebracht werden können, sind sie zudem attraktiv für den Beleuchtungsmarkt. Um jedoch tatsächlich eine ernstzunehmende Technologie für diesen Bereich darzustellen, gilt es noch einige Hürden zu überwinden. Zwei davon stellen sowohl die benötigte lösungsmittelresistente Ladungsträgerinjektionschicht als auch die Extraktion von Licht, welches im Bauteil gefangen ist, dar, für welche im Rahmen dieser Arbeit Lösungsvorschläge präsentiert werden.

Die erste Hürde wird durch die Einführung einer neuartigen, kostengünstigen lösungsmittel-basierten Fertigungsstrategie des p-Typ Halbleiters Kupfer (I) Thiocyanat adressiert. Durch die vorgestellte Methode wird, wie durch Röntgenphotoelektronenspektroskopie bestätigt, die Formation von unerwünschten sekundären Oxiden verhindert. Weiters führt die vorgestellte Methode zu einer Planarisierung der Oberfläche, einer Notwendigkeit für den stabilen Betrieb von organischen Leuchtdioden. Von großer Bedeutung für organische Leuchtdioden sind die im Vergleich zur Referenz gesteigerten Lochmobilitäten, welche sich auf reduzierte Defektdichten zurückführen lassen. In Kombination führen diese Vorteile in zwei verschiedenen Arten von organischen Leuchtdioden zu einer klaren Effizienzsteigerung um bis zu 83 %, was die Effektivität als auch die universelle Einsatzbarkeit dieser Methode unterstreicht.

Um die Erzeugung als auch die Extraktion von Licht zu verbessern, werden im Zuge dieser Arbeit kollektive Gitterresonanzen, welche durch Gitter, bestehend aus Aluminiumnanopartikeln erzeugt werden, erforscht. In einem ersten Schritt wird die Existenz der kollektiven Gitterresonanzen in einer schwachen Resonatorstruktur bestätigt. Danach wird der Einfluss wichtiger Parameter, wie Gitterkonstante, Partikelgröße als auch der Dicke der Aktivschicht, Schritt-für-Schritt untersucht. Durch die Verwendung optimierter Parameter kann die Effizienz von blau-emittierenden organischen Leuchtdioden schließlich um 35% gesteigert werden. Durch eine Superposition von zwei Gittern lässt sich dieses Konzept zudem für die Anwendung in weißlicht-emittierenden organischen Leuchtdioden erweitern womit deren Effizienz ebenfalls um 23% gesteigert werden kann.

List of included publications

This PhD thesis is based on the articles already or about to be published within the journals mentioned below. The author of this thesis is the first author of the listed publications and wrote the manuscripts, unless otherwise noted. The permission to reproduce the content was obtained from each journal. Parts of the reproduced content have been modified.

Tuning of the emission color of organic light emitting diodes via smartly designed aluminum plasmonics

M. Auer-Berger, V. Tretnak, F.-P. Wenzl, J. R. Krenn and Emil J.W. List-Kratochvil

Proceedings of SPIE 10101, Organic Photonic Materials and Devices XIX, 101010C, 2017 [doi:10.1117/12.2252327]

Contribution: The author carried out all experimental work and wrote the manuscript. The manuscript was finalized with the co-authors.

Adjusting the emission color of organic light emitting diodes through aluminum nano disc arrays

M. Auer-Berger, V. Tretnak, F.-P. Wenzl, J. R. Krenn and Emil J.W. List-Kratochvil

OE 56(9), 097102 (19 September 2017) [doi:10.1117/1.OE.56.9.097102]

Contribution: The author carried out all experimental and simulation work and wrote the manuscript. The manuscript was finalized with the co-authors.

Aluminum-nano disc-induced collective lattice resonances: Taking control of the light extraction in organic light emitting diodes

M. Auer-Berger, V. Tretnak, F.-P. Wenzl, J. R. Krenn and Emil J.W. List-Kratochvil

Appl. Phys. Lett. 111, 173301 (2017) [doi: 10.1063/1.4998802]

Contribution: The author carried out all experimental and simulation work and wrote the manuscript. The manuscript was finalized with the co-authors.

Superimposed Al nanoparticle gratings: Broadband enhancement of organic white light-emitting diodes

M. Auer-Berger, V. Tretnak, F.-P. Wenzl, J. R. Krenn and Emil J.W. List-Kratochvil

Article under preparation; Target journal Organic Electronics

Contribution: Investigated gratings were fabricated by V. Tretnak. Characterization of the gratings, fabrication of the OLEDs as well as the simulation work was carried out by the author. The author writes the manuscript and finalizes it with the co-authors.

Copper(I) Thiocyanate (CuSCN) / ammonium formate binary HIL/HTL layer system obtained from spin-coated aqueous solutions for high efficiency organic light emitting diodes
M. Auer-Berger, Alexander Fian, Paolo Melgari, Andreas Klug and Emil J.W. List-Kratochvil
Article under preparation; Target journal Advanced Electronic Materials
Contribution: The author performed all work on his own except for XPS, TEM and EELS characterization. Acquisition of the XPS spectra was performed by Alexander Fian. Acquisition of TEM images and EELS spectra was performed by Daniel Knez at FELMI Graz. In these cases, the author still performed evaluation of the acquired raw data. The author writes the manuscript and finalizes it with the co-authors.

List of not included publications

Blue light emitting polyphenylene dendrimers with bipolar charge transport moieties
G. Zhang, M. Auer-Berger, D.W. Gehrig, P.W.M. Blom, M. Baumgarten, D. Schollmeyer, E.J.W. List-Kratochvil and Müllen, K.
Molecules **2016**, *21*, 1400 [doi:10.3390/molecules21101400]

All-solution-processed multilayer polymer/dendrimer light emitting diodes
M. Auer-Berger, R. Trattnig, T. Qin, R. Schlesinger, M. V. Nardi, G. Ligorio, C. Christodoulou, N. Koch, M. Baumgarten, K. Müllen and E.J.W. List-Kratochvil
Organic Electronics, 35, 164-170 (2016) [doi:10.1016/j.orgel.2016.04.044]

Tetraaryl pyrenes: photophysical properties, computational studies, crystal structures, and application in OLEDs
T. H. El-Assaad, M. Auer, R. Castañeda, K. M. Hallal, F. M. Jradi, L. Mosca, R. S. Khnayzer, D. Patra, T. V. Timofeeva, J-L Brédas, E.J.W. List-Kratochvil, B. Wex and B. R. Kaafarani
Journal of Materials Chemistry C, 4, 3041-3058, 2016 [doi: 10.1039/C5TC02849C]

Properties of transparent and conductive Al:ZnO/Au/Al:ZnO multilayers on flexible PET substrates
T. Dimopoulos, M. Bauch, R.A. Wibowo, N. Bansal, R. Hamid, M.Auer, M. Jäger and E.J.W. List-Kratochvil
Materials Science and Engineering: B, 200, 84-92, 2015 [doi: 10.1016/j.mseb.2015.06.008]

Core-and-Surface-Functionalized Polyphenylene Dendrimers for Solution-Processed, Pure-Blue Light-Emitting Diodes Through Surface-to-Core Energy Transfer

G. Zhang, M. Baumgarten, M. Auer, R. Trattnig, E.J.W. List-Kratochvil and K. Müllen

Macromolecular Rapid Communications, 35(22), 1931-1936, 2014 [doi:10.1002/marc.201400439]

CHAPTER 7: Solution Processed Multilayer Organic Light Emitting Diodes

M. Auer, L. Pevzner, S. Sax and E.J.W. List-Kratochvil

Supramolecular Materials for Opto-Electronics, 226-272, RSC Publishing, 2014 [doi: 10.1039/9781782626947-00226]

Table of Content

1

Introduction

Organic light emitting diodes successfully established themselves as a superior technology for display applications. Once issues such as efficient solution-processible device stacks and lifetimes are solved, organic light emitting diodes are poised to also take a significant share of the lighting market

Starting with the introduction of the first Samsung Galaxy smartphone, displays driven by organic light emitting diodes (OLEDs) have continued to gain share in the small display market. With the recent introduction of the first iPhone featuring an OLED display it is clear that this technology, which started out as a niche player, has finally gained market acceptance and it is projected that by the end of this decade the majority of small area displays found in smartphones, smartwatches, etc. will be driven by OLED technology. This is in large parts possible by the low switching times, high contrast ratios, selectively active areas and the possibility to fabricate these displays on curved substrates. With recent advances with respect to the technology as well as the manufacturing capabilities the introduction of mass-market large area TV sets based on OLED technology by LG was made possible. A similar revolution has taken place in a related market, namely the lighting sector. Here, the venerable but inefficient incandescent lighting bulbs have been relegated to a niche position in the market thanks to regulations demanding more efficient means of light generations. Besides well-known fluorescent tubes, this allowed the field of solid state lighting (SSL) to become a major player in the lighting market. Here the efficiency gains result from the spectrally highly selective generation of light enabled by the radiative recombination process of electron-hole pairs. While highly efficient and compact designs are made possible by this technology, it suffers from the fact that the used inorganic light emitting diodes (LEDs) are point-sources. On top of that, inorganic LEDs are inherently inflexible, even though less elegant solutions that put several of these point-sources on a flexible foil exist. A better solution to mitigate these issues would be the usage of OLEDs. Specifically, OLEDs can be produced as area luminaires on a flexible substrate via a solution based roll-to-roll process compared to expensive vacuum sublimation techniques commonly used for the fabrication of OLED displays. This gives designers new possibilities for the design of lighting solutions as depicted in Figure 1-1. Specifically, using the fact that OLEDs can be area luminaires enables new forms of room illumination (see Figure 1-1.a) whereas fabrication on flexible substrates allows even curved light-generating areas (see Figure 1-1.b).

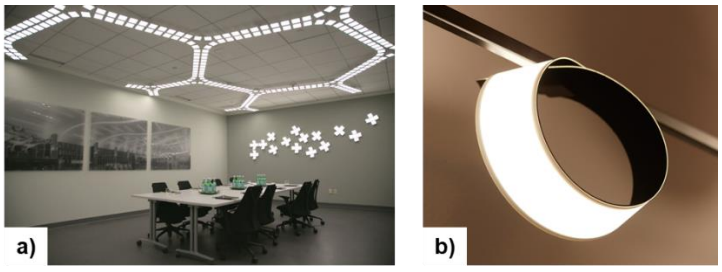

Figure 1-1. (a) Room lighting system and (b) a flexible OLED by LG (reproduced from [1] and [2] respectively)

Unfortunately, for a variety of reasons OLED luminaires are not yet mass-market products and are only available in limited quantities. The biggest challenges remain lower efficiencies and lifetimes when compared to inorganic LEDs. Complicating matters further is the fact that low-cost solutions processes required for mass-market penetration currently lead to even lower efficiencies and lifetimes and up till now often still require specially designed materials to avoid erosion of already processed layers.[3]

1.1 Structure of this work

This thesis investigates two avenues important for the further commercialization of OLED technology for lighting as well as display applications. To achieve that goal, the fabrication of combined hole injection and transport layers from a cheap solution processed route is presented as well as a strategy to facilitate the generation and outcoupling of light from the device. Therefore, the work is divided into two main chapters dealing with the respective subject.

Chapter 2 provides the theoretical background for the concepts that are presented within this thesis. Due to its broad scope, the theory chapter is divided into three subchapters. Chapter 2.1 introduces the reader to basic concepts of OLEDs, their working mechanism as well as to important quantities characterizing the light emission and color. Chapter 2.2 provides the basics required to understand collective lattice resonances (CLRs) as well as the extensively used optical simulation methodology. Lastly, Chapter 2.3 provides the reader with basic knowledge on amorphous metal oxide semiconductors.

Chapter 3 deals with a novel way of processing copper (I) thiocyanate using aqueous ammonia as a solvent to prepare hole injecting and transporting films via a low-cost solution processing route. A brief introduction is given after which the surface energy and morphology of the processed films is characterized followed by a compositional analysis via X-ray photoelectron spectroscopy as well as electron energy loss spectroscopy. The optical bandgap as well as the optical constant are determined via absorptance and ellipsometry measurements. Through impedance spectroscopy and electrical characterization of hole-only devices, the trap density of states as well as other important parameters affecting the transport of charge carriers are investigated. Finally, the effectiveness of the presented layers is demonstrated using the example of two different OLED stacks.

Chapter 4 highlights a promising way to facilitate the generation and extraction of light from OLEDs using CLRs induced by aluminum nano disc arrays. After a short introduction into recent efforts, the presence of the CLRs within the weak optical resonator configuration of an

OLED is verified. Then the dependency of these CLRs on parameters such as the lattice constant, the disc size and the thickness of the emissive layer is elucidated. Using optimized values, the influence of this optimized configuration on the efficiency of a monochromatic device is explored. Then, the presented concept is expanded by superimposing a second grating which results in the formation of CLRs over a spectrally broad range that allows application in a white light emitting OLED. Analogously to the monochromatic OLED, the impact of these gratings on the operating behavior as well as the device efficiency is investigated.

Chapter 5 provides a short summary and conclusion of the presented work.

2

Theory

Basic concepts, necessary to follow the work in this thesis, are presented. Starting with the operating principle of OLEDs as well as the characterization of light, the reader is further introduced to the field of plasmonics. Culminating in the basic principle of collective phenomena, the foundations of metal oxide semiconductors are detailed which encompass concepts of charge transport in amorphous metal oxide semiconductors.

2.1 Organic light emitting diodes

2.1.1 Organic semiconductors – A little history and basics

The first foray into the world of organic semiconductors happened when Williams and Schadt investigated electroluminescence (EL) properties of an anthracene crystal.[4] With the high bias voltages of 100 V necessary to obtain EL it was clearly only the start of the field of OLEDs. Nonetheless, this work sparked considerable research interest that culminated in the first reasonably efficient OLED by Tang and VanSlyke in 1987[5] which was based on evaporated small molecules. Around the same time, Heeger et. al demonstrated that electrical conductivity in organic polymers can be increased through doping.[6–8] The next breakthrough occurred with the demonstration of an OLED based on solution-processed polymers.[9] With the development of first organic photovoltaic cells (OPV) the field of organic semiconductors finally transitioned from fundamental to applied research which has continued to this day.

Before more complex topics can be discussed, it is necessary to define what actually constitutes an organic semiconductor. A perfect example is given by the aromatic molecule benzene (see Figure 2-1). It consists of six carbon atoms which are arranged in a ring. The alteration between single- and unsaturated double bonds that result from sp_2-hybridization leads to the formation of a delocalized π-electron system (orange ring in Figure 2-1.a). From molecular orbital theory (MO-theory)[10] it follows that these molecular orbitals (MOs) can be expressed as a linear combination of the contributing atomic orbitals. It's this combination of the s- and p_z-orbitals of carbon which causes the formation of bonding (σ, π) and antibonding orbitals (σ^*, π^*) (Figure 2-1.b). Since the binding energy of π-orbitals is lower, the highest and lowest occupied molecular orbitals (HOMO, LUMO) are formed solely by π and π^* orbitals. A band like behavior is induced by the fact that the individual π-orbitals are not at the same energy level which results in a behavior qualitatively comparable to inorganic semiconductors. Finally, the semiconducting properties stem from the contrast between a fully occupied bonding π-orbital versus a fully depleted antibonding π^*-orbital.[11] Thus, the band gap is defined by the delocalization of the π-electrons which further depends on the geometry and the elemental composition of the molecule.

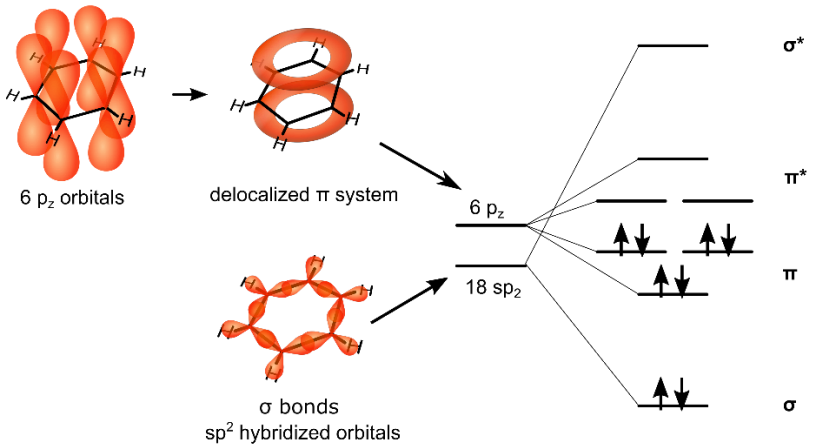

Figure 2-1. Formation of HOMO and LUMO in benzene through hybridization of sp^2 orbitals and consecutive overlap of $\boldsymbol{\pi}$-bonds (modified from [12]).

2.1.2 Excited states and optical transitions

An important difference between organic and inorganic semiconductors stems from the pronounced electron-lattice coupling. In detail, this entails a reaction of the lattice upon the addition or removal of an electron as well as the promotion of an electron to an excited state. As a result of these relaxation processes, the excited states in organic semiconductors are markedly more localized than the ones in their inorganic counterparts.[13] This makes it useful to describe them as quasi-particles which consist of the localized excitation as well as the resulting lattice relaxation. For the operation of an OLED two types of quasi-particles, the singly charged polaron and the exciton, are of particular importance.

For an actively driven semiconductor device to perform something useful, a charge carrier first needs to be introduced into the system. For an organic semiconductor this means that upon the injection of a charge carrier, the lattice of the organic semiconductor relaxes to accommodate the disturbance introduced by the carrier. This results in the formation of a polaron which, depending on the type of charge carrier, is either positively (hole) or negatively (electron) charged. As a consequence of the electron-lattice coupling, these quasi-particles are rather localized. Furthermore, due to the affected change of the electronic energy, intra-band states are formed within the π-π* gap of the undistorted system.

Having seen the effects of an introduced additional charge, it's time to discuss the quasiparticle that gets formed upon the optical excitation or the merger of two oppositely charged polarons within an organic semiconductor. Here, the formed quasi-particle, the exciton, is neutral and consists of an electron-hole pair bound by coulombic interaction.[14] Akin to the polaron, the formation of an exciton involves a change in the lattice geometry and again leads to the formation of intra-band states. This allows the formation energy of an exciton to be lower than

the π-π* energy gap. As a consequence of the localization and the binding energy the exciton is classified as a Frenkel exciton. An important distinction between the exciton and the polaron lies within the number of the overall spin of the electron-hole pair. Since both charge carriers are fermions, they have a spin of ±1/2. Due to the Pauli's principle either the spatial or the spin part of the wavefunction needs to be asymmetric. Therefore, four different states for an exciton exist: one state where the spatial part of the wavefunction is symmetric and the spin is asymmetric with a total spin of 0 and three states with an asymmetric spatial wavefunction and a symmetric spin part with a total spin of 1. The first type is the singlet whereas the second one is the triplet exciton. Of note is the reduced energy of the triplet exciton which arises from the asymmetric spatial wavefunction that leads to lower electron-electron repulsion.

There are several ways by which the exciton can decay to the ground state (depicted in the Jablonski diagram in Figure 2-2). Here, in the context of a molecule, an exciton means the first excited state (S_1). From S_1, the exciton can decay back radiatively to the ground state via fluorescence or non-radiatively by the generation of heat. Another mechanism is provided by intersystem crossing (ISC) where the singlet exciton transforms to a triplet exciton (T_1). As can be inferred from Figure 2-2, from T_1, the ground state can only be reached by non-radiative decay phosphorescence. Singlet excitons can be formed by photo-excitation whereas triplet excitons cannot be directly formed. However, through intersystem crossing, a transfer to the triplet state is also possible albeit less likely.

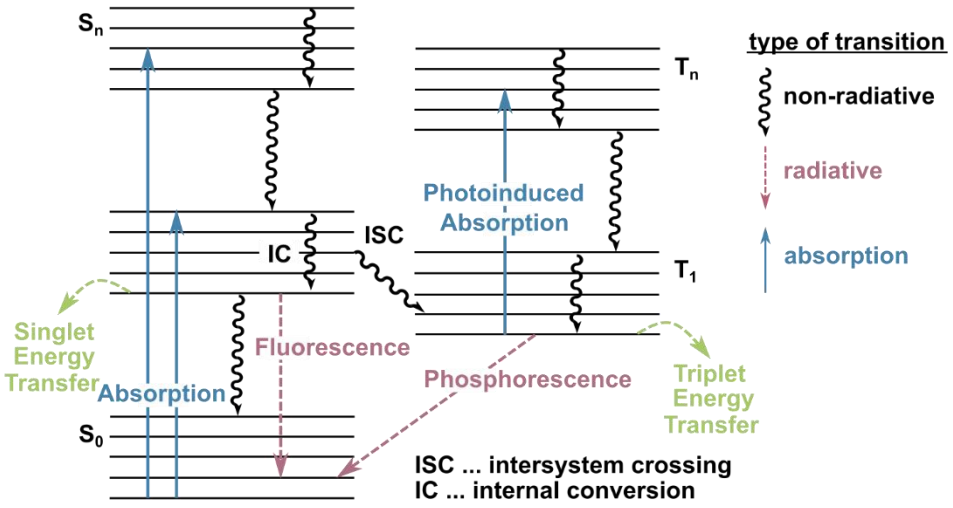

Figure 2-2. Jablonski-diagram depicting the various radiative and non-radiative processes in a molecule

One way to still be able to use these triplet-excitons for the generation of light rests in the usage of phosphorescent emitters that employ strong spin-orbit coupling of transition metals like Iridium (Ir) or Platinum (Pt). These emitters are able to soften the selection rules for electronic

transitions. The phosphorescent emitters used as dopants throughout this work are depicted in Figure 2-3.

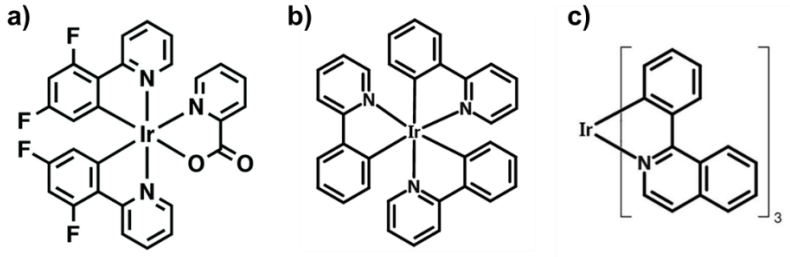

Figure 2-3. Chemical structure of the phosphorescent emitters used throughout this work: (a) FIrpic (blue), (b) $Ir(ppy)_3$ (green) and (c) $Ir(piq)_3$ (red)

To exploit the converting properties of these emitters, they are embedded in a host-guest system that consist of a purely organic semiconducting material (matrix) and the transition metal complex (guest). The matrix fulfills several properties such as charge carrier transport and prohibition of self-quenching often observed in phosphorescent emitters.[15,16] More details can be found in the excellent review by Tao et. al.[17]

An important metric for the efficiency of the fluorescence process is the fluorescence quantum yield η_{PL} which is defined as the ratio between the radiative and non-radiative recombination given by

$$\eta_{PL} = \frac{k_r}{k_r + k_{nr}} \tag{2.1}$$

where k_r is the radiative and k_{nr} is the non-radiative decay rate constant.

2.1.3 Working principle of OLEDs

Injection of charge carriers

In order to obtain efficient organic devices, the injection of charge carriers needs to be efficient as well. The situation of a metal and an organic semiconductor before contact is depicted in Figure 2-4.a. Here, the Fermi level of the metal and the Fermi level of the organic material are clearly different. Once a contact between the metal and the organic is established (see Figure 2-4.b), vacuum level and band bending is assumed, which corresponds to the Mott-Schottky case. This is thought to achieve Fermi level alignment. However, as it has been shown, vacuum level alignment between organic and metal interfaces is inhibited by the formation of interface dipoles[18,19] that can induce a vacuum level shift of up to 1 eV[20]. Sources for this interface dipole, just to name a few, are mechanisms such as charge transfer across the interface, interfacial chemistry reactions and redistributed probability densities of electrons.[21]

This leads to the formation of hole and electron injection barriers, Φ_h and Φ_e which are defined as follows

$$\chi_h = HOMO - \Phi_a - \Delta_a \tag{2.2}$$

$$\chi_e = \Phi_c + \Delta_c - LUMO \tag{2.3}$$

where Φ_a is the work function of the anode, Φ_c is the work function of the cathode and Δ_a as well as Δ_c are the interface dipoles formed between the interface of the organic and the anode as well as the cathode respectively. By convention, a positive value of Δ denotes a rise of vacuum level. Besides the charge carrier barriers, the built-in field is another important factor in obtaining efficient devices which needs to be overcome by an external bias voltage exceeding $V_{bi} = \Phi_{bi}/q$ where

$$\Phi_{bi} = \Phi_a - \Phi_c \tag{2.4}$$

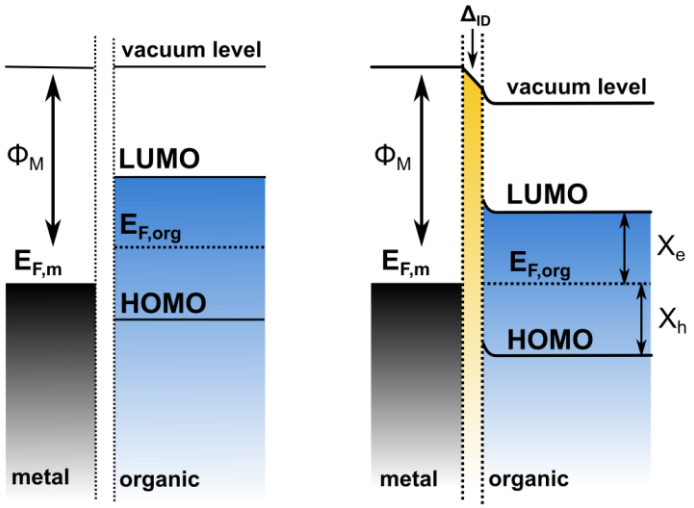

Figure 2-4. (a) Energy levels before contact of a metal and an organic semiconductor. (b) Both materials are in contact and vacuum level alignment with band bending takes place to achieve Fermi level alignment.

Charge carriers need to overcome the injection barriers χ_h and χ_e for holes and electrons respectively. For maximum efficiencies, a balanced injection is required which is described by the charge balance factor γ. Ideally these barriers are close to 0 eV or otherwise the turn-on voltage of the device exceeds V_{bi}.

To overcome the prevalent injection barriers two mechanisms are of relevance. The first one, which is dominant at low electric fields, is a thermionic emission process where the likelihood of overcoming the injection barrier increases with increasing temperatures. The resulting current density is described by the Richardson-Dushman equation[22,23]

$$J = A^* T^2 exp\left(-\frac{q\chi}{kT}\right) \tag{2.5}$$

with the potential barrier χ, the absolute temperature T, Boltzmann's constant k and the material dependent Richardson constant A^*. The temperature dependence of eq.(2.5) reveals that this mechanism only contributes significantly to the current density when the temperature is high. However, as this is generally not the case in organic semiconductors, most of the current density stems from Fowler-Nordheim tunneling[24] through the potential barrier. This tunneling mechanism can be expressed by

$$J = \alpha \frac{E^2}{\chi} exp\left(-\frac{8\pi\sqrt{2m^*}\chi^{\frac{2}{3}}}{3eEh}\right) \tag{2.6}$$

where E is the applied electric field, m^* represents the effective mass of the charge, χ is the potential barrier, e the elementary charge, α is the material constant and h is Planck's constant. From the quadratic dependence on the applied electric field it is clear that this mechanism is the dominant one in OLEDs.

Transport of injected carriers

The injected holes and electrons transport as polarons via the HOMO and LUMO, respectively, to the emissive layer. The balance factor γ is heavily influenced by the transport layers via the mobility of the charge carriers, the injection barriers as well as the charge confinement properties.

Formation of excitons

The transported positive and negative polarons recombine and form an exciton. From simple statistics it follows that roughly 75% of the excitons are triplets and 25% are singlets. For architectures which don't employ phosphorescent emitters to convert the generated triplet excitons into light this puts a severe limit on the attainable efficiency of the device. The ratio between singlet and triplet excitons is measured by $\eta_{S/T}$. As indicated by the dotted arrows in Figure 2-5.b, any lack in confinement by barriers for holes and electrons between the emissive layer (EML) and the electron as well as the hole transport layer also results in an unbalanced γ. The factor γ is defined as

$$\gamma = \frac{j_R}{j_{tot}} \tag{2.7}$$

with the recombination current density $j_R = j_h - j_h' = j_e - j_e'$ and the total current density $j_{tot} = j_h + j_e' = j_e + j_h'$. $j_{e,h}$being the injected electron and hole currents, respectively, while the primed quantities indicate the carriers leaving the device in the opposite direction without

recombination. Values close to unity are obtainable via additional selective carrier and exciton blocking layers.[25,26]

2.1.4 Generation of light

Light is generated from the exciton when it decays radiatively. This is described by the effective quantum efficiency q_{eff} which is a ratio between radiative and non-radiative processes in an environment with different refractive indices or metal electrodes. q_{eff} is defined as

$$q_{eff} = \frac{\Gamma_r^*}{\Gamma_r^* - \Gamma_{nr}} = \frac{F \cdot \Gamma_r}{F \cdot \Gamma_r + \Gamma_{nr}} \tag{2.8}$$

where Γ_r^* is the modified radiative decay rate, Γ_{nr} is the non-radiative decay rate and F is the Purcell factor describing the modification of the decay rate via the Purcell effect[27–29]. Note that Γ_{nr} is not affected by the electric environment.[30] The amount of light that is able to fully escape the device without being reabsorbed, converted to a plasmon or trapped in a waveguide is measured through the outcoupling factor η_{out}.

A graphical summary of these processes is depicted in Figure 2-5.a. Here, a bias voltage sufficiently large to overcome V_{bi} as well as the injection barriers χ_e and χ_h is applied. In the best-case scenario, a balanced injection is possible with only one layer. In reality however, the injection and/or transport of the charge carriers is more efficient for one charge carrier species which manifests itself in reduced device efficiencies. To overcome or at least reduce the magnitude of this issue, highly efficient OLEDs use multilayer structures at least composed of a hole injecting/transporting layer (HIL/HTL), the EML as well as an electron injecting/transporting layer (EIL/ETL) (Figure 2-5.b). Besides lowering the injection barriers by providing an additional step, the additional transport layers provide a barrier for the opposite charge carriers which allows for a more effective confinement of charge carriers which often results in increased device efficiencies.

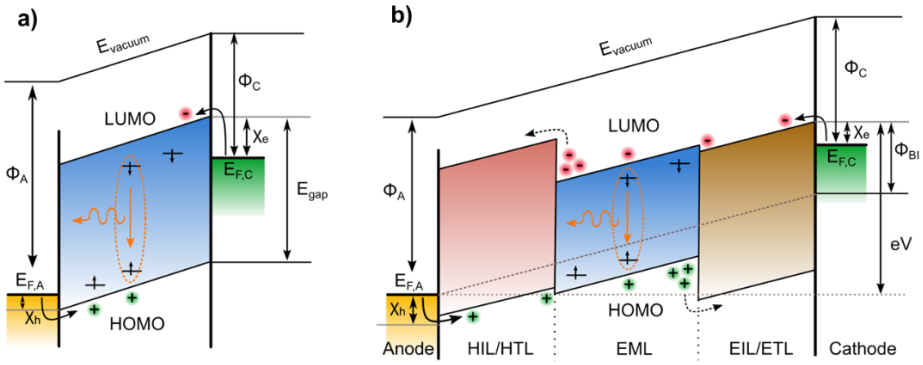

Figure 2-5. Energy diagram (a) of a single layer and (b) triple layer OLED under forward bias with the basic EL generating processes indicated. Here, the applied bias voltage exceeds $\boldsymbol{V_{bi}}$ and charge carriers become injected.

All these processes are reflected in the external quantum efficiency (EQE) of an OLED which is the ratio between injected carriers and emitted photons[31]

$$\eta_{EQE} = \gamma \cdot \eta_{S/T} \cdot q_{eff} \cdot \eta_{out} \tag{2.9}$$

with the charge carrier balance factor γ, the ratio between singlet and triplet excitons $\eta_{S/T}$, the effective quantum efficiency q_{eff} and the outcoupling factor η_{out}.

2.1.5 Outcoupling losses

So far, the η_{out} has been missing. To further discuss this factor, the EQE of a typical OLED is depicted in Figure 2-6 as a function of the ETL thickness. Evidently, trapping of light in various optical modes, such as the substrate, dielectric waveguides as well as surface plasmon polaritons (SPP), is the dominant loss mechanism which results in the outcoupling of only 20% of the generated light for an optimized layer geometry.[32]

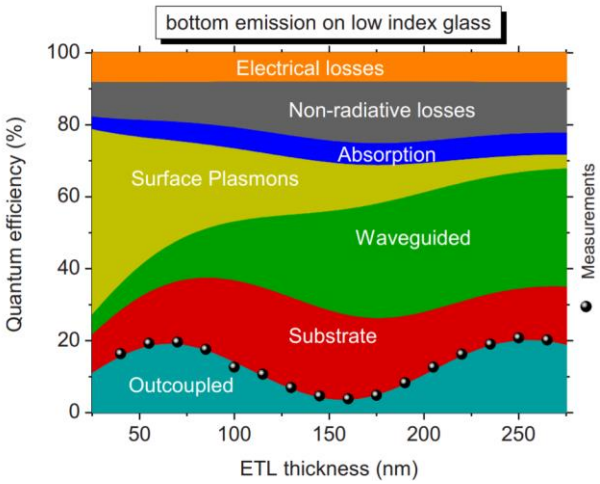

Figure 2-6. Measured EQE of an OLED as a function of the ETL thickness. The distribution of all loss channels are clearly depicted (taken from [33])

Since the active influence on the light extraction behavior of the OLED is an integral part of this thesis, the three major loss mechanisms are schematically pictured in Figure 2-7. The SPPs are excited by the evanescent field from the emitter molecules (Figure 2-7 top) and correspond to a transversal-magnetic (TM) mode. On the other hand, the waveguide and substrate modes are classical optical modes resulting from total internal reflection (see chapter 2.2.5) which is influenced by the refractive indices of the various OLED layers.

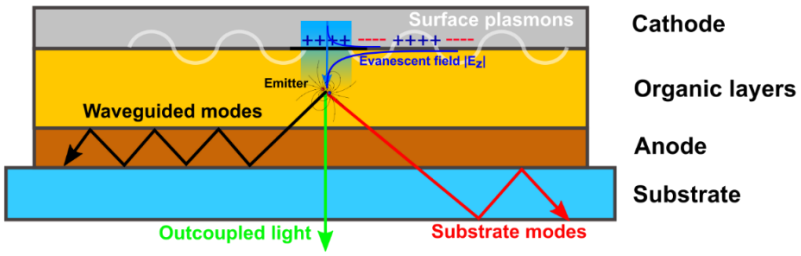

Figure 2-7. Illustration of the different optical loss channels of an OLED. Right hand side shows extraction of substrate mode by an index matched hemisphere whereas the left-hand side has no mechanisms that allow the outcoupling of trapped light.

The key take-away here is that the EQE can only be maximized, when the amount of light trapped in the various optical modes is reduced.

2.1.6 Quantifying light and color of OLEDs

Since the design and measurement of OLEDs is performed by factoring in the way humans perceive light, it is beneficial to talk about the quantities characterizing a light source. Here, two types of quantities exist: the radiometric quantities which are physical properties and the photometric ones, which include the response curve of the human eye. Naturally, quantities that include the human response curve are favored for applications such as lighting or display applications. The conversion between these quantities is performed by the eye sensitivity function (Figure 2-8). The human eye has an observable range between 380 nm and 780 nm with a peak sensitivity at $\lambda = 555\ nm$ in photopic vision (well-lit condition). Presently, the Commission Internationale de l'Eclairage (CIE) defines two sensitivity curves, the CIE 1931 and the CIE 1978 $V(\lambda)$. Even though the latter is more accurate than the former it is not the standard.[34]

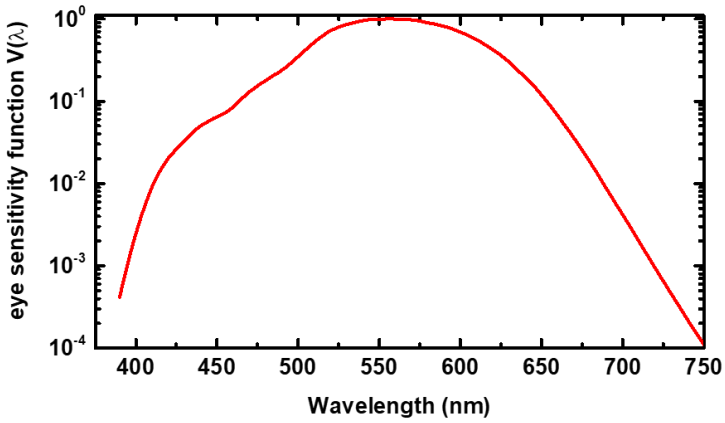

Figure 2-8. Eye sensitivity function $V(\lambda)$ as defined by CIE1931. Peak sensitivity is at $\lambda = 555\ nm$.

Via this definition candela (cd) is defined as[34]: *a monochromatic light source emitting an optical power of (1/683) W at 555 nm into the solid angle of 1 sr has a luminous intensity of 1 cd*. The corresponding photometric quantity, luminous intensity, quantifies the intensity of a light source as perceived by the human eye.

Also, lumen (lm) is defined as[34]: *a monochromatic source emitting an optical power of (1/683) W at 555 nm has a luminous flux of 1 lm*. Here, the corresponding quantity is the luminous flux, which measures the power of light as perceived by the human eye. From these two definitions it follows that 1 $cd = 1\ lm\ sr^{-1}$ and equally that 1 $cd = 4\pi\ lm$ for an isotropic emitter.

The luminous flux per unit area is measured by the illuminance with the corresponding unit being defined as 1 $lux = 1\ lm\ m^{-2}$.

Important especially for display applications is the luminance of a surface source where the ratio of the luminous intensity in a certain direction is divided by the projected surface area $A \cdot cos\ \theta$ where θ is measured against the normal vector of that surface in said direction. Luminance carries the unit 1 $cd\ m^{-2}$.

Table 2-1 provides a summary of relevant radiometric and photometric quantities.

Table 2-1. Radiometric and corresponding photometric units

radiometric unit	dimension	photometric unit	Dimension
radiant flux	W	luminous flux	lm
radiant intensity	$\frac{W}{sr}$	luminous intensity	$\frac{lm}{sr} = cd$
irradiance	$\frac{W}{m^2}$	illuminance	$\frac{lm}{m^2} = lux$
radiance	$\frac{W}{sr \cdot m^2}$	luminance	$\frac{lm}{sr \cdot m^2} = \frac{cd}{m^2}$

Finally, a way to unambiguously characterize the emission color needs to be defined. This is performed by color matching functions which project the way the human eye perceives color. For this reason, three functions for the blue, green and red cone are defined as CIE1931 functions for a standard 2° observer[34] which are reproduced in Figure 2-9.

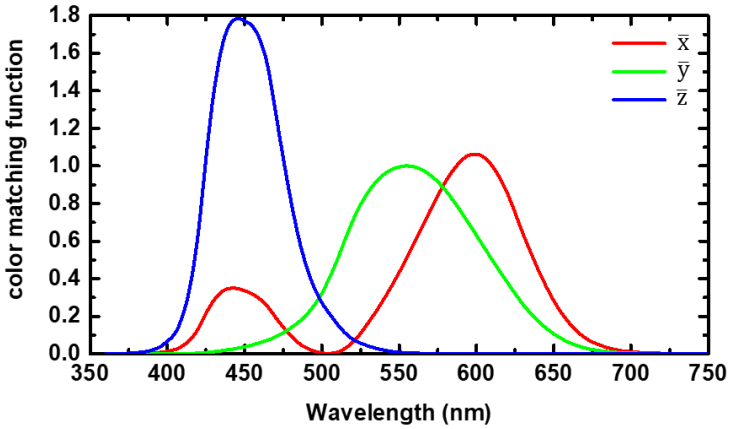

Figure 2-9. Color matching functions $\bar{x}$ (red), $\bar{y}$ (green) and $\bar{z}$ (blue) as defined in CIE1931 for a standard 2° observer.

With the help of these functions the tristimulus values X, Y and Z are calculated by

$$X = \int_{\lambda} \bar{x}\,(\lambda) P(\lambda) d\lambda \tag{2.10}$$

$$Y = \int_{\lambda} \bar{y}\,(\lambda) P(\lambda) d\lambda \tag{2.11}$$

$$Z = \int_{\lambda} z\,(\lambda) P(\lambda) d\lambda \tag{2.12}$$

These values give the power of each of the three primary colors for a given power-spectral density $P(\lambda)$. In a last step, the chromaticity coordinates x, y and z are defined as

$$x = \frac{X}{X+Y+Z} \tag{2.13}$$

$$y = \frac{Y}{X+Y+Z} \tag{2.14}$$

$$z = \frac{Z}{X+Y+Z} = 1 - x - y \tag{2.15}$$

With this definition x and y is sufficient to describe the color of a light source. Furthermore, with the definition of $\bar{y}$, it follows that eq.(2.11) yields the luminance of a color. These values are plotted in a chromaticity diagram as depicted in Figure 2-10. The outline is described by monochromatic light sources. Within the so-called horseshoe all colors are located. The point of equal energy E at $(x, y) = (1/3, 1/3)$ centered in this diagram corresponds to a constant spectral distribution or in other words, white light. Hence, the nuances of white light are located close to this value.

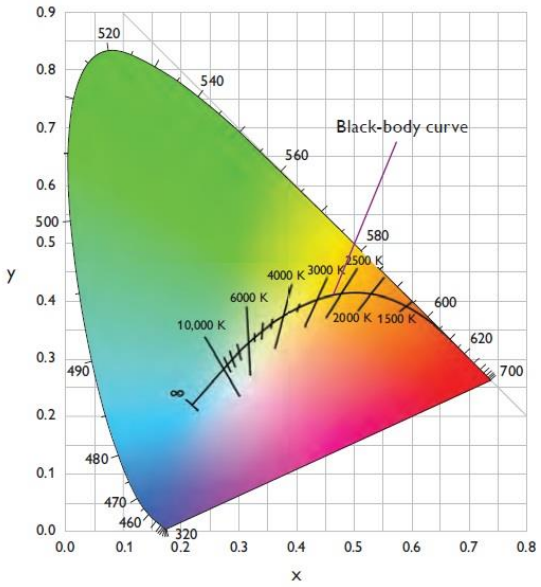

Figure 2-10. CIE1931 chromaticity diagram. (reproduced from [35])

2.2 Collective lattice resonances through guided modes

Plasmonics is a research field dedicated to studying the response of metals to electromagnetic radiation which received its name from the radiatively driven collective, damped, electronic oscillations found in SPPs or localized surface plasmon polariton (LSPP). In this subchapter, a brief overview over historical developments relevant for this thesis is provided. In a next step, the LSPP and the associated loss mechanisms are briefly discussed before focusing on collective resonances and the two major mechanisms driving them. Lastly, the principles behind finite-difference time domain (FDTD) simulation are briefly discussed.

2.2.1 Relevant historic developments

Back in ancient times the optical properties of metal nanoparticles were used to color Roman cups made of dichroic glass[36,37]. In 1908, this behavior was rigorously explained by Gustav Mie, who connected the extinction behavior of these metal colloids to the size dependence of the resonance frequency of surface electromagnetic resonances or LSPPs.[38] This contribution sparked decade long in-depth research which established that the spectral position of the LSPR is not only dependent on the size but also on the geometry of the nanoparticles. With the scattering and absorption properties of these metallic nanoparticles well established, it was only a question of time before the first attempts to modify light emission with these resonances were started. Arguably the first stepping stone in this direction was the far reaching work by Purcell.[39] At a first glance unrelated to the optical properties of metallic nanoparticles, Purcell showed that the lifetime of an excited emitter can be reduced by placing an emitter inside a resonator. This leads to an enhancement of the emission rate proportional to the ratio between

the quality factor of the resonator and the mode's volume. It wasn't before the 1980's when Gersten, Nitzan and co-works examined the fluorescence and Raman scattering behavior of molecules on jagged metallic surfaces.[40,41] Their studies showed the markedly increased fluorescence from molecules located in the valley of nanoscale features of the metal. Around the same time theoretical work appeared which predicted large gains in fluorescence intensity for molecules located between well-defined metallic particles. Still, experimental setup made it difficult to discern between geometric contributions and the lightning rod effect (increased charging of sharp features). From here, work continued with fluorescent emitters located on metallic surfaces where modifications of the decay rate were made possible by the increased photonic mode density provided by the metal.[42,43] These additional decay channels in smooth metal films originate from propagating SPPs[44] whereas the rough metal surface supports the formation of localized SPPs also known as LSPPs. This revelation provided the missing link to Purcell's discovery as the SPPs provide a channel into which emitters can efficiently decay.[45–48] A similar mechanism is provided by the LSPPs.[40,41,49] The next important milestone was achieved in 1998 by Ebbesen and co-workers who observed that at a certain frequency thin metallic film with nanoholes transmitted more light intensity than geometrically incident on the holes.[50] This extraordinary transmission happened at hole diameters much smaller than the incident wavelength, thereby contradicting Bethe's theory which predicts a cutoff with a scaling as $(b/\lambda)^4$ for $\lambda \gg b$. Details describing the role of LSPPs, SPPs through the film as well as diffraction effects can be found in the literature.[51–54] The important aspect of this phenomenon for this work is the fact that at resonance the electromagnetic cross-section becomes larger than the geometric one.[55] Since Babinet's principle is valid, the situation for holes also applies for arrays of nanoparticles with the distinction that the extraordinary transmission becomes extraordinary extinction and nanoparticles don't support the propagating SPPs. In 2003, two groups[56,57] independently recognized that the extraordinary transmission is characterized by a Fano lineshape.[58] This observation was rather remarkable since Fano resonances have originally been observed in the autoionization spectra of Helium as a consequence of the interference of a continuum of states with a discrete state within those states. In the context of classical electromagnetic fields, the occurrence of Fano lineshapes was interpreted as the interaction between transmitted non-resonant and resonant light. The non-resonant transmitted light corresponds to the continuum of states while the resonant transmitted light (Rayleigh anomalies, guided modes as discussed later in this theory section) assumes the role of the discrete state. Based on these observations, theories regarding plasmonic resonances in sub-wavelength hole and nanoparticle arrays emerged where the interference effects as described by Fano stem from the coupling of two Lorentzian oscillators with broad and narrow resonances.[59] These contributions proofed valuable for the recent

formulation of a coupled oscillator model which was found to describe the transition between the weak and strong coupling regime.[60]

2.2.2 Localized surface plasmon polaritons

Plasmons are the consequence of the electron density following the incident electromagnetic fields. In the case of a metal film, this results in the formation of propagating SPPs as mentioned earlier. In the case of metallic particles, the SPPs are confined by the geometry which leads to the propagation of the SPP along the interface of the particle and the dielectric. This results in the polarization of the electron gas when an electromagnetic wave hits the metallic nanoparticle (NP). Through the restoring force a plasmonic oscillation forms as depicted in Figure 2-11. The geometry and the material properties of the NP defines the oscillator and thus governs the optical properties.[61]

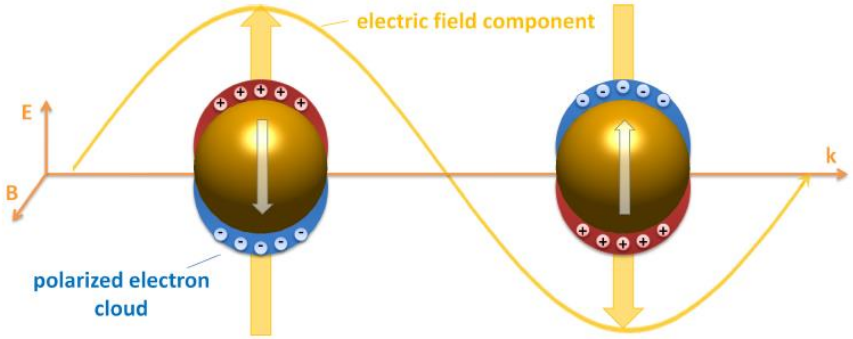

Figure 2-11. Excitation of a LSPP. The plasmons oscillate with a 90° phase difference at the resonance frequency. The magnetic polarization can be neglected most of the time. (reproduced from [62])

Generally, to describe the LSPP of an arbitrarily shaped particle requires a multipole expansion of the field within the nanoparticle of several plasmon modes at a given frequency. For simplicity, often only the dominant term in the expansion is considered. As previously mentioned, a full analytical model for spherical and spheroidal particles is provided by Mie's theory.[63] Even further simplifications can be made for NPs considerably smaller than the wavelength of the impinging light.[64] Within this quasi-static approximation (also known as Rayleigh approximation)[65] the LSPP can be described through simple expressions with known parameters. This allows to calculate the polarizability of small spherical NPs by

$$\alpha(\lambda) = 4\pi\varepsilon_0 R^3 \left| \frac{\varepsilon(\lambda) - \varepsilon_m(\lambda)}{\varepsilon(\lambda) + 2\varepsilon_m(\lambda)} \right| \tag{2.16}$$

with ε_0 being the vacuum permittivity, R the particle radius, ε_m and $\varepsilon = \varepsilon' + i\varepsilon''$ are the real relative permittivity of the surrounding medium and the complex relative permittivity of the

particle. With the polarizability of the particle the scattering and absorption cross-sections are given by:

$$\sigma_{sca} = \frac{k^4}{6\pi\varepsilon_0^2}|\alpha(\lambda)|^2 \tag{2.17}$$

$$\sigma_{abs} = \frac{k}{\varepsilon_0}|Im(\alpha(\lambda))|^2 \tag{2.18}$$

Using eq.(2.17), the scattering cross section of the NP can be calculated for a spherical gold particle. From Figure 2-12.a. the effect of the diameter on the position of the LSPP can be seen. To also elucidate the geometry aspect, a sphere is squeezed to a rod-like particle as depicted in Figure 2-12.b which has reveals a strong dependence of the location of the LSPP on the aspect ratio. From Figure 2-12.c, the strong dependence of the position of the resonance on the dielectric medium surrounding the particle is visible.[66]

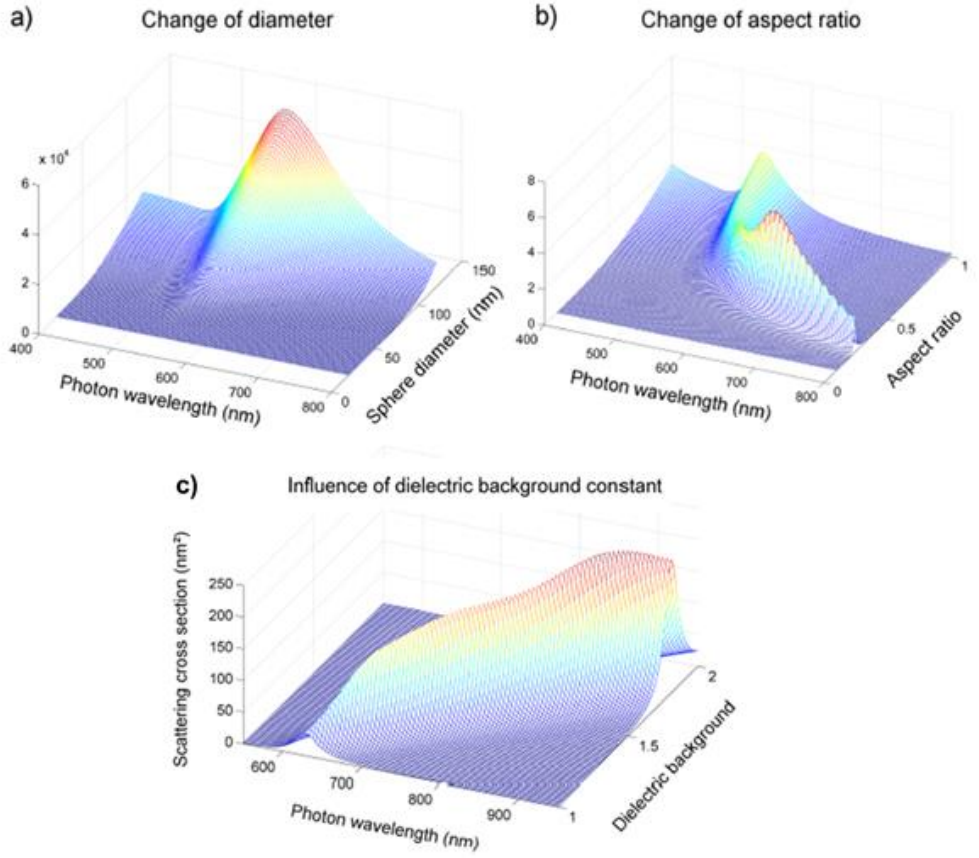

Figure 2-12. Tunability of the LSPP of a gold nanosphere with respect to (a) changing the diameter and (b) squeezing its aspect ratio. (c) Dependence of the scattering cross section of a gold nanorod with 10 nm diameter and 35 nm arm length is plotted. All plots depict the scattering cross section (taken and modified from [62])

2.2.3 Loss mechanisms in LSPPs

Recalling that the LSPPs are coherent charge density oscillations of the electron gas induced by an external field it is clear that coherence can easily be lost by scattering events. An easy way to picture this dephasing would be the ejection of an electron from this coherent motion caused by an impurity, phonon or other electrons. Even though the loss in kinetic energy is minimal, the phase coherence gets destroyed which diminishes the quality of the resonance. An overview of the dominant processes is given in Figure 2-13.

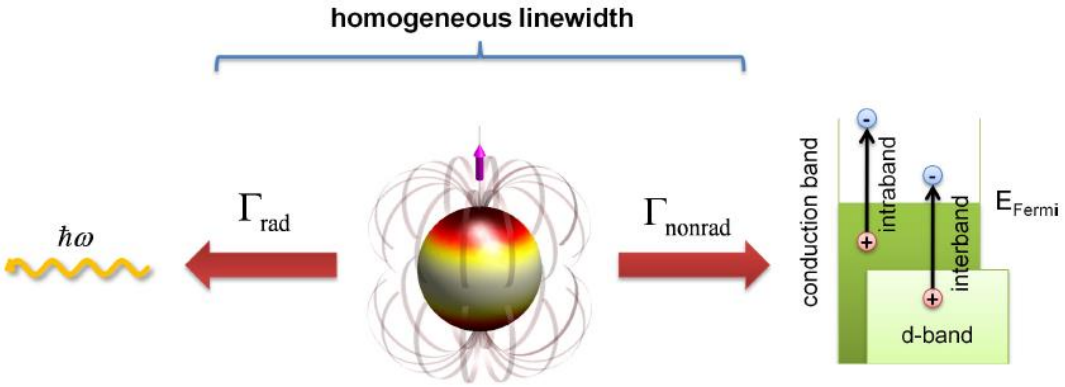

Figure 2-13. Shortly after the excitation the plasmon starts to decay. This happens either via intra- and interband transitions (right) or radiatively (left). These decay channels contribute to the homogeneous linewidth Γ. (taken from [62])

As a consequence of the radiative and nonradiative decay processes highly excited electron-hole pairs further thermalize on a sub-ps scale through additional collision processes[67,68] to a distribution of hot charge carriers[69]. The time scales of these processes are plotted in Figure 2-14. The homogeneous linewidth Γ is defined as the full width at half maximum of the spectral resonance of a plasmon and is proportional to the inverse of the decay time τ.

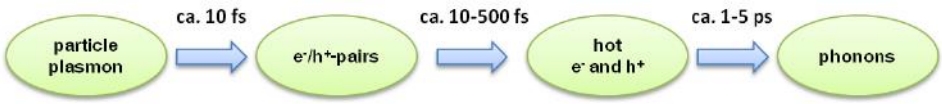

Figure 2-14. Typical plasmon decay times[69]. Approximately 10 fs after the excitation of a particle plasmon it decomposes into electron-hole pairs. On a sub-ps timescale, a distribution of hot electrons and holes is formed. In a final step the heat is transformed to the lattice as heat through electron-phonon coupling (taken from [62]).

Thus, it is clear that increased damping is caused by impurities and defects in the crystal structure of the nanoparticle which leads to broadened spectral linewidths.

2.2.4 Optical antennas

An optical antenna provides an efficient interface between free-space radiation and localized energy. In term of metallic NPs this means a coupling between the LSPP and a light source or receiver.[70–76] In modern technology, antennas are ambiguous for transmitting and receiving data sent on RF bands. An important distinction however remains in the fact that the excitation of an LSPP results in an electric field that is not zero within the metallic NP. This in turn disables the simple scaling law for antennas with respect to the frequency. Here, the dielectric function of the metal leads to a frequency dependence of the antenna behavior. As the frequency approaches the plasma frequency of the metal, electrodynamic effects become ever more important. This allows to tune the field penetration as well as the energy dissipation in the metal and gives metallic nanoparticles their published antenna properties. Specifically, by coupling them to nanoscale light sources they can provide directivity gains[77–80], polarization control[81,82], intensity enhancements[71], decay rate enhancements[83,84] as well as spectral shaping[85,86]. As will be demonstrated in the next subchapter these beneficial properties of single nano antennas can be further enhanced by coupling them with photonic modes.

2.2.5 Collective lattice resonances

So far, the electromagnetic response of a single metallic NP has been discussed. While the observed effects are interesting, richer physics is unveiled when at least two particles are coupled. In the context of an OLED this can happen through Rayleigh anomalies or guided modes. First however, it is educational to demonstrate the impact of the coupling on the shape of the plasmonic resonance of a metallic nanoparticle. For this reason, the behavior of two coupled metallic NPs is studied by treating them as coupled harmonic oscillators. For this simple system the equations of motion in matrix form are

$$\begin{pmatrix} \omega_1^2 - \omega^2 - i\gamma_1\omega & \Omega^2 \\ \Omega^2 & \omega_2^2 - \omega^2 - i\gamma_2\omega \end{pmatrix} \begin{pmatrix} x_1 \\ x_2 \end{pmatrix} = \begin{pmatrix} \frac{F}{m} e^{-i\omega t} \\ 0 \end{pmatrix} \tag{2.19}$$

where the eigenfrequencies of the two oscillators are $\omega_{1,2}$, $\gamma_{1,2}$ are the loss rates and the coupling rate is given by $\Omega_{1,2}$. The dissipated power in steady-state is given by $1/2\Re[F^*\dot{x}_1]$ is depicted in Figure 2-15 for the values $\omega_1 = \omega_0$, $\omega_2 = 1.4\omega_0$, $\gamma_1 = 0.4\omega_0$, $\gamma_2 = 0$ and $\Omega = 0.35\omega_0$. Interestingly, a broad peak similar in shape to the resonance of a single, uncoupled resonator appears near ω_0 and is only slightly shifted towards lower frequencies by the coupling with the second oscillator. The aforementioned destructive and constructive interference between the two oscillators is responsible for the fast transition between suppressed and then enhanced dissipation peaking at $1.4\omega_0$. To put this simplistic view into perspective with the situation of an OLED the loss rate of the second oscillator was deliberately

set to $\gamma_2 = 0$ which is equivalent to a bound mode without any intrinsic losses. The important point here is the fact that even without any dissipation a feature with a non-zero line shape is present at ω_2. Hence, it is obvious that the magnitude of the coupling strength Ω between the two oscillators puts a limit on the minimum width on the feature near ω_2.

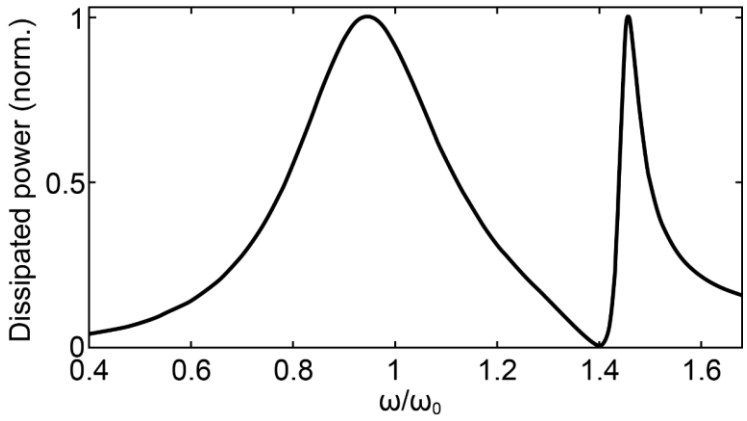

Figure 2-15. Power dissipated by the first oscillator as obtained from eq.(2.17). The values of the parameters are specified in the text.

As will be seen in chapter 4, this simple picture comes pretty close to the shape of the extinction spectrum of particle arrays coupled to a guided mode. Here, the guided mode is the equivalent to the bound mode albeit with added dissipation caused by the embedded grating.

Having discussed the effect of coupling a metallic NP to a bound mode it is time to deal with the two possibilities for bound modes within the OLED. The first one is the guided mode or often also called dielectric slab guide mode which allows confining and guiding light within a layer of high refractive index n_{wg}. Confinement can be tuned by the contrast of the refractive indices n_s and n_c of low-index layers and the high-index n_{wg} guiding layer as well as the thickness d of the waveguide (see Figure 2-16). To obtain total internal reflection $n_{wg} > n_s, n_c$ and the angle of incidence θ_{wg} has to be larger than the critical angles $\theta_{c,s}$ and $\theta_{c,c}$ respectively:

$$\theta_{wg} \geq \theta_{c,s} = \arcsin\frac{n_s}{n_{wg}} \tag{2.20}$$

$$\theta_{wg} \geq \theta_{c,c} = \arcsin\frac{n_c}{n_{wg}} \tag{2.21}$$

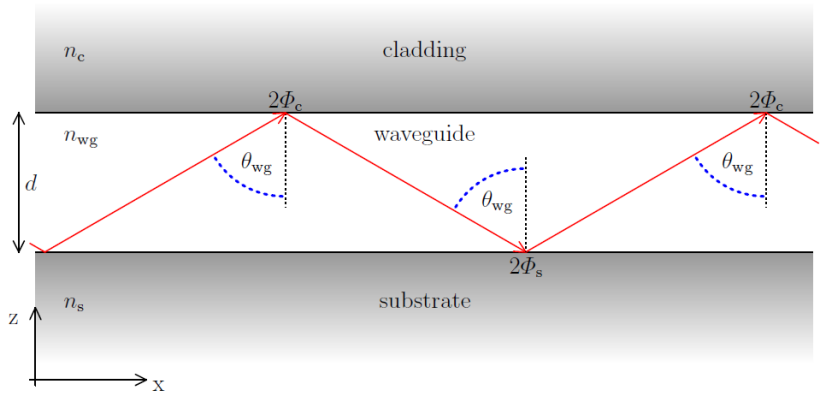

Figure 2-16. Simplest form of a dielectric waveguide structure (reproduced from [87]). For confinement it is required that the refractive index of the center layer fulfils $n_{wg} > n_s, n_c$ and $\theta_{wg} > \theta_{c,s}, \theta_{c,c}$

Reflection at the interface between the substrate and the guiding layer leads to a phase shift of $2\Phi_s$ and likewise reflection between the cladding and the waveguide layer adds an additional shift of $2\Phi_c$ to the phase. To obtain constructive interference the phase shift needs to be a multiple of 2π:

$$2\mathrm{d}k n_{wg} cos\theta_{wg} - 2\Phi_c - 2\Phi_s = 2\pi m \tag{2.22}$$

where $m = 0,1,2, \ldots$. Of course, this expression is different for s- and p-polarization. More details regarding this topic can be found in literature.[88]

Another way to obtain coupling between the metallic NPs are Rayleigh anomalies. Briefly, these anomalies are diffracted orders radiating grazing to the surface of a grating. In the modern form, this condition is formulated as a momentum conservation law where the de Broglie relation is used to relate the wave vector $\vec{\mathrm{k}}$ to the momentum. Traveling along a grating with a reciprocal vector $\vec{G} = \frac{2\pi}{g}\vec{u}$ the wave has to satisfy the condition

$$\vec{\mathrm{k}}_{\mathrm{II}}^{\mathrm{out}} = \vec{\mathrm{k}}_{\mathrm{II}}^{\mathrm{in}} + \frac{2\pi}{g}\vec{u} \tag{2.23}$$

where $\vec{\mathrm{k}}_{\mathrm{II}}^{\mathrm{in}}$ and $\vec{\mathrm{k}}_{\mathrm{II}}^{\mathrm{out}}$ are the projections of the incident and diffracted wave vectors parallel to the grating. Since these anomalies are very sensitive to inhomogeneous refractive index environments[89] they are seldom supported in environments that support guided modes.

2.2.6 Optical simulation: Finite-difference time domain

So far simple models were sufficient to develop an understanding of the matter at hand. However, to predict and understand even more complex structures and physics it is necessary to perform electromagnetic simulations by solving Maxwell's equations numerically. To perform these calculations, some constraints like modeling the complex dielectric functions of

metals at optical wavelengths or the specificity of some update algorithms to certain geometries have to be accounted for. Also, the evanescent fields at metal-dielectric interfaces often require very small discretization steps to accurately model the physical situation. Well established techniques are the finite element method (FEM)[90,91], the discrete dipole approximation (DDA)[92,93], the green dyadic methods (GDM)[94] and the herein presented finite-difference time domain (FDTD) method[95]. Since FDTD was used for the optical simulation only the background required to understand FDTD will be presented. FDTD is a member of the generalized class of grid-based differential numerical modeling methods. Discretization of the time-dependent Maxwell equations is achieved by central-difference approximations of the partial derivatives

$$\frac{\partial \vec{H}}{\partial t} = -\frac{1}{\mu}\nabla \times \vec{E} \;\rightarrow\; \frac{\vec{H}\left(t+\frac{\Delta t}{2}\right) - \vec{\vec{H}}\left(t-\frac{\Delta t}{2}\right)}{\Delta t} = -\frac{1}{\mu}\nabla \times \vec{E}(t) \tag{2.24}$$

$$\frac{\partial \vec{E}}{\partial t} = \frac{1}{\varepsilon}\nabla \times \vec{H} \;\rightarrow\; \frac{\vec{E}(t+\Delta t) - \vec{E}(t)}{\Delta t} = -\frac{1}{\varepsilon}\nabla \times \vec{H}(t+\frac{\Delta t}{2}) \tag{2.25}$$

where $\vec{H}$ and $\vec{E}$ are the magnetic and electric field, ε and μ are the permittivity and the permeability and Δt is the time step. The unique feature of the FDTD method is the way the finite difference equations are solved. Examination of the finite difference equations shows that the time dependent change of $\vec{E}$ is connected to the change of $\vec{H}$ across the space. Thus, the time-stepping mechanism of FDTD for any point in space is dependent on the stored value of $\vec{E}$ at a previous time and the curl of $\vec{H}$ in space. This concerns the stepping relation for the $\vec{E}$ field. Following the update of the $\vec{E}$ field the $\vec{H}$ field is updated. From eq.(2.24) it is clear that a similar stepping relation holds true for the $\vec{H}$ field. After the update of the $\vec{H}$ field, the $\vec{E}$ field is again updated for the next step in time. In literature this update mechanism is often called 'leap-frog'.

$$\begin{aligned}\frac{\vec{H}\left(t+\frac{\Delta t}{2}\right) - \vec{\vec{H}}\left(t-\frac{\Delta t}{2}\right)}{\Delta t} = -\frac{1}{\mu}\nabla \times \vec{E}(t) \;\rightarrow\; \vec{H}\left(t+\frac{\Delta t}{2}\right) \\ = \vec{\vec{H}}\left(t-\frac{\Delta t}{2}\right) - \frac{\Delta t}{\mu}\nabla \times \vec{E}(t)\end{aligned} \tag{2.26}$$

$$\begin{aligned}\frac{\vec{E}(t+\Delta t) - \vec{E}(t)}{\Delta t} = -\frac{1}{\varepsilon}\nabla \times \vec{H}\left(t+\frac{\Delta t}{2}\right) \rightarrow\; \vec{E}(t+\Delta t) \\ = \vec{E}(t) + \frac{\Delta t}{\varepsilon}\nabla \times \vec{H}\left(t+\frac{\Delta t}{2}\right)\end{aligned} \tag{2.27}$$

The robustness of FDTD is owed in large parts to the unique computational grid structure, the Yee lattice.[96] Depicted in Figure 2-17, the vector components of the $\vec{E}$ and $\vec{H}$ field are arranged

in rectangular cells in a way that the vector components of the $\vec{E}$ field are located mid-way between a pair of $\vec{H}$ field components (Figure 2-17.b) and vice versa (Figure 2-17.a). In a 3D simulation this rectangular unit cells become cubes following the same scheme (Figure 2-17.c).

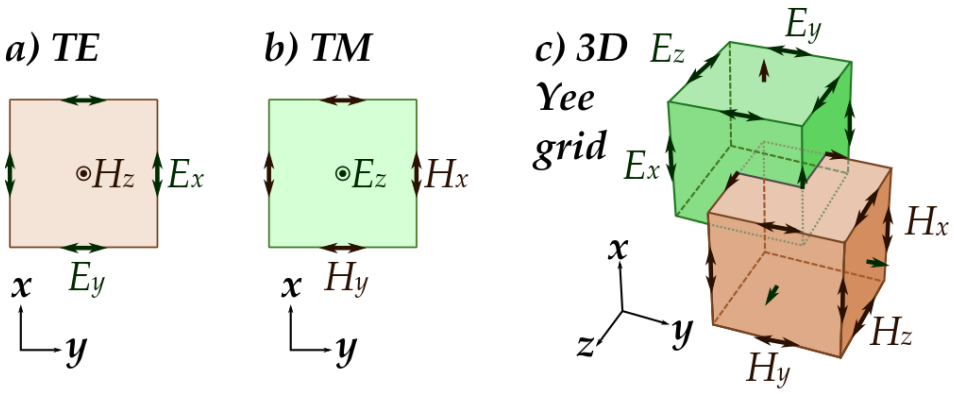

Figure 2-17. Discretization of space in FDTD. For systems with translation symmetry along an axis, (a) TE and (b) TM problems can be solved separately. The Yee cell, as the general case is depicted in (c). (taken from [97])

This explicit time-stepping enables FDTD to return the explicit fields at every time step allows following the time-dependent evolution until the steady-state is reached. Being a time-domain technique, the behavior of a system can be studied over a large bandwidth which is extremely useful for situations where the resonance frequency of a system is unknown. The grid-type nature of the scheme allows easy specification of the material at any point on this grid. Also, the sources of errors are well known for this method. Naturally, FDTD also suffers from certain drawbacks. A major one arises from the otherwise beneficial gridded computational domain in the limit of tiny and closely spaced structures. Here, the grid must be sufficiently fine to still resolve the electromagnetic wavelength and the smallest geometrical features of the model which leads to long simulation times due to the large computational domains. This issue can be alleviated somewhat by the use of conformal mesh technologies.[98–100] Also since FDTD obtains the steady-state by propagating the fields in time, the dispersion of the medium in which the fields are travelling needs to be expressed as a limited sum of Lorentzian oscillators which can make it difficult to model the response of some materials. Another issue stems from the leap-frog integration scheme used to obtain the solution for the next time step. Here the Courant-Friedrichs-Lewy condition needs to be satisfied which puts a limit on the largest possible time step or otherwise the update scheme becomes unstable.

Also, the memory requirements scale with $V \cdot (\lambda/dx)^3$ while the simulation time even scales with $V \cdot (\lambda/dx)^4$. Here dx is the step size of the mesh, λ is the smallest wavelength and V is the computational volume. From this it is clear that an optimization of the mesh size potentially allows significantly reduced simulation times as well as memory requirements.

All in all, FDTD provides a good balance between usability, power and disadvantages which has allowed this method to become dominant in computational electrodynamics.[95]

2.3 Amorphous inorganic p-type semiconductors

In principle, the same physics that successfully describes classic crystalline semiconductors such as Si or III-V compounds applies to nontraditional metal oxides or the investigated solution-processed copper pseudo halide. Importantly however, due to the severely increased amount of disorder caused by defects, impurities and varying degrees of crystallinity diverging behavior from the idealized equations can be found. This subchapter first provides a short overview on common semiconducting metal oxides and the reason why the achievement of n-type conductivity is easier than p-type. Then the band structure and electrical conductivity of metal oxides are discussed. Lastly, since reduced crystallinity as well as added impurities significantly affect the charge transport in inorganic metal oxides (even more so in oxide layers obtained from a low temperature solution-process), some common models used for the interpretation of charge carrier transport are presented.

2.3.1 Crystalline metal oxide semiconductors

Before diving into the intricacies of amorphous metal oxide semiconductors it is helpful to first start with crystalline metal oxides. For this class, essentially the same semiconductor physics applies and only some mechanisms will be discussed (in-depth discussion can be found in the well-regarded book 'Introduction to semiconductor physics' by Kittel[101]). Importantly, semiconducting behavior arises from the movement of electrons within the potential of the lattice of the material. Being periodic in nature this gives rise to the formation of an electronic band structure that determines the electrical properties of the material. This band structure or also known as dispersion relation links the momentum to the energy of these electrons. Naturally, these electrons aren't allowed to move freely as they undergo scattering processes as well as columbic interaction with other electrons and atomic nuclei. These processes can be summed up in a quantity termed the effective mass m^* which allows the usage of the equation of motion for an electron in free space but with m^* instead of the electron rest mass m_0. For the case of an isotropic crystal (i.e. uniformity along all crystal axes) the effective mass can be defined as

$$\frac{1}{m^*} = \frac{1}{\hbar^2}\frac{d^2E(k)}{dk^2} \tag{2.28}$$

with the reduced Planck constant $\hbar$ defined as ($\hbar = h/2\pi$).[101]

Transport in semiconductors occurs near the edges of the bands. Thus, the dispersion relation and the effective mass near the band edges dominates the carrier transport. These edges are termed valence (VBM) and conduction band maximum (CBM).

2.3.2 Semiconducting properties and band structure

The nature of the bonding mechanism between oxygen and metals most of the time leads to a unipolar charge carrier transport characteristic. Especially the hybridization mechanism between the metal and the oxide atomic orbitals heavily influences the transport behavior of common metal oxides. This situation is illustrated in Figure 2-18 where the calculated partial density of states (PDOS) for the common metal oxides indium oxide (In_2O_3), stannic oxide (SnO_2) and zinc oxide (ZnO) is depicted. Here, the oxygen (O) *2p* and metal (M) *ns* orbitals lead to the formation of the VBM and CBM. Clearly, the PDOS of the *2p* states of O dominate the valence bands of the presented oxides. At the same time, the conduction bands are mainly composed of the M *ns* orbitals with minor contributions from the O *2p* states. The most important aspect however is that the high degree of hybridization between the M ns states and the O *2p* states ensures a highly dispersive CBM while the mainly O *2p* character of the VBM leads to a localizing VBM. Naturally, electrons can move way more easily in these oxides than the localized holes near the VBM. Compared to the effective electron masses, this of course leads to significantly larger effective hole masses in these oxides and in turn an n-type characteristic. For reasons that will be discussed in a moment this situation is present for most metal oxide semiconductors, some of which are able to achieve mobilities exceeding 10 $cm^2 V^{-1} s^{-1}$ with record values even exceeding 100 $cm^2 V^{-1} s^{-1}$.[102,103]

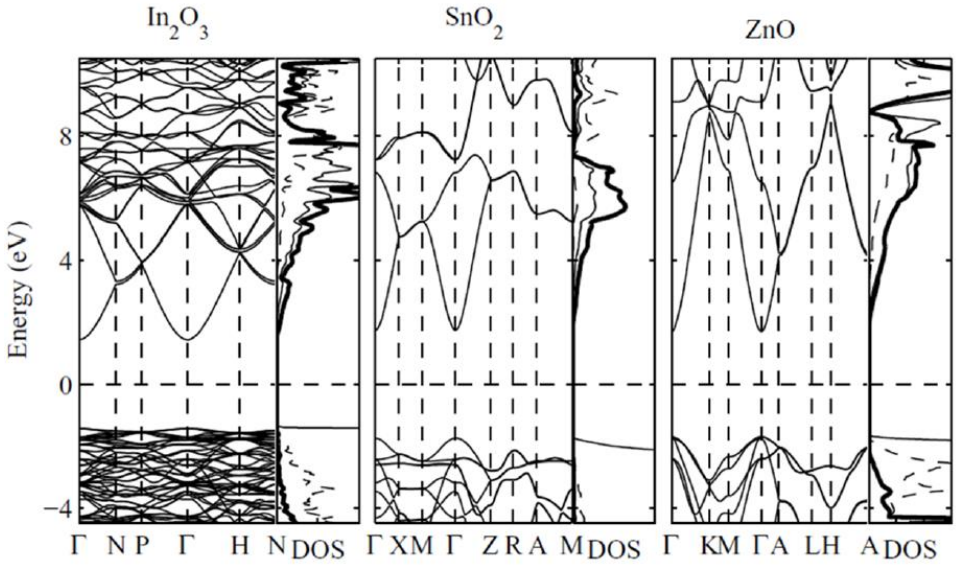

Figure 2-18. Electronic band structure of the common semiconducting metal oxides In_2O_3, SnO_2 and ZnO. The thin, dashed and thick lines refer to oxygen *p*, metal *p* and metal *s* states, respectively. (taken from [104])

Another interesting aspect of n-type metal oxide semiconductors is their ability to retain their good electron transporting capabilities even in the amorphous state. In contrast, Silicon experiences a drop in mobility from 1450 $cm^2\ V^{-1}\ s^{-1}$ in the single crystalline state[105] to 1 $cm^2\ V^{-1}\ s^{-1}$ in the amorphous state.[106] The reason for this behavior is illustrated in Figure 2-19. Here, the M *ns* orbitals are spherical and far reaching enabling extended conduction pathways even in the amorphous state.[107–109] Silicon on the other hand experiences the formation of localized states within the mobility gap and thus reduced electron mobilities.

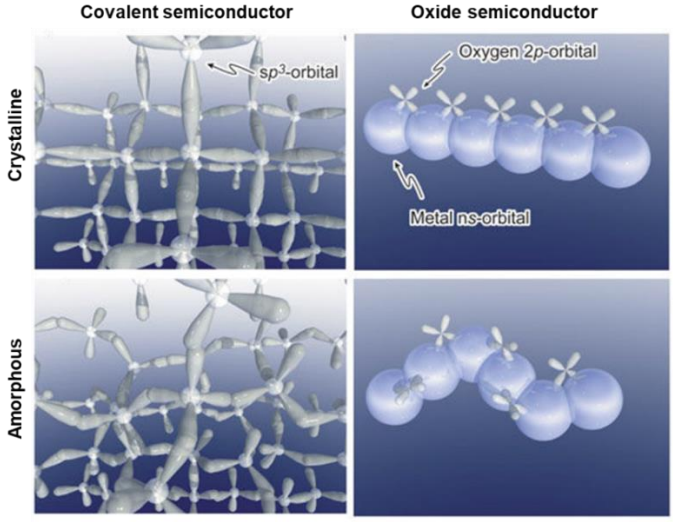

Figure 2-19. Electron transporting orbitals in crystalline and amorphous phases of covalent and oxide semiconductors (taken from [109]).

The key takeaway from this little venture into the world of n-type metal oxides is the fact that in order to obtain a p-type metal oxide semiconductor, a combination that leads to the formation of a dispersive VBM needs to be found. A common class of materials where this property has been realized are compounds based on Cu(I), such as cuprous oxide (Cu_2O). A property many Cu(I) compounds share is evident from Figure 2-20.b, which is composed of a hybridized Cu *3d* and O *2p* orbitals. The top of the VBM is mainly composed of Cu *d* state which result in more dispersive and hence higher attainable hole mobilities.[110–114]

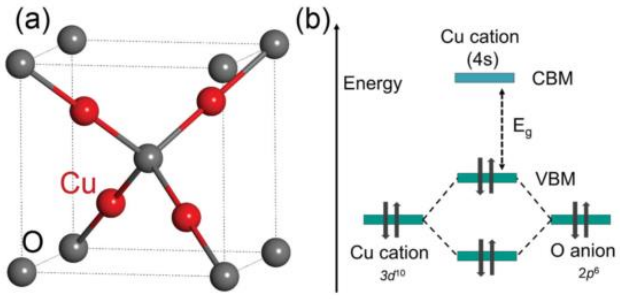

Figure 2-20. Crystal structure of Cu_2O. Valence band maximum hybridization schematically illustrated. (taken from [115])

A similar effect occurs in in stannous oxide (SnO) where hybridization of the Sn *5s* and O *2p* states create a similar dispersive VBM[116–118] (see Figure 2-21) that results in good p-type conductivities.[118]

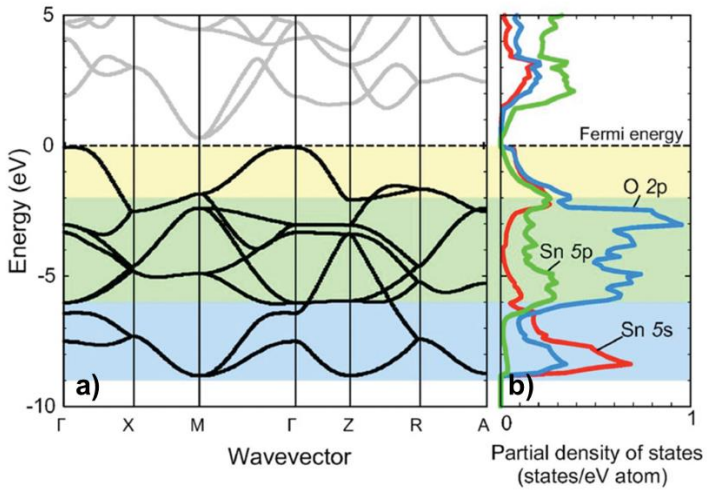

Figure 2-21. (a) Band structure and (b) PDOS of the unit cell of a perfect SnO crystal. The background of the band structure as well as the PDOS indicate three different energy regions within the valence band. (taken from [118])

So far, the hybridization between the metal and oxygen orbitals has proven to be a successful strategy in obtaining good p-type metal oxides. A similar effect is observed in copper (I) thiocyanate (CuSCN), a pseudohalide closely related to the presented metal oxides. Theoretical modelling of this compound showed hybridization between the *3p* orbitals of Sulphur and the *3d* orbitals of copper although in this case the character of the VBM is dominated by the *3d* orbitals of copper.[119] As before, this leads to a highly dispersive VBM (see Figure 2-22) and good p-type properties.

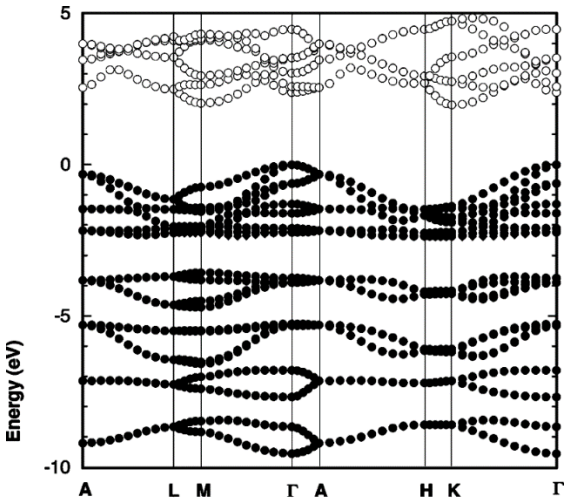

Figure 2-22. Calculated band structure of β-CuSCN. Conduction band is characterized by open symbols whereas the valence band is indicated with solid ones. (modified from [119])

So, from the discussion above, it is clear that a viable strategy to obtain good hole transport properties exists. Still, from the drift-diffusion model (eq.(2.29)) it follows that good electrical conductivities require sufficiently large amounts of free charge carriers on top of good mobility values. With the diffusion term omitted, the current can be written as

$$J_p = e n_p \mu_p E \tag{2.29}$$

where e is the elemental charge, n_p is the density of free holes, μ_p is the hole mobility and E is the applied electric field. The otherwise desirable large bandgap prohibits the formation of thermally generated carriers which is the reason for the common association of pure metal oxides with low intrinsic conductivities. Coming back to the originally introduced n-type oxides (In_2O_3, SnO_2 and ZnO), intrinsic conductivity was observed without doping when these oxides were grown under metal-rich/oxygen-deficient conditions. The resulting non-stoichiometry of the system increased their conductivity through the formation of oxygen vacancies (V_O) and metal interstitials (M_i).[120–122]

In principle, this way of generating free charge carriers sounds simple but the effects of thermodynamics need to be taken into account, especially with respect to the formation energies of these defects which might be too high to develop within these materials. Coming back to the p-type materials, which are of interest within the present work, the mechanism regarding free charge carrier generation is similar. Here, the basic defects are thought to form from oxygen interstitials (O_i) and metal vacancies (V_M). With respect to CuSCN, it was reported that the formation energy of V_{Cu} is sufficiently low with possible equilibrium concentrations as high as 10^{19} cm^{-3}. Due to the closed-packed structure of the hexagonal crystal the formation of interstitials is limited. More information on the subject can be found in the excellent work by Jaffe et. al[119].

2.3.3 Localized states, mobility edge and mobility gap in non-crystalline semiconductors

Conventional crystalline semiconductors exhibit a well-defined band structure with sharp edges and a forbidden energy gap. Naturally, some disorder in the form of impurities, defects lattice vibrations (thermal disorder), etc. exists which creates localized states[123] outside and within the band gap.[124] These localized features are described by wave functions that decay exponentially away from the disorder.[124] Usually these impurities are described by sharply defined energy levels within the gap without disturbing the charge carrier transport. Transitioning from the crystalline to the polycrystalline or even amorphous regime these sharply-defined energy levels transform into a continuous distribution of localized states

within the energy gap. Obviously, with these localized states, the term *energy gap* is an inadequate description of the physical reality and in the context of disordered semiconductors it is often referred to as the *mobility gap*[125–127] for reasons which will soon be uncovered.

Figure 2-23 shows the density of states (DOS) of an amorphous semiconductor. Two distinct regions exist: (I) the interval spanning ε_v and ε_c is the already mentioned mobility gap while (II) the areas bellow and beyond the mobility gap are called the *extended states* which are separated from the localized states by the *mobility edges*. Importantly this second region often still retains some sort of short range order that allows these *extended states* to retain the band structure found in the corresponding crystalline material.[127] States near the mobility edge are often called *band tails* while those further within the gap are called *deep states*.[127,128] With respect to the transport properties, many models assume the mobility edge to be the transition between areas of mobile and immobile states meaning that only the extended states allow the carriers to travel as waves. Besides band-like transport, there is of course still hopping between localized states which is still permitted for localized states.

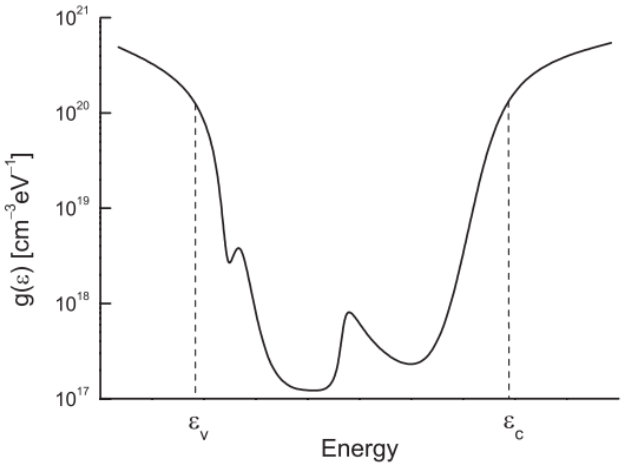

Figure 2-23. Typical DOS of a non-crystalline semiconductor (taken from [127])

As with the mobility gap, the VBM and CBM also change names more adequate for the description of non-crystalline semiconductors. Here, the VBM and CBM become the hole and electron mobility edges, respectively.

2.3.4 Charge transport in non-crystalline semiconductors

Having discussed the properties of metal oxides it is now time to briefly talk about the transport mechanism in polycrystalline or even amorphous metal oxide semiconductors. To this end, the most commonly used model, the multiple trapping and thermal release model (MTR) is briefly introduced. [129–133] The model is based on two major assumptions: (I) The

trapped charge carriers are thermally released and (II) near a trap site, charge carriers are instantaneously trapped. As depicted in Figure 2-24, it is clear that the conduction takes place via the delocalized extended states. At the same time a large fraction of charge carriers is trapped in localized states which are able to return to the delocalized bands via thermal excitation. Once the extended states are reached, the charge carrier is essentially a free carrier that can move at the mobility edge.

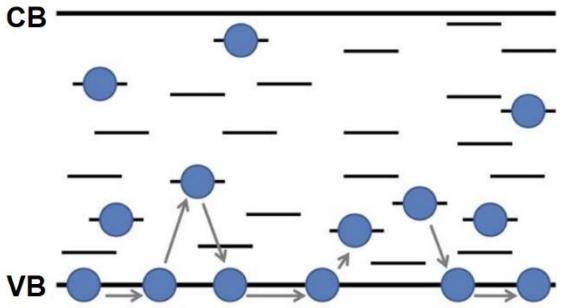

Figure 2-24. Working principle of the MTR-transport mechanism. A hole from the VB is trapped by a localized state within the mobility gap. After thermal excitation, the charge carrier returns back to the VB. (modified from [134])

In order to discuss the implications of the MTR, a DOS often encountered in real materials is depicted in Figure 2-25. Typically, the density of carriers that are excited to the transport band n_{band} can be written as

$$n_{band} = N_b \exp\left(\frac{E_F}{kT}\right) \tag{2.30}$$

where the effective density of states in the transport band is given by N_b, k is Boltzmann's constant, T the temperature and E_F is the Fermi energy defined negative with respect to the mobility edge.

The tail states are characterized by an exponential distribution of traps with the general form

$$n_{trapped} = N_t \exp\left(-\frac{E_F}{E_t}\right) \tag{2.31}$$

where the characteristic energy describing the width of the distribution is defined as $E_t = kT_c$ and N_t is the total number of tail states at $E_F = 0$. To allow a simplified qualitative discussion low temperatures ($T \ll T_C$) are assumed (further details can be found in the excellent work by Servati et. al[135]). Evidently n_{band} and $n_{trapped}$ are both dependent on E_F albeit with differing activation energies. Band carriers have a smaller activation energy which increases the density of conducting carriers when the carrier concentration is increased. Naturally, this results in a field and temperature dependence of μ.

This allows expressing n_{band} in terms of the trapped carriers n_{band}

$$n_{band} = \frac{N_b}{N_t^{T_C/T}} n^{T_C/T} \tag{2.32}$$

with $n = n_{band} + n_{trapped} \sim n_{trapped}$ since $n_{trapped} \gg n_{band}$

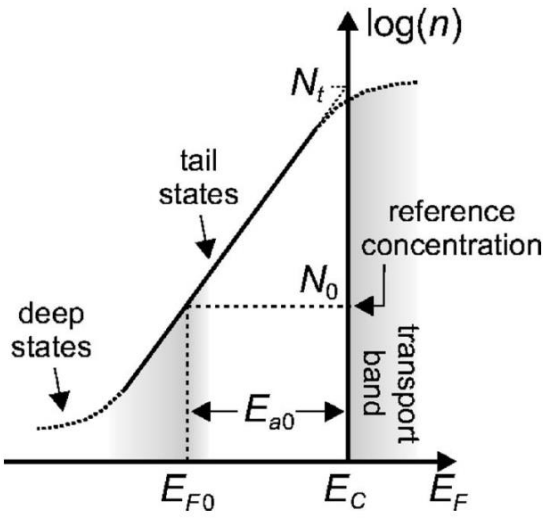

Figure 2-25. DOS of trapped carriers as a function of E_F. (taken from [135])

Since conductivity originates from charge carrier transport in the transport band, the electrical conductivity is defined as

$$\sigma = e\mu_{band} n_{band} \tag{2.33}$$

These considerations allow for a definition of an effective mobility μ_{eff} that includes the ratio T_C/T and the conductivity at a reference concentration N_0 (see Figure 2-25) as

$$\mu_{eff} = \frac{\sigma|_{n=N_0}}{eN_0} = \mu_{band} \frac{N_b}{N_0} \left(\frac{N_0}{N_t}\right)^{T_c/T} \tag{2.34}$$

Finally, recasting eq.(2.34) into a shape where the temperature and bias dependence becomes more obvious yields

$$\mu_{eff} = \mu_{eff0} \exp(-E_{a0}/k_B T) \tag{2.35}$$

where

$$\mu_{eff0} = \mu_{band} \frac{N_b}{N_0} \quad \text{and} \quad E_{a0} = kT_c ln\left(\frac{N_t}{N_0}\right) = -E_{F0} \tag{2.36}$$

This reveals an Arrhenius type behavior for the effective mobility with an activation energy corresponding to the position of the Fermi level E_{F0} associated with the reference concentration N_0. This is nothing less than the energy required for charge carriers to thermalize from E_{F0} to the mobility edge which is evidently bias independent. Bias dependence, however, arises when the Fermi level E_{F0} moves closer to the mobility edge to a position E_{F1}. In turn the reference carrier concentration increases, and the activation energy decreases in accordance with the experienced shift. This in turn leads to an increase of μ_{eff}. In the limit of $E_F = 0$ it is clear that a bias independent μ_{eff0} is recovered.

3

Charge injection: Solution processed pseudo halide hole transport layers

An environmentally friendly method for fabricating copper (I) thiocyanate from aqueous ammonia/formic acid solutions is presented. The addition of formic acid results in the formation of a bilayer structure composed of copper (I) thiocyanate/ammonium formate which possesses superior hole injection/transport and electron blocking capabilities. This allows organic light emitting diodes with this bilayer to exceed the efficiency of reference devices by up to 83 %.

The content of this chapter is based on the work that is about to be published and was partly modified:

> **Copper(I) thiocyanate (CuSCN) / ammonium formate binary HIL/HTL layer system obtained from spin-coated aqueous solutions for high efficiency organic light emitting diodes**
> M. Auer-Berger, Alexander Fian, Paolo Melgari, Andreas Klug and Emil J.W. List-Kratochvil
> *Article under preparation; Target journal Advanced Electronic Materials*
> Contribution: The author performed all work on his own except for XPS, TEM and EELS characterization. Acquisition of the XPS spectra was performed by Alexander Fian. Acquisition of TEM images and EELS spectra was performed by Daniel Knez at FELMI Graz. In these cases, the author still performed evaluation of the acquired raw data. The author writes the manuscript and finalizes it with the co-authors.

3.1 Introduction

Driven by the potential cost savings mentioned in chapter 1, interest in developing all-solution processes is strong. The main issue, however, stems from the fact that most organic materials are soluble in similar organic solvents resulting in an erosion of already put-down layers. Even though clever processing strategies (e.g. inkjet-printing[136], slot-die coating[137], orthogonal processing[138], film-transfer[139]) have been successfully devised, these schemes often either require special material chemistries (e.g. cross-linking functionalities) or selective solubility (orthogonality of solvents) to work and hence are not universally applicable for achieving the required multilayer structures. At the same time, energy harvesting devices such as organic- (OPV) and hybrid- (perovskite) photovoltaic devices have seen tremendous progress with their respective power conversion efficiencies closing in on 10 and 20%. However, fully solution-processed devices suffer from the same solvent-induced erosion problem as OLEDs. Especially susceptible to solvent erosion are the HIL and HTL or the hole-extraction layer, important for efficient OLEDs and perovskite solar cells respectively. Furthermore, most approaches to date require two individual layers, hence two processing steps are necessary to achieve efficient hole injection or -extraction. These approaches encompass self-organized gradient poly(3,4-ethylenedioxythiophene) polystyrene sulfonate (PEDOT:PSS) layers[140], self-assembled monolayers[141], graphene oxide layers[142] or cross-linkable HTLs[143].

Recently, a better approach utilizing the metal pseudo halide CuSCN, a wide bandgap p-type semiconductor with high optical transparency, was reported.[119,144] Making this compound even more intriguing is its solution-process ability via sulfonated solvents like dipropyl sulfide

(DPS) and diethyl sulfide (DES). While maximum attainable film thicknesses with DPS are in the range of 20 nm[145], the application of DES allows for thickness values exceeding 100 nm. Coupled with low root-mean-square (RMS) roughness values of 3-5 nm, CuSCN represents an important building-block towards efficient all-solution processed OLEDs[146–148], thin-film transistors[149–151], photodetectors[152], OPVs[153] and perovskite solar cells.[154–156] Better yet, CuSCN has been demonstrated to be processable by various solution-processes such as spin-coating, electrochemical deposition[157–159] and ink-jet printing.[160,161] Still, the usage of sulphurated speciality solvents bars this layer to be used in many industrial applications where the utilized filters are readily attacked by radical sulphur species. Adding to that are the inherent high costs of sulphurated speciality solvents such as DPS and DES which are only produced in low quantities world-wide.

An alternative might be the well-known complexation reaction of Copper(II) oxide (CuO) in concentrated aqueous ammonia solutions by forming the blue $[Cu(NH_3)_4H_2O]^{2+}$ tetraammine copper (II) complex while Copper(I) oxide (Cu_2O) first forms the colorless $[Cu(NH_3)_2]^+$ which is further oxidized in air to give the already described tetraamine copper (II) complex.[162] Recently, it was shown, that this complexation route indeed lends itself to the fabrication of CuSCN films.[163] However, this resulted in the formation of unwanted secondary oxides and is only suitable for thin films (~10 nm). [163]

Within this work, ethanol was used to reduce the surface tension as well as the boiling point of the aqueous ammonia coating solutions which allowed to put down CuSCN layers with a thickness of ~30 nm, enough for the application as a HTL within an OLED. Still, x-ray photoelectron spectroscopy also confirmed the earlier reported finding of unwanted secondary oxides. To prevent this oxidation from happening, the reducing properties of formic acid were exploited by adding it to the CuSCN/ammonia complex. This was found to effectively suppresses the formation of unwanted byproducts by reducing Cu(II) back to Cu(I) while also leading to increased crystallinity as well as the formation of a capping ammonium formate layer. Compared to only using aqueous ammonia, these effects led to a significant improvement in hole mobilities by a factor of ~10 as well as 12.1-fold reduced trap densities as obtained by space charge limited current and density of states reconstruction. Furthermore, through atomic force microscopy as well as contact angle measurements, superior RMS surface roughness and wettability behavior of CuSCN layers processed by the aqueous ammonia/formic acid route was observed. Finally, the performance of CuSCN layers obtained from aqueous ammonia with and without formic acid treatment was compared to CuSCN layers processed from DES as well as PEDOT:PSS layers in two solution-processed OLED stacks. Through this study, it was confirmed that the combination of high hole mobilities, outstanding

wettability as well as the presumably enhanced electron blocking capabilities of the obtained CuSCN/ammonium formate bilayer led to best in class performance (82 % enhancement compared to CuSCN processed from DES) of the formic acid treated CuSCN layers which are even able to mitigate the previously observed drawback of reduced brightness values in OLEDs (compared to PEDOT:PSS).[164]

3.2 Experimental

Overview

The analysis work carried out for this chapter encompassed a multitude of measurement techniques, which themselves required different substrate and device geometries. An overview of these measurement techniques with the connected substrate and device geometries is depicted in. The patterned Indium Tin Oxide coated float glass substrates (ITO) had a sheet resistance of 15 Ω sq^{-1} and were purchased from KINTEC Hong Kong. The silicon wafers (Si) without a grown oxide layer were purchased from Siegert wafer. The fused quartz substrates with high optical transparency of >92% within the spectral range of 290-2500 nm were purchased from Delta technologies. Details regarding the preparation of the solutions required for the fabrication of the HIL/HTL films as well as the individual measurement techniques are given in the respective paragraphs of this subchapter.

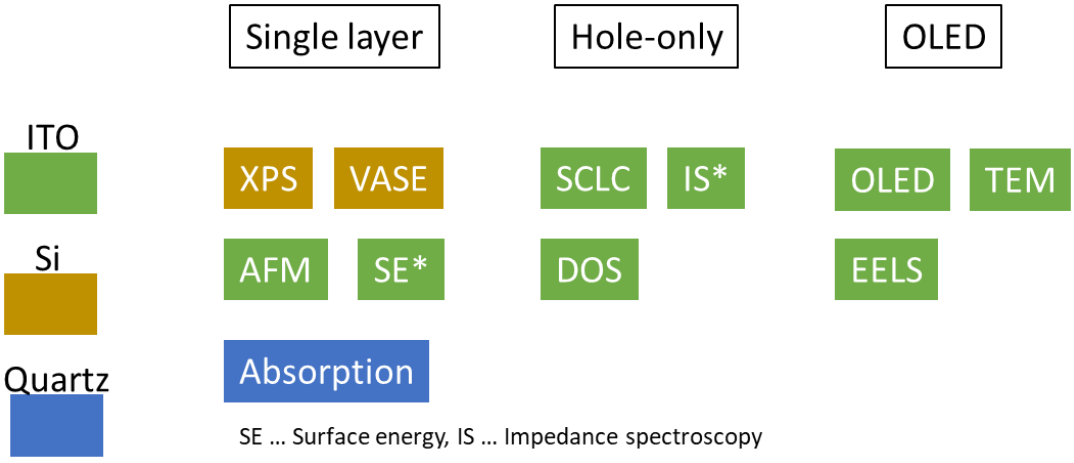

Figure 3-1. Overview of the experiments carried out for this chapter. The color of the rectangles indicates the substrate type while the label of the individual column stands for the geometry fabricated on top of the substrate. Details regarding the individual measurements are given in the following paragraphs.

Preparation of the solutions

CuSCN powder, diethyl sulfide, ammonium hydroxide (14.8M NH_3) and formic acid (96%) were purchased from Sigma-Aldrich.

NH4 solutions were prepared by dissolving CuSCN powder in a binary solvent mixture consisting of 80 wt% ammonium hydroxide (14.8M NH_3, Aldrich) and 20 wt% ethanol (absolute 99%, Merck) at concentrations of 24 mg mL^{-1}. The solutions were left to stir for 2 hours at room temperature uncovered to allow for ample supply of oxygen for the complexation reaction to proceed. After this time, the solutions were characterized by a deep-blue color with some precipitates stemming from tertiary oxidation products on the glass walls. Long term tests (>1 week) revealed no further precipitation or change in color, thus confirming that the solutions were in thermodynamic equilibrium.

FA solutions were prepared by adding 1 wt% of formic acid to the ready to use NH4 solution followed by stirring the solution for another 30 minutes. After this time, the precipitates had disappeared and the solution was ready to use.

DES solutions were prepared by the dissolution of CuSCN powder in DES at a concentration of 12 mg ml^{-1} and stirred in air for 30 minutes. After this time clear yellowish solutions formed.

PEDOT:PSS (Clevios VP Al-4083) was purchased from Heraeus and used as received. To enhance the readability of this chapter, CuSCN films obtained by processing from NH4, FA or DES solutions are labeled as NH4, FA and DES, respectively.

Preparation of the HIL/HTL films

The substrates used in this study were treated in ultrasonic baths of 2 vol% Hellmanex III for 20 minutes at a temperature of 50°C. Subsequently, the substrates were carefully rinsed with DI water and cleaned for 10 minutes in an ultrasonic bath of acetone followed by isopropyl alcohol (IPA). The cleaning was completed by a final IPA rinsing and nitrogen dry-blowing step. The substrates were immediately transferred to a plasma cleaner and subjected to an oxygen plasma (Diener Femto) at 100 W for 5 minutes.

Undissolved material was removed by a syringe filter made of polyvinylidene fluoride for NH4, FA and PEDOT:PSS solutions and polytetrafluoroethylene for DES solutions, respectively, with a pore size of 0.2 μm directly before application of the solution to the substrate.

Spin-coating was performed at room temperature at 2000 for DES and 2500 rpm for NH4, FA as well as PEDOT:PSS solutions respectively. Annealing of the as-spun films was done on a hot plate at 120 °C for 5 minutes after which the films were ready for further processing or analysis.

Structural and morphological characterization

Topography and phase images as well as film thickness measurements were recorded via a Veeco Dimension V atomic force microscope (AFM) equipped with a Nanoscope V controller in tapping mode.

Surface energy

Surface energy was characterized by measuring the contact angles with a KRÜSS DSA 100 contact angle measuring instrument. Here, thin films prepared as described above were used to determine the contact angles of water (except FA before heat treatment), ethylene glycol, dodecane and diiodomethane. For each test liquid, at least four measurements were conducted. Surface energies were calculated from the averages of the determined contact angles according to the method of Owens and Wendt.[165]

Optical Characterization

UV-vis-NIR spectra were acquired from HIL/HTL films deposited on Quartz substrates by a Perkin Elmer Lambda 900 equipped with a Spectralon-coated integrating sphere. Absorbance was obtained via $A = -\log(\frac{T}{1-R})$ where T and R are the transmittance and reflectance, respectively. From this value, the absorption coefficient was obtained by normalizing the absorbance through the film thickness (determined via AFM).

Variable angle spectroscopic ellipsometry

Ellipsometry measurements were carried out by spin-coating NH4, FA and DES on cleaned Si wafers (modelling included a small silicon oxide layer with 2 nm thickness). The optical properties and the thickness of the films were measured by means of variable angle spectroscopic ellipsometry (VASE) (J. A. Woollam Co., Inc). Spectra were acquired for a spectral range of 300 to 1300 nm at angles of incidence of 65, 70 and 75° with respect to the substrate normal. Modelling of the acquired VASE data was performed using the WVASE software package (J.A. Woollam Co., Inc). Modelling was based on coupled Lorentzian oscillators as well as Cauchy layers. Additionally, the presence of inhomogeneous thin films exhibiting isotropic behavior was assumed.

Transmission electron microscopy and electron energy loss spectroscopy analysis

OLED structures fabricated on top of ITO substrates were investigated by means of a Tecnai TF20 from FEI Company for analytical transmission electron microscopy (TEM) and high-resolution TEM (HRTEM) measurements. The microscope is equipped with a field emission gun source, a high resolution Gatan imaging filter with an UltraScan CCD camera (2048 px x

2048 px) for TEM imaging and electron energy loss spectrometry (EELS). The microscope was operated at 200 kV acceleration voltage. All TEM sample preparation was carried out in a dual-beam focused ion beam (FIB) microscope (FEI Nova 200) with Ga+ ion milling.

Space charge limited current and density of states analysis

HIL/HTL films were processed on ITO substrates as described earlier. To conduct space charge limited current measurements (SCLC), hole-only devices with an ITO/(HIL/HTL)/MoO_3(5 nm)/Ag architecture were built. The thin layer of molybdenum trioxide (MoO_3) deposited by thermal evaporation was used due to its position of the valence and conduction band that allows charge carrier species selectivity.[166,167] The HIL/HTL layer thicknesses were selected to reflect the thicknesses used in OLEDs. Since this can be dangerous with respect to the reliability of the obtained mobility values, the thickness was increased by a 4-fold (>80 nm) to check for any significant deviations. Accurate thickness values are important for the determination of mobilities from the hole-only devices. Thus, the substrates with evaporated cathodes were shortly dipped into a 2M solution of ammonium hydroxide and successively rinsed with isopropyl alcohol. Afterwards, a scotch tape was applied to the substrates and the evaporated metal contacts were peeled from the substrate. This way the metal contacts acted as masks which formed sharp edges that made an accurate determination of the thickness via AFM of the HIL/HTLs possible.

Impedance spectroscopy

Impedance spectroscopy of hole-only structures fabricated on ITO was performed using a Keysight E4980A Precision LCR meter. A small sinusoidal voltage with an amplitude of 50 mV was set for the measurement and superimposed on the selected DC bias voltage. Measurements were carried out over the frequency range of 20 Hz and 2 MHz inside an argon-filled measurement cell. Open and short circuit corrections were performed to minimize the impact of the wiring and the measurement cell on the quality of the measurements.

XPS studies

Thin-films coated on top of Si wafers were transferred into an Omicron Multiprobe surface analysis system equipped with a DAR 400 X-ray source, an XM 500 quartz crystal monochromator (X-ray excitation energy of 1486.7 eV, Al Kα1) and an EA 125 hemispherical electron energy analyzer with a 5-channel pulse counting channeltron. At the applied pass energy of 20 eV, the overall energy resolution of the system was 0.5 eV. In addition, the binding energy was corrected considering that the binding energy of C in the C-C bond is 284.9 eV, which is a result of residual hydrocarbon surface contaminants. The obtained spectra were

fitted by convolution of a Lorentzian and a Gaussian line shape (Voigt function) using the XPS-data processing software Unifit 2017.

OLED fabrication and characterization

HIL/HTLs were fabricated on ITO substrates as earlier described. For this study, high efficiency green emitting phosphorescent as well as high brightness blue emitting fluorescent OLEDs were used. The layer geometries as well as the energy level alignments are depicted in Figure 3-2. The phosphorescent OLEDs (Figure 3-2.a) were fabricated from solutions of the binary solvent mixture of dichloromethane:tetrahydrofurane (DCM:THF) in a 1:1 ratio where Tris(4-carbazoyl-9-ylphenyl)amine (TCTA) and 4,4′-Cyclohexylidenebis[N,N-bis(4-methylphenyl)benzenamine] (TAPC) were mixed in a 3:1 ratio. The phosphorescent green-emitting dye Tris[2-phenylpyridinato-C2,N]iridium(III) $Ir(ppy)_3$ was added at a concentration of 6 wt%. The EML was spin-coated and the thickness was set to approximately 35 nm. After the spin-coting step, the EML was annealed at a 110°C for 30 min under high vacuum. 45 nm of 1,3,5-Tris(3-pyridyl-3-phenyl)benzene (TmPyPB) was evaporated on top of the solution-processed EML to function as the ETL. 10 nm of Calcium (Ca) functioning as the EIL and 80 nm of aluminum were evaporated on top of the organic stack to complete the OLED. For the fluorescent OLEDs (Figure 3-2.b), CP-AE and CP-ABCD were used as HTL and EML, respectively.[168] Here CP-AE and CP-ABCD were dissolved in toluene at a concentration of 3 and 4 mg ml^{-1}, respectively. CP-AE was spin coated on top of the processed HIL/HTL layers and thermally stabilized at 200°C for 1 hour to yield a film thickness of approximately 20 nm. Subsequently, the EML consisting of CP-ABCD was deposited and dried at 100°C for 30 minutes under high vacuum. Similar to the phosphorescent OLEDs, 45 nm of TmPyPb, 10 nm of Ca and 80 nm of Aluminum were evaporated on top the solution processed stack thereby completing the OLED assembly.

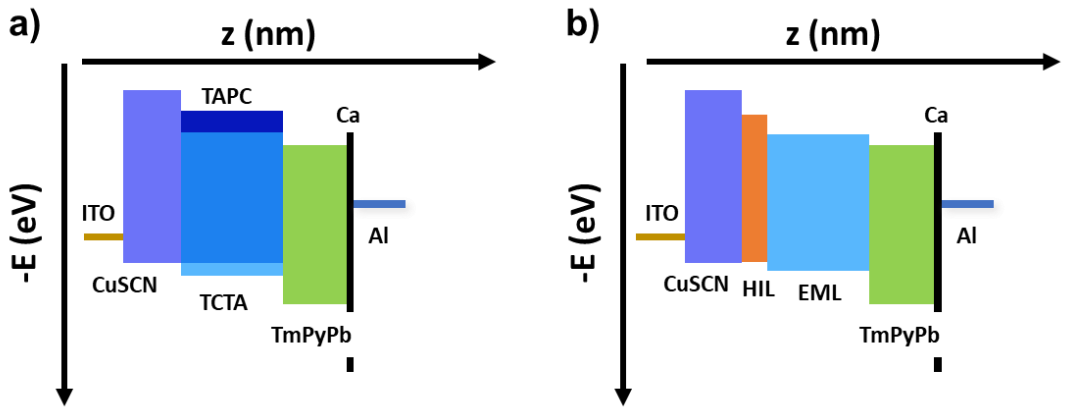

Figure 3-2. Schematic of the layer assembly and energy level alignment in the (a) phosphorescent and (b) fluorescent OLEDs used within this study.

3.3 Morphology & chemical analysis

AFM

As it is well known, owing to inhomogeneities in ITO, any HIL/HTL should provide sufficient planarization capabilities, characterized by a RMS surface roughness, to reduce leakage current. To assess the suitability of the processed HIL/HTL-layers for solution-processed electronic devices, AFM was performed on ITO substrates coated with CuSCN from DES, NH4 as well as FA. The phase images, as measured by AFM, are displayed in Figure 3-3 (see appendix A.1 for corresponding topography images). CuSCN films deposited from DES exhibited a RMS surface roughness of 3.0 nm and oval-/rod-like shapes with several tens of nanometers in length and diameter (see Figure 3-3.a), which is in line with previous results from literature.[145] By changing to NH4 as a solvent mixture, a dramatic change in surface topography was noticeable (see Figure 3-3.b). The RMS surface roughness dropped to an exceptionally low 0.7 nm on ITO, demonstrating superior planarization capabilities. Furthermore, the film more closely resembled as closed film with individual crystal sizes massively decreased to approximately 10-20 nm. Lastly, FA again revealed a significantly different phase image as compared to the layers obtained from the other solvents with a RMS surface roughness of 1.0 nm (see Figure 3-3.c). Interestingly, the addition of FA to the concentrated ammonia solutions resulted in the formation of almost spherical nanocrystals with a diameter of 20-30 nm.

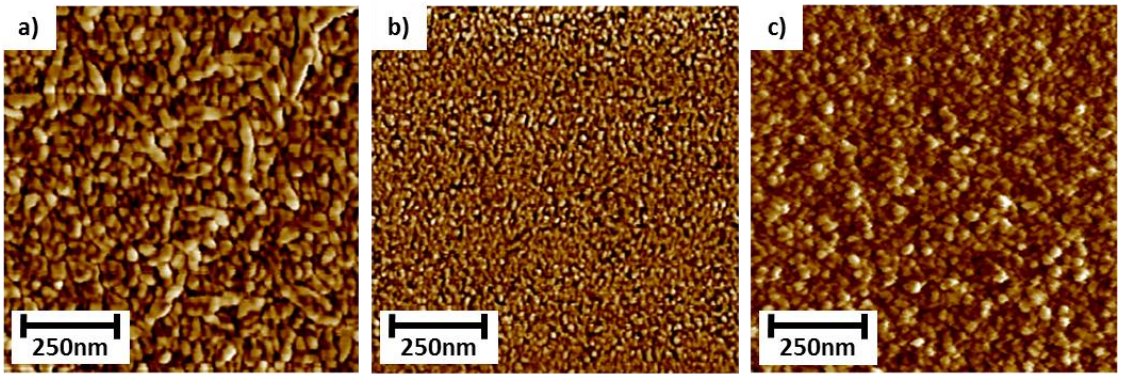

Figure 3-3. AFM phase images of CuSCN layers processed from (a) DES, (b) NH4 and (c) FA solutions.

Surface energy

Concomitant to a low RMS roughness, surfaces should also exhibit a high surface free energy which significantly enhances the surface wettability and hence the results of the coating process. Therefore, the surface free energy was determined by the method of Owens and Wendt.[165] The results are presented in Table 3-1. Noticeably, films from DES were characterized by a quite low surface free energy of 35.7 mJ/m^2 which was unsurprisingly a

direct result of the almost non-existing polar components. Quite the opposite was observable for NH4, where, owing to significant polar contributions, the surface free energy was raised to 60.3 mJ m^{-2}. Compared to NH4, FA saw very minor polar contributions with only 6.4 mJ m^{-2}. However, a further increase in dispersive components resulted in a sizeable increase of the surface free energy to 43.0 mJ m^{-2}. From these results, it is clear, that just from the point of surface free energy NH4 and FA layers should exhibit better coating properties than DES layers. As it is generally known, the addition of a base to an acid leads to the formation of a salt. In the case of the FA solutions the produced salt is ammonium formate. Since this salt is volatile at temperatures > 180°C the investigated layer was subjected to a heat treatment of 200°C for 5 minutes after which the surface free energy was rechecked. Remarkably, the surface free energy increased to 57.7 mJ m^{-2} because the polar contributions increased dramatically. At this point of the investigation, this behavior is explained by the decomposition of the ammonium formate layer.

Table 3-1. Dispersive, polar and total free surface energy of CuSCN films deposited from different solvents as determined by Owens-Wendt method

Layer	Annealing [°C]	Polar [mJ m^{-2}]	Dispersive [mJ m^{-2}]	Total [mJ m^{-2}]
DES	120	1.8	33.9	35.7
NH4	120	31.0	29.3	60.3
FA	120	6.4	36.6	43.0
	200	25.7	32.0	57.7

XPS

To further elucidate the chemical structure of the deposited films, XPS studies were conducted. The risk of a change in chemical composition induced by the investigations was reduced by not performing a removal of adventitious carbon by soft argon sputtering. The survey spectra (see Appendix A.2) exhibited the already known characteristic signatures[119] of Cu, S, N in all three films while a clear deviation in the recorded intensities of the O1s peak for NH4 was evident. Therefore, high resolution spectra for Cu2p, O1s, N1s and S2p were collected. To simplify the discussion of the effects of the different solvent combinations on the chemical composition of the deposited films, the Cu2p, O1s, N1s as well as S2p spectra are normalized and depicted in Figure 3-4 (detailed peak fits as well as survey spectra of all films are depicted in the Appendix A.2). Starting the discussion with $Cu2p_{3/2}$ features (Figure 3-4.a), a characteristic Cu(0)/Cu(I)

peak at 932.4 eV for all investigated films is visible. While the $Cu2p_{3/2}$ spectra of DES and FA are virtually identical, the formation of characteristic Cu(II) shake-up structures in the range of 938-945 eV was observable for the NH4 layers. As a consequence, the newly emerged shoulder at energies above the Cu(0)/Cu(I) peak was assigned to the formation of CuO at 933.6 eV and $Cu(OH)_2$ at 934.7 eV.[169] The S2p core-level (Figure 3-4.b) of all three films is characterized by a doublet with a peak at 163 eV typical for the S-C bond. Additionally, NH4 films demonstrate the formation of an additional doublet at higher binding energies of 168.6 eV which was ascribed to the creation of SO_4^{2-}.[170] N1s core-level spectra (Figure 3-4.c) for DES and FA are again practically identical with the main peak at 398.8 eV belonging to the triple bond C≡N.[144] While the NH4 spectrum is also similar to DES and FA, it includes a significantly increased contribution at 398.9 eV which is a signature of the C=N double bond.[144] Lastly, the O1s spectra (Figure 3-4.d) reveal only minor amounts of oxygen incorporated in the films cast from DES and FA as is evident by the poor S/N ratio. However, quite the opposite can be ascertained for NH4 where the counts per second were two orders of magnitude higher than for DES and FA signaling drastically higher amounts of oxygen in the film. Concluding this section, it is clear that the dissolution of CuSCN in NH_4OH:EtOH leads to severe chemical degradation by further oxidizing CuSCN to CuO and $Cu(OH)_2$. This in turn leads to a decomposition of the SCN^- ion to secondary products as evidenced by the high-resolution core spectra (see Appendix A.2). Remarkably, the reducing property of 1wt% of FA is strong enough to effectively counter the chemical degradation.

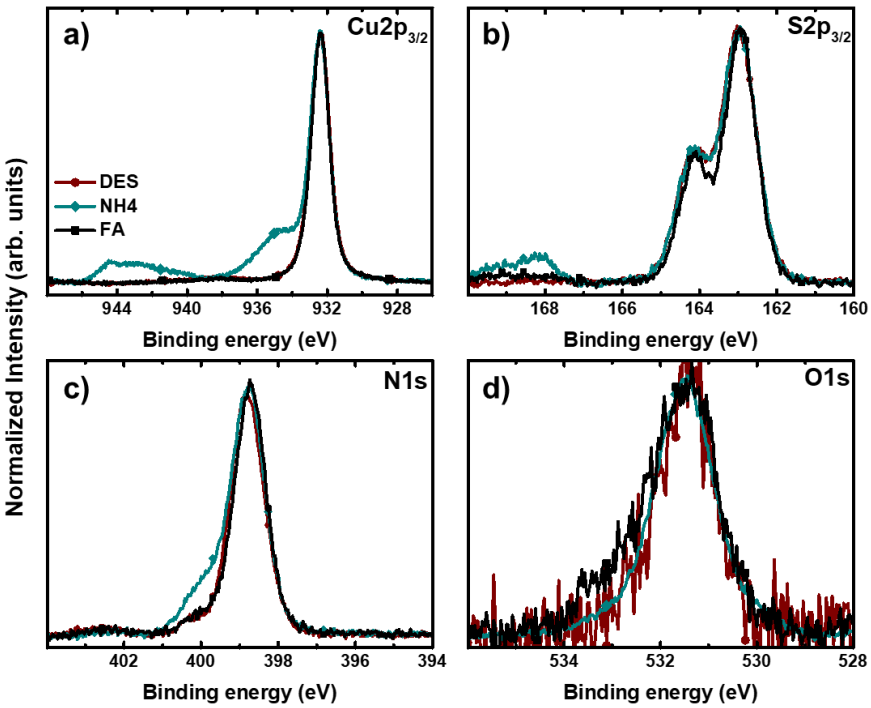

Figure 3-4. High resolution core line spectra of (a) Cu2p, (b) S2p, (c) N1s and (d) O1s of spin-coated DES (red line), NH4 (green line) and FA (black line) films.

This is further emphasized when the film stoichiometry is analyzed. This was estimated by the peak areas after subtracting the Shirley background from each peak. The results of this analysis are summarized in Table 3-2. For this discussion two aspects are important. The first is the stoichiometry between Cu, S, C as well as N. The presence of adventitious C makes this analysis somewhat difficult, however, considering that Cu, S as well as N are roughly equal, it is reasonable to assume that roughly a 1:1:1:1 stoichiometry is achieved for all layers. The second point relevant for this discussion is the amount of oxygen present in the layers. Here, a drop from 17 to 4 at% was witnessed through the addition of the formic acid to the NH4 solution which highlights the effectiveness of this approach.

Table 3-2. Elemental ratios in atomic % as obtained by peak fit analysis

HTL	Cu [at%]	S [at%]	C [at%]	N [at%]	O [at%]
DES	23	25	31	20	1
NH4	19	18	17	21	17
FA	22	23	29	22	4

Surprisingly, no clear signs of ammonium formate were detected in the presented XPS investigations even though the surface energy characterization already hinted towards the presence of this compound in the HIL/HTL films obtained from FA solutions.

It is suspected, that the volatile nature of ammonium formate causes this compound to evaporate from the substrate under ultra-high vacuum conditions. Naturally, this would have to be confirmed by further measurements.

TEM

It is generally accepted that the crystallinity of a material has important implications on the mobility of charge carriers. In the case of CuSCN, several studies indicated that it can exist in a hexagonal/rhombohedral β-phase as well as an orthorhombic α-phase.[145] To get an idea about the impact of the different complexation route via NH_4OH and FA on the crystallization of CuSCN, FIB cross-sections were performed of OLEDs fabricated on ITO substrates with either a NH4 or FA HIL/HTL. The micrographs of NH4 and FA (Figure 3-5.a and b respectively) include the interface regions to ITO as well as the EML. To allow for a better comparison, the two micrographs along the ITO interface were aligned and the scale was set equal for both

images. Comparing both images, it is immediately apparent that NH4 exhibits a significantly reduced intermediate range crystalline order with a mean lattice spacing of 6.3 ± 0.4 Å (Figure 3-5.a). FA on the other hand, besides a markedly increased intermediate range crystalline order, also features monocrystalline domains (Figure 3-5.b, marked region). Upon Fourier transformation the obtained electron diffraction pattern reveals several sharp peaks with d-spacings of 3.2 ± 0.2 Å as well as 6.4 ± 0.2 Å. Clearly, nanocrystalline structures lead to additional peaks due to the interference of different lattice orientations in the individual crystal and therefore Fourier transformation is not sufficient to obtain reliable information about the crystal structure, but it is pointed out that according to a recent study, the d-spacing of 3.3 Å is also a signature of the α- as well as the β-phase.[145] At the same time, the origin of the d-spacing at 6.3 (NH4) and 6.4 Å (FA) is currently not known. However, based on the XPS data, it is reasonable to suspect that the presence of additional secondary products leads to the formation of alternate lattice structures. Again, it has to be pointed out that more detailed work regarding the polymorphism and the structure of these films needs to be performed. Nonetheless, from this superficial analysis of the crystal structure it is obvious that the mobility of charge carriers in FA should be superior to NH4 since increased crystallinity is known to enhance charge carrier mobility as well as leading to a reduced amount of localized states.[103,171–173]

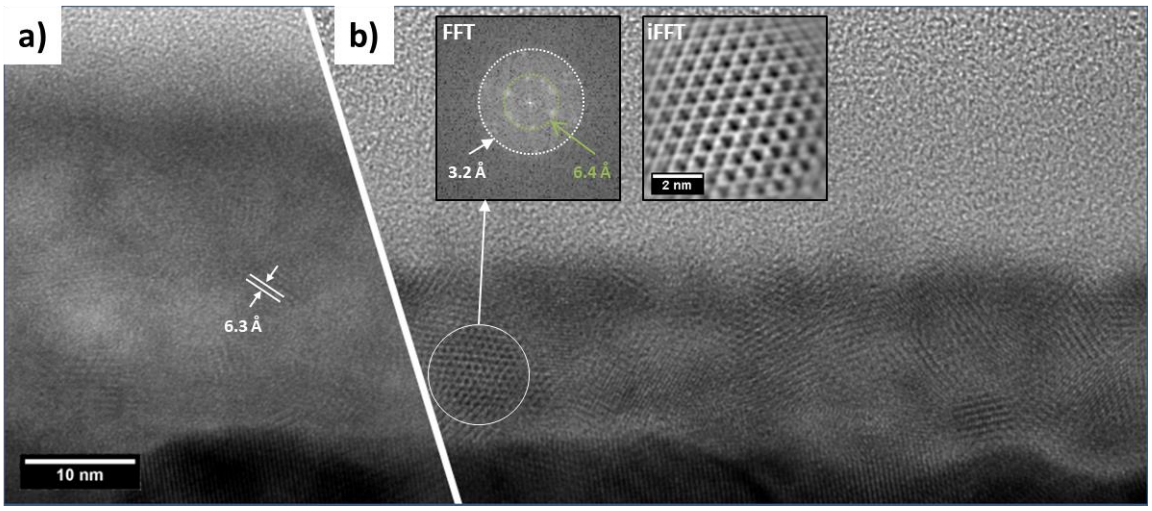

Figure 3-5. HR-TEM images of (a) NH4 and (b) FA respectively. A fast fourier transform (FFT) was computed for an area of increased crystallinity (inset). An enhanced lattice image was obtained by inverse fourier transformation (iFFT) taking only the diffraction spots in the FFT into account.

Having determined that FA films exhibit increased nano crystallinity, the elemental composition of the HIL/HTL films was probed by EELS on both films in scanning transmission electron microscopy (STEM) mode. Particularly, the Cu L and O K shell was probed in FA while only O K proofed sufficient for NH4 (the addition of formic acid to the NH4 based solution is

not expected to change the distribution of Cu). The area investigated spanned 25 x 55 nm and also included the interface between ITO, and CuSCN as well as the interface between CuSCN and the organic layer. The distribution of Cu as well as O for FA is depicted in Figure 3-6.a and O for NH4 is visible in Figure 3-6.b. Starting with the distribution of O, in both layers most O is concentrated in the ITO layer. However, upon entering the CuSCN layer, the O concentrations start to diverge with more O present in NH4 than in FA. This behavior is in line with XPS measurements which also attested more oxygen to be present in NH4 than FA (Table 3-2). Moving even further to the interface between CuSCN and the organic, NH4 shows an uptick in oxygen at the interface between the organic and CuSCN which was attributed to surface oxidation. In the case of FA, the observed punctual increase at the interface extends over a large range of approximately 20 nm before the oxygen concentration goes back to virtually 0 (see Figure 3-6.a). This extended layer of oxygen is attributed to the presence of an ammonium formate layer on top of CuSCN. Remarkably, Cu was found to be concentrated in the area between the two interfaces (see Figure 3-6.a, Cu L). While the onset of Cu concentration is relatively sharp at the ITO/CuSCN interface, a broader decrease in concentration is noticeable at the interface between CuSCN/ammonium formate. This is attributed to a less well-defined interface region between these two layers.

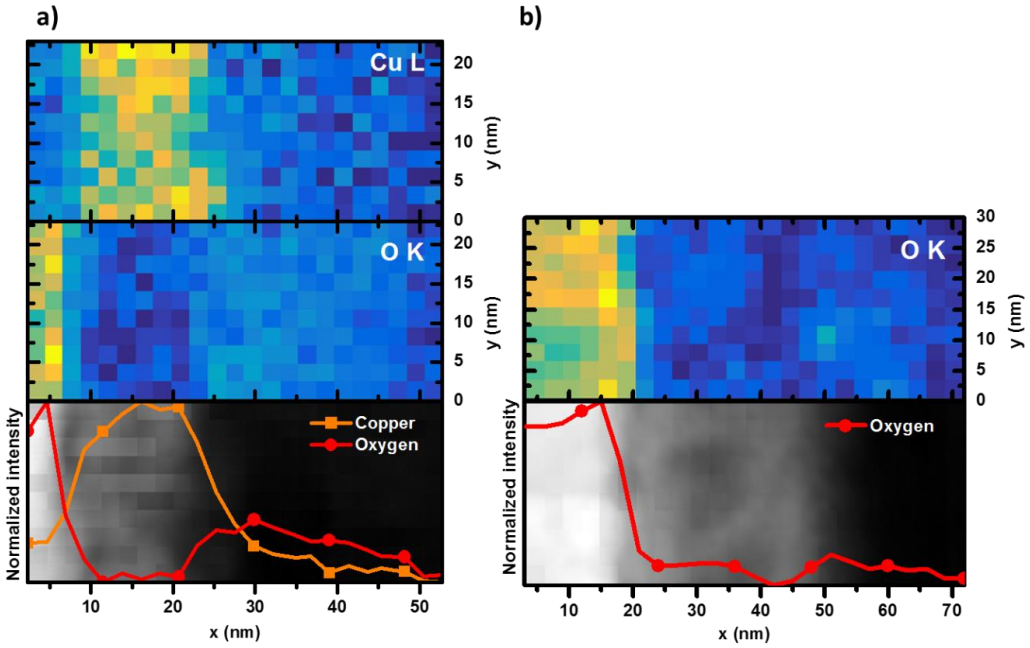

Figure 3-6. Electron energy loss spectroscopy elemental map of (a) FA and (b) NH4 for Cu and/or O as well as STEM bright field image (bottom) with the integrated elemental distribution overlaid.

3.4 Optical properties

CuSCN is widely regarded for its superior optical transparency.[145] To confirm that this key feature is still present even after the cast films are chemically altered by the different solvent combinations, transmission/absorption spectra of freshly prepared films were recorded. Figure 3-7.a depicts the absorption coefficient α (absorbance normalized by film thickness) as well as the transmittance (inset) where the contributions from the quartz substrate were subtracted. The reference is characterized by an onset of absorption at around 325 nm as well as two distinct peaks at 302 and 235 nm. In contrast, NH4 features a similar albeit attenuated absorption peak at 235 nm. However, the distinct feature at 302 nm found in DES is now a less pronounced shoulder followed by a region of higher absorbance compared to the reference. This behavior is attributed to the decomposition of CuSCN into secondary oxides and various byproducts which lead to an attenuation of the peak associated with the optical bandgap as well as the increased absorption at higher wavelengths. Turning our attention to FA, the effect of FA can be clearly seen, as FA exhibits a similar spectral shape as the reference with the onset of absorption as well as the position of the distinct peaks being the same while the magnitude of the absorption coefficient being largely the same. This again highlights the reducing power of FA which effectively suppresses chemical degradation of CuSCN. Since the optical transparency of an HTL is important for the performance of an OLED the transmittance from 400 up to 1500 nm (inset of Figure 3-7.a) was recorded. Over the important visible range between 390 to 750 nm DES, NH4 and FA had high mean transmittance values of 93, 93 and 95%.

Inspired by the work of Pattanasattayavong et al.[145] the optical bandgap E_{OPT} was extracted via Tauc plots by taking the calculated absorption coefficients α and plotting $(\alpha h\upsilon)^n$ versus hυ where h is Planck's constant and υ is the frequency of light. As shown previously, it is possible to not only extract the direct bandgap (n=1) but also the indirect transition bandgap (n=1/2). As can be seen in Figure 3-7.b and -c regions of linear dependence are present in both types of transition in NH4 and FA and, thus, it is possible to extract E_{OPT} by extrapolating these two regions to intercept the energy axis. For DES (see Appendix A.3) 3.83 and 3.34 eV were obtained for the direct and the indirect transition, respectively. The direct transition is in line with earlier findings while the indirect transition is off by more than 0.1 eV. By this method a direct and indirect bandgap of 3.80 and 3.29 eV was found for NH4 (Figure 3-7.b) and 3.81 and 3.38 eV for FA (Figure 3-7.c), respectively. From the minor variances in E_{OPT} it is deduced that the direct transition is not altered by NH4 nor by FA. However, E_{OPT} of the indirect transition rises by almost 0.1 eV by using FA in the solution. This modification again might be explainable by the presence of secondary oxides or different crystal structures.

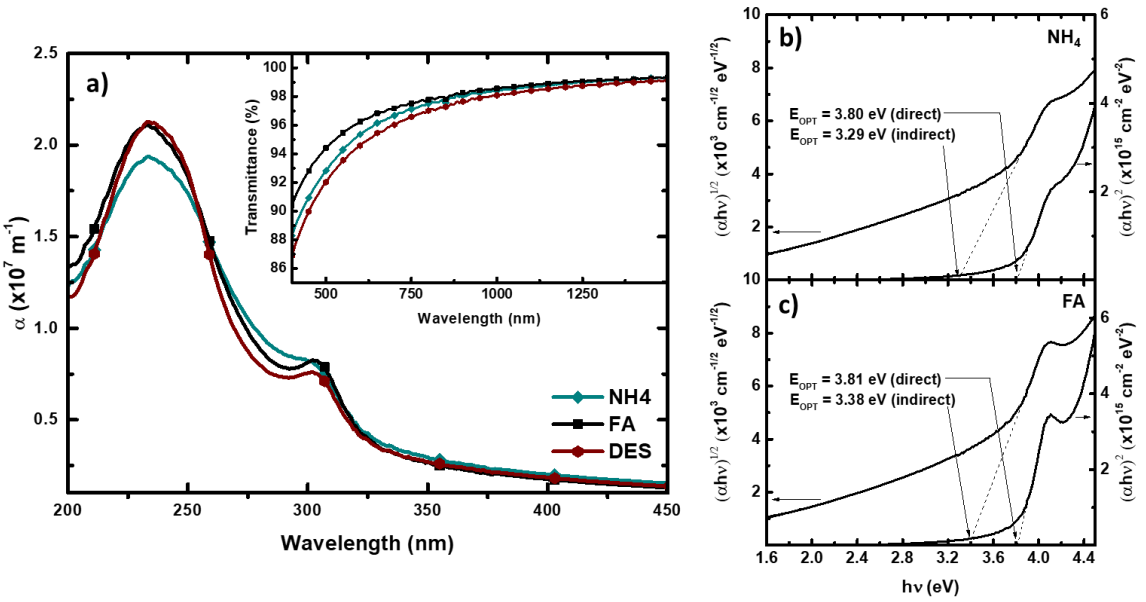

Figure 3-7. (a) Absorption- and transmission spectra (inset) of the investigated films. Tauc plots of films from (b) NH4 and (c) FA.

Concluding this section, it can be summarized that the high optical transparency as well as the high energy of E_{OPT} is preserved in NH4 and FA.

Beyond the absorption VASE measurements of DES, NH4 and FA were carried out. The refractive index (n), extinction coefficient (k) and the film thickness was obtained by modelling the real and the imaginary parts of the refractive index via a combination of Lorentzian oscillators (see Appendix A.4).

As evident from Figure 3-8.a, the layers processed via the aqueous route show a significantly increased refractive index of 1.90 and 1.91 for NH4 and FA respectively. Furthermore, to obtain a good fit for FA, modelling of two separate layers was necessary. The second layer is the ammonium formate layer with a refractive index between 1.68 and 1.57 for the depicted range, which is plausible when comparing to other organic dielectrics and salts.[174,175]

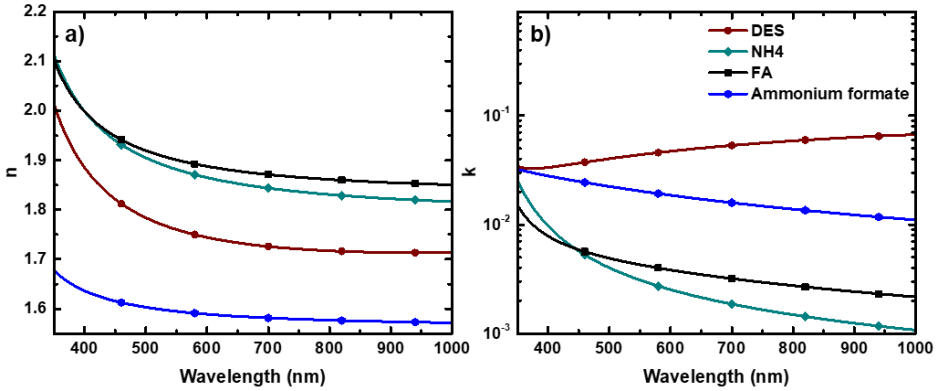

Figure 3-8. (a) Refractive index and (b) extinction coefficient as determined by ellipsometry for the investigated films

3.5 Electrical characterization

The results from the last subchapter would lead to the expectation that FA performs better than NH4. However, the presence of ammonium formate, an insulator, might proof to be detrimental for its performance as a HIL/HTL. In order to gain further insights into the impact of the ammonium formate layer on the electrical transport it is necessary to obtain the dielectric permittivity. To this end, C-V measurements were performed via impedance spectroscopy on ITO/HTL/MoO_3/Al devices. With the DC bias to 0 V, the capacitance for the parallel circuit was evaluated by[176,177]

$$C_{corr} = -\frac{1}{\omega}\left[\frac{Z'' - \omega L}{(Z' - R_s)^2 + (Z'' - \omega L)^2}\right] \tag{3.1}$$

with the reactance Z'', the resistance Z', the angular frequency $\omega = 2\pi f$, the series resistance R_s and the parasitic inductance L. Here, parallel to the capacitance a resistance R_s and in series a parasitic inductance is modelled. This allows obtaining the dielectric constant by

$$\varepsilon_r = \frac{C_{corr} d}{\varepsilon_0 A} \tag{3.2}$$

where ε_0 is the vacuum permitivity, A is the area of the device and d is the thickness of the HTLs. The frequency dependent capacitance measurements (Figure 3-9.a) reveal a strong dependence of the capacitance on the frequency for NH4 as well as FA while DES is largely stable. This is explained by the presence of polar groups at the interface which relax at lower frequencies.[178] At higher frequencies, DES and FA stabilize at the geometric capacitance C_0 whereas NH4 still experiences a continuous decline. With respect to the dielectric constant (see Figure 3-9.b) this of course also means a large variation for NH4 and FA where the dielectric constant drops from 17.5 and 16 at 20 Hz to 6.5 and 3.4 at 2 MHz, respectively. For DES a minor variance from 7 at 20 Hz to 4.2 at 2 MHz was observed which agrees reasonably well with the value of 5.1 previously obtained in an MIS diode geometry.[179] Going forward, the obtained ε_r will be treated as a quasistatic dielectric constant of the HTL and 17.5, 16 and 7 are going to be used for FA, NH4 and DES, respectively.

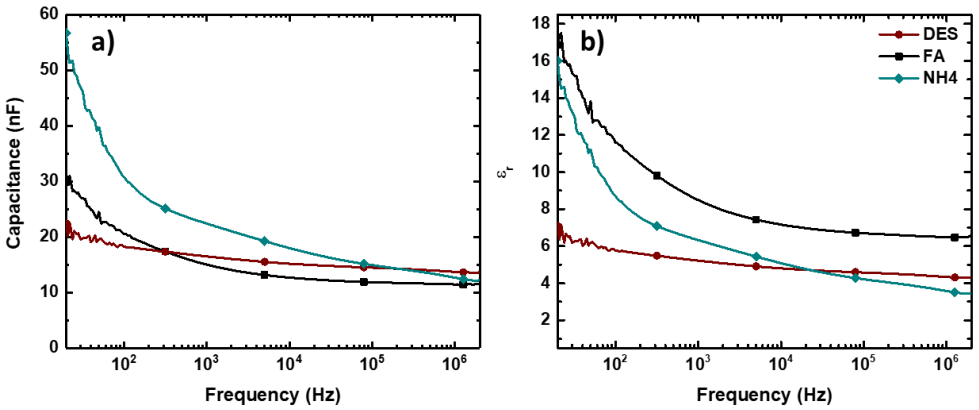

Figure 3-9. (a) Corrected capacitance and (b) dielectric constant in dependence of the frequency of the investigated films at 0 V applied DC bias.

To investigate charge transport characteristics of holes in DES, FA and NH4, hole-only devices with an ITO/HTL/MoO_3/Al geometry were fabricated. The obtained current density-voltage (J-V) characteristics are shown in a log J-log E form in Figure 3-10.a. In accordance with the theory of space-charge-limited-current (SCLC), different domains are recognizable. Starting at lower bias voltages e.g. small electric field strengths, the slope of log J – log E is 0.7, 1 and 1.3 for NH4, DES and FA, respectively, which reflects an ohmic behavior

$$J_{Ohm} = qN_0\mu\frac{U}{d} \tag{3.3}$$

where the scaling exponent m = 1.[180,181] This is also often an indicator for an ohmic contact, which is necessary to sustain a steady state space charge limited current (SCLC).[182] Increasing the electrical field strength further resulted in a deviation from the linear relationship between bias and current density. At a certain crossover voltage, the injected carrier density became larger than the thermally free intrinsic carriers which lead to the build-up of an electric field larger than the externally applied one. This first occurred for FA, then for NH4 and lastly for DES which might indicate the presence of more free charge carriers in DES than in NH4 or FA. Since trap-free or trap-filled SCLC follows a $J \propto U^m$ dependence where the scaling exponent m=2, it is obvious that the presence of higher-order scaling exponents m=2.7, 3.6, 3.6-5.1 for FA, DES and NH4 is caused by the presence of charge traps. Curiously, NH4 exhibits two different scaling exponents whereas the other two layers are fully characterized by a single exponent before crossing over to the trap-filled limit which is indicative for more than one type of charge trap. Lastly, increasing the bias further lead to a filling of the trap states and allowed for a recovery of the $J \propto U^2$ behavior. The transition to the trap-filled SCLC limit occurred first for FA and then DES while NH4 was not able to reach the trap-filled limit before short-circuiting.

In this regime, Childs law

$$J_{SCLC} = \frac{9}{8}\mu\varepsilon\frac{U^2}{d^3} \tag{3.4}$$

with the hole mobility μ, the layer thickness d and the relative permittivity ε holds and allows for a determination of the hole mobility for FA as well as DES. This way a mobility μ of 9.8 x 10^{-6} cm^2 $V^{-1}s^{-1}$ for FA and 4.9 x 10^{-6} cm^2 $V^{-1}s^{-1}$ for DES was obtained. These values represent the mobilities for typical layer thicknesses used in OLEDs. In general, care has to be taken since at 30-50 nm layer thickness, the injecting contacts might have a profound impact on the bulk mobility. To exclude such an effect, the measurement was redone with twice the thickness of DES. Again, the mobility amounted to 3.2 x 10^{-6} cm^{-2} V^{-1} s^{-1} which is quite close to the value obtained for thinner layers. While it is acknowledged that reliable mobility values require further variations, it is pointed out that for the comparison in performance between these layers the accuracy of the obtained mobility values is sufficient. Comparison with recently published field-effect mobilities in the range of 10^{-3}-10^{-2} cm^2 V^{-1} s^{-1} for bottom gate bottom-contact transistors, reveals that the bulk mobilities obtained in this study are about 3 to 2 orders of magnitude lower than the reported field effect mobilities.[145] This is plausible since the field effect mobility is a property of the interface.[183,184] Also, additional charges are accumulated in the channel and the mobility is highly sensitive to additional charges in systems with a certain amount of disorder. [129,183,185,186]

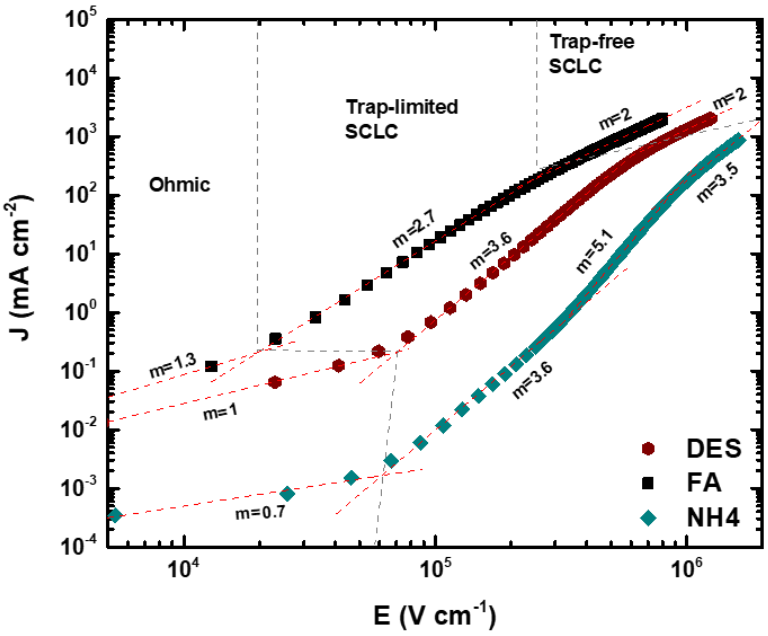

Figure 3-10. Current density versus electrical field for all investigated films. Scaling exponents *m* for the different regimes are also indicated.

To get an insight into the distribution of the trap states, an analysis method proposed by Nepurek et. al, which allows to recover the energetic profile of localized states via a differential method, is used.[187,188] In this method, the position of the quasi-Fermi level at the collector is calculated by

$$\mathrm{E}_F(D) = kTln\frac{D}{\kappa_1 N_0 e\mu} + kTln\frac{j}{U} \tag{3.5}$$

where k is Boltzmann's constant, T the temperature, D the thickness of the layer, $\kappa_1 = (2m - 1)/m$, N_0 are the free charge carriers, e the elementary charge and μ the charge carrier mobility. Increasingly larger bias values shift the position of the quasi-Fermi level towards the extended states. The spectroscopic character of this method originates from the change in occupancy of the traps in dependence on the shift of the quasi-Fermi level and thus allows to resolve the energetic distribution of the traps. The localized density of states (DOS) is then obtained by

$$n_t(\mathrm{E}_f) = \frac{\varepsilon\kappa_1\kappa_2}{2eD^2kT}\frac{U}{m-1} \tag{3.6}$$

where $m = \partial(\ln j)/\partial(\ln U)$, $\kappa_2 = [(2m-1)/m](1+\mathrm{B})$ and $B = -\frac{1}{m(m-1)(2m-1)}\frac{\partial m}{\partial \ln U}$ is a second-order correction.

Figure 3-11.a shows the localized states DOS extracted from the corresponding J-E characteristics depicted in Figure 3-10. To calculate the position of the quasi Fermi-level E_F, N_0 was extracted by fitting Ohm's law in the ohmic regime of the respective layers, while μ was obtained by fitting Child's law to the trap-filled region. Since the range of the DOS depends on the bias-induced change of the quasi Fermi-level, the resolvable energy ranges differ depending on the investigated layers. Thus, the DOS of NH4 spans 0.24 eV while DES and FA cover 0.17 and 0.15 eV of the energy range. The magnitude of the localized DOS spans the range between 10^{17} - 10^{21} cm^{-3} which is in agreement with other bulk trap DOS.[189] The localized DOS of DES and FA appears to be well characterized by an exponential distribution of localized states, which is in accordance with the detected superquadratic exponents as well as literature.[190,191] While also being well characterized by an exponential distribution, NH4, however, exhibits a further type of trap energetically located between 0.50 and 0.54 eV whose origin is attributed to the presence of significantly increased chemical impurities. Exponential distributions of the type $n_t \propto exp(E_F/E_t)$ have a characteristic energy $\mathrm{E_t}$ describing the energetic spread of the localized states which can be retrieved by fitting the linear regime in the semilogarithmic plot. This way an $\mathrm{E_t}$ of 40, 65 and 100 meV was obtained for FA, DES and NH4.

Beyond ~0.63 eV (see Figure 3-11.a), the localized DOS of the layers starts to deviate from the exponential behavior. Remarkably, this deviation takes place between 0.63-0.67 eV which is in excellent agreement with UPS measurements that positioned the mobility edge at 0.63 eV below the fermi level.[144] This allows the localized DOS to be repositioned relative to the mobility edge (Figure 3-11.b) and hence an extraction of N_t by the general expression of the exponential localized DOS by

$$g(E) = \frac{N_t}{E_t} \exp\left(-\frac{E}{E_t}\right) \tag{3.7}$$

yielding a concentration of 3.9 x 10^{17}, 7.0 x 10^{17} and 4.7 x 10^{18} cm^{-3} for FA, DES and NH4, respectively.

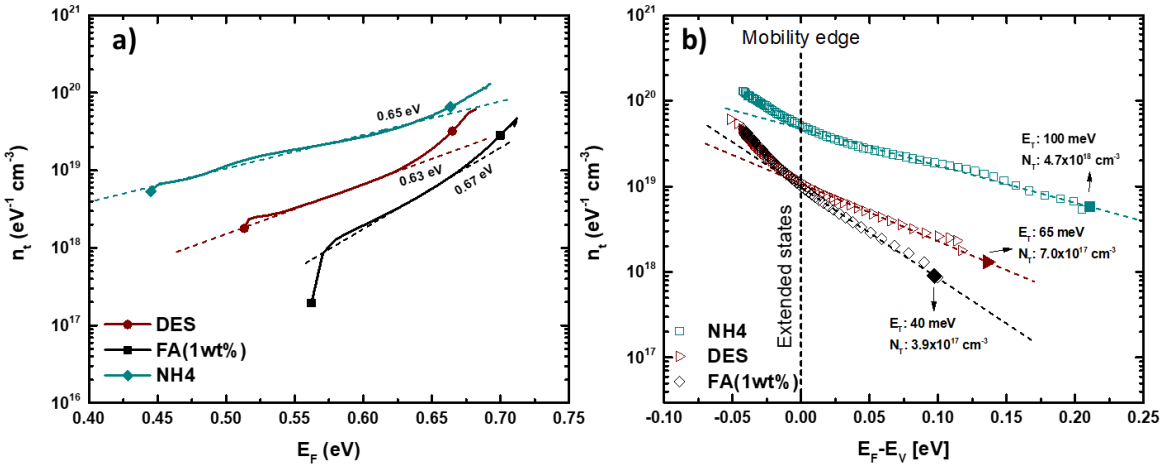

Figure 3-11. (a) Density of localized states n_t for DES, NH4 as well as FA. (b) Density of localized states n_t for DES, NH4 as well as FA repositioned relative to the hole mobility edge. Dashed lines represent the respective exponential fits of the trap density with the trapping energies listed in Table 2.

Based on the assumption that the onset of the DOS corresponds to the Fermi level in thermal equilibrium E_{FN0}, the effective DOS in the valence band, N_V can be determined by[192]

$$E_V - E_{FN0} = kT \ln\left(\frac{N_V}{N_0}\right) \tag{3.8}$$

which yields 5.6 x 10^{17}, 3.6 x 10^{18} and 2.8 x 10^{17} cm^{-3} for NH4, DES and FA. Credibility of these values was checked by calculating the density of charge carriers in the valence band via the effective masses for holes obtained by Jaffe et. al.[119] for CuSCN by means of band structure calculations. The density of charge carriers in the valence band was found to be on the order of 10^{18} cm^{-3} which is in excellent agreement with the results obtained from SCLC.

Table 3-3. Important parameters for charge carrier transport obtained by SCLC measurements and DOS reconstructions

Layer	μ ($cm^2\ V^{-1}s^{-1}$)	N_0 (cm^{-3})	N_V (cm^{-3})	N_t (cm^{-3})	E_t (meV)
DES	4.9×10^{-6}	3.8×10^{16}	3.6×10^{18}	7.0×10^{17}	65
FA (1wt%)	9.8×10^{-6}	6.1×10^{15}	2.8×10^{17}	3.9×10^{17}	40
NH4	$<9.2 \times 10^{-7}$	2.0×10^{14}	5.6×10^{17}	4.7×10^{18}	100

As observed by Pattanasattayavong et al.[179] the most important parameter with regards to charge carrier transport is the characteristic energy E_T which is reaffirmed by the determined mobilities. Since the hole mobility is among the most important quantities that characterizes the effectiveness of a HIL/HTL, the field dependence of the mobility was further probed via impedance spectroscopy.[193] Specifically, the Im(Z) method[194] was used where the peak frequency response on the applied bias field is exploited to determine the characteristic transit times. It was previously demonstrated that the connection between the obtained time constant τ_p and the real transit time τ_{DC} can be made by applying a constant numerical factor κ.[195] The exact value of this constant, however, varies widely from 0.29 up to 0.75.[196–198] Tripathi et. al. put the origin of this constant on a solid foundation by linking it to the dispersive character of the material.[194] While a more thorough investigation would require fitting the model to the data, a value of $\kappa = 0.47$ was used for the assumed situation of non-dispersive transport. With $\tau_{DC} = 0.47x\tau_p$ the mobility under DC bias is obtained by

$$\mu_{DC} = \frac{4d^3}{3\tau_r E} \tag{3.9}$$

where d is the thickness of the HTL and E is the applied electric field. Since often a Poole-Frenkel type field dependence of $\sqrt{E}$ is observed, the mobilites were plotted versus the square-root of the applied field (Figure 3-12). Evidently, FA and DES exhibit a field dependence only for low bias fields and quickly saturate around $1x10^{-5}$ cm^{-2} V^{-1} s^{-1} and $7x10^{-6}$ cm^{-2} V^{-1} s^{-1}. At the same time the obtained mobility values nicely match with the obtained SCLC mobility for FA and a reasonable agreement for DES is found, strengthening the choice for κ. While the mobility of both HIL/HTLs are already plateauing at low bias fields, FA even exibits a minor decrease at high electric fields. Moving on to NH4 and the obvious Poole-Frenkel type[199] dependence of the mobility, the well-known Poole-Frenkel like field-dependent mobility model $\mu = \mu_0 \exp(\gamma\sqrt{E})$ was used. In particular, a field enhancement factor γ=$2.96x10^{-3}$ $V^{0.5}$ $cm^{-0.5}$ and a zero-field

mobility μ_0=1.29x10^{-8} cm^{-2} V^{-1} s^{-1} were obtained by fitting the linear regime of the field-dependence (straight line in Figure 3-12). Remarkably, the mobility starts to deviate from the Poole-Frenkel type field-dependence at higher field strengths which is similar to the behaviour exhibited by DES and FA. To conclusively unveil the hole transport mechanism in the investigated films further characterization with respect to the temperature dependence of the mobility would be required which is out of the scope for the present work. Nonetheless, a dependence between E_t as well as N_t and the field dependence of the mobility can be found. Namely, FA, which exhibits the lowest E_t, only shows modest field-dependent mobility, followed by a slightly increased field-depedence of DES and lastly the severe dependence of NH4 with the highest value of E_t and N_t. With the observed saturation at higher applied electric fields, it seems reasonable to suspect the transport mechanism to be best described by the multiple trapping and release (MTR) model.[129,135,200,201] Of course differences in grain size might also play a role.[173,202,203]

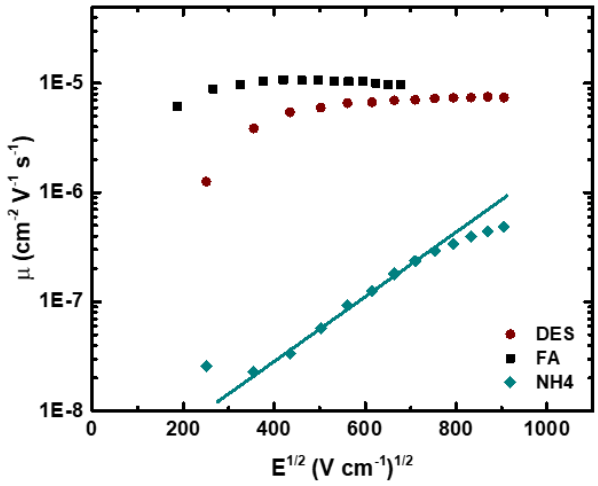

Figure 3-12. Field dependence of the hole mobility determined by impedance spectroscopy of the investigated films.

Another interesting phenomenon arises when the capacitance at high electric fields is inspected. As depicted in Figure 3-13, all HIL/HTLs reveal a negative capacitance or inductive behavior. This is generally associated with the injection and redistribution of additional charges in hole-only devices.[197] Until a critical frequency closely associated with the transit time is reached, the resulting current lags behind the applied ac field which results in a negative contribution to the capacitance.[197,198] Noteworthy is that at f=20 Hz DES and NH4 exhibit a similar value of negative capacitance. At the same frequency, FA shows a value twice as large as the former two. It has been suggested that the amount of negative capacitance is proportional to recorded current density.[204] This would imply, that the current density at the same applied electric field has to be significantly larger than the one recorded for DES and NH4,

which, at least in the case of DES, is not the case (see Figure 3-10). More likely, this increased negative capacitance originates from additional relaxation mechanisms within the ammonium formate layer as it was suggested by recent work.[205]

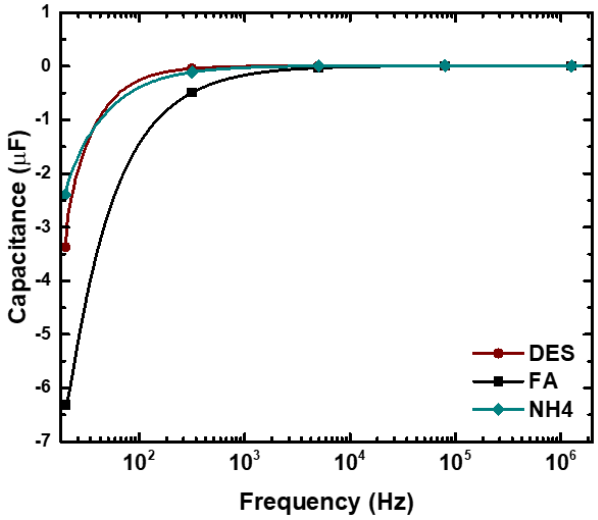

Figure 3-13. Capacitance of the films at an applied electric field of 8.2×10^6, 4.6×10^6 and 8.2×10^6 V cm^{-1} for DES, FA and NH4 respectively.

Concluding these investigations, it is clear that the improved crystallinity as well as the significantly reduced chemical byproducts allowed the FA layer to exhibit superior hole mobilities when compared to NH4 and even DES. Furthermore, the mobility was found to be largely independent of the applied bias field for FA and DES whereas the opposite was true for NH4. This is likely attributable to the quite large value of E_T which is more than twice as large as the value obtained for FA. Lastly, the ammonium formate layer of FA exhibited a markedly increased negative capacitance which was attributed to additional relaxation mechanisms within the ammonium formate layer.

3.6 Performance in an OLED

So far, the properties of FA were studied and it was found to be equal or even better than the reference DES processed CuSCN HIL/HTL. Especially with respect to the surface energy and hole mobilities it is clearly superior while it remedies the situation with the introduced impurities and reduced crystallinity found in NH4 layers. With all these important qualities checked, it is now important to benchmark FA against NH4, DES and PEDOT:PSS. Crucially, it has to be checked whether the present ammonium formate layer negatively impacts the device performance. Pure intuition would dictate that the insulating properties of salt should effectively reduce the device performance compared to the other layers. It has already been surprising that the salt layer has not massively impacted the results obtained during the

electrical characterization. To get a good picture, two solution-processed OLED stacks were used as benchmark platforms. This provides even more insight into impact of the FA HIL/HTL on OLED stacks with different weaknesses while also building a strong case for the universal applicability of the layer. The first stack (PhOLED) is built around the green-emitting phosphorescent dopand $Ir(ppy)_3$ and a mixed host system comprised of the small-molecular materials TCTA and TAPC.[206] Compared to state of the art OLED stacks which are vacuum deposited[207–209], a comparably simple yet reasonably effective three-layer (HIL/HTL, EML, ETL) architecture was used. As the ETL, TmPyPB, a high electron mobility material suitable for this performance test was selected.[210,211] Efficient electron injection was guaranteed by a layer of calcium and aluminum as the cathode material. A TEM cross-section of OLED stacks with FA and NH4 is depicted in Figure 3-14. The first striking difference between these two stacks is the presence of the ammonium formate layer, which, based on the EELS measurements in chapter 3.3 is approximately 21 nm thick. At the same time, the thickness of CuSCN itself is reduced to 18 nm whereas the NH4 layer is 31 nm thick. Evidently, the ammonium formate layer is not attacked by the successive spin-coating step, which demonstrates the orthogonality between chlorobenzene and the ammonium formate layer.[138,212–214] However, presumably due to the low melting point of ammonium formate, the interface to the EML is a little bit washed out. Since the material contrast between the EML and the ETL is similar, the interface between these two layers can't be resolved. In this case, the data of the quartz crystal microbalance used to control the ETL thickness was utilized, which yields an EML thickness of 34 and 39 nm for the FA and NH4 based OLED, respectively.

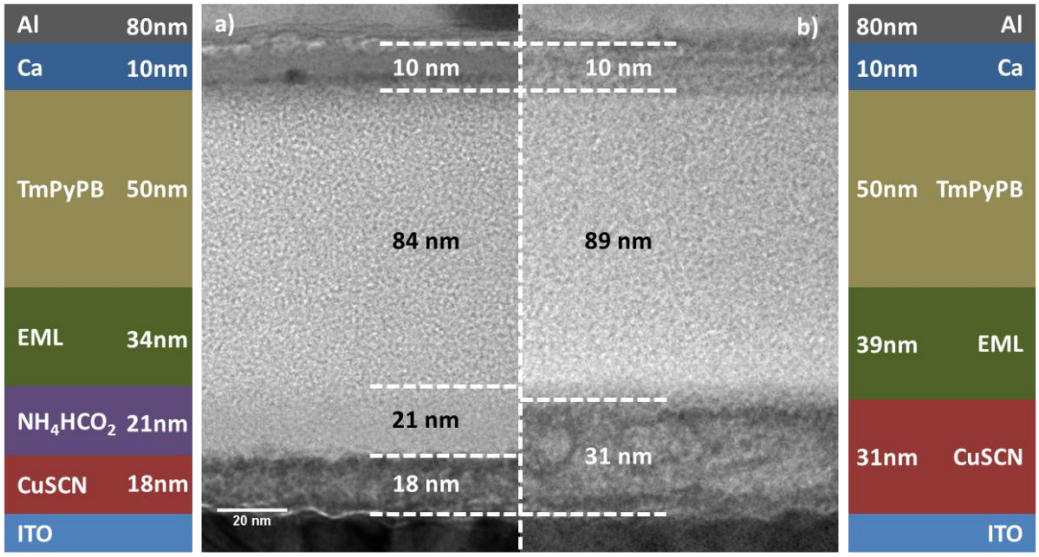

Figure 3-14. TEM image of focused ion beam (FIB)-milled cross sections of (a) FA and (b) NH4 HIL/HTL OLEDs. The schematics are indicated on the left- and right-hand sides respectively. The interface between EML and ETL is not resolvable due to the lacking material contrast. ETL value was taken from SQC value which allows to assign the remaining thickness to the EML.

Figure 3-15.a shows the current density versus the bias voltage for the green-emitting phosphorescent OLED. Compared to the PEDOT:PSS reference device, the CuSCN based devices exhibit a significantly (approximately 100-fold) reduced leakage current under reverse bias.[164] This is in line with earlier reports and a direct consequence of the favorable position of the conduction band that provides sufficient electron blocking capabilities. Under forward bias, all CuSCN based devices show a sharp transition from the injection limited to the space charge limited current regime. Notably, DES already transitions at 2 V while NH4 and FA experience this transition at 3.3 V. Expectedly, this sharp transition is absent for the PEDOT:PSS device which most certainly can be attributed to a work function mismatch.[164] The behavior of the current density characteristics is closely mirrored by the luminance characteristic (see Figure 3-15.b). Again, starting with the PEDOT:PSS device, a high turn-on voltage of 7.1 V was recorded even though a significant current density was recorded, again, a clear sign that one charge carrier species experiences significant injection barriers. Focusing on the CuSCN based devices, turn-on was observed at 3.7 V for NH4 and FA and 4.0 V for DES. In accordance with the current density characteristics, the increase in luminance was slower in the case of DES than for NH4 or FA. This seems rather curios, especially in the context of the mobility and DOS measurements which would suggest that the performance of this HIL/HTL would be closer to FA than PEDOT:PSS. A cause might be the low surface energy of the DES layer which could be detrimental to the formation of a clean interface.[139,215–217] This is further substantiated by comparing the performance of NH4 which possess a rather high surface energy and thus superior wettability. NH4 exhibits similar current density and luminance characteristics as FA under low bias voltages. However, the low hole-mobility of this layer soon leads to a deviation from the best performing FA. Considering that there is an ammonium formate layer of approximately 21 nm thickness present it is remarkable that such a performance advantage is attained. In terms of peak luminance, 7068, 7438, 7481 and 8359 cd m^{-2} were attained by DES, PEDOT:PSS, NH4 and FA, respectively. Regarding the emission spectrum of the investigated devices, it is clear from the inset in Figure 3-15.b that except for PEDOT:PSS, which shows increased contribution towards the green and red part of the spectrum, all CuSCN based devices feature a virtually identical emission profile. These findings provide an important starting point for the discussion of the recorded current efficiency (Figure 3-15.c) and luminous power efficiency (Figure 3-15.d) characteristics of the investigated HIL/HTL powered OLED devices. Again, starting with the PEDOT:PSS reference, the impact of the injection barrier is clearly visible by the bias dependent increase in current as well as luminous power efficiency caused by the increased amount of charge carriers that are able to penetrate the injection barrier. The CuSCN layers on the other hand show no such signs and hence start at reasonably high current and luminous power efficiency values already at low luminance

values. All layers show a minor increase in current efficiency up to approximately 100 cd m^{-2}. After that a slow efficiency roll-off in current efficiency which accelerates dramatically in the vicinity of 1000 cd m^{-2} is noticeable. At approximately 1500 cd m^{-2} the increased hole-mobility of DES shows and allows this layer to pull ahead of NH4. Close to the peak luminance values the current efficiency characteristic of PEDOT:PSS crosses the one of NH4 and DES while FA is still able to maintain its lead. Even though the overall behavior is largely the same, the attainable efficiencies vary drastically. In detail, at a brightness of 100 cd m^{-2} peak current efficiencies of 6.0, 19.1, 24.6 and 29.2 cd A^{-1} were attained. A 10-fold increase in luminance levels yields 11.0, 17.2, 18.8 and 25.2 cd A^{-1}. With respect to luminous power efficiency, all CuSCN based OLEDs exhibit a minor efficiency roll-off up to a brightness of 100 cd m^{-2}. From this point on, the roll-off increases and at 1500 cd m^{-2} the luminous power efficiency of NH4 and DES is virtually identical. As before close to peak luminance, PEDOT:PSS is able to show slightly superior luminous power efficiency values compared to NH4 and DES but it is still not able to surpass FA. In line with previous work, the absence of any injection barrier as well as sufficiently large hole mobilities are required to obtain best possible performance.[164] In this context, it is rather surprising that the ammonium formate layer doesn't impose an injection barrier for holes.

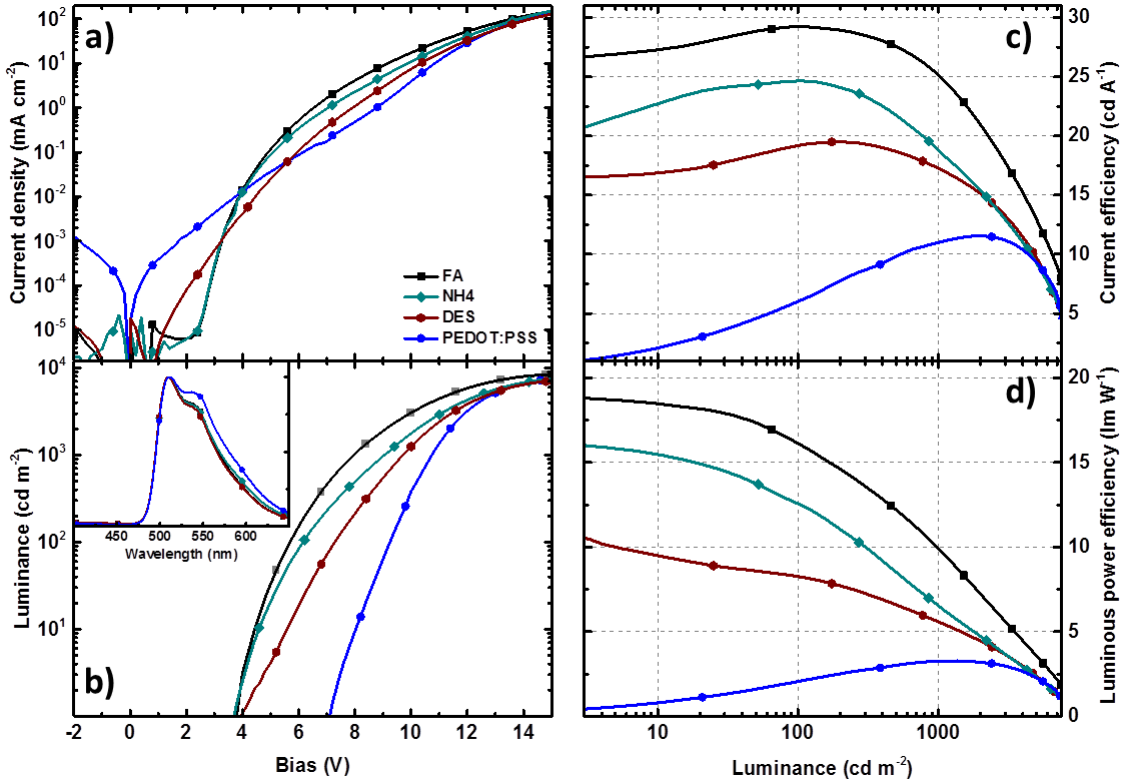

Figure 3-15. (a) Current density and (b) luminance versus bias voltage (the inset depicts the normalized EL recorded at a current density of 10 mA cm^{-2}). (c) Luminous efficiency and (d) luminous power efficiency versus luminance for green-phosphorescent OLEDs with ITO/FA, NH4, DES and PEDOT:PSS used as HIL/HTL.

FA as well as NH4 were able to perform remarkably well when applied to a solution-processed PhOLED stack. This was attributed to several beneficial properties such as better wettability, absence of injection barriers and in the case of FA high hole mobilities. To strengthen the case for the application of FA and NH4 in OLEDs, a fluorescent blue-emitting OLED stack was picked.[168,218] Optimized to work in conjunction with PEDOT:PSS, this stack is able to provide high luminance values at comparably good current efficiencies. To perform this comparison, all layers were processed as they would have been with PEDOT:PSS forgoing any optimizations. Overall, the devices featured an ITO/HIL,HTL/CP-AE/CP-ABCD/Ca/Al configuration. This means that the CuSCN layers now mainly perform as a HIL. Starting the discussion with the current density characteristics (Figure 3-16.a) it can see that the introduction of CP-AE further reduced the leakage current for FA and NH4. By the reduced leakage current for PEDOT:PSS, it can be seen that CP-AE fulfils its function as a HTL. Since there are now two separate HIL and HTLs, the situation under forward bias becomes somewhat more complicated. Here, PEDOT:PSS, DES and NH4 show a sharp transition from the injection limited to the space charge limited current regime. The same is of course true for FA but the injection limited current is about two orders of magnitude above the other layers for reasons presently unknown. One possibility might be that the heat treatment step required for the insolubilization of the HTL attacks the ammonium formate layer thus effectively thinning the HIL. However, in spite of the low reverse bias current this is deemed rather unlikely. Focusing on the luminance characteristics (Figure 3-16.b) it can be seen that FA already turns on at 2.9 V followed by DES at 3.2 V and PEDOT:PSS at 3.4 V. NH4, however, turns-on at a comparably high voltage of 3.8 V. Except for NH4, all HILs see a sharp increase in luminance after the onset. The low hole mobility of NH4 was already apparent in the PhOLED but is now severely limiting in this high luminance stack. The impact of the hole mobility is also reflected in the peak luminance values. Here, PEDOT:PSS attained the best value of 28972 cd m^{-2} closely followed by FA with 28035 cd m^{-2}. DES attained 20408 cd m^{-2} and NH4 was still able to hit 17991 cd m^{-2} at 10 V, approximately 2 V above the other peak values. Regarding the emission spectra (inset, Figure 3-16.b), as with the PhOLEDs, all CuSCN based devices exhibit virtually identical emission spectra, while in the case of PEDOT:PSS a higher intensity at the first vibronic shoulder was recorded. Current efficiency (Figure 3-16.c) and luminous power efficiency (Figure 3-16.d) of all HILs is characterized by a continuous increase in efficiency up to luminance values between 10^2 and 10^3 cd m^{-2}. This behavior is attribute to a slight barrier for electrons due to the usage of Ca instead of cesium carbonate (Cs_2CO_3).[168] At a brightness of 100 cd m^{-2} FA is able to attain a current efficiency of 2.9 cd A^{-1} followed by 1.6 cd A^{-1} for DES, 1.4 cd A^{-1} for PEDOT:PSS and a low 0.3 cd A^{-1} for NH4. With increasing luminance values the number of available holes becomes even more important. As a consequence, PEDOT:PSS

increases more strongly in efficiency as the other layers and surpasses DES around 200 cd m^{-2} and FA close to 1100 cd m^{-2}. This again highlights the beneficial combination of high charge carrier mobility and superior wettability. Luminous power efficiency characteristics closely mirror the behavior of the current efficiency. At 100 cd m^{-2} luminous power efficiency values of 2.4, 1.2, 1.1 and 0.2 lm W^{-1} were recorded.

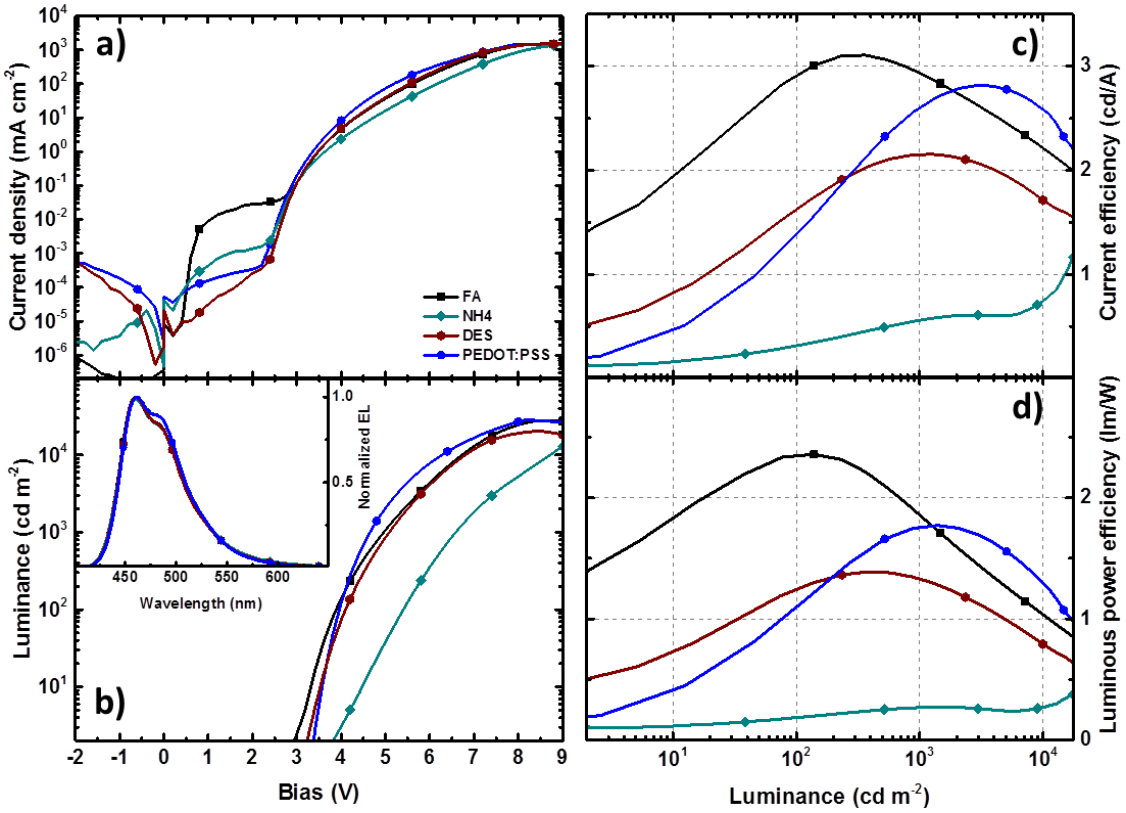

Figure 3-16. (a) Current density and (b) luminance versus bias voltage (the inset depicts the normalized EL recorded at a current density of 10 mA cm^{-2}), (c) luminous efficiency and (d) luminous power efficiency versus luminance for blue-fluorescent OLEDs with ITO/FA, NH4, DES and PEDOT:PSS used as HIL

Remarkably, FA was clearly superior to the other investigated HIL/HTLs in both structures. As indicated above, this is attributed to the high hole mobility of FA and superior wettability necessary for solution-based processes. While the ammonium formate layer had obvious negative impact, motivated by the 2-fold increase in negative capacitance determined for hole-only devices, it is assumed that charge carrier confinement is improved. Of course, this would have to be verified by follow-up investigations.

Interestingly, DES was unable to consistently be the second-best option even though its hole mobilities were far superior to NH4. This highlights that on top of high hole mobilities good wettability is a stringent requirement for efficient HIL/HTLs.

A summary of the presented device performance data for all layers in both stacks is given in Table 3-4.

Table 3-4. Device performance data for $Ir(ppy)_3$ and PIF based OLEDs

OLED System	HIL/HTL	Onset voltage [a] [V]	Peak Luminance [cd m^{-2}]	Luminous efficiency [cd A^{-1}]		Luminous power efficiency [lm W^{-1}]	
				100cd m^{-2}	1000cd m^{-2}	100cd m^{-2}	1000cd m^{-2}
$Ir(ppy)_3$ [b]							
	DES	4.0	7068 (15.0 V)	19.1	17.2	8.3	5.5
	PEDOT:PSS	7.1	7438 (15.2 V)	6.0	11.0	2.1	3.2
	NH_4	3.7	7481 (15.0 V)	24.6	18.8	12.6	6.6
	FA	3.7	8359 (15.0 V)	29.2	25.2	16.1	9.9
PIF [c]							
	DES	3.2	20408 (8.4 V)	1.6	2.2	1.2	1.3
	PEDOT:PSS	3.4	28792 (8.2 V)	1.4	2.6	1.1	1.7
	NH_4	3.8	17991 (10 V)	0.3	0.6	0.2	0.3
	FA	2.9	28035 (8.6 V)	2.9	2.9	2.4	1.7

[a] voltage at a luminance of 1 cd/m²; [b] ITO/HIL/TCTA:TAPC:$Ir(ppy)_3$/TmPyPb/Ca/Al;
[c] ITO/HIL/ CP-AE/CP-ABCD/Ca/Al

3.7 Conclusion

In this chapter, a novel route to process CuSCN from ammonium hydroxide was investigated. By means of the observed deep-blue color, it was confirmed that a complexation reaction of CuSCN to $[Cu(NH_3)_4H_2O]^{2+}$ takes place. Since this route introduces secondary oxides, it was attempted to prevent and even revert the unwanted oxidation process by the addition of formic acid. Spin coating solutions containing EtOH and EtOH:FA yielded smooth films with superior surface roughness and surface energy when compared to processing from DES solutions. XPS studies of NH4 and FA were able to confirm the formation of unwanted secondary oxides and more astonishingly an almost complete absence in the case of FA. HRTEM investigations also confirmed a higher degree of crystallinity in the case of FA than NH4. Furthermore, by EELS measurements of the Cu L and O K spectral region of the ITO/(HIL/HTL)/organic interface region it was shown that the formation of two phase separated layers consisting of pure CuSCN and ammonium formate, a byproduct of the acid-base reaction, takes place. Notably, the optical

bandgap determined via the Tauc method revealed similar values of 3.8 eV for the direct band gap while the introduced impurities in NH4 resulted in a shift of the indirect one by 0.1 eV compared to FA. Through SCLC measurements and DOS reconstructions it was established that FA exhibits lower trap densities than NH4 which is in line with the observed increased crystallinity as well as the higher purity. NH4 and FA exhibited an exponential trap distribution which is common for amorphous semiconductors. Here the characteristic energy of the exponential distribution was at a low 40 meV while the distribution of NH4 was characterized by an E_T of 100 meV. Furthermore, the additional impurities lead to an additional trapping type visible in the DOS. The higher crystallinity combined with the reduced E_T lead to a clear advantage in bulk mobility when compared to NH4 and even DES. Field dependence was resolved with impedance spectroscopy. Here, only NH4 exhibited a typical Poole-Frenkel type field dependence whereas FA showed only minor field dependence. All films exhibited a negative capacitance in a hole-only configuration which can be expected. Still, an unusually large negative capacitance was exerted by FA which was attributed to additional charge relaxation mechanisms in the ammonium formate layer. Importantly, benchmarks of FA against DES and PEDOT:PSS in an efficient phosphorescent and a fluorescent high luminance OLED architecture always resulted in a clear advantage for the FA layer. Here the superiority of FA was attributed to the higher surface energy, excellent hole mobilities and possibly enhanced electron blocking capabilities through the ammonium formate layer. Even though this work unveiled and answered some questions it is also clearly only a first step. Especially the reduction mechanism of FA and studies regarding the impact of the amount of added FA would be of great interest. Naturally, the role of the ammonium formate layer would also lend itself to further studies. Also, more thorough investigations on the hole-mobility or temperature and field dependent studies regarding the charge transport would be very welcome.

4

Light extraction: Aluminum nano particle arrays in mono- and polychromatic OLEDs

The formation and dependency of collective lattice resonances originating from arrays of aluminum nano particles embedded within an organic light emitting diode stack are investigated. Through optimization of key parameters, the efficiencies of monochrome blue as well as a broadband white light emitting organic diodes are increased by 35 and 23 %, respectively.

The content of this chapter is based on work that has been published and was partly modified:

Tuning of the emission color of organic light emitting diodes via smartly designed aluminum plasmonics

M. Auer-Berger, V. Tretnak, F.-P. Wenzl, J. R. Krenn and Emil J.W. List-Kratochvil

Contribution: The author carried out all experimental work and wrote the manuscript. The manuscript was finalized with the co-authors.

Adjusting the emission color of organic light emitting diodes through aluminum nano disc arrays

M. Auer-Berger, V. Tretnak, F.-P. Wenzl, J. R. Krenn and Emil J.W. List-Kratochvil

Contribution: The author carried out all experimental and simulation work and wrote the manuscript. The manuscript was finalized with the co-authors.

Aluminum-nano disc-induced collective lattice resonances: Taking control of the light extraction in organic light emitting diodes

M. Auer-Berger, V. Tretnak, F.-P. Wenzl, J. R. Krenn and Emil J.W. List-Kratochvil

Contribution: The author carried out all experimental and simulation work and wrote the manuscript. The manuscript was finalized with the co-authors.

Superimposed Al nanoparticle gratings: Broadband enhancement of organic white light-emitting diodes

M. Auer-Berger, V. Tretnak, F.-P. Wenzl, J. R. Krenn and Emil J.W. List-Kratochvil

Article under preparation;

Contribution: Investigated gratings were fabricated by V. Tretnak. Characterization of the gratings, fabrication of the OLEDs as well as the simulation work was carried out by the author. The author writes the manuscript and finalizes it with the co-authors.

4.1 Introduction

With the recent introduction of thermally activated delayed fluorescence (TADF) emitter systems, the fabrication of OLEDs with high internal quantum efficiencies (IQE) across the whole visible spectrum[219] is achievable. Since no further improvements to their cost effectiveness[220] are attainable via increases in IQE, the next improvements have to come from advances in device stack technology. Indeed, on average only 20% of the generated light can escape the stack, while the rest is trapped in surface plasmon, waveguide and substrate modes.[32] Even though SPP losses can be largely minimized by increasing the thickness of the ETL[32], waveguide modes are much more difficult to handle and generally put a limit on the achievable EQE. Accordingly, a lot of work was put into recovering parts of the trapped light.[32] Besides outcoupling schemes[209,221–231], research also focused on enhancing the radiative recombination rate[232,233] raising the amount of available light or decreasing the efficiency roll-off at high brightness conditions. Here, the high near-field enhancement in the vicinity of plasmonic NPs plays an important role which proofed especially useful in sensing applications via surface-enhanced fluorescence (SEF)[71,234–244] or Raman scattering by means of surface enhanced raman scattering (SERS)[245–259]. Embedded within an OLED[260–278], these particles enhance the EQE through mechanisms such as increased scattering of light or near-field enhancement. While impressive gains in device efficiency were achieved by a clever exploitation of the beneficial properties of plasmonic NPs, this approach suffers from the introduction of an additional non-radiative decay channel[279,280], which puts a limit on the achievable efficiency gain for high quantum efficiency emitters.[281] On top of that, an ideal placement of the emitters with respect to the metal NPs is paramount to obtain peak enhancement values.[76,239] Avoiding these obstacles, regular arrays built from plasmonic NPs have recently been investigated. As a straightforward and cost effective method, these arrays feature CLRs [282–284] that enable an excellent degree of control for the outcoupling of light. Besides silver and gold, aluminum has attracted considerable interest as a low-cost and self-passivating material, exhibiting good plasmonic properties from the UV up to the NIR. Significant improvements in light emission were reported with Al NP arrays embedded in the color conversion layer in solid state lighting devices, attributed to enhanced light generation and -outcoupling.[282] Furthermore, high tunability of the emission color and directionality of the emission was shown. While clearly OLEDs could also greatly benefit from Al induced CLRs, at the time of writing, only one report investigated Al NP within an OLED.[285] Curiously, the authors failed to observe any CLRs, even though they fabricated arrays of Al nanorods, which makes this report questionable at best.

Within this chapter the aspects that influence the formation and magnitude of these AL NP induced CLRs are investigated for the first time in the context of an embedding within an OLED. Through these studies optimized values are found that result in an efficiency enhancement of a blue-emitting OLED by 35 %. Then two concepts are presented that allow for a formation of CLRs distributed across the whole visible spectrum which is required for the enhancement of white light emitting organic diodes (WOLED). Here, with a first set of parameters an enhancement of up to 23% was realized.

4.2 Experimental procedure

Substrate cleaning

The substrates used in this study consist of a 1 mm thick float glass coated with 100 nm ITO. The ITO substrates were treated in ultrasonic baths of 2 vol% Hellmanex III for 20 minutes at a temperature of 50°C. Following that time, the substrates were carefully rinsed with DI water after which another 10 minutes of ultrasonication in acetone and isopropyl alcohol (IPA) followed. The cleaning was completed by a final IPA rinsing and nitrogen dry-blowing step.

Fabrication of Al NP arrays

All investigated gratings were fabricated by electron-beam lithography. The simpler Al ND arrays investigated for enhancement of monochromatic OLEDs (chapter 4.3-4.5) were fabricated in-house using a Raith eLine system. For this, a poly(methyl methacrylate) (PMMA) resist with an average molecular weight of 950k was purchased from Allresist GmbH Germany. It was dissolved in Anisole (3 wt% concentration). The resist was deposited on the cleaned ITO substrates via spin-coating (film thickness of 200 nm). Before the substrates were transferred to the e-beam system, they were baked-out for 5 minutes at 100 °C. Electron-beam exposure was performed via dot exposure with an acceleration voltage of 10 kV and a 30 µm aperture. Following exposure, the substrates were developed in an IPA bath and thoroughly rinsed with deionized water. After metallization with Al, the lift-off was performed by immersing the substrates in acetone overnight. As a final step, the substrates were subjected to mild ultrasonic treatment in acetone and IPA and dried by a stream of nitrogen. Broadband enhancing gratings investigated in chapter 4.6 were fabricated using an advanced Raith eLine Plus system located at the institute of physics at the University of Graz. Compared to the dot exposure used for the monochromatic gratings these gratings were fabricated using area exposure at an acceleration voltage of 20 kV and a 20 µm aperture.

Fabrication of the OLED structures

CuSCN[179] was dissolved at a concentration of 22 mg ml^{-1} in DES and stirred for 1 hour. For spin-coating, the solution was applied to the patterned and cleaned substrates with a syringe complimented by a suitable 0.2 µm polytetrafluoroethylene filter. The spin-coating parameters were set to yield a film thickness of approximately 50 nm. After spin-coating, the substrates were baked at 120°C for 5 minutes before transferring them to an argon-filled glovebox. The EML was prepared by adding the host molecules TCTA and TAPC in a 3:1 ratio in a 1:1 mixture of DCM:THF. The concentration of the solution was set to 10 g/L. For monochromatic OLEDs Bis(3,5-difluoro-2-(2-pyridyl)phenyl-(2-carboxypyridyl)iridium(III) (FIrpic) was added to the solution as a blue dopant in a 10 wt% ratio. WOLEDs, however, had 15 wt% FIrpic, 0.1 wt% of the green-emitting $Ir(ppy)_3$ and 0.6 wt% of the red-emittingTris(1-phenylisoquinoline)iridium(III) ($(Ir(piq)_3$) added to the solution. Spin-coating parameters were chosen to yield a 100 nm thick layer. After spin-coating, the substrates were baked at 110°C under high vacuum for 30 minutes before they were transferred to an evaporation chamber, where 45 nm of TmPyPb[206] was deposited at a base pressure of 10^{-6} mbar. For OLED investigations, an active area of 1.5x1.5 mm^2 was defined by evaporating the cathode through a shadow mask. Figure 4-1.a shows the architecture of the finished OLED while the energy level alignment required for an efficient operation of the OLED is depicted in Figure 4-1.b.

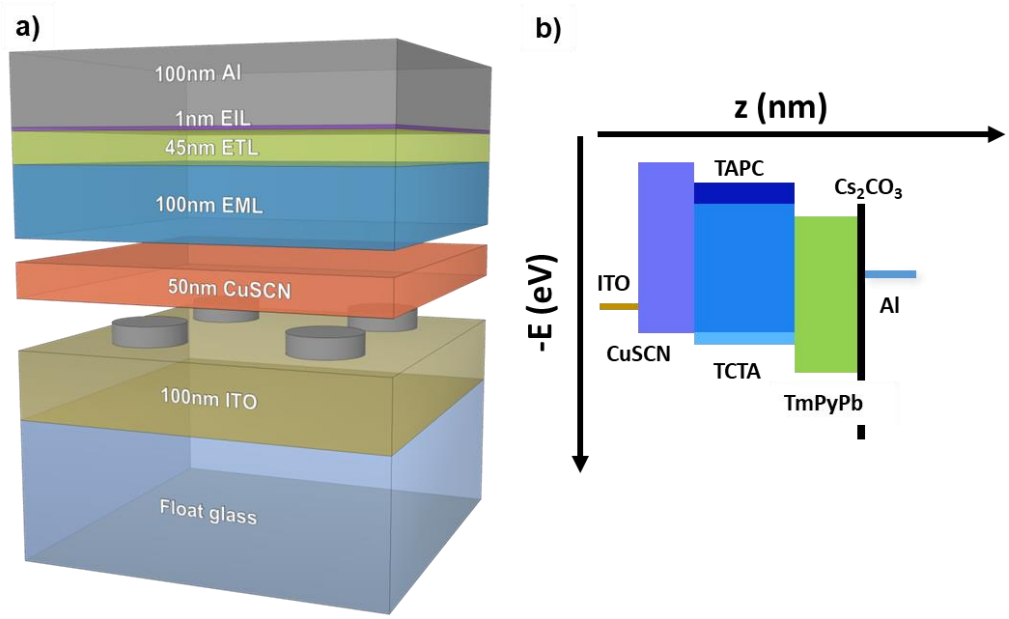

Figure 4-1. (a) Sketch view of the OLED stack used in this chapter and (b) the corresponding energy diagram drawn to scale for the individual layers

Angle-resolved large area extinction and photoluminescence investigations

Large area (2x2 mm^2) angle-resolved measurements were carried out using an Instrument Systems Gon360 goniometer setup connected to a CAS 140CT array spectrograph. The goniometer setup had an angular resolution of 0.01° with an accuracy of ±0.3° for the illumination as well as the detection angle. To record the full half-space above the device (e.g. 0-90°), the illumination arm, which injected the light from a stabilized halogen source, was set to 15°. Extinction is defined as $1-R/R_0$ where R is the reflectance of a patterned area normalized to the reflectance R_0 of a non-patterned area on the same substrate. Photoluminescence (PL) measurements were carried out using an UV light source with a wavelength of 365 nm which produced a divergent beam.

Small area extinction and fluorescence investigations

Extinction and fluorescence microscopy measurements of smaller test samples (< $1mm^2$) were performed with a 20x objective and an effective sampling full angle of 2.2°. Extinction is defined as $1-R/R_0$ where R is the reflectance of a patterned area normalized to the reflectance R_0 of a non-patterned area on the same substrate. Fluorescence studies were performed by exciting the emitter with a halogen lamp and a bandpass filter with a central wavelength of λ=360 nm and a bandwidth of 10 nm.

OLED investigations

Except for the different objective (effective sampling full angle of 3.5°), PL measurements were performed as described above. Current/luminance/voltage (I–L–V) characteristics were recorded in a customized setup. To determine the I–V characteristics, a Keithley 2612A source measurement unit was used. A calibrated photodiode connected to a Keithley 6485 picoampere meter was employed to record the luminescence. EL spectra were acquired using an ORIEL spectrometer with a calibrated charge-coupled device camera attached.

AFM characterization and thickness measurements

AFM topography images were recorded in tapping mode using a Veeco Dimension V. To obtain accurate thickness information for the simulations the truly put-down layer thickness of the individual layers had to be determined. This was done step by step starting with the ETL thickness which was determined from the edge formed by the substrate holder. In a next step, the substrate was subdued to a short rinse with acetone and IPA followed by a dry-blowing step. In a final step, the substrate was rinsed with DES and again dry blown. By stripping the cathode using an adhesive tape it was possible to accurately determine the thickness beneath the electrodes via the resulting edges. Doing so and averaging over several positions returned

the total thickness of the stack. Another rinse with acetone, IPA and consecutive dry-blowing allowed for the determination of the CuSCN layer thickness and thus the thickness of the EML was calculated by subtracting the ETL and CuSCN layer thickness values.

Ellipsometry

Ellipsometry measurements were carried out by spin-coating the EML and evaporating 50 nm of the ETL on cleaned Si wafers with no grown native oxide (modelling included a small silicon oxide layer with 2 nm thickness). The optical properties and the thickness of the films were measured by means of VASE (J. A. Woollam Co., Inc). Spectra were acquired for a spectral range of 300 to 1300 nm at angles of incidence of 65, 70 and 75° with respect to the substrate normal. Modelling of the acquired VASE data was performed using the WVASE software package (J.A. Woollam Co., Inc). Modelling was based on coupled Lorentzian oscillators and assumed the presence of inhomogeneous thin films exhibiting isotropic behavior.

Numerical simulations

Finite difference time domain (FDTD) simulations were carried out using FDTD Solutions from Lumerical. For the OLED geometry an ultra-fine mesh size of 1 nm was used. The simulation area was defined by periodic boundary conditions for the lateral dimensions and a perfectly matching layer (PML) in the outcoupling direction as well as a perfect electrical conductor (PEC) in a distance of 30 nm from the ETL/cathode interface. The symmetry of the square shaped array allowed for a reduction of the simulation volume. The respective thicknesses of the individual layers of the OLED stack (as input values for the simulations) were known with an error of ±2 nm, as after full PL/EL characterization the devices were disassembled in a layer-by-layer fashion for measuring layer thicknesses by AFM. The electric field intensity inside the EML was recorded using a volume monitor while transmission or reflectance spectra were recorded by a field monitor placed 300 nm from the layer structure. As a light source, a plane wave illumination was chosen.

Dipole simulations were also carried out and were performed on a simulation volume spanning 15x15 μm^2. To model the incoherent nature of dipole relaxation inside an OLED, the simulation was performed several times with different dipole polarizations and placement. Enhancements were calculated by duplicating this step for an OLED without a grating. To carry out the simulation, the mesh size had to be coarse along the x and y direction with a 20 nm spacing while the z-direction was finer with a 10 nm spacing.

4.3 Quasi-guided modes within an OLED micro cavity

From chapter 2.2.5 it is known that light can be confined inside a waveguide structure by total internal reflection. This occurs at the interface between two materials with a different index of refraction. A special case of this general effect is the dielectric slab waveguide, which, in its simplest form, consists of three layers with different refractive indices which extent infinitely in the directions parallel to the interfaces. For the light to be confined to the layer in the middle, the refractive index of this layer needs to be larger than the surrounding ones. Besides common applications like laser diodes and integrated optical circuits, waveguiding opens the door to rich physics when an interaction with a metal NP is considered. First observed as a suppression of extinction by Linden et. al.[286], these interactions were soon described as waveguide-plasmon polaritons[287], quasi-guided modes[283,288] or more generally CLRs. For the sake of understanding, CLR will be the term of choice for this work even though the other terms are also valid and commonly found in literature. Besides the aforementioned suppression of extinction, the formation of Fano resonances[289] and electromagnetically induced transparency (EIT)[290,291] was observed soon after. Recently, these CLRs were found to increase fluorescence through an increased local density of states (LDOS) and enhanced outcoupling at resonance while benefiting greatly from the aforementioned far-field transparency and the concomitant reduced absorption losses.[283,292] Further work concluded that the magnitude of the enhancement depends on the thickness of the waveguide structure[60,293], the overlap between the guided mode with the LSPR (e.g. the position and the shape of the NP)[60] as well as the position of the emitters within the waveguide.[288] Applying this concept to an OLED, it is immediately clear that the optical cavity of such a device would provide the required slab waveguide structure. At the same time a major loss mechanism, light trapping inside these guided modes[32], could be mitigated herby raising the overall efficiency of such a device. While a lot of research effort has been dedicated towards uncovering the physical foundations of these quasi-guided modes, studies regarding the interaction of the weak-cavity, found in an OLED, with CLRs are so far lacking. This situation is especially pressing, because ideal waveguide thickness values were found to be larger than 300 nm, a value too large for an efficient OLED device.[294] As a first step towards addressing this limitation, the impact of the top-cathode and hence the weak-cavity on the position of the CLRs is investigated by performing extinction spectroscopy at an angle of 0° for an Al ND array with a disc diameter of 90 nm and a lattice constant of 300 nm. By determining the optical constants via ellipsometry measurements the guided modes of the cavity as well as their spatial profile are calculated. Using FDTD simulation, the disturbance of the electric field intensity caused by an Al ND array with a lattice constant of 300 nm is modeled.

Impact of top-cathode on extinction

For this first study, the thickness of the EML was set to 100 nm. Before the top-cathode was evaporated, the extinction was acquired by measuring the transmission through the Al ND arrays (Figure 4-2, black line). In line with observations reported in literature, the Al ND array leads to the formation of two areas of reduced extinction within the LSPR of the Al NDs. At lower wavelengths, this area is mainly a small dip centered on 452 nm and a minimum normalized extinction of 0.46. The second area, however, is much larger spanning a spectral range from 466 all the way up to 555 nm. Here, the normalized extinction reduces from 0.9 at 466 nm down to 0 at 527 nm before sharply increasing again to 0.95 at 555 nm. Also in line with previous reports is the formation of two minor extinction peaks at 514 and 519 nm.[286,295] After the transmission measurement, the Al cathode was evaporated on top and the extinction was determined again but this time through reflection measurements (Figure 4-2, red line). The added cathode transformed the dip in extinction at 452 into a shoulder from which the extinction increases sharply to 1 at 463 nm. The area characterized by a very low extinction is now reshaped into two distinct transmission features. The first is centered at 486 and the second at 520 nm. Lastly, the formation of an additional dip in extinction centered at 573 nm leads to a splitting of the peak belonging to the LSPR tail into two. Important for the application in OLEDs is the fact that the added Al cathode introduces two additional windows of increased transparency which points towards the formation of additional CLRs.

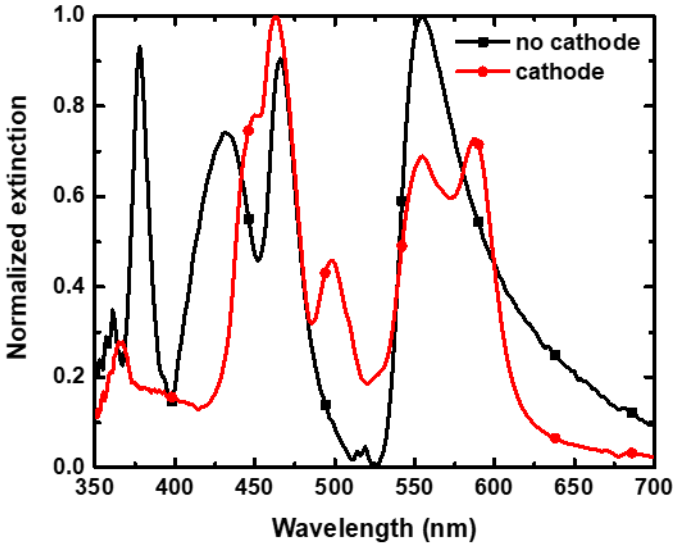

Figure 4-2. Normalized extinction of an OLED stack determined before and after evaporation of a reflective Al cathode obtained via transmission and reflectance spectroscopy respectively.

The obtained extinction spectrum for the OLED device hints at four CLRs, meaning there should be four distinct guided modes present in the device. To confirm this assumption, FDTD was used to simulate the optical response of the OLED layer geometry.

Calculation of optical modes

To obtain accurate results from the optical simulations, the refractive indices and extinction coefficients of the individual layers were determined by ellipsometry (data for ITO, however, was taken from Palik[296]). The obtained data is depicted in Figure 4-3.a and b, respectively. Expectedly, the refractive indices of the organic layers are quite similar and thus markedly lower than the refractive index of CuSCN. A totally different response with respect to n is exhibited by ITO which up to a wavelength of 600 nm is even larger than CuSCN. Thus, it can be expected that the ITO layer will be the guiding layer. The extinction coefficient on the other hand reveals no anomaly and confirms that the chosen materials are transparent above a wavelength of 400 nm.

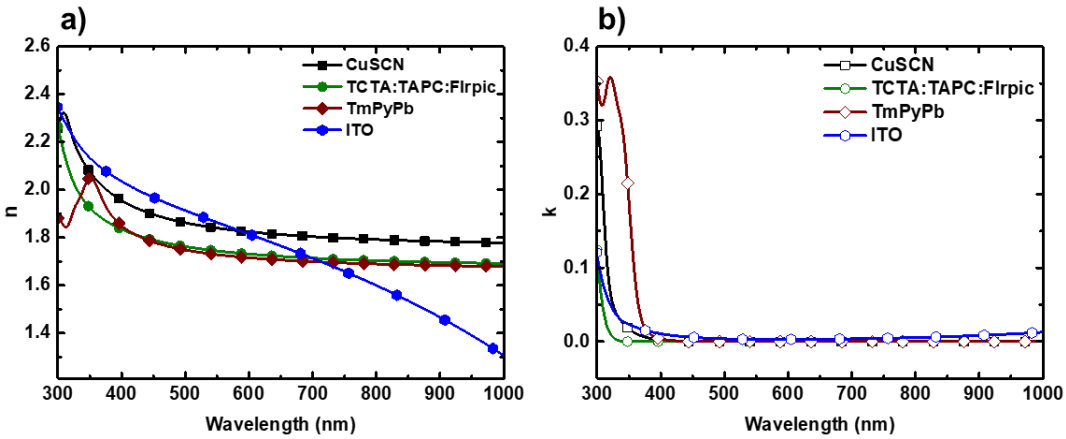

Figure 4-3. (a) Refractive indices n and (b) extinction coefficients k of the individual materials of the OLED stack, as listed in the figure legends.

Using the experimental (n, k) values, the integrated mode source of the FDTD Solutions Toolbox was used to inject light into the guided modes supported by the OLED layer geometry. Figure 4-4.a and Figure 4-4.b show the normalized energy density profile of the supported modes in s- and p-polarization for a wavelength of 450 nm as well as the real part of the refractive index of the individual layers. In s-polarization, 2 TE guided modes are supported. Likewise, the calculation yields 2 TM modes corresponding to a SPP as well as a coupled SPP/dielectric mode. Evidently, the spatial concentration of these guided modes within the OLED stack varies significantly for the individual modes. As mentioned earlier (and will be demonstrated later in chapter 4.4.4), a good spatial overlap with the Al ND array is required to obtain an efficient coupling and, hence, strong field enhancement as well as outcoupling improvements.

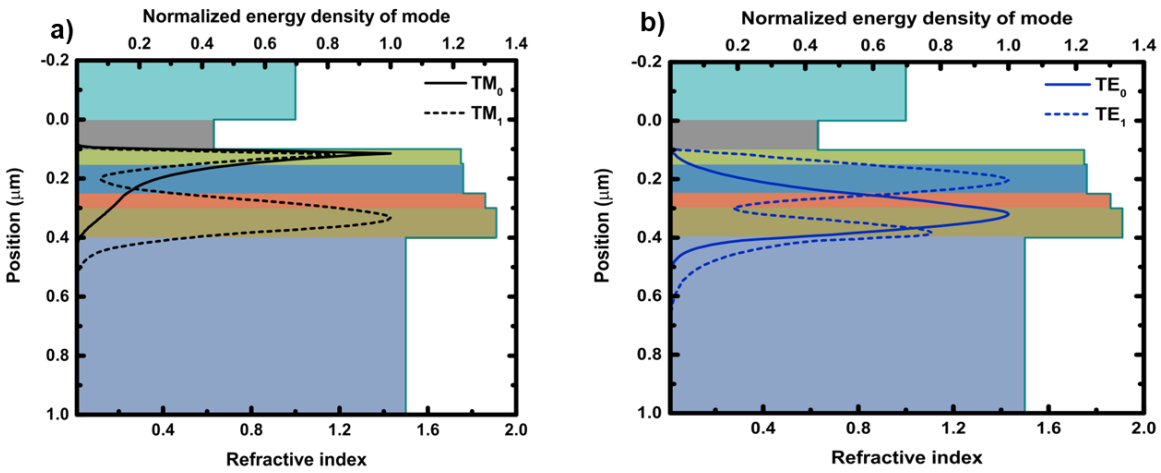

Figure 4-4. Calculation of optical modes within the cavity of the OLED stack used for the study. The normalized energy density of the (a) TM and (b) TE modes is displayed in dependence of the position. The refractive indices of the used layers are drawn in the background.

Field modification of the micro cavity system

Besides the creation of additional guided modes, the top-cathode, as mentioned before, also leads to the formation of a micro cavity system. Since only the top cathode is highly reflective, this cavity is usually called a weak micro cavity.[297] As is known, cavities lead to the formation of standing waves and the associated nodes (points of negligible electric field intensity). The location of these nodes within the resonator depends on the wavelength of the wave and increasing wavelengths cause the position of the nodes, to shift towards the anode interface (Figure 4-5.b).[298] Due to the severely reduced field intensity at these nodes any emitter located at this position exhibits a reduced emission intensity due to a drastically reduced density of optical modes into which the excited state can decay. Therefore, during the optimization phase of an OLED stack, the thickness of the layers and the placement of the emitters is usually chosen in such a way that the position of the emitters doesn't coincide with a node. This optimization strategy is not as stringent when the Al ND array is incorporated. As can be seen from Figure 4-5.a, the array significantly disturbs the cavity and considerably strengthens the electric field intensity at the position of the nodes over a wide spectral range. To confirm this effect, large area OLED simulations with dipole sources located at different distances from the HTL were performed. Indeed, the modifications lead to markedly increased emission intensities (Figure 4-5.d). Besides dealing with the reduced field intensity at the nodes, the formation of the CLRs also leads to a field intensity enhancement at 440, 490 and 550 nm, which are the positions of the CLRs for an observation angle of 0° (Figure 4-5.c).

From these first results, it is clear that the additional top cathode doesn't impair the formation of CLRs and instead increases the amount of CLRs by means of additional modes to which the Al ND array can couple. With the existence of CLRs within the OLED stack having been

demonstrated, a more rigorous analysis of the parameters that could influence the coupling will be carried out in the next chapters.

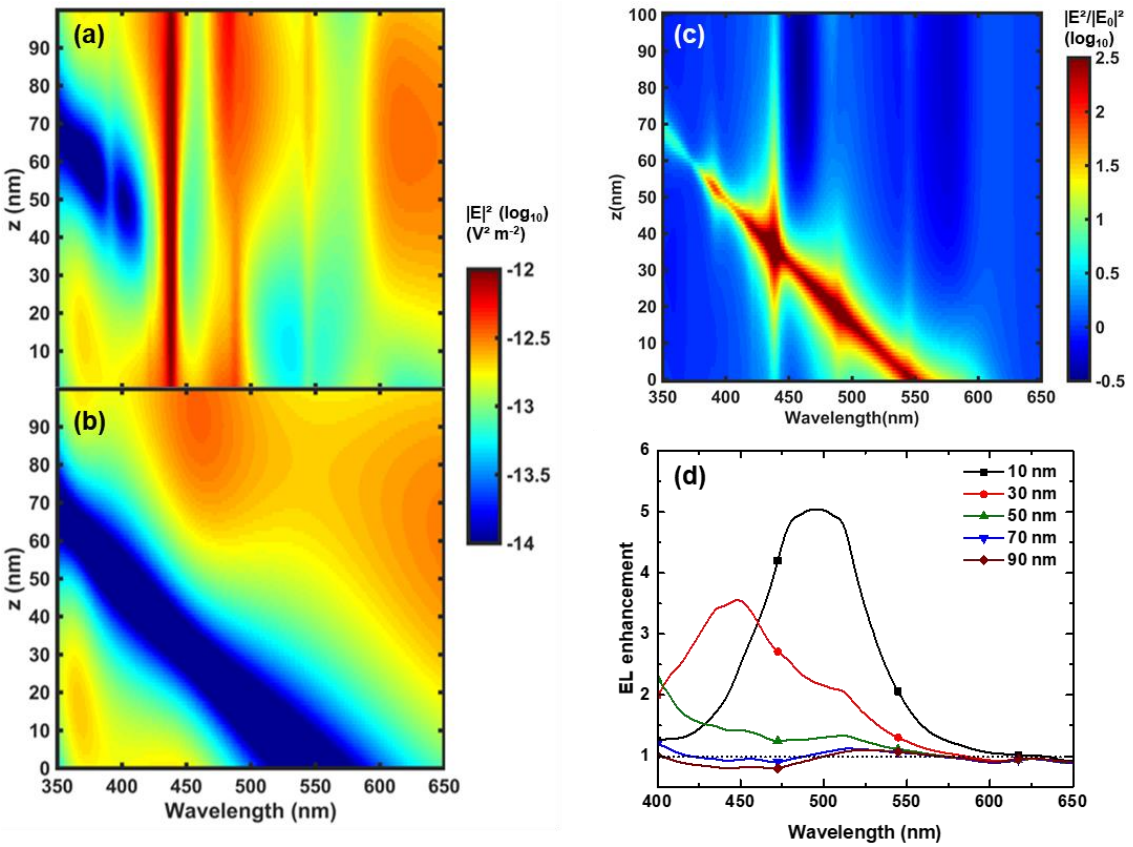

Figure 4-5. Electric field intensity spatially resolved for the vertical axis of the EML integrated in an OLED cavity (a) with and (b) without an embedded 300 nm Al ND grating. (c) Spatially along the z-axis resolved field enhancement $|E|^2/|E0|^2$ induced by the grating. (d) Possible EL enhancement simulated for dipoles located at the specified distance away from the HTL interface.

4.4 Parameters affecting the field and outcoupling enhancement

4.4.1 Introduction

With the basic principle of operation established in chapter 4.3, it is now important to identify the key parameters that govern the field as well as outcoupling enhancement for the given OLED system. Considering the number of parameters provided by the system as well as the Al ND array it is clear that factors such as the lattice constant of the array, the disc size and height, placement within the OLED as well as thicknesses of the individual layers play an important role. Since the target is to improve the performance of an OLED under operation, only those factors and parameters that don't impact the operation of the device should be considered. For example, a placement of the array within the EML would lead to metal-induced quenching and as a consequence severely affect the device performance. Also, being thin-film devices, the total OLED layer thickness should not exceed 200 nm or otherwise efficient operation of the device

will be endangered.[294] This in turn forces the height of the Al NDs to be as low as possible while still being above the skin-depth of Al.[51] These considerations culminate in a height of 30 nm. So, with these constraints put into place, this section will deal with the remaining ones, which are the lattice constant, the disc size and the thickness of the EML. Before moving on to chapter 4.4.2 it has to be noted that for the sake of simplicity thickness dependence of the remaining layers was purposefully neglected.

4.4.2 Lattice constant

Introduction

Among the parameters under investigation, the lattice constant easily has the most noticeable effect. From the condition for Bragg scattering (Eq.(2.23) it can be expected (and in fact has been reported previously) that the wavelength of light outcoupled in the direction perpendicular to the surface will experience a red shift with increasing lattice spacings. However, the impact on the magnitude of the coupling has, to the best of the authors knowledge, not been explored.

Therefore, the lattice constant was varied from 220 to 360 nm and the change of the CLRs in dependence on the lattice constant by extinction- and PL measurements perpendicular to the substrate surface was recorded. Through embedding within an OLED it was confirmed that the findings of the PL investigations also translate over to EL. Lastly, FDTD simulations substantiated that CLR induced field enhancement as well as cavity modulations play a major role. The later ones allowed for a modification of the emission color by dampening the contribution in the red part of the spectrum.

Fluorescence investigation

The individual arrays were fabricated over areas of 200 x 200 μm^2 and the characterization of the Al ND arrays was performed through the glass side. A microscope image depicting the 16 Al ND arrays is shown in Figure 4-6.a. Clearly, the anticipated color shift from blue to a more reddish appearance induced by increasing lattice constants was present. The corresponding fluorescence image (Figure 4-6.b) reveals a modulation in brightness as well as a shift in the emission color as a function of the lattice constant.

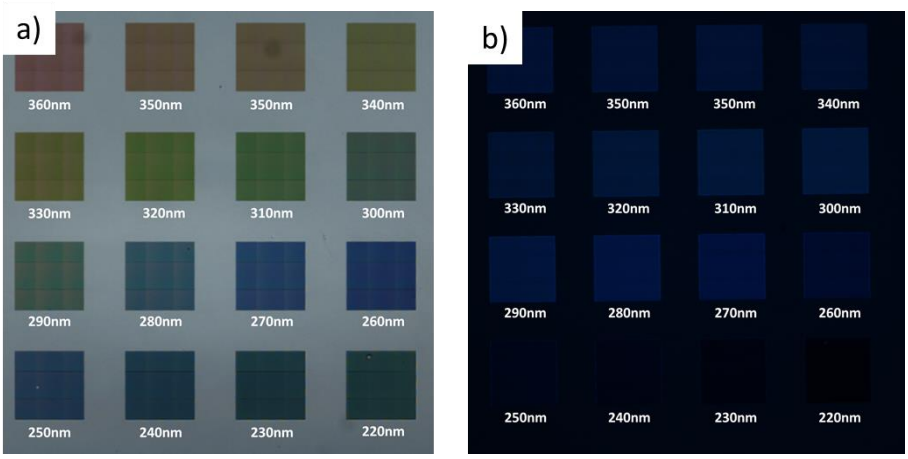

Figure 4-6: (a) Reflection and (b) fluorescence images of 16 200 x 200 μm^2 Al ND arrays with increasing lattice constants (as noted in the figure), embedded in an OLED stack including the cathode. Images were acquired through the glass substrate.

The origin of these color shifts becomes more obvious by summarizing the extinction spectra of the different arrays versus their lattice constants in the color plot in Figure 4-7.a. From this figure, two types of extinction features become evident. The broad extinction feature located at a wavelength around 650 nm for a lattice constant of 220 nm first experiences a blue shift with increasing lattice constants and then stabilizes around 580 nm for a lattice constant of 300 nm. For larger values of the lattice constants this feature starts to diminish until it is largely suppressed for a lattice constant of 360 nm. Besides this broad extinction feature, a rather sharp feature, which is beyond an amenable S/N ratio for smaller lattice constants, emerges at a wavelength of 460 nm for a lattice constant of 260 nm. With increasing lattice constants, this feature shifts almost linearly towards longer wavelengths while losing in intensity until it reaches a wavelength of 590 nm for a lattice constant of 360 nm. For a lattice constant of 280 nm, a similar band starts to form at 450 nm which linearly shifts to a wavelength of 520 nm for a lattice constant of 360 nm. Finally, a third band with low intensity becomes apparent for a lattice constant of 340 nm. The broad features are ascribed to the localized surface plasmon resonance (LSPR) of the individual Al NDs, while the narrower features at lower wavelengths are due to CLRs.

In Figure 4-7.b the fluorescence enhancement spectra of the Al ND arrays versus the lattice constant is shown. From this figure, similarly as for the extinction spectra, the formation of two distinct fluorescence enhancement bands that correlate with the CLR extinction bands becomes evident. However, while the extinction bands are, at least partially, of a narrower nature, both fluorescence enhancement bands are of comparably broad nature, hence, providing a general increase in fluorescence intensity. Nonetheless, the enhancement is still quite selective as it can be appraised from Figure 4-7.b. Noteworthy, the magnitude of

enhancement also depends on the lattice constant with the largest enhancement of fluorescence intensity recorded for a value of 300 nm and wavelengths in between 500 and 520 nm. In contrast, no or just a minor enhancement can be found at the location of the LSPR. Interestingly, smaller lattice constants show an effective decrease in fluorescence which changes to an enhancement for lattice constants larger than 280 nm.

The modification of the emission spectra by selective enhancement or attenuation of individual wavelength ranges results in modifications of the emission colors as depicted in Figure 4-7.c. Compared to the reference CIE1931 (*x,y*) chromaticity coordinates of (0.17, 0.34) for a device without Al ND arrays, the emission of FIrpic experiences a rather large blue-shift of the chromaticity coordinates to (0.15, 0.23) for a Al ND array with a lattice constant of 220 nm. For a lattice constant of 230 nm the chromaticity coordinates shift slightly to (0.14, 0.23) before they gradually change in accordance with the extinction and fluorescence enhancement spectra towards a more greenish appearance with chromaticity coordinates of (0.14, 0.27) at 250 nm and (0.15, 0.34) at 300 nm. A further increase of the lattice constants only weakly impacts the shift of the emission color towards greenish with the device having the largest lattice constant value investigated, 360 nm, featuring chromaticity coordinates of (0,15, 0.35).

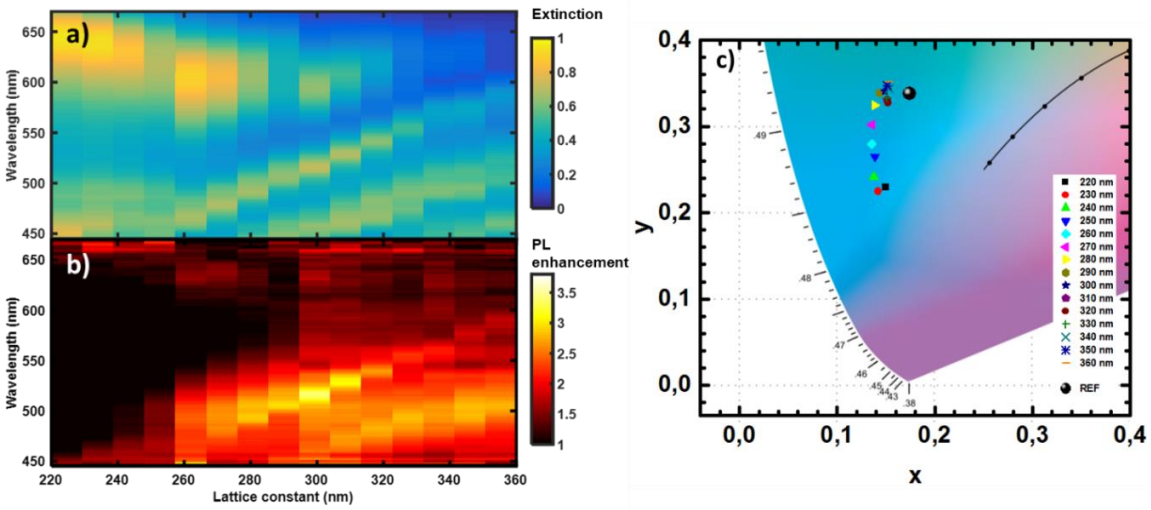

Figure 4-7: (a) Extinction spectra of Al ND arrays embedded in an OLED stack with cathode and (b) fluorescence enhancement compared to a non-patterned area. The corresponding CIE1931 (*x,y*) chromaticity coordinates are depicted in (c).

OLED performance

To study how the results of the PL measurements on the OLED stack correlate with EL, an OLED with an integrated Al ND array with a lattice constant of 250 nm was exemplarily investigated. This value was chosen since it still provides a pronounced blue-shift of the emission. As a reference, an OLED without an Al ND array was used. At this lattice constant, the Al ND array

induces a large blue-shift of the emission color together with an enhancement in the range of the peak emission as also observed in PL. The results of the characterization of this device are depicted in Figure 4-8. The current-density characteristics (Figure 4-8.a) highlight that there is no notable leakage current, i.e. no additional short-circuit pathways were introduced by the Al ND array. The EL spectrum (Figure 4-8.d) of the OLED with the Al ND array exhibits a strongly reduced contribution from the greenish portion of the typical emission spectrum of FIrpic. Analogous to the PL studies, this causes a blue-shift of the CIE1931 (*x,y*) chromaticity coordinates from (0.17, 0.35) to (0.18, 0.26). Because of the reduced sensitivity of the human eye in this spectral range, the device with the embedded Al NDs exhibits reduced luminance values of 4120 cd m^{-2} versus 6554 cd m^{-2} (see Figure 4-8.b) and reduced luminous efficiency values of 5.6 cd A^{-1} versus 9.4 cd A^{-1} at 1000 cd m^{-2} (see Figure 4-8.c) for the reference device. A calculation of the spectral overlap with the luminosity function of the human eye yields a reduction of the luminescence by 42 % which is in line with the observed decreases in brightness as well as efficiency. Clearly, this approach highlights a strategy to obtain a pure bluish emission from FIrpic, which is of high relevance for OLED applications for which an increased (blue) color purity is required.

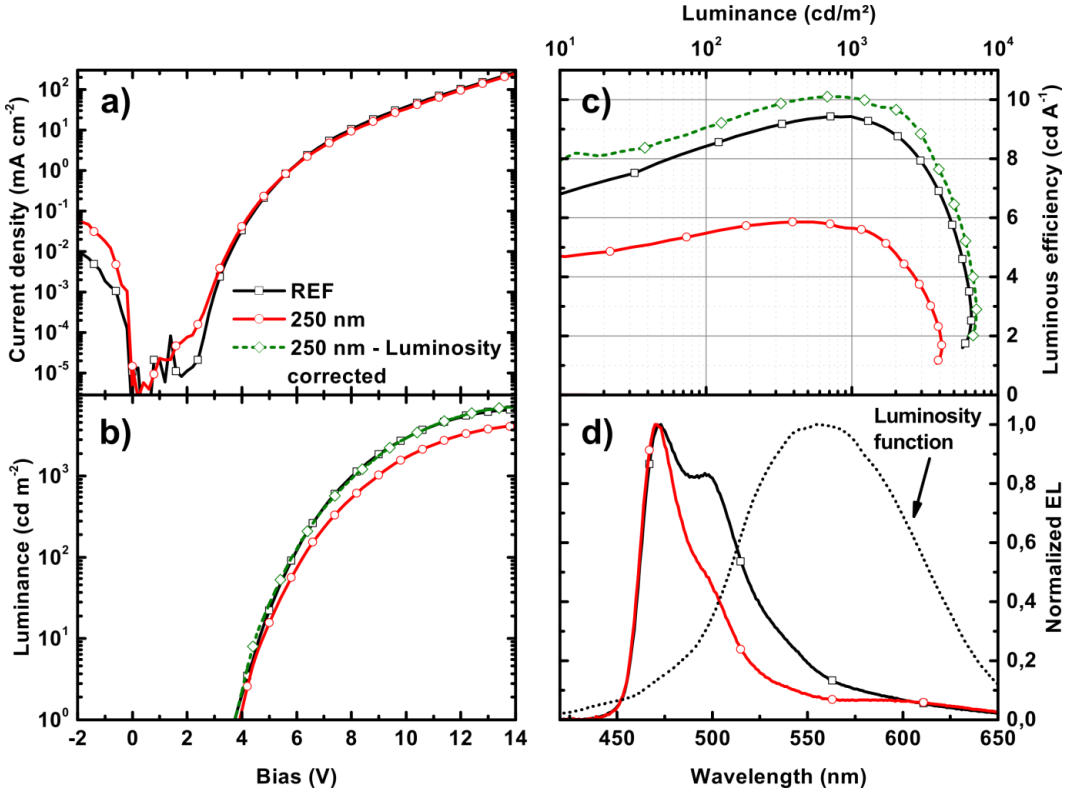

Figure 4-8: Performance characteristics of an OLED with an embedded Al ND array with a lattice constant of 250 nm and an OLED without an embedded array (reference REF). (a) Current density and (b) luminance versus bias voltage characteristics, (c) luminous efficiency versus luminance characteristics, (d) EL spectra.

FDTD simulation

To clarify the origin of the ND array induced modifications of the FIrpic emission spectrum, detailed FDTD simulations of the OLED with the embedded Al ND array were performed.

In detail, the emission perpendicular to the device surface and the electric field in the volume occupied by the emitters (i.e. the EML) was recorded with and without the presence of the Al ND array. Considering the fact, that the emission probability of a dipole in the direction of the illumination is proportional to the intensity enhancement (IE) of the electric field along the orientation of the dipole moment at the position of the emitter, the resulting total IE in that direction can be defined as

$$IE(\lambda, \Omega) = \frac{\int_V |E(x, y, z, \lambda, \Omega)|^2 dV}{\int_V |E_{ref}(x, y, z, \lambda, \Omega)|^2 dV} \quad (4.1)$$

where Ω is the solid angle (here the forward direction), $E(x,y,z,\lambda,\Omega)$ and $E_{ref}(x,y,z,\lambda,\Omega)$ are the electric fields with and without an Al ND array at the wavelength λ at the position of the emitter and V is defined as the volume encompassing the EML. The results of this calculation as well as the PL and EL enhancements are presented in Figure 4-9.a as dotted, black, and red lines, respectively. Apart from a spectral blue shift of approximately 20 nm, a good qualitative agreement between experiment and simulation is obtained in EL as well as PL. This very good agreement confirms that the observed color change is the consequence of a modulation of the electric field within the emissive layer of the OLED. The spectral region where a decrease in fluorescence is observed coincides with a reduced electric field intensity and, therefore, reduced emission intensity. This effect has also been observed in experiments where the microcavity formed between ITO and the cathode contact was modified by strips of silver.[299–301] On the other hand, the enhancement peaks at 437, 471 and 606 nm correspond to CLRs and a LSPR. This can be clearly concluded from the electric field maps depicted in Figure 4-9.b-c, respectively. Evidently, the enhancement at 606 nm originates from a LSPR of the individual particles since the electric field is highly localized around the ND (Figure 4-9.c), while the features at 437 and 471 nm are delocalized in nature and are thus corresponding to CLRs (Figure 4-9.b and c).

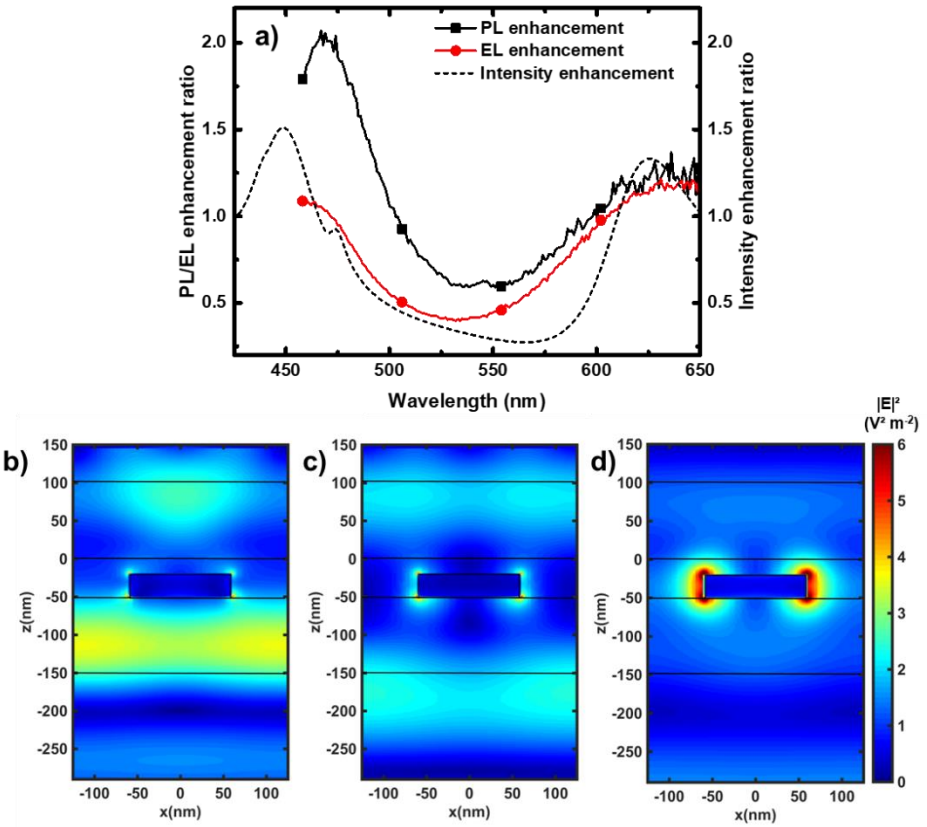

Figure 4-9. (a) PL and EL enhancements in comparison with simulated intensity enhancements. $|E|^2$ maps for (b) 437, (c) 471 and (d) 606 nm (lines indicate the borders of the individual layers).

Conclusion

In this subchapter, the impact of Al ND arrays on the emission color of an OLED was investigated. For this reason, extinction spectroscopy on OLED stacks including Al ND arrays with lattice constants of 220 to 360 nm in the wavelength range from 450 to 670 nm was performed. In dependency of the lattice constant, one or more distinct extinction features were detected in this spectral range. For features corresponding to CLRs, an enhancement in fluorescence intensity was found to result in a selective change of PL and, hence, an effective change of the emission color. In addition, lower lattice constants induce a filtering effect in the green part of the spectrum which contributes to the observed blue-shift of the emission color. The combination of these effects results in a pronounced modification of the emission spectrum towards the bluish CIE1931 (*x,y*) chromaticity coordinates of (0.142, 0.223) at a lattice constant of 230 nm. The effect was demonstrated to be also present in EL. For this, an OLED with an Al ND array having a lattice constant of 250 nm was investigated under operation. The blue-shift observed in PL was also found for EL, which proves the effectiveness of Al ND arrays for adjusting the emission color of OLEDs. Via FDTD simulations the origin of

the high degree of color tunability was ascribed to a combination of a modulation of the micro cavity effect of the OLED stack, combined with a selective enhancement provided by CLRs. Obviously, Al ND induced CLRs also provide designers with a way to accurately tune the emission colors of OLEDs simply by selecting an appropriate lattice constant. The study shows that this can be done without strong reductions of device efficiency. With respect to adjusting the emission color, the lattice constant is only one parameter that can be varied. Therefore, more studies regarding the interplay between lattice constants, ND dimensions and stack layer thicknesses need to be performed to further enhance the range of accessible colors and lower the loss of device efficiency.

4.4.3 Disc size

Introduction

In the last subchapter, the influence of the lattice constant on the spectral position of the CLRs was explored. Evidently, the lattice constant is the key parameter in the sense that it defines the spectral position of the CLRs. This allows fine tuning of the emission color (chapter 4.4.2) as well as an enhancement of device efficiency. Nonetheless, the lattice constant is not the only parameter that might affect the performance of the Al ND array. Enhancement of device performance can only occur by minimizing losses while still providing a significant interaction with the light field. The major loss mechanism with respect to the Al ND arrays is the LSPR of the individual Al NDs.[302] As was already discussed in chapter 2.2.2 (and shown later within this subchapter) the resonance can be adjusted by the disc size itself. For single particle systems, the general observation, that larger particles exhibit higher scattering cross sections while smaller disc sizes have higher absorption cross sections, can be made.[303,304] For coupled systems, however, this relationship between size and optical properties might not be realized. While quite a substantial amount of reports regarding the disc size in arrays embedded in different systems can be found,[230,262,305–310] the microcavity formed by the OLED stack has so far remained unexplored in that regard. Therefore, the lattice constant was fixed at 300 nm while the disc sizes were varied from 50, 70, 90 and 150 nm. Through extinction measurements as well as simulation of the progression of the scattering cross section it is shown that a disc size that balances the LSPR induced losses at larger disc sizes and the reduced cross section at very small disc sizes exists. This is confirmed in PL as well as EL measurements.

Cross sectional- and extinction analysis

An important parameter regarding the disc size is the spectral position and magnitude of the scattering cross section. Therefore, as a first step, simulations of the scattering cross section of the Al ND particles embedded inside the OLED stack but without the top cathode (Figure

4-10.a.) were performed. Aside from the tip at 440 nm, which is likely caused by the interference of the Al NDs with the layers of the OLED, an expected red shift of the peak with increasing disc diameters is evident. Furthermore, the magnitude of the scattering increases with the diameter until it reaches a maximum at 90 nm. A further increase results in a decrease in the magnitude, which is also in line with reports in literature.[302] This transformation of the scattering cross section of course has to reflect in the measurement (Figure 4-10.b). Aside from the overestimation of the simulation in the case of the 50 nm diameter, an increase in extinction as well as a slight red shift of the CLR induced transparency windows can be witnessed. Now, performing the extinction measurement on the full OLED stack including the top-cathode, mirrors the aforementioned situation (Figure 4-10.c, bottom) except for the curious disappearance of the LSPR in the red part of the spectrum which can't be explained at the time of writing. While the simulated extinction spectra depicted in Figure 4-10.c, top, exhibit only a modest agreement with the measurement, they nonetheless depict the same slight red shift as well as an increase in extinction in accordance with the cross section of the discs.

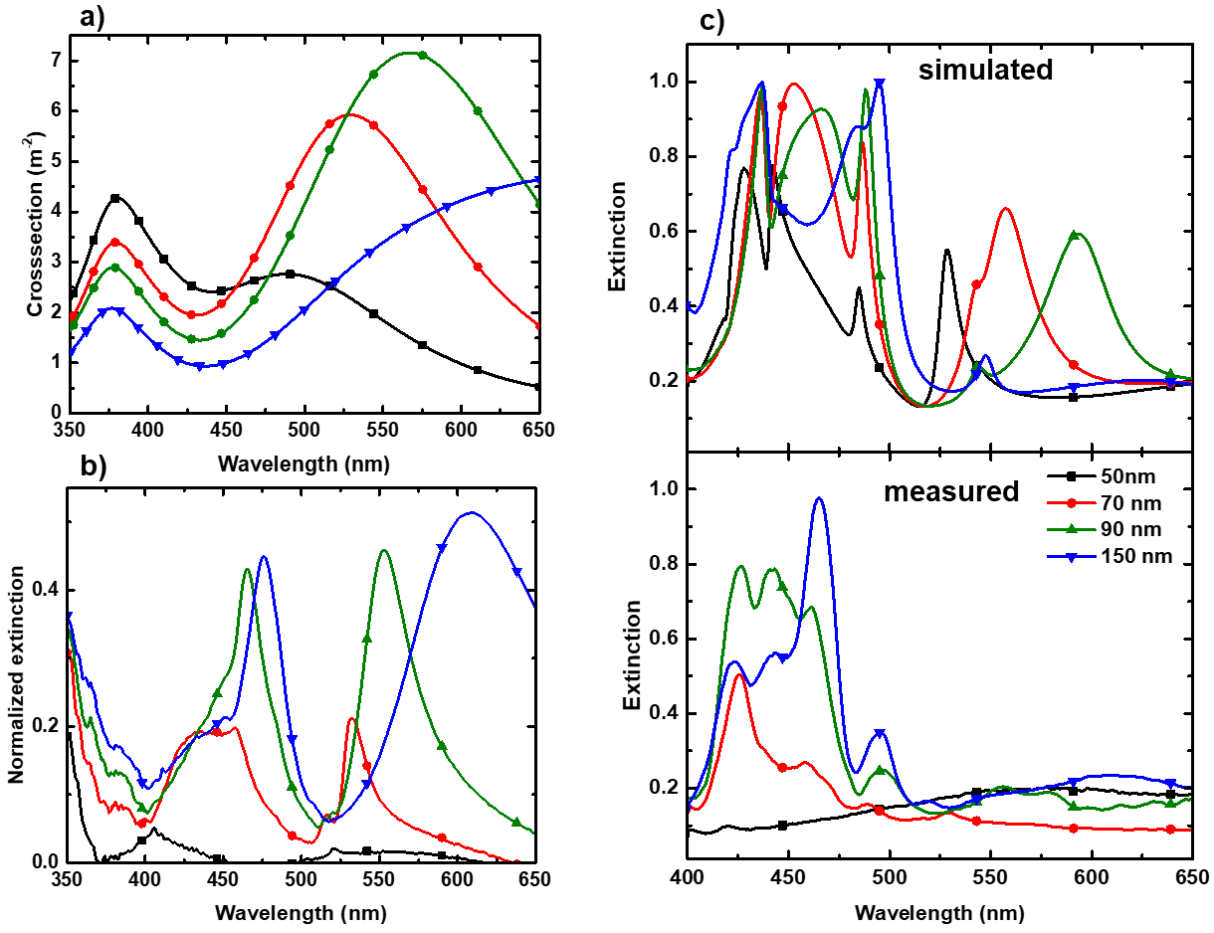

Figure 4-10. (a) Calculated scattering cross section for Al NDs of different diameters embedded within the OLED stack. (b) Measured extinction of an Al ND array embedded in CuSCN. (c) Simulated and measured extinction spectra of Al ND arrays embedded within the OLED stack with a top cathode

To identify any size dependence of the coupling between the grating and the guided modes, angle-resolved extinction measurements were performed (see Figure 4-11). Starting with the extinction map of the device with the disc size of 50 nm (Figure 4-11.a.), no signatures of the Al ND array are detectable. This weak form of interaction is not surprising since the LSPR of the aluminum ND of this size is in the UV range while the magnitude of the scattering cross section is comparably small. Increasing the diameter to 70 nm is already enough to shift the resonance towards the visible part of the blue and to facilitate a strong enough interaction of the grating with the waveguide (Figure 4-11.b.). This way the (+1,0) orders of the grating interact with the TE_0, TM_1 and TE_1 modes supported by the OLED structure. On top of that, (-1,0) order interaction with the TE_0 mode is also evident. At an angle of approximately 10° the onset of the TM_0, TE_0, TM_1 modes coupling with the (±1, ±1) order is noticeable. At 90 nm disc size, the LSPR shifts even further towards the green part of the spectrum (Figure 4-11.c.). This allows for the detection of the LSPR which can now be found centered around 570 nm. Of note is the high degree of fragmentation of the individual extinction bands caused by the stronger interaction of the (+1,0), (-1,0), (0, ±1) and (±1, ±1) grating orders with each other. This strong interaction is again suppressed at a distinctly increased disc diameter of 150 nm. At this diameter the LSPR further shifts into the red part of the visible spectrum. Now, the (-1,0) order coupling to the TM_0 or TE_0 mode is visible as an increased extinction signal (Figure 4-11.d.).

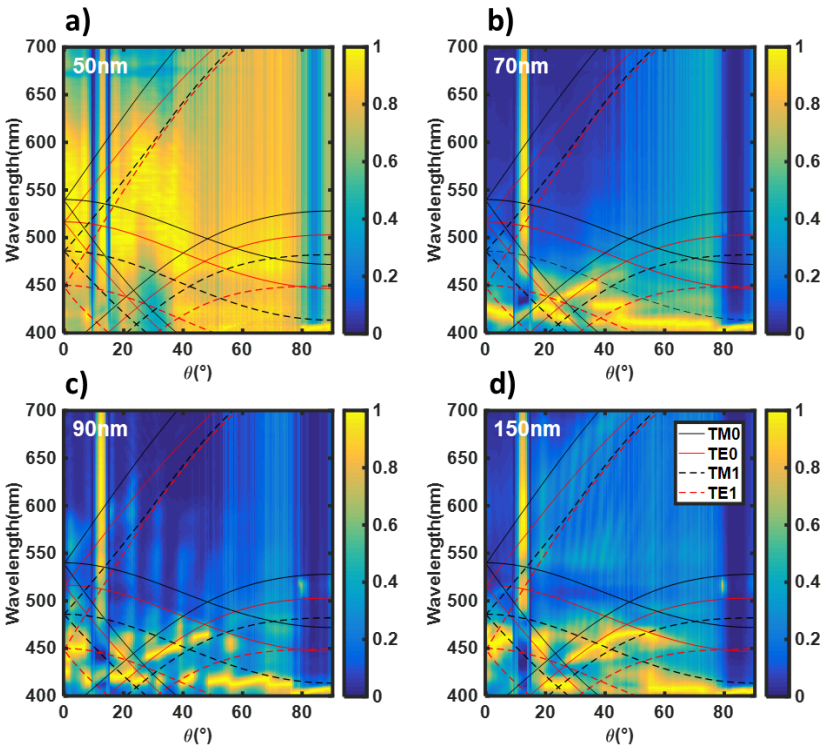

Figure 4-11. Variable-angle extinction spectroscopy of Al ND arrays embedded within an OLED stack with disc diameters of (a) 50 nm, (b) 70 nm, (c) 90 nm and (d) 150 nm.

As anticipated, the disc diameter is important. From the results gathered in this subchapter the lattice with disc diameters of only 50 nm should, if at all, only weakly enhance the PL and EL. Efficient coupling between the grating and waveguide modes was detected for disc diameters of 70 nm and above.

Photoluminescence investigations

Next, the impact of the disc diameter on the PL was studied. From the angle resolved extinction measurements it can be expected that a significant enhancement will be observable at disc diameters above 70 nm. The angle-resolved PL enhancement plots are depicted in Figure 4-12. Starting with the 50 nm disc diameter (Figure 4-12.a.), surprisingly, an enhancement is detectable for the TE_0 mode coupling with the (+1,0), (0,±1) and (+1,±1) grating mode. As can be expected, this enhancement is only very weak. In line with the results from the extinction measurements, stronger PL enhancements (up to a factor of 1.3) were realized for a disc size of 70 nm (Figure 4-12.b.). Unlike the 50 nm disc diameter grating, the enhancement not only originates from the TE_0 waveguide coupled to the (+1,0), (-1,0) and (+1,±1) grating mode but also from the TM_0 coupled through the (0,±1) mode. At 0° an enhancement at the position calculated for the TE_1 is also visible, however, a clear association with a grating mode is not possible. Curiously, increasing the disc size even further to 90 nm (Figure 4-12.c.) again shifts the observed enhancement and, hence, the coupling between the waveguides and the grating again. While an enhancement originating from the TE_0 mode coupled to the (0,1) is still visible, the TM_0 signature has vanished. Instead a weak contribution originating from the TM_1 coupled to (-1,0), (+1,0) and (0, ±1) is present. Also of note is the enhancement following the (-1,0) mode coupled to the TE_1 waveguide as is the weak enhancement at the intersections of the (0, ±1) modes coupled to TE_0 and TM_0 with the (+1,±1) mode coupled to the TM_0 and TE_0 mode, respectively. Lastly, a different picture is provided by the 150 nm disc size array (Figure 4-12.d.). While the peak enhancement is lower compared to the 70 and 90 nm disc size lattices, the visible enhancement bands are again shifted. Now, the enhancement follows the TE_0(0,±1), TM_1(-1,0), TM_1(+1,0), TM_1(0,±1), TE_1(+1,0) couplings. Similar to the 90 nm disc size array an enhancement at the intersection of TE_0(0,±1) and TM_1(+1,±1) is also present.

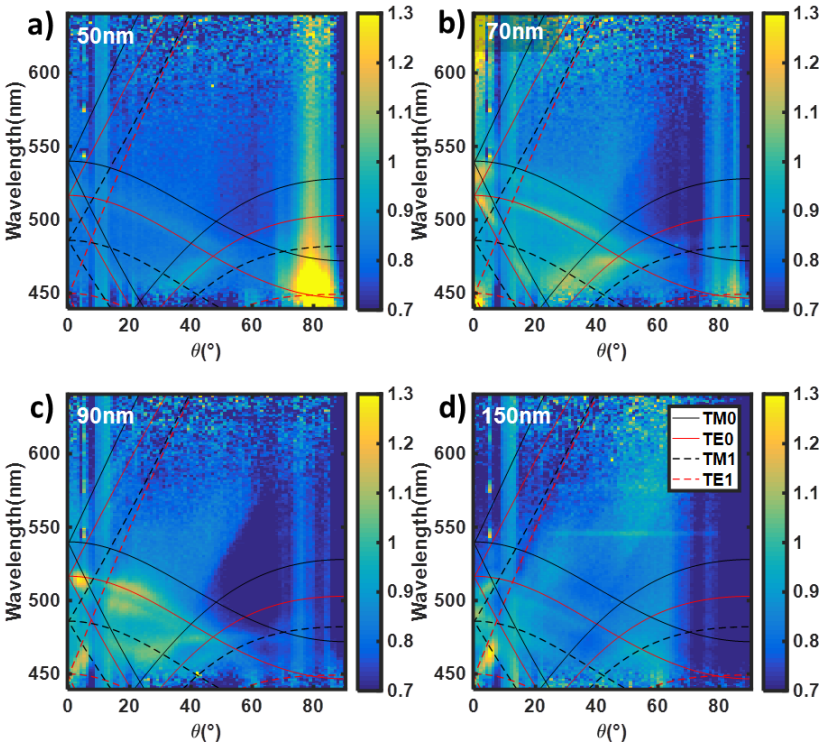

Figure 4-12. Variable-angle fluorescence spectroscopy of Al ND arrays embedded within an OLED stack with disc diameters of (a) 50 nm, (b) 70 nm, (c) 90 nm and (d) 150 nm.

Mirroring the extinction measurements, the disc size plays an important role in the PL enhancement. Even though the observed enhancement either occurred along the calculated dispersion or at the intersection of two otherwise dark modes, the disc size had a major influence in determining if a mode is bright or dark. Therefore, to conclude this paragraph, besides a proper lattice constant, the size of the discs has to be carefully selected to attain optimal PL enhancement.

Angle-resolved electroluminescence

From the angle-resolved PL measurements it is known that the disc size plays a major role in deciding whether a mode is bright or dark. Keeping in mind that the spatial profile of the four present optical modes in an OLED is different, it is clear that a wrong choice in disc size might result in a mode with the best spatial overlap to go dark and in turn a decrease in enhancement. While this situation is a problem for an enhancement of PL, it becomes an even greater issue in the case of electrical excitation because the recombination zone is rather narrow (~5 nm width). Therefore, it is further required to study the angular dispersion of the enhancement for an OLED in EL. To this end the devices incorporating the different gratings were driven under a constant current density of 10 mA cm^{-2} and the results are depicted in Figure 4-13.

At a diameter of 50 nm (Figure 4-13.a), minor enhancement is found for the $TE_0(0,\pm1)$, $TE_0(-1,0)$ and $TM_1(0,\pm1)$ interactions. Additionally, a contribution of the $TE_0(+1,\pm1)$ might also be present, but the reduced angular resolution renders a definite assignment impossible. Increasing the disc size to 70 nm (Figure 4-13.b) allows the coupling of $TM_0(0,\pm1)$, $TE_0(0,\pm1)$ and $TM_1(0,\pm1)$ to be bright. At the same time areas of decreased EL intensity become visible. As shown in chapter 4.3, this behavior originates from a modulated field profile within the emissive layer which exhibits a high spatial dependence on the location of the recombination zone. Moving to a disc size of 90 nm (Figure 4-13.c) shifts the bright couplings again to $TE_0(0,\pm1)$, $TM_1(-1,0)$, $TM_1(+1,0)$ and $TM_1(0,\pm1)$. Notably absent so far were the enhancements at the intersections of different CLRs. Starting with 90 nm disc size however, these enhancements at the intersections of $TM_0(-1,0)$ with $TE_0(0,\pm1)$, $TE_0(-1,0)$ with $TM_1(0, \pm1)$, $TE_0(0, \pm1)$ with $TM_0(0, \pm1)$ and $TM_1(0, \pm1)$ with $TE_0(0,\pm1)$ are present. As with the 70 nm grating spots of reduced intensity are again prevalent. However, the magnitude and shape of these intensity decreases has increased, which is again in line with a field modulation caused by the ND array. Lastly, at 150 nm (Figure 4-13.d) an enhancement following the dispersion of $TM_1(0, \pm1)$, $TE_0(-1,0)$ as well as $TM_1(+1,0)$ is detectable. Unlike the 90 nm diameter grating, only one enhancement spot at the intersection of $TM_1(0,\pm1)$ and $TE_0(+1,\pm1)$ exists.

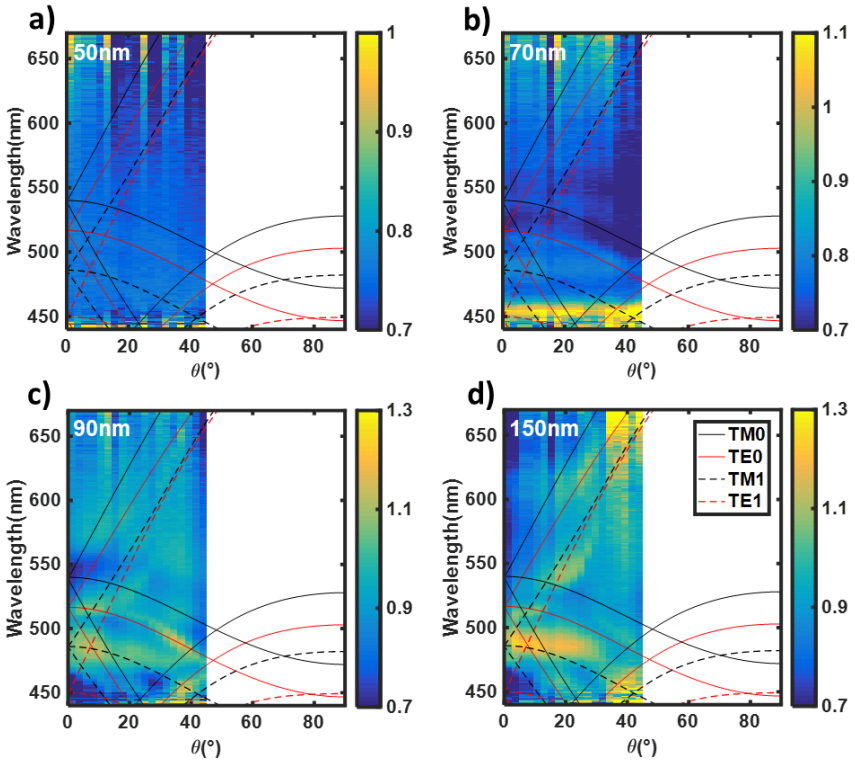

Figure 4-13. Variable-angle EL spectroscopy of Al ND arrays embedded within an OLED stack with disc diameters of (a) 50 nm, (b) 70 nm, (c) 90 nm and (d) 150 nm.

Angle-resolved EL measurements closely resemble the results from PL. Unlike PL, where the whole emissive layer contributes to the generation of light, however, only a small fraction of the available volume is available in the case of electrical excitation. This fact is clearly mirrored by the areas of significantly reduced EL intensity. It is clear that at larger disc diameters these areas become even more pronounced causing to an overall loss of EL intensity and thus brightness.

Lifetime

So far, an enhancement in EL at the defined position of CLRs was observed. According to the working hypothesis, these enhancements are the product of enhanced light generation as well as an increased out coupling of trapped light. While a precise determination of the contribution of each of these two factors was beyond the scope of this work, lifetime measurements were performed to gain further understanding about the contribution of the enhanced light generation due to an increased radiative LDOS. An indicator for an enhanced LDOS is a decreased phosphorescence lifetime. For this reason, a transient electroluminescent characterization of the OLEDs at a bias voltage of 6.5 V was performed by applying a square shaped pulse. For the interpretation of the recorded EL intensity decay the bi-exponential function

$$y = y_0 + A_1 e^{-\frac{x-x_0}{\tau_i}} + A_2 e^{-\frac{x-x_0}{\tau_r}} \tag{4.2}$$

was used to extract τ_i, the intrinsic lifetime of triplets and τ_r, the time constant of the recombination-induced luminescence, whereas y_0, A_1, A_2 and x_0 are fitting constants. While the meaning of τ_i is clear, τ_r is the lifetime of the quasi steady state after turning off and therefore directly proportional to the trapped charges in the EML.[311–313] Thus it is clear that any electrical field intensity enhancements in the EML will affect τ_i while any leakage or charge carrier injection barriers induced by the Al ND array will show up in a decreased τ_r. Before starting the discussion, it has to be pointed out that the bias voltages were kept low in order to make the impact by effects such as triplet-triplet annihilation (TTA), triplet-polaron annihilation (TPA) or field induced exciton dissociation negligible.[314–316] The bi-exponential decay is in excellent agreement with the recorded transients as can be seen in Figure 4-14.a-e. First, the impact of the disc size on the intrinsic lifetime τ_i is discussed. Here, the reference device exhibits a τ_i of 1011 ns (Figure 4-14.a) which drops to a mere 710 ns for a disc size of 50 nm (Figure 4-14.b) and even further down to 652 ns for a diameter of 70 nm (Figure 4-14.c). From this point the lifetime starts to recover by rising to 777 ns at 90 nm disc size (Figure 4-14.d) and at 150 nm it is again equivalent with the reference with a value of 1030 ns (Figure 4-14.e). Next is τ_r which amounts to 6607 ns for the reference device. At 50 nm disc size, a minor

decrease to 6147 ns is obtained which then drastically decreases to 5373 ns at 90 nm disc size. τ_r further decreases to 4900 ns for a disc diameter of 90 nm only to drastically rise well beyond even the reference value, to 7347 ns.

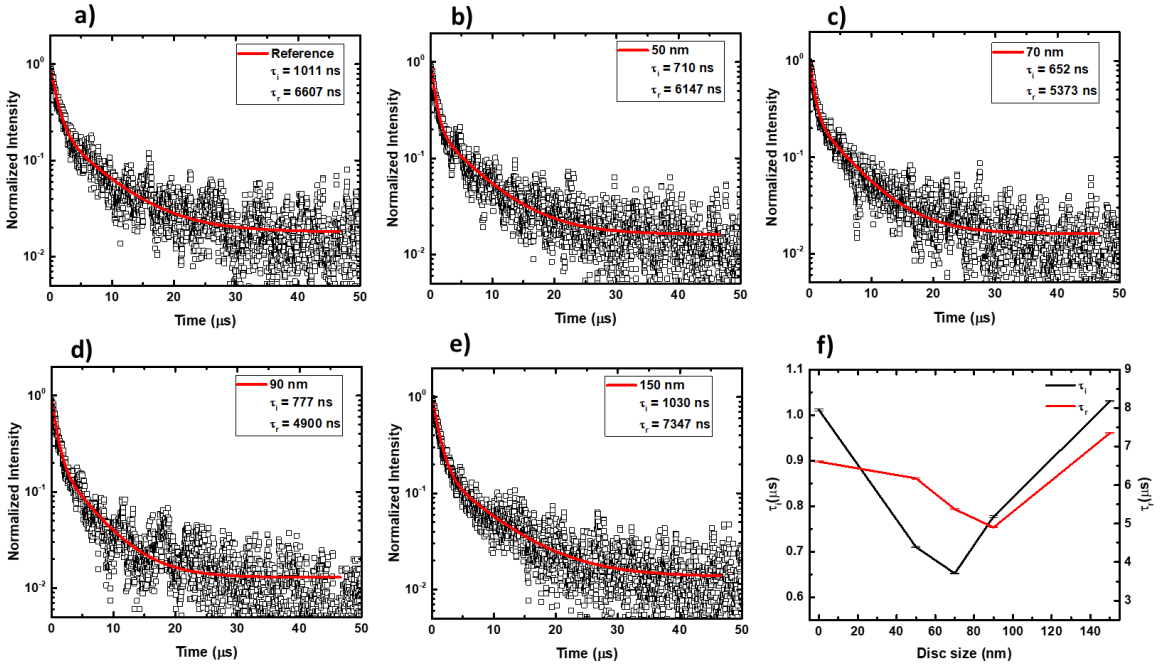

Figure 4-14. Transient electroluminescent characterization for a reference OLED (a) as well as OLEDs incorporating a grating with (b) 50 nm, (c) 70 nm, (d) 90 nm and (e) 150 nm disc sizes. (f) The obtained lifetimes $\boldsymbol{\tau_i}$ and $\boldsymbol{\tau_r}$ versus the disc size.

Discussing the obtained results, a clear impact of the disc size on the intrinsic lifetime has been found. In line with expectations, a sweet spot with respect to τ_i exists (in our case at 70 nm disc diameter). However, the quite dramatic decrease of τ_i by 359 ns between the reference and the device with an embedded lattice with a disc size of 70 nm is almost certainly not only attributable to an enhancement of the electric field intensity within the EML. Of course metal-induced quenching by the NDs[279,280] could be an explanation for the severely reduced intrinsic lifetime. However, since metal-induced quenching is a comparably fast process, this effect should be visible by a fast third component, which was absent in the measurements. At this point it is thinkable that effects like TTA or TPA play a role for the devices incorporating gratings. As to why these effects would solely appear for devices with incorporated Al ND arrays obviously would require more in-depth studies. With respect to the quasi-steady state lifetime, it can be seen that τ_r continuously decreases with the disc diameter. This behavior is attributed to variations in charge-injection, which is required to generate a balanced ratio of trapped electron and holes.

Furthermore, the markedly increased quasi steady-state lifetime of the 150 nm disc size device is attributed to a surplus of injected charge carriers and hence more pronounced charging.

Enhancement

Intrigued by the large decreases in intrinsic lifetime, the electric field intensity enhancement in the EML in dependence of the disc size was studied since the enhancement of spontaneous emission is driven by an increased field intensity. Thus, the electric field enhancement over the whole EML was simulated and the obtained enhancements were compared with the experimentally determined EL enhancements. From the results in Figure 4-15 it can be seen that a reasonably good qualitative agreement between the experiment and the calculated field enhancement is obtained for disc sizes larger than 50 nm. It has to be pointed out though that similar to chapter 4.4.2, the simulation cannot reproduce the TE_0 mode while the field enhancement peak ascribed to the TM_0 mode is not found in the experiment. Nonetheless, the general shape of the EL enhancement is reproduced. For the sake of completeness, it is noted that there is again no agreement between the simulation and the enhancement for the device with a 50 nm disc size, which at this point cannot be explained. To unravel any correlation between the field enhancement and the witnessed lifetime decreases, the area under the field enhancement curve was integrated and the reference value was subtracted. This way, a quantity termed integrated field enhancement (IFE) was obtained which describes the enhancement over the whole visible spectrum. In accordance with the lifetime (and neglecting the questionable calculated field enhancement for the 50 nm disc size for a moment) an increase in IFE to 84 at a disc size of 50 nm (Figure 4-15.a) which rises to 147 for a diameter of 70 nm (Figure 4-15.b) is witnessed. However, this correlation already breaks down at 90 nm (Figure 4-15.c) where the IFE reaches a marginally higher value of 152 whereas the intrinsic lifetime was found to increase. Furthermore, at 150 nm (Figure 4-15.d) the IFE drops a bit to 141 while the intrinsic lifetime fully recovers the reference value. Clearly, this analysis is just an estimation and a z-dependent field enhancement would have to be calculated to obtain the field enhancement at the position of the recombination zone. However, the simulation was sufficient to show that the witnessed lifetime reductions are not solely attributable to a field enhancement by the Al ND array. At a disc size of 70 nm the LSPR, centered at 550 nm and an overlap with the TM_0, is clearly visible. As expected, the resonance of the LSPR shifts towards longer wavelengths with increasing disc diameters. Coinciding with this shift is an increasing part of the spectrum where the electric field becomes attenuated, which was attributed to ohmic losses in the NDs. This last aspect is especially important to consider when attaining high efficiency enhancements is of utmost importance.

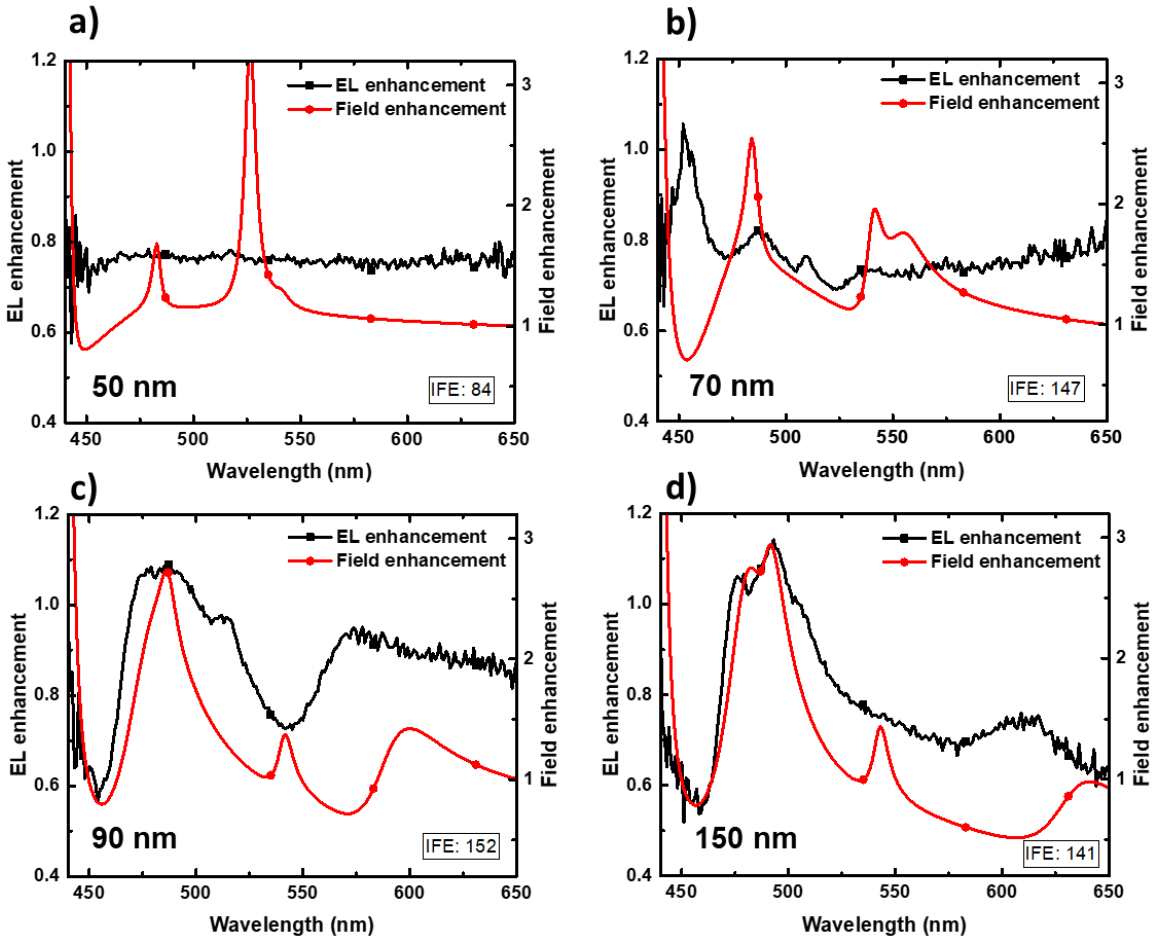

Figure 4-15. EL enhancement for OLEDs incorporating Al ND arrays with disc sizes of (a) 50 nm, (b) 70 nm, (c) 90 nm and (d) 150 nm. The corresponding field enhancements across the whole EML obtained by FDTD simulations are represented by the red line. Furthermore, the integrated field enhancement (IFE) is also indicated.

From this comparison between the field enhancement and the observed modifications in the EL spectrum, it is again reinforced that a disc size above 70 nm is required to achieve best possible efficiency enhancements. At the same time, larger disc sizes introduce increasingly large areas of reduced intensity which of course counteract the gains realized by the CLRs.

Conclusion

In this subchapter, the influence of the size of the individual NDs on the coupling strength of the grating modes supported by the square-lattice Al ND array with the optical modes of the OLED micro cavity was explored. Through angle-resolved measurements of the extinction, PL and EL it was confirmed that the coupling strength between individual modes depends on the resonance frequency of the LSPR. Furthermore, at a small disc size of 50 nm the resonance of the individual NDs is significantly detuned and has a low cross section which results in only minor interactions of the grating with the cavity modes. Further factoring in lifetime modifications as well as modelling of the electric field intensity, it is clear that for FIrpic the

best performance can be expected at 70 or 90 nm disc size, since larger disc sizes induce even more attenuation in the green part of the spectrum due to ohmic losses.

4.4.4 EML thickness

In the last subchapters, the dependence of the fluorescence enhancement on key parameters, like the lattice constant or the disc size, was explored. As already mentioned in chapter 2.2.5, the properties of guided modes strongly depend on the refractive indices of adjacent layers as well as the layer thicknesses. Dependent on the thickness, the amount of possible modes continuously increases. After considering all these parameters, it would be negligent not to consider the influence of the thickness of the emissive layer on the fluorescence enhancement. Since obtaining accurate layer thicknesses from solution-processes is cumbersome and prone to errors, FDTD was utilized to shed some light on this situation. Specifically, FDTD was used to simulate the extinction spectra for EML thicknesses between 30 and 350 nm (Figure 4-16). To make comparisons with the previous subchapters possible, this analysis was performed on the basis of a lattice constant of 300 nm. The obtained map reveals quite a profound impact of the thickness on the number as well as on the magnitude of extinction features. Starting with the more obvious features, bands exist, which move from low wavelengths and low EML thickness values to higher wavelengths at larger thicknesses, that effectively suppress the formation of extinction features. While the disappearance of the sharp extinction features might be understandable in the sense of periodicity and the inherent interference effects, the vanishing of the LSPR between 550 and approximately 620 nm (width varies with the EML thickness) is not. Coming back to the extinction features themselves, a region of significant and largely overlapping extinction can be localized between approximately 420 and 500 nm for an EML thickness between 50 to 140 nm. For the next period (higher thickness values) these features separate and form discrete signatures between 150 and 280 nm. From this map and the field simulations, it is clear that a proper choice of the EML thickness is paramount to obtain the maximum amount of fluorescence enhancing quasiguided modes. To reveal the implications of this rather profound thickness dependent changes in extinction, more in-depth simulations were performed to unravel the field enhancement in the volume occupied by the emitters. As before, this enhancement was obtained by recording the electric field intensity in the EML and using the unstructured reference, the field enhancement for thicknesses ranging from 50-350 nm was calculated. To allow for a better quantitative comparison of the expected field enhancement, the enhancement was obtained by integrating over the important range between 450 and 650 nm. By doing so (diamonds in Figure 4-16), it can be seen that the integrated field enhancement for this range continually rises with an increasing thickness of the EML until it reaches a first local maximum at 100 nm. From there it decreases again until it

reaches peak enhancement for a thickness of 250 nm. As before, the field enhancement again experiences a significant drop but does not recover with an increase in layer thickness as before.

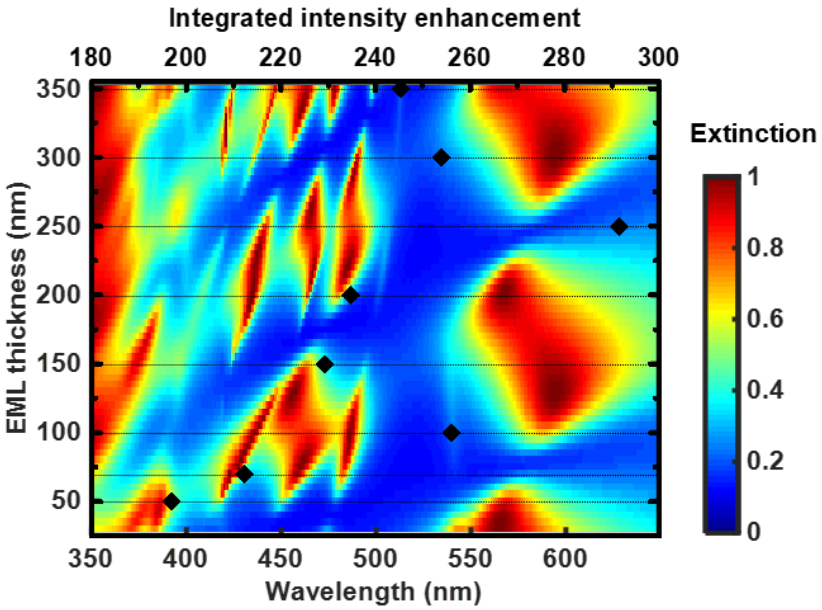

Figure 4-16. Dependence of CLR formation on the thickness of the emissive layer simulated for a quadratic lattice with a lattice constant of 300 nm. The black diamonds are the integrated intensity enhancement values obtained by integrating the field enhancement for the interval between 450 and 650 nm. Higher integrated intensity enhancement is better. The black lines indicate EML thickness values for which the integrated field enhancement was obtained.

Arguably, the choice of the layer thickness is an important one on the quest to achieve optimal device efficiency. To gain more insight, the modal profile as well as the effective refractive index n_{eff} of the TM_0, TE_0, TM_1 and TE_1 modes (higher order modes were neglected) were calculated for the thickness values where the detailed field analysis was conducted. From the modal profile, it was possible to calculate the percentage of the E field overlap of the guided modes with the Al NDs in dependence of the chosen EML thickness (Figure 4-17). For the TM_0 (Figure 4-17.a), expectedly the best overlap between the mode and the Al ND array was found at lower thickness values. This overlap drastically diminishes for increasingly larger EML thicknesses. This is not surprising considering that the mode is concentrated at the Al cathode and, hence, an increased EML thickness naturally reduces the overlap with the Al ND array. Moving on to the TE_0 mode (Figure 4-17.b), the best overlap was also obtained for smaller thickness values. However, while a decreased overlap was observed, it was by far not as severe. This dependence can again be explained by a dilution of the modal concentration which spreads out into the increased volume. Obviously, these zeroth order modes have the highest overlap percentages which were as high as 12% in the relevant spectral region (~500 nm). Taking a closer look at the TM_1 mode (Figure 4-17.c), only an overlap of approximately 8% was realized. Of note is the

fact that compared to the zeroth order modes, the overlap now increases with increased EML thicknesses and reaches a peak value of approximately 8 % for a thickness of 350 nm. For modes bellow 100 nm the cut-off was within the investigated spectral range which can be seen by the drop to almost 0 % around 550 nm for the 50 nm device which increases in accordance with the increased cut-off wavelength to 570 nm for 70 nm and so on. The TE_1 mode (Figure 4-17.d) portrays a similar evolution albeit the fact that the mode is not fully supported across the investigated spectral range for the majority of the investigated devices is obvious by the drop of the overlap.

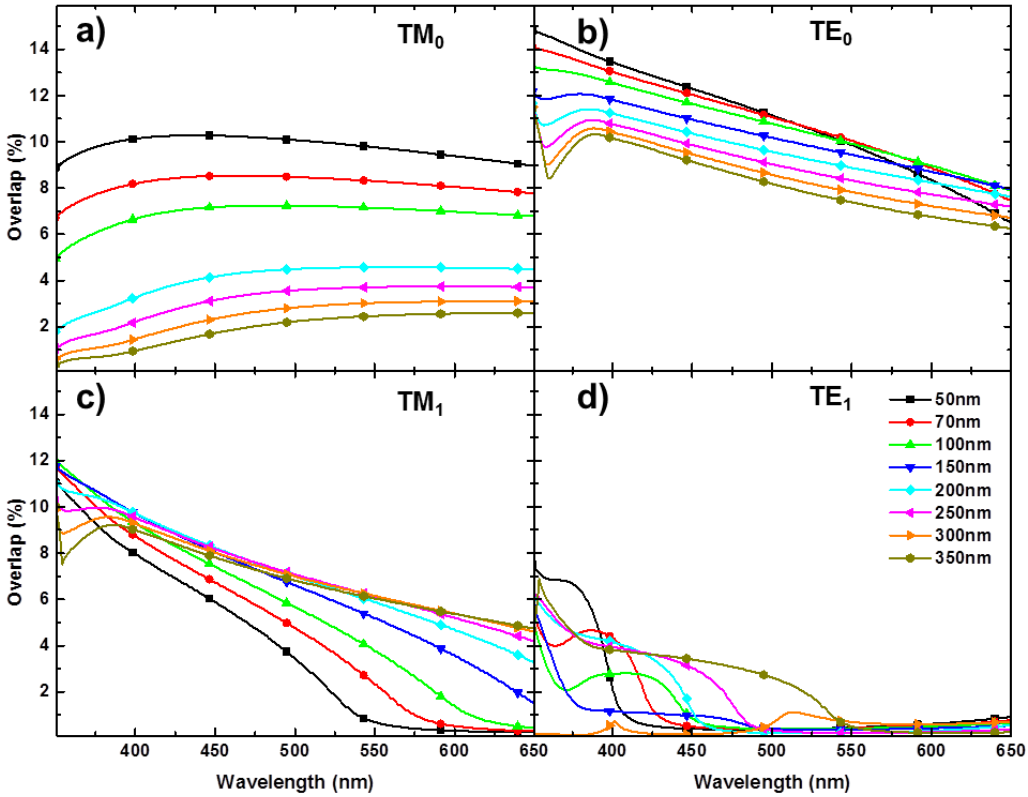

Figure 4-17. Percentage of field intensity overlap of the Al ND particles with the (a) TM_0, (b) TE_0, (c) TM_1 and (d) TE_1 modes.

From these considerations, the TE_0 and TM_0 modes should more significantly impact the enhancement at lower thickness values while higher thickness values favor the higher order TM_1 and TE_1 modes. This hypothesis was tested by calculating the wavelength which gets outcoupled by the Al ND array perpendicular to the device surface and these wavelengths are indicated on the electric field intensity enhancement for the investigated layer thicknesses (Figure 4-18).

In general, and with the exception of the RAs which will be discussed separately, a dip in enhancement is found for the CLRs. Following this dip, an enhancement in electric field intensity at higher wavelengths can be observed. Starting the discussion with the TM_0 CLR, it

is seen that the enhancement caused by this mode reaches its peak at 100 nm thickness followed by a decrease until the signature of this mode completely vanishes. A comparison with the modal profile of the TM_0 mode reveals barely any remaining modal overlap and, hence, the weak coupling prevents this mode to have any effect on the electric field intensity within the EML. The TE_0 CLR again is not detectable in the FDTD field simulations for reasons which at the time of writing this thesis were not understood. Advancing the discussion to first-order guided modes interacting with the array, the signature of the TM_1 CLR is found for all EML thicknesses. Again, the overlap plays a crucial role as the field enhancement increases from a factor of 1.3 at 50 nm to 2.7 at 100 nm. It is this range of EML thicknesses where the modal overlap changes the most and, thus, it is only logical that the field enhancement will increase the most in this range. For the TE_1, the picture is a bit different, mainly because the cut-off wavelength for the TE_1 mode is well below 450 nm for layer thicknesses below 150 nm and even at higher EML thicknesses the overlap is rather poor, valuing below 2%. Still, the signature of the TE_1 is present at all layer thicknesses and due to the poor overlap at all thicknesses, field enhancement is not increased with larger layer thicknesses. Having discussed the several CLRs, the occurrence of the RAs needs to be analyzed. At the position of the RAs, so called surface lattice resonances (SLRs), which are also part of the CLRs, can form. These features, characterized by comparatively sharp peaks of high field enhancement, start at 420 nm (50 nm thickness) and experience a bathochromic shift with an increase in layer thickness which shifts this RA to 498 nm at a thickness of 350 nm. This behavior is explained by the increase in effective index of refraction inflicted by the increased amount of (compared to glass) higher refractive index material. It is rather intriguing that the simulation reveals the presence of RAs since these modes are easily disturbed by an inhomogeneous environment[283,317,318] and the OLED layer structure exhibits materials with refractive indices ranging between 1.4 and 2. While an experimental follow-up is warranted by this key observation, it has to be pointed out that with the chosen lattice constant the positions of the RAs and, thus, of the SLRs, are only coinciding with the emission spectrum of FIrpic for layer thicknesses of at least 250 nm. Needless to say, these layer thicknesses are too much for efficient OLEDs, rendering the SLR irrelevant for the envisaged use in a blue-emitting OLED driven by FIrpic.[294]

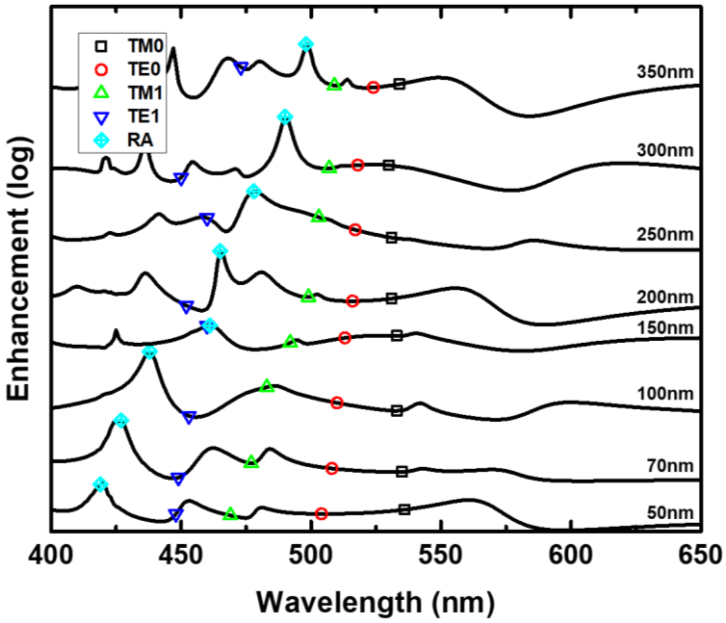

Figure 4-18. Simulated field enhancement for a grating with a 300 nm lattice constant in dependence of the thickness of the EML. Wavelength of grating induced outcoupling perpendicular to the device surface indicated by the symbols.

Concluding this discussion, it was found that the field enhancement by the CLRs does indeed benefit from a better modal overlap. Also, enhancement was visible for the TM_0 and TM_1 CLR, while the TE_0 mode was again not observable for unknown reasons.

Evidently, these Al ND arrays have a profound impact on the electric field distribution within the weak micro cavity of the OLED. To gain more insight into the induced field intensity modifications inside the EML, z-resolved field enhancement simulations were again performed. The results for the investigated layer thicknesses are depicted in Figure 4-19. As was already demonstrated in chapter 4.3, the grating successfully enhances the electric field within the EML at the position of the node of the standing wave within the micro cavity. With increasing layer thicknesses, the length of the resonator increases and the first order nodes are supported for even higher wavelengths (Figure 4-19.a-c). Reaching 150 nm (Figure 4-19.d), the resonator is long enough to support the second node and again, as the layer thickness continues to increase, even longer wavelengths feature a second node (Figure 4-19.e). At 250 nm (Figure 4-19.f) the first third node is supported and at 350 nm (Figure 4-19.h) the first fourth node is visible. In general, through engineering of the individual layer thicknesses, the recombination zone is chosen in such a way, that it doesn't coincide with such a node where the severely diminished field intensity results in a reduced number of modes the emitters can decay into. However, under higher biases, the changes of the charge carrier balance might shift the recombination zone into such a node. While detrimental for an unstructured device, devices with the Al ND arrays don't suffer from the same issue, since these nodes are effectively

neutralized by the Al ND array. Even though the Al ND array modifies the electric environment in a mostly positive manner, the formation of spots of decreased field intensity is also of note (and was detected in chapters 4.4.2 and 4.4.3). However, as revealed by Figure 4-19, the magnitude and extend of these regions exhibits a strong dependence on the layer thickness. This can be seen most clearly on the basis of a layer thickness of 250 nm (Figure 4-19.f) where no area of reduced field intensity is evident. Increasing or decreasing the thickness restores the areas of reduced intensity in the range between 550 and 610 nm.

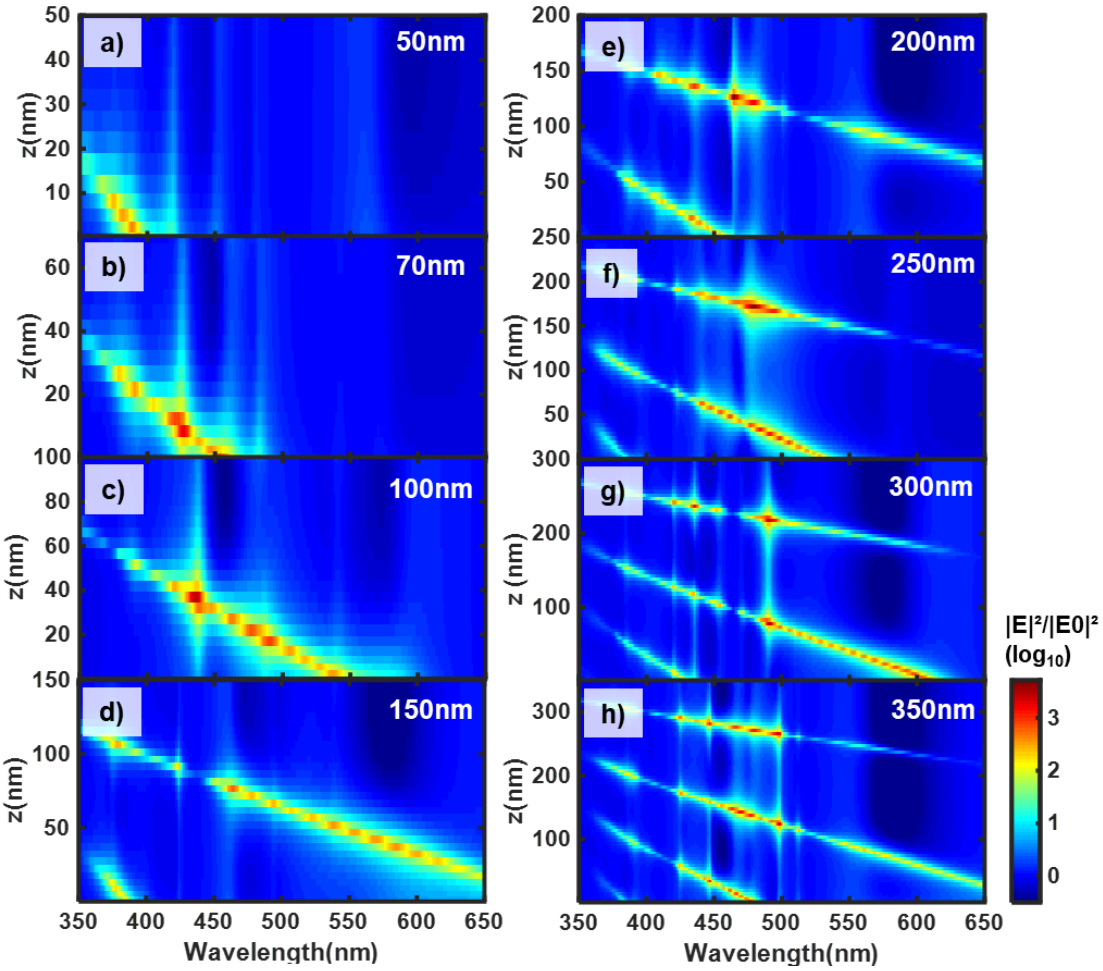

Figure 4-19. Z-dependent field enhancement map for different EML thicknesses.

Concluding this short investigation, it is clear that on top of the disc size of the ND grating and the lattice constant, attention has to be paid on the thickness of the emissive layer as well. Simulations revealed that the overlap between the guided modes of the OLED stack and the Al ND arrays depends on the thickness. An increased thickness leads to a reduced overlap for the fundamental TE and TM modes and in turn reduced field enhancement. At the same time, increased layer thicknesses shift the SLRs, which have an extraordinarily high field enhancement, within the bandwidth of the emitter material. To obtain an efficient OLED, the

thickness of the OLED stack should be as small as possible to reduce ohmic losses.[294] For all the presented reasons, a thickness value of around 100 nm was identified as a good tradeoff between optical and electrical performance.

4.4.5 Conclusion

As outlined in the introduction, a clear dependence of the observed CLRs with respect to lattice constant, disc size and EML thickness was found. In line with theory and previous reports, the spectral position of the CLRs can be adjusted by the lattice constant which obviously makes this parameter quite important. With the aim to raise the efficiency of a blue-emitting OLED, best overlap of the CLRs with the emission spectrum of the emitter was obtained for a lattice constant of 300 nm. While the change of the lattice constant had a large impact on the position of the CLRs, a variation in disc size led to a subtler modification. For small disc sizes, the scattering cross section is too small and, hence, no formation of the CLRs is possible. At the same time, picking a large disc size resulted in increased losses in the green part of the spectrum. A sufficiently large scattering cross section and only minor attenuation in the green part of the spectrum was found for a disc size of 90 nm. With these factors fixed it is also important to choose the thickness of the EML carefully since an improper choice also causes the magnitude of the CLRs and in turn the field enhancement to vanish. Here, a thickness of 100 nm provided a large field enhancement while still satisfying the electrical constraints. Even though these parameter variations already provide a good picture of the impact of each of the individual factors, the quite possibly complex interplay between these parameters was purposefully neglected. It is obvious that further work on unraveling these relationships is warranted.

4.5 Increase the amount of outcoupled light via aluminum induced collective lattice resonances

Introduction

In the last subchapters, the factors that govern the coupling efficiency between the NDs and the guided modes, which in turn set the limit for the achievable field and outcoupling enhancement, were explored. Next, it was attempted to use the obtained best values for the respective factors to increase the efficiency of the device. From chapter 4.4.2 it is known that a lattice constant of 300 nm yields the largest enhancement for the used emitter FIrpic. Moreover, chapter 4.4.3 revealed that a good performance can be expected from a 90 nm disc size. Last but not least, the thickness of the EML should be 100 nm (see chapter 4.4.4) to obtain

best performance. Using these values in an actual device, a 35% enhancement in current efficiency could be obtained when compared to an unstructured reference device.

Figure 4-20.a shows the Al ND array placed on top of ITO. Overcoating the Al ND array where the height of the individual NDs amounted to 30 nm with 50 nm of CuSCN effectively lowered the particle induced surface roughness of 10.7 nm to 2.5 nm while also functioning as a hole transport and electron blocking layer.[164] The first aspect is clearly visible in Figure 4-20.b since no traces of the Al ND array can be found.

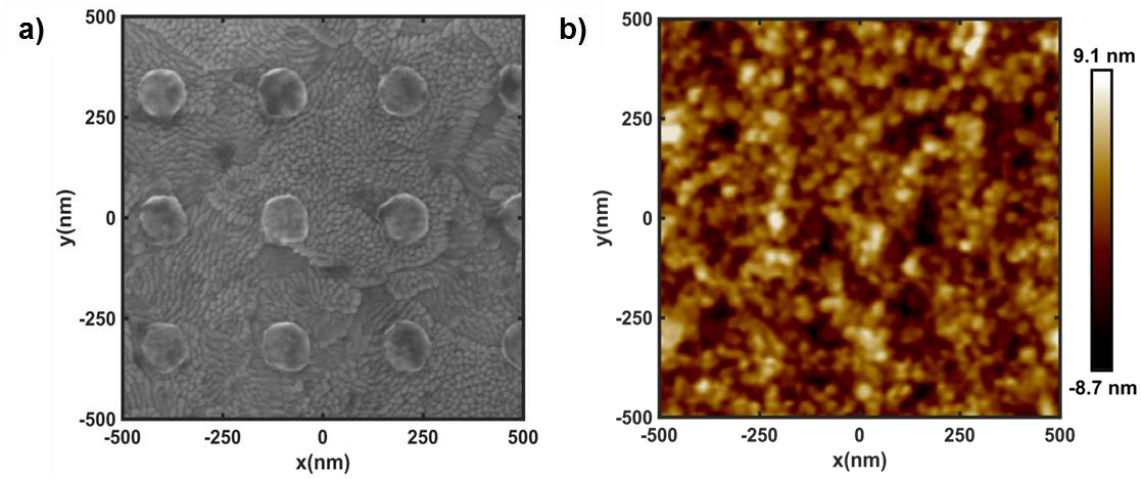

Figure 4-20. (a) Top view SEM image of a quadratic array of aluminum nanoparticles on ITO with a lattice constant of 300 nm and (b) ND array overcoated with a 50 nm thick layer of CuSCN.

Photoluminescence

The presence of the CLRs was verified by angle-resolved extinction spectroscopy (Figure 4-21). As can be seen by the calculated angular dispersion of the CLRs a clear interaction of the (±1,0), (0,±1) and (±1,±1) order of the grating with the TE_0 and the TM_1 mode is visible. Even though a faint signature of the (0, ±1) order coupling to the TM_0 mode is there, no further signs of the TM_0 mode are present. Considering the weak overlap between the TM_0 and the Al ND array (see chapter 4.4.4) this is not surprising. The weak overlap as well as the cut-off close to 450 nm also explains the absence of any signature of the TE_1 mode coupled to the array.

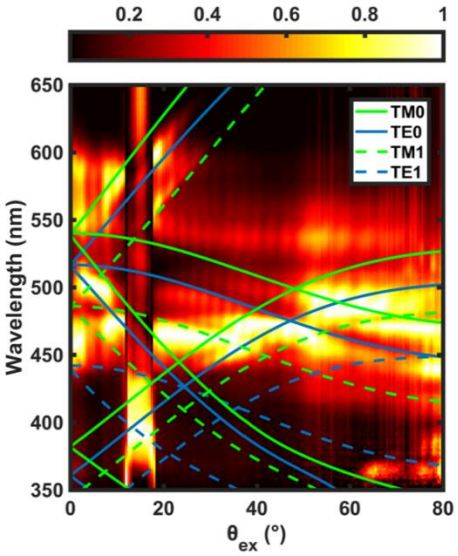

Figure 4-21. Measured extinction spectra of the OLED stack with an Al ND array featuring a lattice constant of 300 nm. Analytical solutions for the CLRs are overlayed.

While the angular dispersion is an important tool for detecting and identifying the presence of any mode coupling, the enhancement of light in the direction perpendicular to the diode surface is the truly important quantity for measuring efficiency increases. Therefore, the extinction spectrum at 0° as well as the simulated extinction spectrum along the same direction is depicted in Figure 4-22.a. Generally, a good agreement between experiment and simulation can be observed. Some deviations in the spectral range between 430 and 490 nm are most likely due to limited applicability of the available permittivity (n, k) data for polycrystalline Al films[296] to NDs where the ratio between oxide and Al core might be different. From the measurement, extinction features were located at 447, 463, 497, 510, 550 and 588 nm. The features at 550, 510 and 497 nm were already identified as the TM_0, TE_0 and TM_1 modes. The other modes are identifiable by using the knowledge gained from chapter 4.4. This allows to assign the peak at 588 nm to the LSPR of the ND. The feature at 447 nm on the other hand might be ascribable to the SLR predicted by the simulation (at 100 nm the SLR and the TE_1 mode are close together, see chapter 4.4.4). This leaves the feature at 463 nm still unassigned. For this reason and to provide additional proof of the validity of the modal association, the electric field intensity within the OLED stack (Figure 4-22.c-f, the corresponding layer structure of the simulated unit cell is shown in Figure 4-22.b) was calculated. Clearly, the feature at 463 nm (Figure 4-22.d) shows signs of near-field enhancement around the Al ND but also significant field intensity within the ITO layer. Thus, it carries the signature of a LSPR coupled to the guided mode formed by the ITO layer. Focusing on the strong near field enhancement in the vicinity of the Al ND for the peak at 588 nm, it is confirmed that this a LSPR dominated mode

(Figure 4-22.g). At the position of the CLRs, the intensity profiles reveal a significant concentration of the electric field intensity in the EML for the SLR or TE_1- (Figure 4-22.c), TM_1- (Figure 4-22.e) as well as the TM_0-mode (Figure 4-22.f). As typical throughout the conducted studies, FDTD was not able to resolve the enhancement at the position of the TE_0-mode (as will be shown later, fluorescence enhancement at this position was detected).

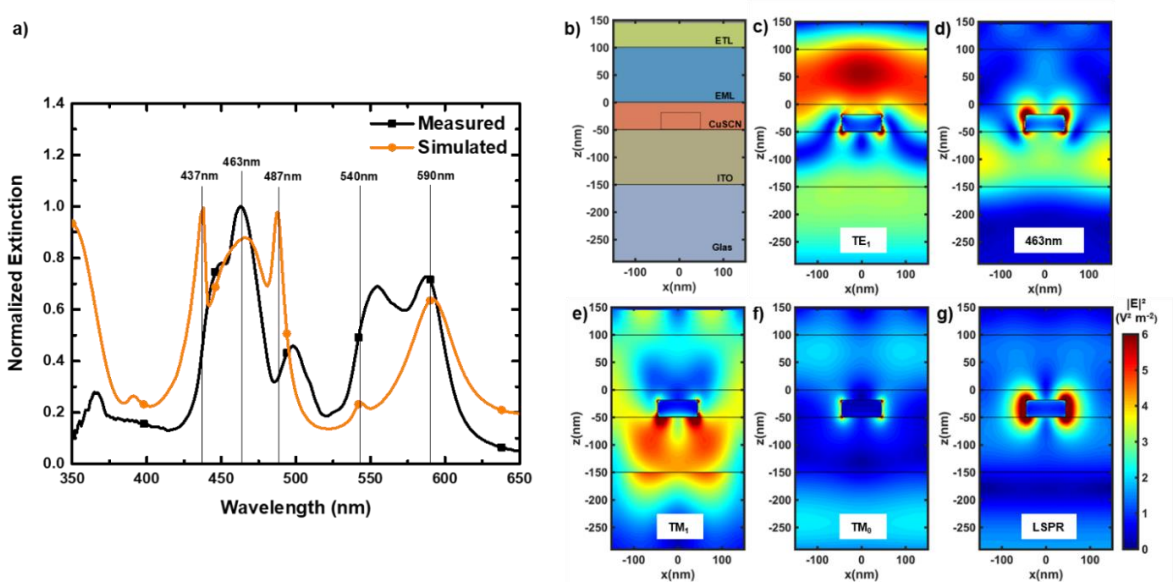

Figure 4-22. (a) Measured and simulated extinction spectrum. (b) Schematic of the OLED stack as guidance for the eye. $|E|^2$ due to the embedded grating at (c) 437, (d) 463, (e) 487, (f) 540 and (g) 590 nm. The color bar applies to all field maps.

Moving the discussion along, it is clear that these modifications in the field distribution should also modify the emission spectrum via an increased radiative local density of states (RLDOS). Since an enhancement in the forward direction is of interest, a fractional RLDOS which, by reciprocity, is the field enhancement obtained by illumination in forward direction can be defined. Thus, the field enhancement (FE) can then be set as the integral of the intensity enhancement over the volume which is occupied by the emitters

$$FE(\lambda,\Omega) = \frac{\int_V |E(x,y,z,\lambda,\Omega)|^2 dV}{\int_V |E_{ref}(x,y,z,\lambda,\Omega)|^2 dV} \tag{4.3}$$

where Ω is the solid angle (in this case the forward direction), $E(x,y,z,\upsilon,\Omega)$ and $E_{ref}(x,y,z,\upsilon,\Omega)$ is the electric field with- and in the absence of the Al ND array at the wavelength λ at the location of the emitter and V is defined as the volume encompassing the EML. The results of this calculation are plotted as dashed lines in Figure 4-23. Coinciding with the results from the electric field calculations, an enhancement in PL intensity can be expected at 437, 487, 540 as well as 590 nm. These results were verified by PL studies performed by exciting the emitters in the OLED stack at a wavelength of 360 nm. Curiously, the observed enhancement is matched

for the TM_0 as well as the TE_1 or SLR CLRs while no enhancement was detected at the position of the TM_1 CLR. Additionally, the forecast enhancement at the position of the LSPR was also not evident in the measurement. While the absence of the enhancement at the TE_0 position is explained by FDTDs inability to resolve this mode, the missing enhancement at the TM_1 as well as the LSPR is attributed to the preferred excitation of the TE_0 and the TM_0 by enhanced excitation through higher order lattice modes at the spectral position of the excitation source which results in a preferred excitation of these two modes.

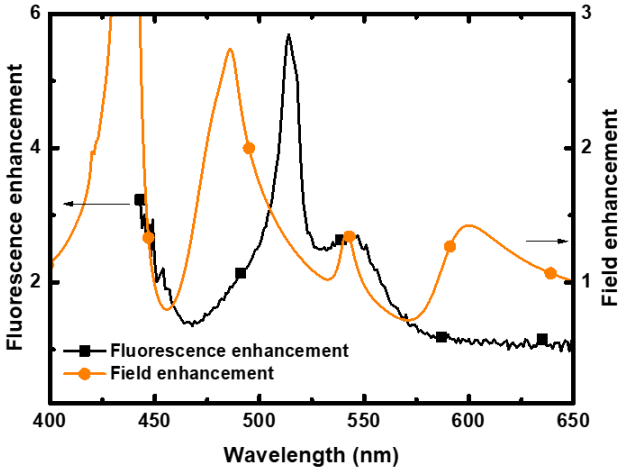

Figure 4-23. Fluorescence enhancement in forward direction. The dotted line is the electric field intensity enhancement

As was demonstrated before, there is a fundamental difference between optical and electrical excitation of the emissive layer. While the whole EML participates in the case of optical excitation, only a narrow zone, the recombination zone located somewhere within the EML is responsible for the generation of light. Therefore, the presented PL investigations solely provide a first hint at the positions where an enhancement can be expected.

Impact of Al NDs on charge injection

Clearly, the Al ND array raises the amount of light generated and outcoupled from the OLED stack. However, if at the same time, electrical operation is impaired by the formation of charge injection barriers or electrical shunts, the gains made at the optical side would be more than compensated with losses stemming from the electrical behavior of the device. Even though several investigations on the importance of energy level alignment have been carried out, the impact of injection barrier created by the presence of Al and Al_2O_3 was also probed within the presented studies.[21,319,320] To this end, the ITO electrode was fully covered with 10 nm of Al, an OLED was fabricated on top and the recorded current density was compared to a reference device (Figure 4-24.a). Neglecting the sizeable reverse current for a moment and focusing on

the current under forward bias, the impact of the Al induced injection barrier is evident. Obviously, a full coverage with Al should be prevented. Having studied the worst-case scenario, the focus was set on the present situation within the OLED. Here, with the given lattice parameters the coverage of ITO with Al amounts to 7.1 %. The impact of the grating on the hole-injection behaviour can be assessed by the fabrication of hole-only devices.[321] In this case an ITO/Al ND/CuSCN(50nm)/MoO_3(8nm)/Al geometry was chosen and the results were compared to a device without the array. From the virtually identical current density characteristics of both device (Figure 4-24.b) it is confirmed that the Al ND array does not impact the injection of holes.

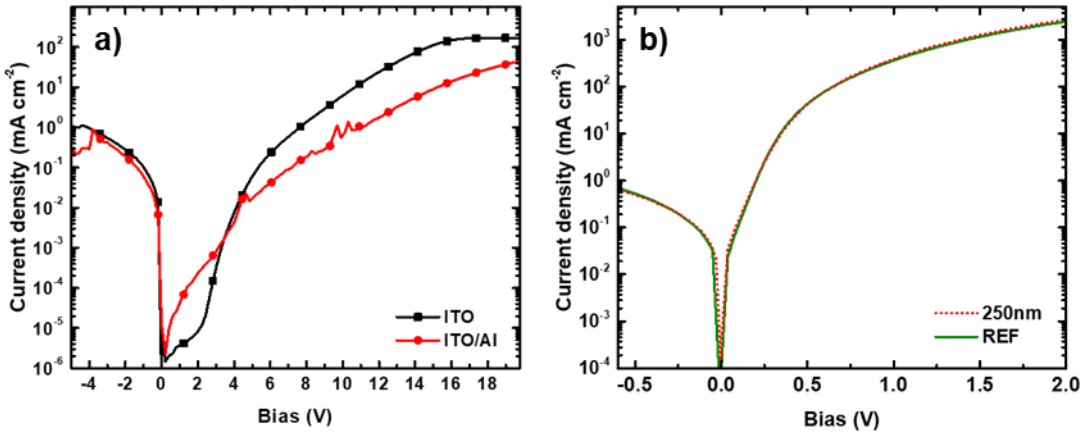

Figure 4-24. (a) Current density characteristic of an OLED fabricated on top of ITO and ITO/Al(4nm). (b) Current density characteristics of an ITO/CuSCN/MoO_3/Al device with a 250 nm lattice constant and 120 nm disc diameter grating as well as a pristine reference device.

Impact of guided modes on EL

Next, the electro-optical properties of OLEDs with and without an Al ND array were investigated. The current efficiency values are shown in Figure 4-25.b. Onset voltages were 3.7 and 3.6 V for the reference device and the device with a 300 nm lattice constant Al ND array, respectively, with peak luminance values of 6558 and 8739 cd m^{-2} and current efficiencies of 9.4 and 12.7 cd A^{-1} at 1000 cd m^{-2}. In terms of performance relative to the reference, this amounted to an increase of 35% in current efficiency. In line with the previous study, the J-V characteristics show no signs of increased leakage current.[148] At the bottom of Figure 4-25.c, the recorded EL spectra of the investigated devices under forward bias as obtained with a calibrated CCD spectrometer are depicted. The reference device exhibits the typical FIrpic emission profile with the main peak at 472 nm corresponding to CIE1931[322] coordinates of (0.17, 0.35). As observed, the Al ND array enhances the FIrpic emission between 473 and 542 nm, causing the EL peak to shift to 485 nm with associated CIE1931 coordinates of (0.17, 0.37). Additionally, the vibronic structure is significantly distorted by enhanced emission spanning

the range between 475 and 533 nm. A better picture of the Al ND array induced changes is provided by the relative EL enhancement (top of Figure 4-25.c), which indicates the presence of three distinct enhancement peaks at 485, 514 and 519 nm. Furthermore, two dips below unity are notable, with the reduction in EL intensity at 462 nm being sharp in nature whereas the feature at 551 nm is rather broad. These spectral modifications are linked to a modified radiative local density of states which is proportional to the field enhancement obtained from simulation by assuming illumination perpendicular to the stack interfaces.

The calculated FE for the emissive layer obtained by eq.(4.3) is depicted in Figure 4-25.d. On top of significantly modifying the electric field configuration within the cavity, this FE map also allows to explain the measured enhancement by exploiting the fact that the width of the recombination zone of an OLED is rather narrow.[323] At a distance 70 nm away from the HTL interface, a good agreement between the FE and the EL enhancement was obtained (top of Figure 4-25.c) except for the pronounced enhancement at 514 and 519 nm. Since this feature is closely located to the TE_0 CLR, the absence in the FE is ascribed to the inability to determine said mode with the chosen simulation settings.

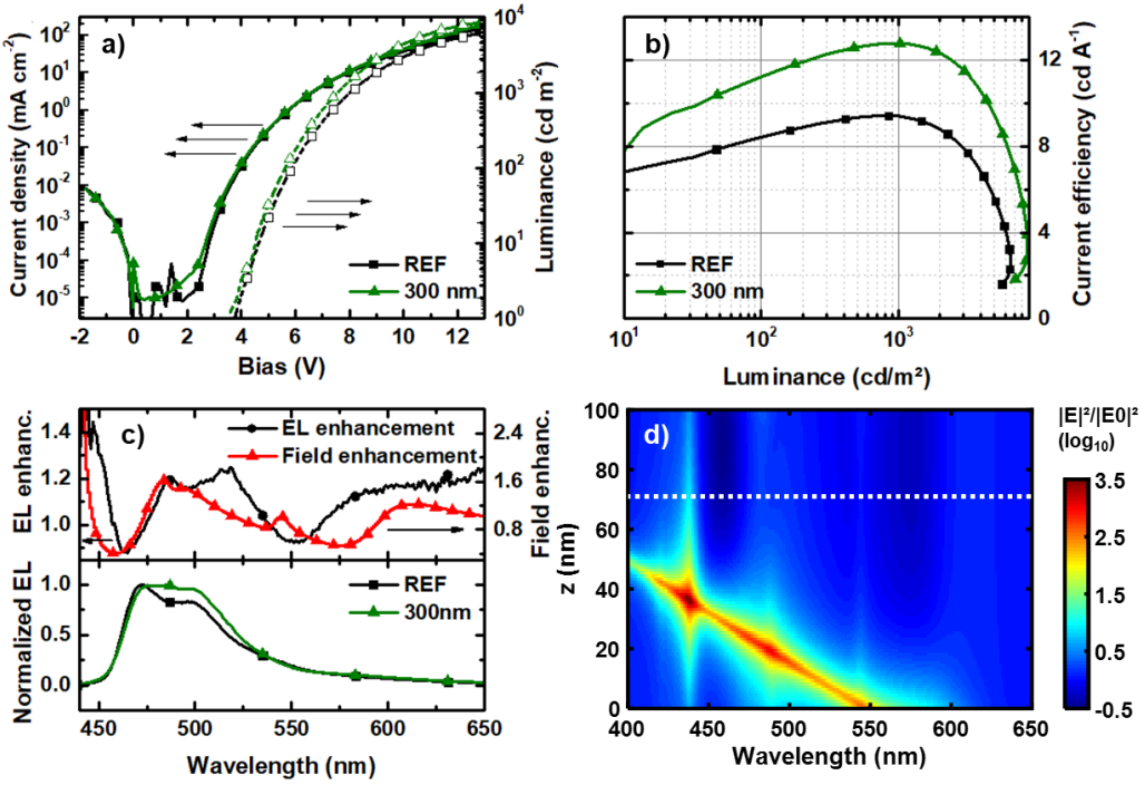

Figure 4-25. Characteristics of the OLED including an Al ND array with a lattice constant of 300 nm and the reference OLED: (a) bias dependent current density and luminescence, (b) current efficiency and (c) emission spectra (bottom) as well as measured enhancement and calculated field enhancement for a recombination zone 70 nm in a distance from the HTL (top). (d) The calculated field enhancement throughout the emissive layer, the location of the recombination zone is indicated by the dotted line.

Conclusion

In summary, it was demonstrated that incorporation of Al ND arrays directly into the stack of a solution-processed blue-emitting phosphorescent OLED is an effective way to enhance specific performance parameters of the device. With parameters optimized for the emitter type as well as device architecture, the Al ND arrays support the emergence of CLRs which very selectively enhance the EL by a considerable field enhancement for on-resonance wavelengths. By this means, an increase in current efficiency of 35 % for standard test conditions at a luminance of 1000 cd m^{-2} was demonstrated. Thus, it is clear that with techniques like nanoimprint lithography the use of low cost Al NDs could provide a cheap and mass-producible way to enhance OLED performance.

4.6 Broadband enhancement - Grating structures for white-light emitting OLEDs

Encouraged by the promising results with the monochromatic OLEDs, the focus was shifted towards the interaction of the gratings with a WOLED. Until now, it was sufficient for the CLRs to be narrowly placed to achieve a good enhancement without significantly modifying the emission color. However, the spectral width of a WOLED typical spans from 450 to 700 nm. This can be seen from the spectrum of a reference WOLED (see Figure 4-26) which is built on the concept of the blue-emitting FIrpic devices[206] but extends this single-emitter system with $Ir(ppy)_3$ and $Ir(piq)_3$, a green- and a red-emitter to achieve the required broadband light generation.[324] Here, it is clear that a sole enhancement in the blue spectral range would not only yield marginal performance improvements but also significantly affect the emission color. Obviously more CLRs in a broader spectral range are required for a successful application of an Al ND grating for WOLEDs. Within this subchapter two routes to achieve such a broadband enhancement are explored. At first, a rigorous approach around the superposition of two point gratings which exhibits a multitude of CLRs throughout the required spectral range is presented. The second approach is simpler in the way that it solely enhances the blue and green spectral range which requires only one grating.

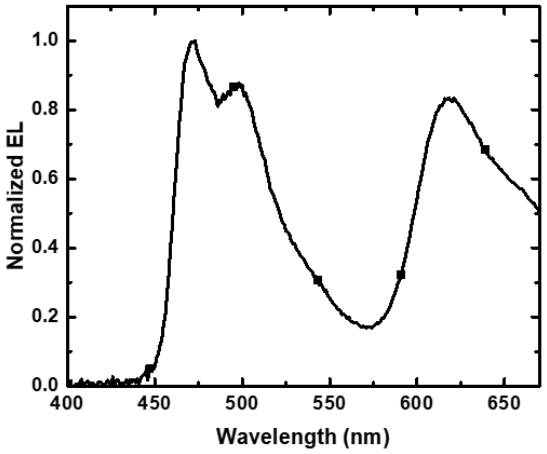

Figure 4-26. Normalized EL spectrum of a reference WOLED with a triple-emitter system consisting of FIrpic, $Ir(ppy)_3$ and $Ir(piq)_3$.

4.6.1 Superimposed grating structures for white-light emitting OLEDs

Introduction

To achieve the required broadband enhancement, a superimposed grating structure (see Figure 4-27) was designed which consisted of two gratings where one was comprised of nanoellipses (NE) sized 138 x 85 nm and the other retained the disc-shaped NPs with a diameter of 90 nm. Both gratings were rectangular-shaped and the lattice constant in the p-polarization was matched at 340 nm. Furthermore, the short axis of the NEs was also along the p-polarization. In n-polarization the NE grating had a lattice constant of 310 nm which was also the long axis of the NEs whereas the ND grating was characterized by a lattice constant of 280 nm along the same axis.

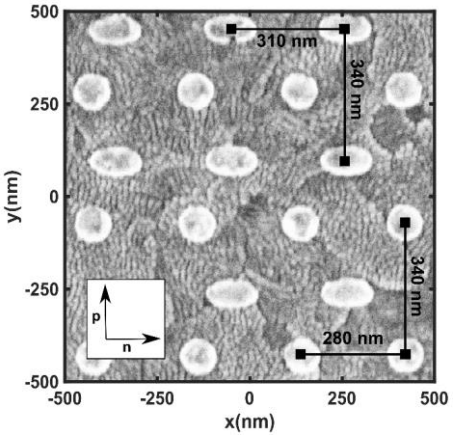

Figure 4-27. Superimposed grating structure consisting of an NE- as well as ND grating in a rectangular lattice configuration.

In the next subchapters, the interaction of this superimposed grating with the optical modes supported by the OLED stack are studied by means of angle resolved extinction, PL-, and EL measurements. Impact of the performance is assessed by an OLED characterization.

Extinction

The angle-resolved extinction spectra of a WOLED with the presented superimposed grating are recorded and discussed. Since these gratings are rectangular (and feature NEs) the angle resolved extinction measurement was performed by tilting the detector along the p- and n-polarization direction. To resolve the contributions of the individual grating modes no interaction between the two gratings were assumed. This way, calculating the angular dispersion of the CLRs was trivial and the results of this calculation overlaid on top of the measurement for the NE and the ND grating are depicted in Figure 4-28.

Generally, it can be stated that the calculation based on the assumption of no interaction produced a surprisingly good match with the extinction spectra. By the observed dispersion of the extinction features it can be seen that all features at 0° can be ascribed to the formation of CLRs.

Due to the NE and ND grating both having the same lattice constant along the p-polarization it is impossible to assign any extinction features following the (±1,0) grating mode to either one grating. Equally it is safe to assume that the interactions along the p-polarization are indeed the consequence of both gratings interacting with the guided modes of the OLED cavity. The extinction spectra in p-polarization reveal an interaction of the (-1,0) grating mode with the TM_0, TE_0, TM_1 as well as TE_1 guided modes. Another contribution stems from the interaction of the (+1,0) mode with either the TM_0 or TE_0 guided mode. Along the (0,±1) direction of the grating mode, the difference in lattice constants along the n-polarization makes it possible to clearly assign the TM_0 CLR starting at 555 nm at 0° to the NE grating, while the ND grating supports a CLR starting at 510 nm at 0°. There are further signatures of the (0,±1) order interacting with the other guided modes. However, the overlap between these features again makes a clear assignment impossible. At larger angles, the (+1,±1) grating order becomes visible where the TE_0 and TM_1 modes couple to the ND grating.

In n-polarization the issue of equal lattice constant is remedied for the (±1,0) direction of the ND and NE gratings. The TM_1 guided mode couples to the (+1,0) order of both gratings which results in the formation of two distinct TM_1 CLRs. Not as clear is the origin of the extinction band corresponding to a coupling of the TM_0 mode since the calculated dispersion relation of both gratings would produce a matching signature. A more clear-cut assignment, however, is possible for the TE_1 which forms a CLR with the NE grating. For the (+1,±1) orders of the ND

and NE gratings, the resulting CLRs could either originate from the NE or the ND grating since the dispersion relations would produce a match for either one. Even though one might argue that the calculated dispersion for the (+1,±1) order of the ND grating provides a better match with the experimentally observed extinction bands than the ones for the NE lattice, the NE grating would still be within the margin of error for this kind of modal assignment.

Even though the presented analysis of the superimposed grating is unable to uncover the origin of the individual observed CLRs with high confidence, it is still able to demonstrate the increased amount of CLRs in the required spectral range compared to the previously studied square-lattice gratings. The increased amount of CLRs should provide the possibility to broadly increase light out coupling as well as light generation.

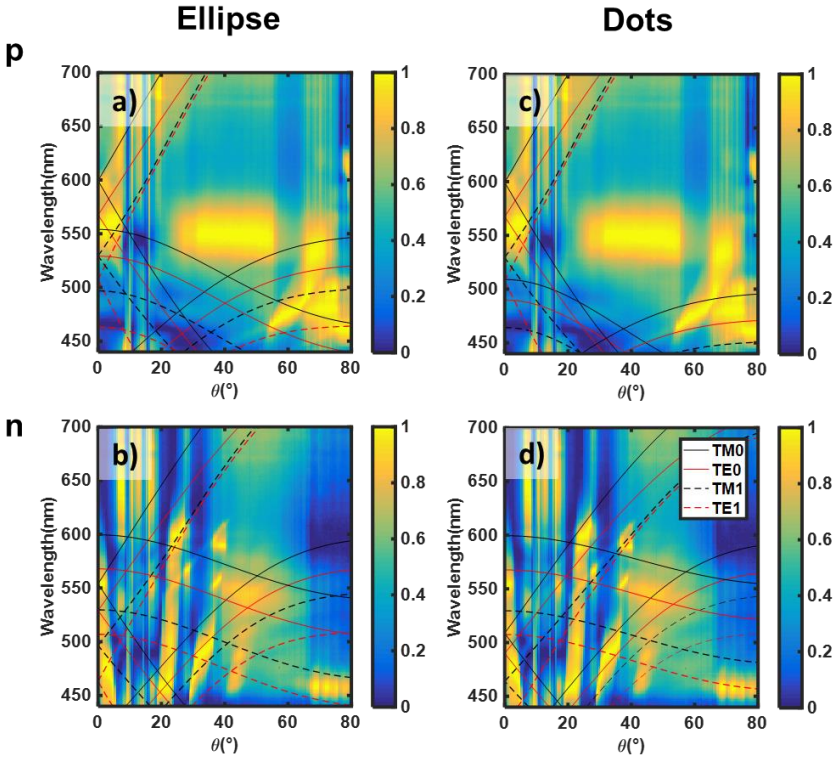

Figure 4-28. Angle-resolved extinction spectra acquired by tilting along the p- and n-polarization axis. The dispersion of the CLRs along the p- and n-polarization is depicted in (a) and (b) for the NE grating as well as (c) and (d) for the ND grating.

Photoluminescence

In the last paragraph, it was verified that both gratings can couple to the guided modes in the OLED stack and thus both gratings together are able to generate more CLRs for out coupling as well as light generation improvements. To confirm this claim, angle-resolved PL spectroscopy was used. The results of this measurement as well as the calculated dispersion relation for the NE grating (Figure 4-29.a, b) and the ND grating (Figure 4-29.c, d) for the p- and n-polarization are depicted.

At first glance, the anticipated broadband enhancement character of the double grating is confirmed. In detail, the enhancement again follows the calculated dispersion relation. For the p-polarization this means an enhancement along the (±1,0) direction of the TM_0, TE_0, TM_1 and TE_1 guided modes. Normal to the device, e.g. at 0°, these enhancements are centered at a wavelength of 601, 569, 531 and 501 nm. Furthermore, along the (0,±1) direction the NE grating facilitates the formation of TM_0, TE_0 and TM_1 CLRs which yield a minor fluorescence enhancement. In n-polarization, the TM_0(+1,0) CLR arising from the ND lattice yields an enhancement of the fluorescence. In the (-1,0) direction both gratings yield a minor fluorescence enhancement in the area of the calculated dispersion. The largest gains, however, clearly stem from slowly dispersive (0,±1) grating modes coupling to the TM_0 as well as the TE_1 modes. For normal incidence, these enhancements are spectrally located at 601 (TM_0) and 507 nm (TE_1). For the (+1,±1) direction and, hence, at angles greater than 20°, fluorescence enhancement along the TM_0, TE_0 and TM_1 dispersion relation is noticeable.

Of note are the areas of increased fluorescence close to the points where two CLRs meet, such as the area of markedly increased fluorescence from 517 at 11.5° down to 487 nm at 18.7° (Figure 4-29.a).

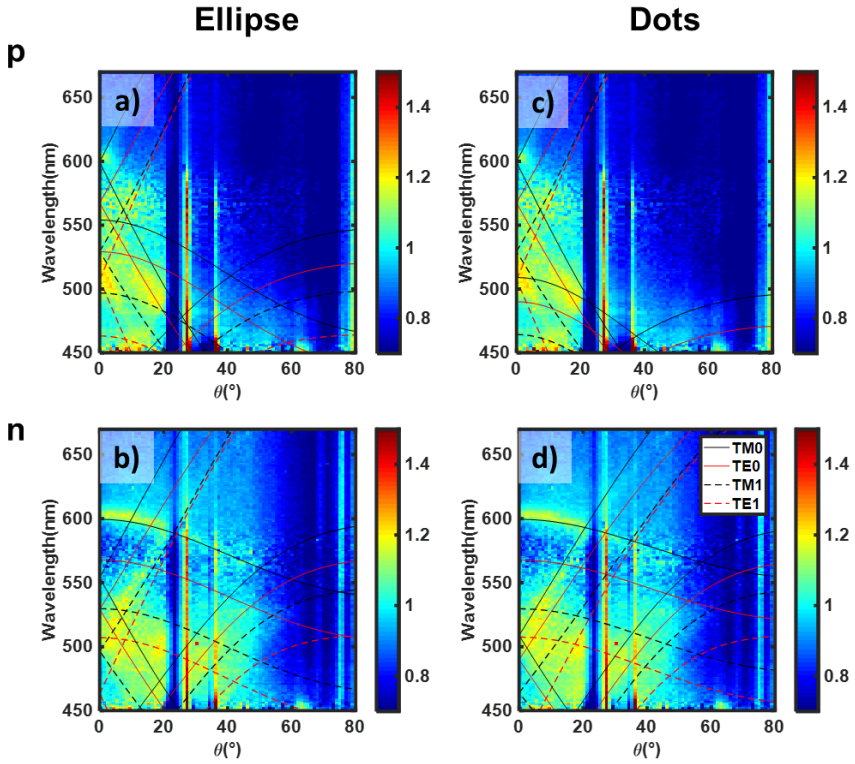

Figure 4-29. Angle-resolved PL spectra acquired by tilting along the p- and n-polarization axis. The dispersion of the quasiguided modes along the p- and n-polarization is depicted in (a) and (b) for the NE grating as well as (c) and (d) for the ND grating.

From the results of the angle-resolved PL investigations, the merits of the superimposed grating concept for broadband enhancement is clear. Through the investigated superimposed grating, an enhancement from 500 nm up to 600 nm was achieved. Peak enhancement was relatively low with a factor of 1.3 at 569 nm, but as stated in the experimental section, this can be attributed to the low intensity of the UV light source and, hence, the poor fluorescence intensity in general. Also, determination of the peak enhancement value was not the scope of this experiment since the enhancement in EL is important.

Electroluminescence

After successful verification of the increased amount of CLRs and the concomitant broad fluorescence enhancement, it is time to focus on the enhancement possible under electrical excitation. Alongside OLED characterization (Figure 4-31) also angle-resolved EL measurements (Figure 4-30) were performed. Key performance metrics regarding the reference and the superimposed grating device are given in Table 4-1.

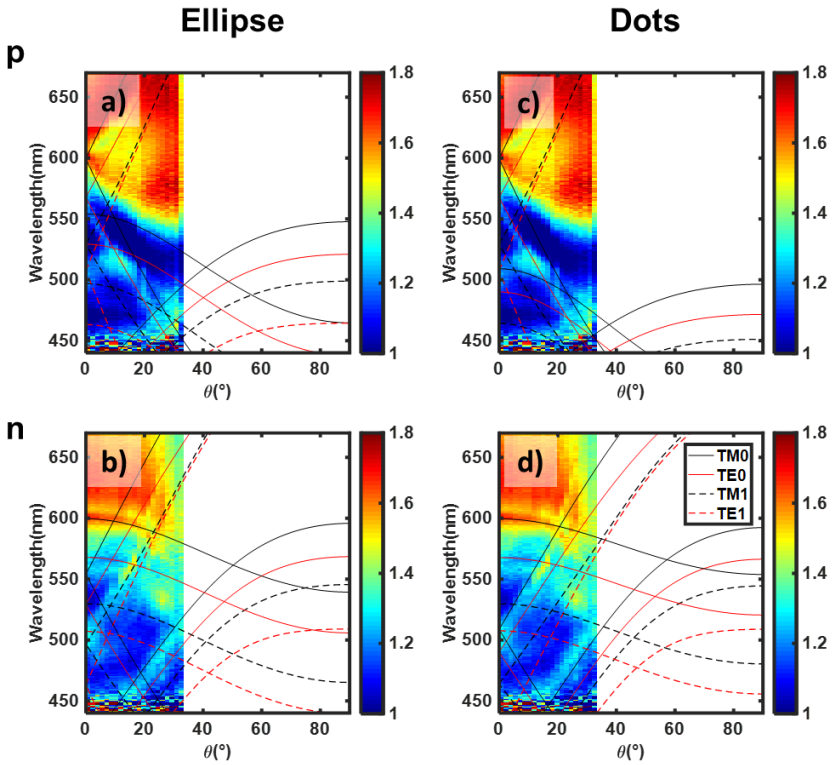

Figure 4-30. Angle-resolved EL spectra acquired by tilting along the p- and n-polarization axis. The dispersion of the CLRs along the p- and n-polarization is depicted in (a) and (b) for the NE grating as well as (c) and (d) for the ND grating.

Consistent with the angle-resolved PL measurements clear enhancements following the calculated dispersions of the several CLRs are visible. While a detailed assignment of the enhancement is not attempted, the origin of the pronounced enhancement starting at 590 nm

at 0° (Figure 4-30) still needs to be discussed especially since this feature was not present in the PL investigations. Noteworthy is the fact that this feature does exhibit dispersion at shorter wavelengths and is clearly affected by the CLRs traveling in the (+1,0) direction. For this reason this enhancement is ascribed to the LSPR of the NEs which in p-polarization is enhanced by the TM_0 CLR along the (0,±1) direction of the NE grating. Later, when the enhancement in the direction perpendicular to the OLED will be discussed, the ramifications of this strong enhancement with respect to the color quality of the OLED are also going to be shown.

First, the impact of the broadband fluorescence enhancement on the performance of the OLED was assessed. The results of the measurements are depicted in Figure 4-31 and the key parameters for quantifying the performance of the OLEDs are summarized in Table 4-1. Starting the discussion with the current density characteristics (Figure 4-31.a), a clear drop in current density compared to the unstructured reference device can be observed at similar applied bias voltages. At the onset of the emission, the current density is only 45% of the reference. With increasing bias voltages, the gap between the reference and the grating device continues to widen and reaches a low of only 31% at a bias of 16.8 V. This severe discrepancy is easily explained by the coverage of ITO with Al NPs which at the chosen lattice constants equates in a surface coverage of close to 18% by Al. Seemingly, this value is high enough to significantly obstruct the injection of holes into the device. Remarkably, at a total coverage of 12.6% no deviation in the carrier injection behavior (see chapter 4.5) was found while at 18% less than half the current density was observable. Clearly, follow up investigations are warranted by this behavior.

Moving on to the luminance (Figure 4-31.b), a peak value of 4420 cd m^{-2} at 18.2 V was recorded while the device with the superimposed grating was only able to achieve 4107 cd m^{-2} at an even higher bias of 20.3 V. Without a doubt, a clear consequence of a deteriorated injection of holes. Even though peak luminance is reduced by the superimposed grating, the luminous efficiency (Figure 4-31.c) witnessed an increase by 22.8 % with a value of 2.6 versus 2.1 cd A^{-1} for the reference at 1000 cd m^{-2}. As was already demonstrated in the angle-resolved EL spectra, the introduction of the superimposed grating led to a shift of the peak wavelength to 621 nm from 471 for the reference (Figure 4-31.d). Furthermore, the superimposed grating equalized the magnitude of the characteristic twin peak formation at 471 and 497 nm. A better picture at the enhancement in forward direction is provided by the EL enhancement for an observation angle of 0° (Figure 4-32.a).

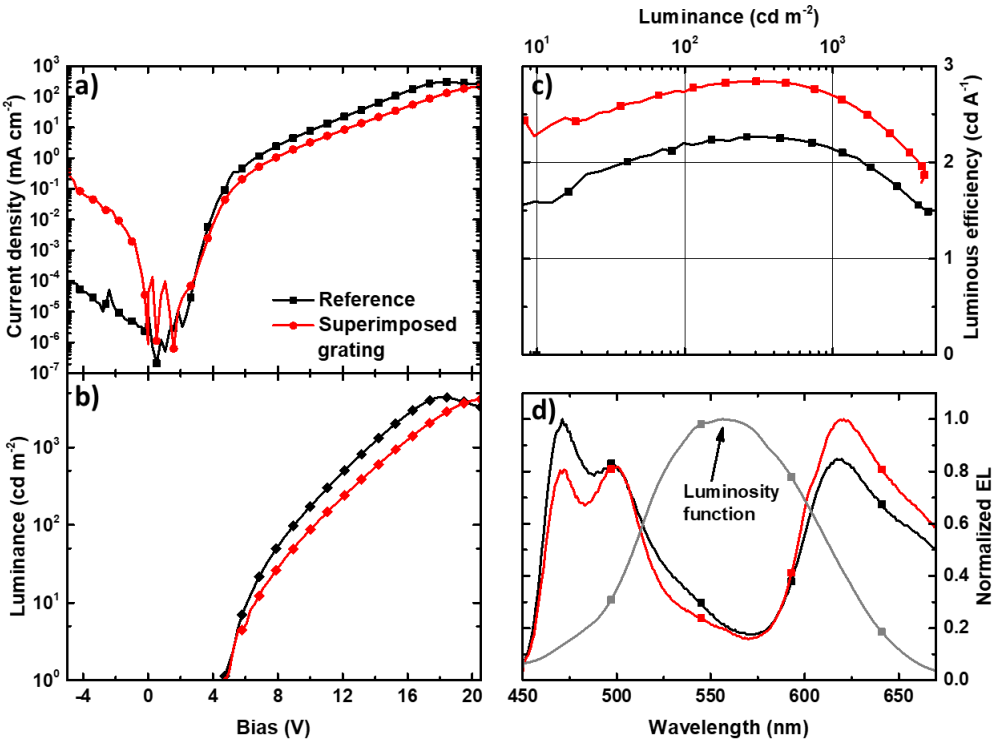

Figure 4-31. OLED characteristics for a reference and superimposed grating device. (a) Current density and (b) luminance versus applied bias voltage. (c) Luminous efficiency versus luminescence. (d) Normalized EL emission spectra. (grey line) Luminosity curve of the human eye.

In detail, enhancements at 471, 501, 561, 601 as well as a broad enhancement centered at 631 nm are noticeable. All enhancements except for the broad one at 631 nm are the direct consequence of CLRs while the last one has been ascribed to originate from the LSPR of the NEs. While the situation regarding the CLRs has already been elaborated in great detail, the occurrence of the strong LSPR induced enhancement under EL needs more elucidation. For this, it is required to keep in mind that in a WOLED host:guest system with three dopants, the generation of white light has to rely on the fact that at some point the red emitter, which has the lowest bandgap in the system, will saturate because of the high lifetime of phosphorescent emitters. Only then will excitons migrate to the other emitters, green and blue, and recombine there. Even though the near field enhancement provided by the LSPR of the NE is not as high within the EML as the one provided by the CLR, its comparably broad nature seems to be enough to decrease the lifetime a bit and thus shift the point of saturation towards a higher voltage. As implied earlier, these modifications have a profound impact on the emission color (Figure 4-32.b) which shifts from a value of (0.36,0.35) for the reference to (0.40,0.35) for the superimposed grating device, which is further away from the white point of (0.33, 0.33).

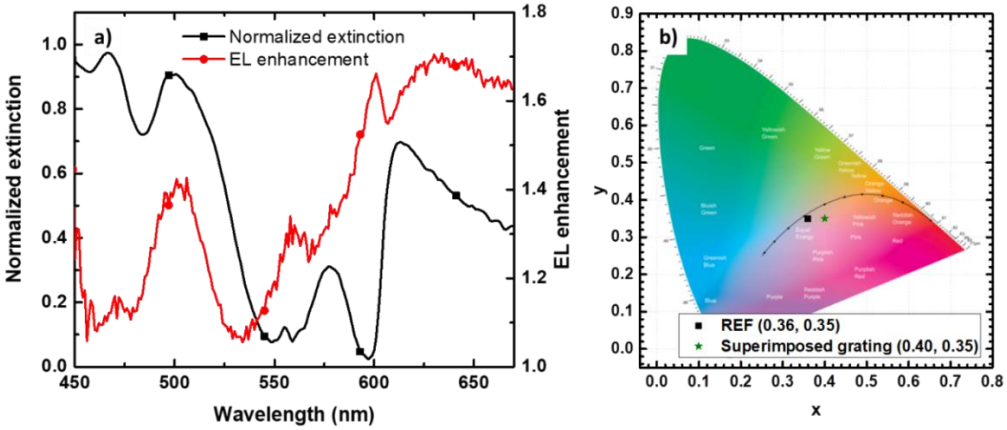

Figure 4-32. (a) Enhancement of the EL versus wavelength for the superimposed grating with respect to a reference device. (b) CIE1931 chromaticity chart for the reference and the double grating device.

Table 4-1. Key performance indicators for the operation of a reference- and a double grating OLED

Device	Onset[a] [V]	Peak luminance [cd m^{-2}]	Luminous efficiency [cd A^{-1}]		Enhancement [%]	Peak wavelength [nm]	CIE1931[b] (x,y)
			10^2 cd m^{-2}	10^3 cd m^{-2}			
Reference	4.7	4420 (18.2 V)	2.2	2.1	-	471	(0.36, 0.35)
Superimposed grating	4.7	4107 (20.3 V)	2.7	2.6	22.8	621	(0.40, 0.35)

[a] at 1 cd m^{-2}; [b] at a current density of 5 mA cm^{-2}

4.6.2 Rectangular lattice grating structure

In chapter 4.6.1, the superposition of two-point gratings exploited to obtain more CLRs for a broadband enhancement of light. While first results are already promising, the observed decreased charge carrier injection as well as the pronounced red shift coupled with the difficulty of fabricating such dense gratings on a larger scale make it worthwhile to explore a simpler solution. For this reason, a different avenue was explored with a focus on using just one-point grating. Since an enhancement in the red is not required and even detrimental (as seen in chapter 4.6.1) the focus for this new grating solely remained on the blue and green part of the spectrum by using a ND grating. Instead of a square-lattice configuration, a rectangular-lattice configuration (Figure 4-33) was picked which enabled a simultaneous enhancement in the blue and the green part of the spectrum. The NDs had a diameter of 90 nm and lattice constant of 294 and 276 nm in the p- and n-polarizations, respectively.

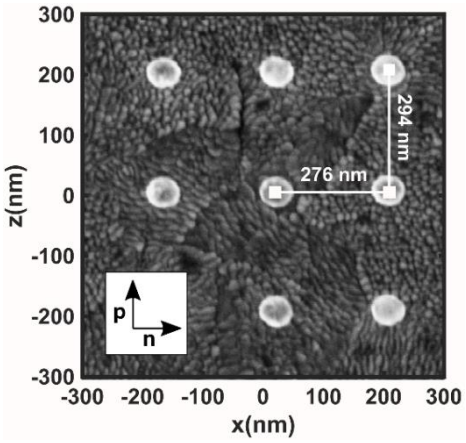

Figure 4-33. SEM image of an ND grating in a rectangular lattice configuration on top of ITO

As before, the position of the CLRs was mapped by comparing the measured angular dispersion of the extinction features with the analytically calculated ones. Then, a probe for a PL and EL enhancement along the dispersion of the CLRs was again performed.

Extinction

Starting with the p-polarization (Figure 4-34.a), the TE_0 is found to couple with the (+1,0), (-1,0) and (0,±1) modes of the grating. Another clear coupling can be identified for the TM_0 guided mode with the (0,±1) grating order. Unfortunately, the poor signal-to-noise ratio above an angle of 50° made it impossible to identify whether the (+1,±1) order also couples to the TM_0 or TE_0 mode.

In n-polarization (Figure 4-34.b), the extinction band is again found to follow the (+1,0), (-1,0) and (0,±1) direction of the grating interacting with the TE_0 mode. As with p-polarization the TM_0 also forms a CLR with the (0,±1) order. Contrary to the p-polarization, the (+1,±1) now couples to the TE_0 mode within the resolved angular range.

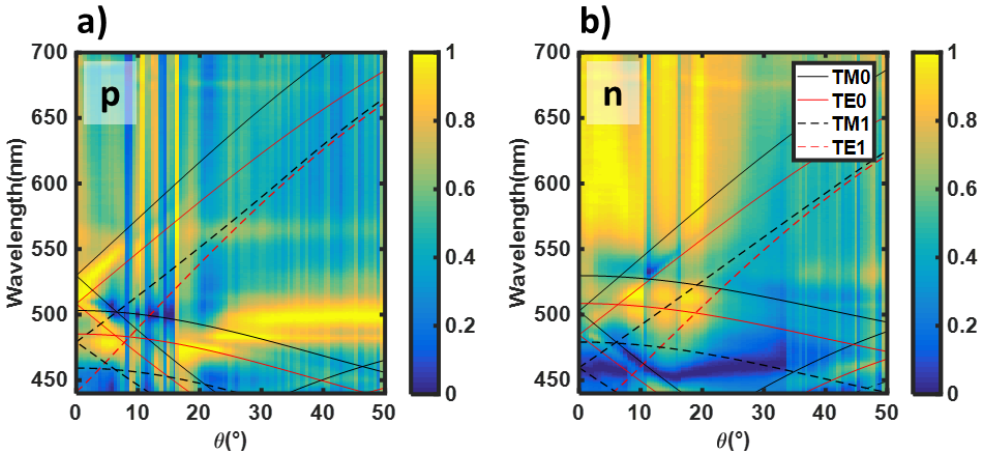

Figure 4-34. Angle-resolved extinction spectra acquired by tilting along the (a) p- and (b) n-polarization axis. The analytically derived dispersion of the quasiguided modes are overlaid.

Photoluminescence

Angle-resolved PL measurements were again performed by tilting the detector along the p- and n-polarization (Figure 4-35.a and b respectively). Along the p- as well as the n-polarization the enhancement can be seen to mostly follow the dispersion of the TE_0 mode coupling to the (+1,0), (-1,0) as well as the (0,±1) grating order in n- and p-polarization starting to disperse at 485 and 508 nm for a detection angle of 0°. Furthermore, a trace of the TM_0 traveling along the (0,±1) direction at 503 nm is visible for p-polarization. Also of note is a minor enhancement at the position of the LSPR in the range between 550 and 600 nm.

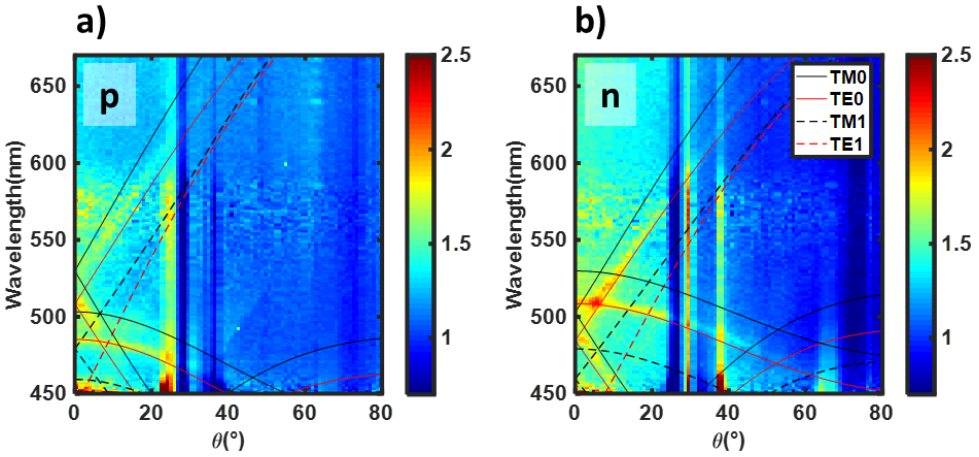

Figure 4-35. Angle-resolved PL enhancement acquired by tilting along the (a) p- and (b) n-polarization axis. The analytically derived dispersion of the CLRs are overlaid.

Electroluminescence

Switching to electrical excitation of the OLED stack and performing angle-resolved spectroscopy yields a similar picture as provided by the angle-resolved PL enhancement measurements (Figure 4-36). Enhancement again follows the TM_0 and TE_0 CLRs.

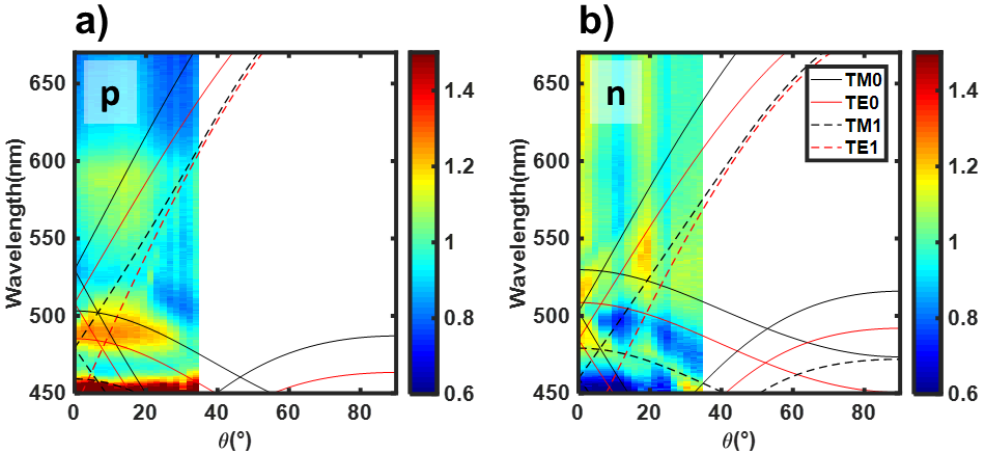

Figure 4-36. Angle-resolved EL enhancement spectra acquired by tilting along the (a) p- and (b) n-polarization axis. The analytically derived dispersion of the CLRs are overlaid.

For an observation angle of 0°, an approximately 1.2-fold peak enhancement at 488 nm was detected along the (0,±1) direction of the TE_0 CLR. Obviously, this enhancement will reshape the emission spectrum of the device which can be seen in Figure 4-37.a. Here, the pronounced enhancement around 485 nm causes the vibronic structure of FIrpic to almost completely vanish. In the green part of the spectrum centered at 527 nm an attenuation of the EL is visible. Importantly, the strong LSPR induced enhancement observed for the superimposed grating (see chapter 4.6.1) is gone.

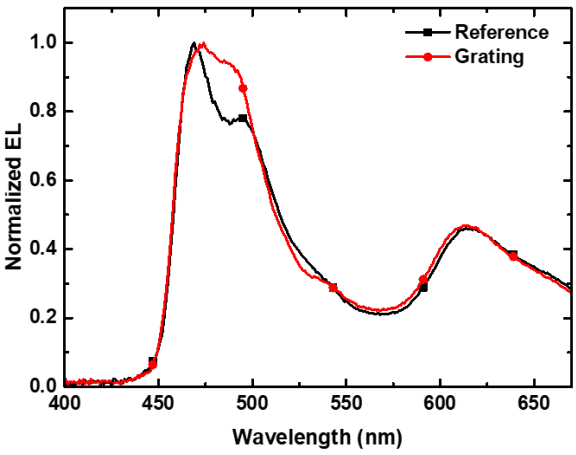

Figure 4-37. Normalized EL of a reference and a single-grating device.

A better picture is provided by the EL enhancement plot (Figure 4-38). Here the effect of the TE_0 mode is clear with an enhancement of 24% at 485 nm. The enhancement at the position of the LSPR is minor with a peak enhancement of 9% at 590 nm. Compared to the reference device (0.31, 0.34), these changes improve the white color quality a bit to (0.31, 0.33) which is closer to the ideal white point of (0.33, 0.33) as evidenced by Figure 4-38.b.

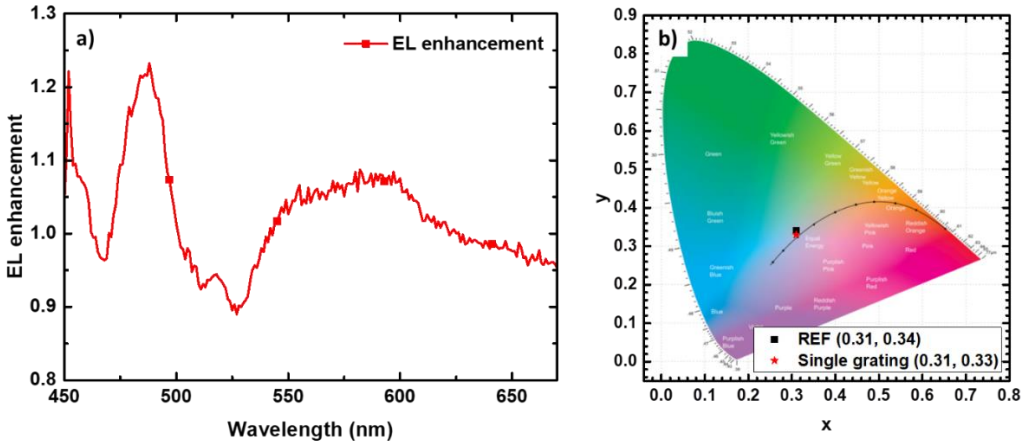

Figure 4-38. (a) EL enhancement by a single-grating device. (b) CIE1931 chromaticity chart for the reference and the rectangular-lattice grating.

4.6.3 Conclusion

In this subchapter, the suitability of Al NP grating for the efficiency enhancement of WOLEDs was investigated by means of a broadband enhancement from the blue all the way to the red part of the visible spectrum. In a first step, this enhancement was attempted by a superimposed grating consisting of two-point gratings based on NDs and NEs with a rectangular unit cell. Through angle-resolved extinction spectroscopy it was shown that the formation of extinction features originating from a coupling of the guided modes with the different grating orders as well as the angular dispersion, was in excellent agreement with a superposition of the results obtained for two single-point gratings. At the position of these extinction features, fluorescence enhancement was detected which also followed the dispersion of the extinction features. Due to the fact that this enhancement was obtained at 502, 560 and 601 nm the desired broadband enhancement was achieved. Nonetheless, the increased density of Al NPs on top of the surface led to a significant impairment of charge carrier injection which was noticeable as a reduced current and, consequently, a reduced peak luminance. Even so, the device with the superimposed grating was able to demonstrate a higher peak efficiency of almost 23% as compared to the reference which is impressive considering that this geometry was only moderately optimized with respect to the resonance positions. However, the inclusion of the superimposed grating also induced an unwanted red shift of the emission color which was linked to the LSPR of the NEs.

Given the fact that the red shift was induced by the grating, a rectangular grating structure was investigated which was only improving the emission in the blue and green spectral range. Extinction spectroscopy revealed a predominant coupling of the TE_0 with the different lattice orders. This led to an enhancement in PL at 485 and 507 nm, while the LSPR of the NDs induced a negligibly small enhancement centered around 575 nm. Under electrical operation, the enhancement at 485 nm as well as at the resonance of the LSPR was retained while an attenuation of light was observed at the former enhancement position of 507 nm. While OLED data was not recorded, the target to retain the CIE chromaticity coordinates by avoiding a strong red enhancement was accomplished.

Nonetheless, the obtained results show that Al NP arrays are not only suitable for monochromatic OLEDs but also polychromic WOLEDs. With a better optimized WOLED stack and further optimizations of the grating parameters even higher efficiency gains should be attainable.

4.7 Overall conclusion

This chapter dealt with a novel route to increase the amount of light that can outcouple from an OLED while at the same time also enhancing the total amount of light generated. In detail, arrays of aluminum NPs were fabricated on top of ITO and embedded into the HTL of the OLED via a solution-process. OLEDs equipped with such an array were found to be free from electrical shunts which proofs the effectiveness of the embedding process. As a first target, the efficiency of a monochromatic organic blue light emitting diode was to be improved by means of an Al ND array. Step by step, the dependency of the possible enhancement on typical parameters, such as the size of the used NDs, the lattice constant and the thickness of the EML was uncovered. It was found that through a proper choice of the lattice constant, the position of the CLRs was able to shift across a wide spectral range which in turn allowed for a tuning of the emission color of an OLED between CIE1931 coordinates of (0.17, 0.35) and (0.18, 0.26).

A proper choice of the size of the individual Al NDs was also found to be important. Here, a tradeoff was found at 90 nm since this value ensured a good balance between coupling efficiency of the array with the guided modes and incurred damping losses at larger diameters. An easily underappreciated factor governing the coupling efficiency is the thickness of the EML. Here, an improper choice results in an attenuation or in the worst case even a full disappearance of the lattice resonances. Contrary to some reports in literature, an appreciable field enhancement was possible even at an EML thickness of just 100 nm. With these individual factors optimized, it was possible to enhance the current efficiency of an OLED by 35% with only a minor green shift of the emission. Since WOLEDs feature a broadband emission of light, an Al ND array in square-lattice configuration would be insufficient to realize any noteworthy performance gains. For this reason, this concept was further extended by the design of gratings which exhibited multiple resonances. As a first approach, a grating which was a superposition of a NE and ND grating both with a rectangular unit cell was fabricated. As expected, this grating exhibited CLRs across the relevant spectrum and a respectable efficiency gain of 23% was realized. Nonetheless, the fabricated grating was dense with respect to the coverage of ITO with Al NPs. Also, the lattice-induced enhancement in the red resulted in an unwanted red-shift of the emission color. As a consequence, an alternative grating was designed which solely consisted of Al NDs aligned in a rectangular configuration. By design, this grating only enhanced the blue- and green part of the relevant spectrum which was evident in PL as well as EL measurements. Furthermore, no shift in emission color was detectable.

While many aspects regarding the formation and the impact of CLRs were studied, it is clear that this work represents just an initial foray. Especially, the placement of the grating could be further optimized by moving the grating to the top cathode or embedding the grating in ITO.

5

Summary & Conclusion

The presented schemes provide an important stepping stone towards the realization of large area and low-cost organic light emitting diode luminaires. On the one hand, the realization of highly performant and low-cost erosion resistant hole injection/transport layers was demonstrated while on the other hand an adaptable approach for enhancing the amount of generated and outcoupled light was presented.

In recent years OLEDs made huge strides and started to displace liquid crystal displays as the dominant display technology. At the same time, OLED technology is also becoming a serious contender to established lighting technologies. Still, to achieve the desired competitiveness efficiencies as well as lifetime of this technology need to increase without compromising the cost savings enabled by comparably cheap solution-processing technologies. While addressing the lifetime was beyond the scope of this work, two important aspects that still hold OLEDs back in the lighting sector were addressed: efficient injection of holes from a combined HIL/HTL obtained via a cheap and environmentally friendly solution-process and enhanced generation and outcoupling of light from the OLED.

The first goal was enabled by the development of a new solution-processing strategy for CuSCN, a p-type pseudo halide. Here the first development achieved in this work was the successful replacement of DES, a solvent which is expensive and harmful to carbon filters. This was possible by the identification of a complexation reaction between CuSCN and the abundant as well as cheap solvent ammonium hydroxide. Layers fabricated from CuSCN dissolved in NH4 exhibited increased surface energies and lower effective surface roughness values which is beneficial for good wettability and as a result the formation of smooth layers with sharp interfaces. However, the complexation route led to additional impurities, a reduced crystallinity and in turn to significantly lowered hole mobilities when compared to layers processed from DES. Nonetheless, CuSCN layers obtained from NH4 solution still turned out to be superior to layers obtained from DES solutions in a low brightness high efficiency solution-processed green-emitting PhOLED stack while the reduced hole mobility started to show in a high brightness stack. The major development in this work rests on the successful prevention of the formation of secondary oxides through the addition of formic acid, a volatile reducing carboxylic acid. The addition of FA to CuSCN dissolved in NH4 was sufficient to obtain layers almost identical to the ones processed from DES in photoelectric spectra. At the same time, a layer of ammonium formate, a byproduct from the acid-base reaction formed on top of the CuSCN layer. Remarkably, this double layer structure exhibited high hole-mobilities and reduced trap states. Coupled with increased surface energies and low effective surface roughnesses this CuSCN/ammonium formate layer was able to significantly outperform all reference layers in the low-brightness high-efficiency green-emitting PhOLED stack. At the same time this layer proofed competitive to PEDOT:PSS at high luminance values and clearly superior at lower luminance when investigated in conjunction with the high brightness stack. This is a remarkable achievement especially when the high intrinsic conductivities of PEDOT:PSS are considered.

To enable the second target, the suitability of a field of research that experienced renewed research focus, collective resonances from plasmonic NP arrays, was investigated. Specifically, keeping in line with preserving the reduced fabrication cost, aluminum, one of the most abundant elements in earth's crust with interesting plasmonic properties, was chosen. The gratings were embedded in a layer of CuSCN which provided sufficient planarization as confirmed by AFM. Since to this date, CLRs haven't been investigated within a weak resonator configuration, the behavior of the CLRs within this environment was investigated through optical modeling coupled with extinction spectroscopy. This revealed that CLRs are present even in this weak cavity configuration. On top of that, the introduced grating weakens the formation of the typical nodes of destructive interference within the emissive layer. Through step by step optimization of important parameters such as the lattice constant, the disc size and the EML thickness an increase in device efficiency by 35% was realized. To apply this concept for WOLEDs, superimposed gratings were investigated where two individual gratings were combined into one. As expected, the superimposed gratings formed CLRs distributed across the relevant spectrum and resulted in an increased efficiency of 23%. Suffering from reduced luminance and deteriorated color coordinates, a simpler approach involving only one grating was presented. Via this approach, the envisaged color coordinates could be achieved.

Even though the presented approaches already provide respectable increases in device efficiency it is expected that the presented work merely provides the basis for further gains in device efficiency.

A

Appendix – Additional data for chapter 3

A.1 CuSCN AFM topography images

Figure A-1 depicts the AFM topography images of the investigated HIL/HTLs. The nanocrystalline nature observed in the phase images in Figure 3-3 is replicated in the topography images as well. For the investigated DES, NH4 and FA topography images a RMS surface roughness of 3.0, 0.7 and 1 nm can be calculated. The low surface roughness of the NH4 (Figure A-1.b) allows to still see traces of the rough ITO surface, even though the surface is effectively planarized.

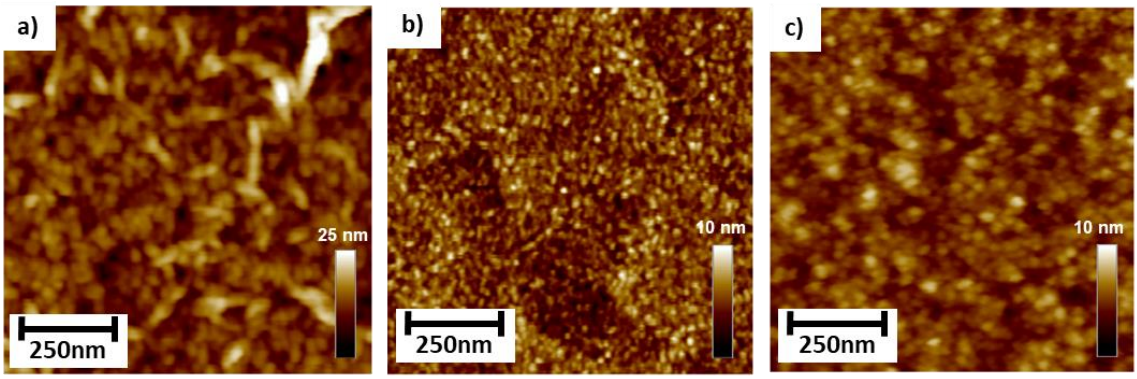

Figure A-1. AFM topography images of (a) DES, (b) NH4 and (c) FA

Overall, NH4 and FA provide superior planarization capabilities when compared to the DES layer. It has to be stated however, that even in the case of DES, the planarization capabilities are sufficient for usage within OLEDs.[164]

A.2 XPS core level spectra

In this subchapter, the results of the XPS peak fits for DES, NH4 and FA are presented. For all spectra, a survey scan spanning the energy range between 1400 and 0 eV was conducted. Necessitated by the contributions to the spectrum, detailed core level scans of the $Cu2p_{3/2}$, O1s, N1s, C1s as well as S2p levels were performed. Starting the discussion with DES (see Figure A-2), the main feature in the $Cu2p_{3/2}$ spectrum is found at 932.4 eV which is ascribed to the Cu(I) oxidation state of copper.[119,325] Expectedly, only superficial oxidation is present which is ascribed to the presence of O-C=O surface contaminants. The N1s high-resolution spectrum reveals a main feature at 398.8 eV which was assigned to the C≡N bond in the SCN^- anion, whereas the feature at 399.8 was ascribed to C=N bonds.[144] The C1s peaks were found at 284.9, 285.4, 286.6 and 291.1 eV which were attributed to adventitious carbon, C=N and C≡N bonds as well as to the formation of a π-π* satellite.[144] As expected, only one doublet at 163.0 eV was found for the S2p level which is assignable to the S-C bond in the SCN^- anion.

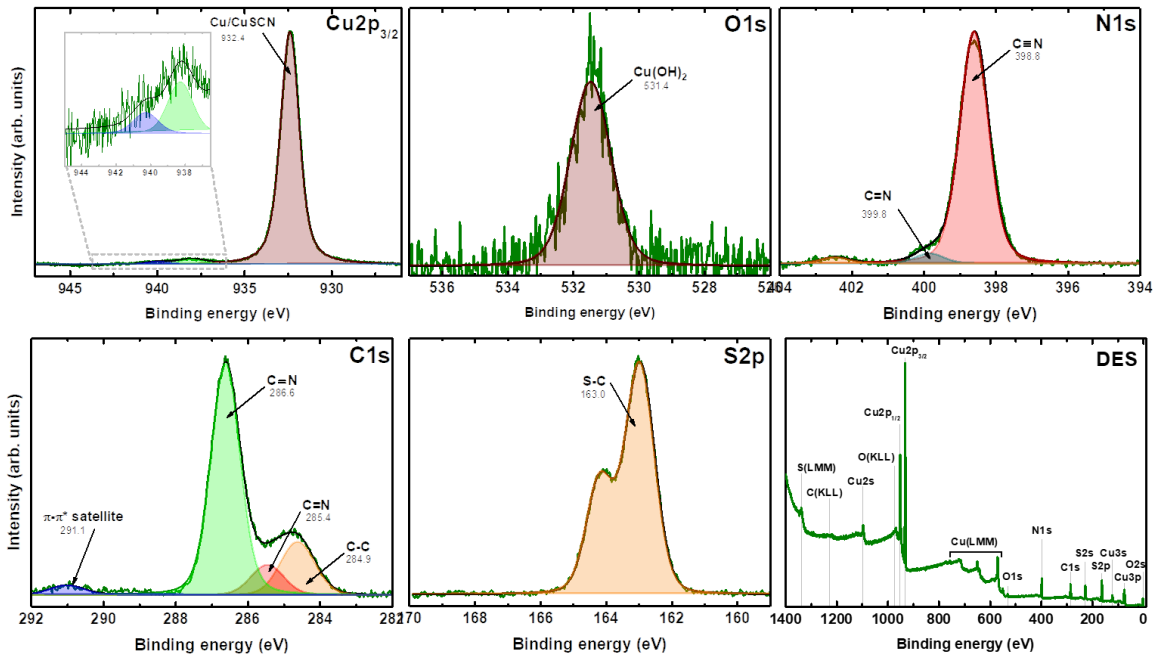

Figure A-2. High resolution of core line spectra of $Cu2p_{3/2}$, O1s, N1s, C1s, S2p as well as a survey spectrum of DES

As already discussed in chapter 3.3, a markedly changed chemical composition is found in the case of NH4 films (see Figure A-3). In detail, $Cu2p_{3/2}$ peaks at 932.4, 933.6 and 934.7 eV are visible which are associated with Cu(I), CuO as well as the $Cu(OH)_2$ copper oxides and hydroxides respectively.[169,325,326] Additionally, a shakeup structure, characteristic to the Cu(II) oxidation state between 940 and 945 eV can be found. These peaks have been associated to the Cu(I), CuO as well as the $Cu(OH)_2$ copper oxides and hydroxides respectively.[169,325,326] The O1s spectrum exhibits peaks at 530.0, 531.4 and 532.1 eV. The first and the last one were associated with CuO and SO_4^{2-} respectively.[169,170,326] The peak at 531.4 eV on the other hand is often shared between different types of oxides and carbonate compounds and in this case attributed to a cumulative feature consisting of contributions of $Cu(OH)_2$ as well as adventitious carbon. The N1s part of the spectrum is characterized by three peaks at 398.5, 398.8 and 399.8 eV which were ascribed to C-N, C=N and C≡N bonds, respectively.[144] The C1s peaks at 284.9, 285.4, 286.6 and 287.7 eV were ascribed to adventitious carbon, C=N, C≡N, C-N bonds. The origin of the peak at 290 eV, however, was not identifiable. Lastly, the S1s spectrum features two doublets at 163.0 and 168.6 eV which are ascribed to the S-C bond of the SCN^- anion as well as SO_4^{2-}.

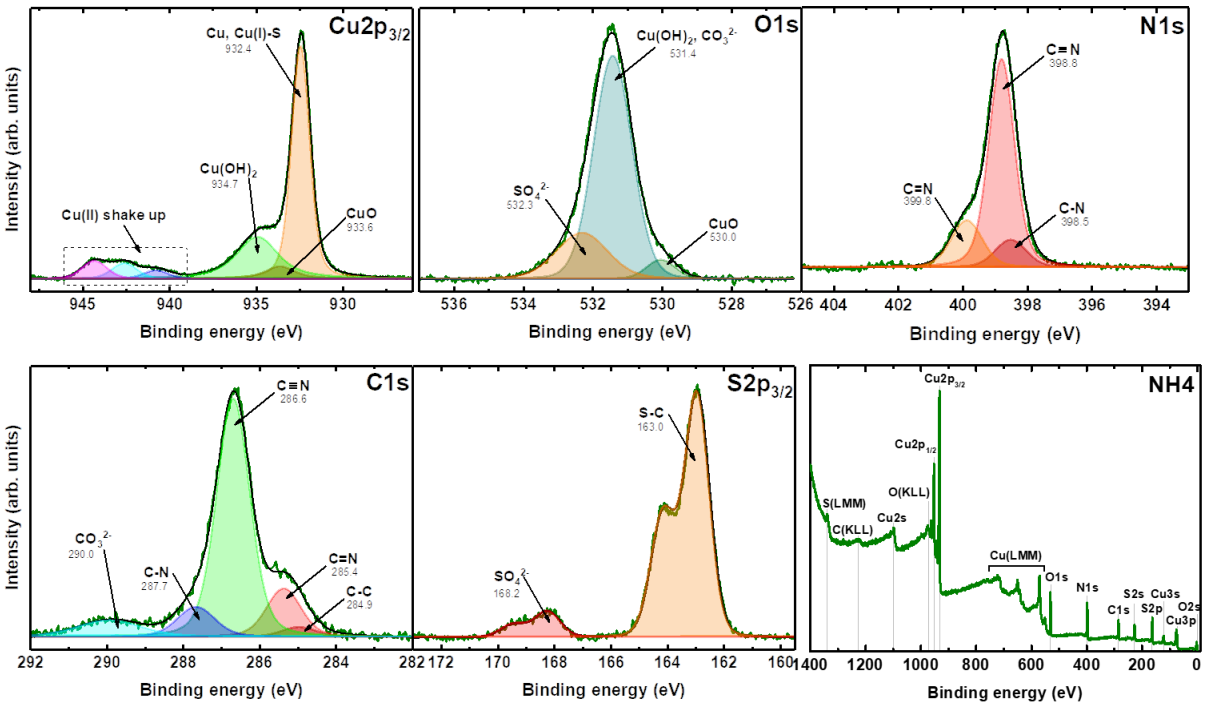

Figure A-3. High resolution of core line spectra of $Cu2p_{3/2}$, O1s, N1s, C1s, S2p as well as a survey spectrum of NH4

For FA (see Figure A-4), a clear Cu(I)/Cu(0) signal is found in the $Cu2p_{3/2}$ spectrum. The O1s spectrum reveals two contributions which are found to originate from SO_4^{2-} (532.1 eV)[170] and O-C=O (531.4 eV). The first one is the result from a dissociation of the SCN^- ion which is reinforced by a small feature centered at 168.8 eV.[170] Resulting from the aforementioned dissociation of the SCN^- ion is the presence of a C=N double bond located at 399.8 eV while the triple-bond between C and N at 398.8 eV is the expected signature of N in the SCN^- ion. For C1s, the adventitious carbon was found at 284.9 eV whereas the signature of the C=N and the triple bond between C and N was determined at 285.4 and 286.6 eV. Noteworthy are the two minor features at 289.2 and 291.0 eV. While the origin of the last one is not known, the former is ascribed to C in the O-C=O bond. Coming to S2p, besides the already mentioned $SO4^{2-}$ feature, the main contribution originates from the S-C bond in the SCN- ion at 163.0 eV.

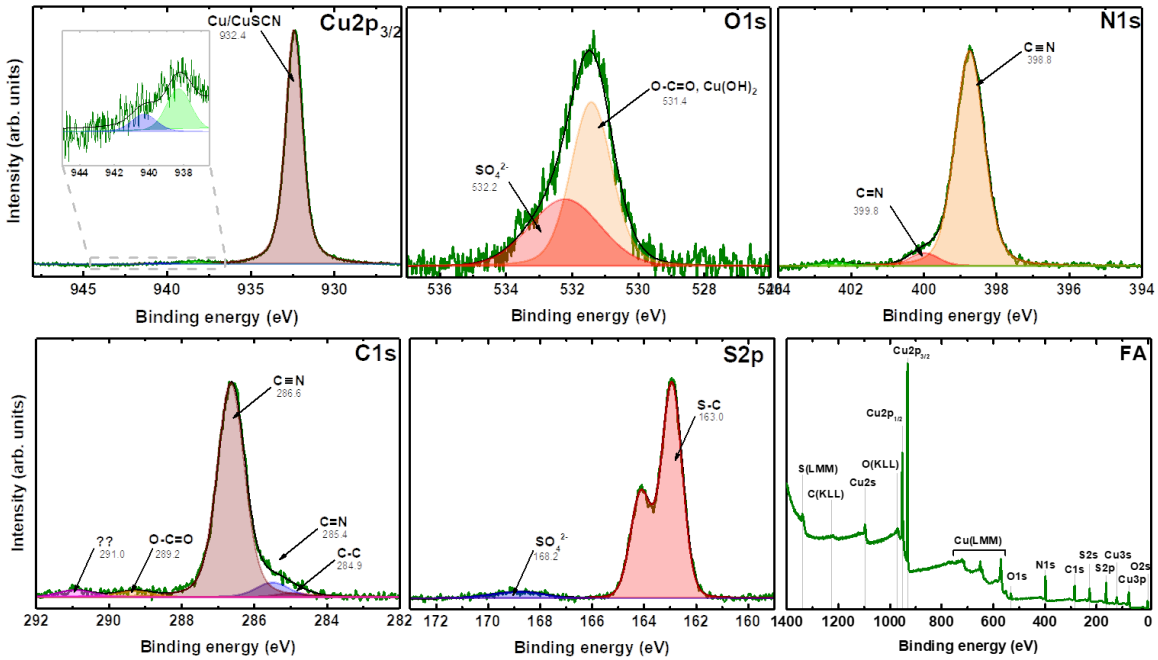

Figure A-4. High resolution of core line spectra of Cu2p3/2, O1s, N1s, C1s, S2p as well as a survey spectrum of FA.

A.3 DES Tauc plot

In chapter 3.4, the Tauc plots for obtaining the direct and indirect bandgaps of the investigated NH4 and FA HIL/HTLs were presented. Here, Figure A-5 depicts the Tauc plot for DES which shows a direct band gap of 3.83 eV and an indirect one at 3.34 eV. Further details can be found in chapter 3.4.

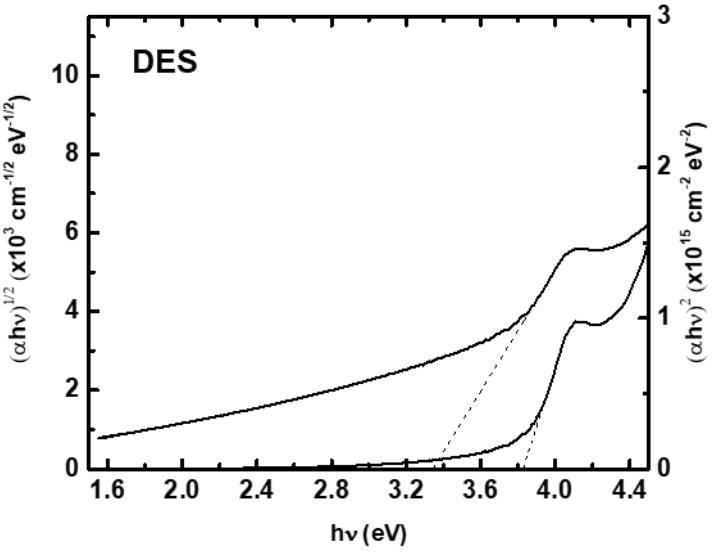

Figure A-5. Tauc plot of a DES film

A.4 VASE parameters

In this subchapter the parameters used for optical modelling of n and k are provided in Table A-1, Table A-2 and Table A-3.

Table A-1. Parameters for the Lorentzian oscillators (CuSCN) and the Cauchy layer (ammonium formate) used to fit the imaginary part of the dielectric function of the two-layer FA system

Layer	Amplitude	Broadening	Energy center
FA(CuSCN)	1.3065	0.001	4.079
Thickness: 33.93 nm	0.35942	0.099548	3.9306
E_∞: 3.8057 eV	-	-	-
$FA(NH_4HCO_2)$	A_n	B_n	C_n
Thickness: 33.4 nm	1.1599	0.12887	-0.0088

Table A-2. Parameters of the Lorentzian oscillators used to fit the imaginary part of the dielectric function of DES

Layer	Amplitude	Broadening	Energy center
DES	1.3934	0.0048649	4.1559
Thickness: 46.1 nm	1.4583	0.01	4.0989
E_∞: 3.2401 eV	1.2393	0.36296	3.9730

Table A-3. Parameters of the Lorentzian oscillators used to fit the imaginary part of the dielectric function of NH4

Layer	Amplitude	Broadening	Energy center
NH4	1.3303	0.0051989	4.1564
Thickness: 45.7 nm	1.2278	0.001	4.1021
E_∞: 3.5369 eV	1.4185	0.47314	3.9257

6

References

1. Acuity Brands. Acuity Trilia and Revel OLED lighting. *cnet* Available at: https://www.cnet.com/pictures/acuity-brands-new-oled-lighting-pictures/5/. (Accessed: 6th October 2017)

2. LG Flexible OLED. Available at: http://www.lgoledlight.com/portfolio_page/400x50mm/. (Accessed: 6th October 2017)

3. Ho, S., Liu, S., Chen, Y. & So, F. Review of recent progress in multilayer solution-processed organic light-emitting diodes. *J. Photonics Energy* **5,** 57611 (2015).

4. Williams, D. F. & Schadt, M. A simple organic electroluminescent diode. *Proc. IEEE* **58,** 476–476 (1970).

5. Tang, C. W. & VanSlyke, S. A. Organic electroluminescent diodes. *Appl. Phys. Lett.* **51,** 913–915 (1987).

6. Chiang, C. K. *et al.* Synthesis of highly conducting films of derivatives of polyacetylene, (CH)x. *J. Am. Chem. Soc.* **100,** 1013–1015 (1978).

7. Chiang, C. K. *et al.* Electrical Conductivity in Doped Polyacetylene. *Phys. Rev. Lett.* **39,** 1098–1101 (1977).

8. Shirakawa, H., Louis, E. J., MacDiarmid, A. G., Chiang, C. K. & Heeger, A. J. Synthesis of electrically conducting organic polymers: halogen derivatives of polyacetylene, (CH) x. *J. Chem. Soc. Chem. Commun.* 578 (1977). doi:10.1039/c39770000578

9. Burroughes, J. H. *et al.* Light-emitting diodes based on conjugated polymers. *Nature* **347,** 539–541 (1990).

10. Heitler, W. & London, F. Wechselwirkung neutraler Atome und homöopolare Bindung nach der Quantenmechanik. *Zeitschrift für Phys.* **44,** 455–472 (1927).

11. Heeger, A. J. Semiconducting and Metallic Polymers: The Fourth Generation of Polymeric Materials †. *J. Phys. Chem. B* **105,** 8475–8491 (2001).

12. Vladsinger. The various representations of benzene. *Wikimedia commons* Available at: https://commons.wikimedia.org/wiki/File:Benzene_Representations.svg. (Accessed: 14th November 2017)

13. Cornil, J., Beljonne, D., Calbert, J.-P. & Brédas, J.-L. Interchain Interactions in Organic π-Conjugated Materials: Impact on Electronic Structure, Optical Response, and Charge Transport. *Adv. Mater.* **13,** 1053–1067 (2001).

14. Roth, S. & David, C. *One-Dimensional Metals: Conjugated Polymers, Organic Crystals,*

Carbon Nanotubes and Graphene. (Wiley, 2015).

15. Baldo, M. A., O'Brien, D. F. & Forrest, S. R. Excitonic singlet-triplet ratio in a semiconducting organic thin film. *Phys. Rev. B* **60,** 14422–14428 (1999).

16. Baldo, M., Adachi, C. & Forrest, S. R. Transient analysis of organic electrophosphorescence.II. Transient analysis of triplet-triplet annihilation. *Phys. Rev. B* **62,** 10967–10977 (2000).

17. Tao, Y., Yang, C. & Qin, J. Organic host materials for phosphorescent organic light-emitting diodes. *Chem. Soc. Rev.* **40,** 2943–70 (2011).

18. Ishii, H., Sugiyama, K., Ito, E. & Seki, K. Energy Level Alignment and Interfacial Electronic Structures at Organic/Metal and Organic/Organic Interfaces. *Adv. Mater.* **11,** 605–625 (1999).

19. Hill, I. G., Milliron, D., Schwartz, J. & Kahn, A. Organic semiconductor interfaces: electronic structure and transport properties. *Appl. Surf. Sci.* **166,** 354–362 (2000).

20. Seki, K. *et al.* Electronic structure of organic/metal interfaces. *Thin Solid Films* **393,** 298–303 (2001).

21. Ishii, H., Sugiyama, K., Ito, E. & Seki, K. Energy Level Alignment and Interfacial Electronic Structures at Organic/Metal and Organic/Organic Interfaces. *Adv. Mater.* **11,** 605–625 (1999).

22. Richardson, O. W. LXVII. The distribution of the molecules of gas in a field of force, with applications to the theory of electrons. *Philos. Mag. Ser. 6* **28,** 633–647 (1914).

23. Dushman, S. Electron Emission from Metals as a Function of Temperature. *Phys. Rev.* **21,** 623–636 (1923).

24. Fowler, R. H. & Nordheim, L. Electron Emission in Intense Electric Fields. *Proc. R. Soc. A Math. Phys. Eng. Sci.* **119,** 173–181 (1928).

25. Adachi, C., Baldo, M. A., Thompson, M. E. & Forrest, S. R. Nearly 100% internal phosphorescence efficiency in an organic light-emitting device. *J. Appl. Phys.* **90,** 5048–5051 (2001).

26. Pfeiffer, M., Forrest, S. R. & Thompson, M. E. Electrophosphorescent p–i–n Organic Light-Emitting Devices for Very-High-Efficiency Flat-Panel Displays. *Adv. Mater.* **14,** 1633–1636 (2002).

27. Becker, H., Burns, S. E. & Friend, R. H. Effect of metal films on the photoluminescence and electroluminescence of conjugated polymers. *Phys. Rev. B* **56,** 1893–1905 (1997).

28. Nowy, S., Krummacher, B. C., Frischeisen, J., Reinke, N. A. & Brütting, W. Light extraction and optical loss mechanisms in organic light-emitting diodes: Influence of the emitter quantum efficiency. *J. Appl. Phys.* **104,** 123109 (2008).

29. Krummacher, B. C., Nowy, S., Frischeisen, J., Klein, M. & Brütting, W. Efficiency analysis of organic light-emitting diodes based on optical simulation. *Org. Electron.* **10,** 478–485 (2009).

30. Wasey, J. A. E., Safonov, A., Samuel, I. D. W. & Barnes, W. L. Efficiency of radiative emission from thin films of a light-emitting conjugated polymer. *Phys. Rev. B* **64,** 205201 (2001).

31. Tsutsui, T., Aminaka, E., Lin, C. P. & Kim, D.-U. Extended molecular design concept of molecular materials for electroluminescence: sublimed-dye films, molecularly doped polymers and polymers with chromophores. *Philos. Trans. R. Soc. A Math. Phys. Eng. Sci.* **355,** 801–814 (1997).

32. Brütting, W., Frischeisen, J., Schmidt, T. D., Scholz, B. J. & Mayr, C. Device efficiency of organic light-emitting diodes: Progress by improved light outcoupling. *Phys. Status Solidi* **210,** 44–65 (2013).

33. Meerheim, R., Furno, M., Hofmann, S., Lüssem, B. & Leo, K. Quantification of energy loss mechanisms in organic light-emitting diodes. *Appl. Phys. Lett.* **97,** (2010).

34. Fred, S. E. *Light-Emitting Diodes*. (2006).

35. Ruya, D. COLOR GAMUT & CORRELATED COLOR TEMPERATURE. Available at: http://lumenhub.com/color-and-cct/. (Accessed: 3rd October 2017)

36. Hugh, T. *Five Thousand Years of Glass*. (University of Pennsylvania Press, 2004).

37. Leonhardt, U. Optical metamaterials: Invisibility cup. *Nat. Photonics* **1,** 207–208 (2007).

38. Mie, G. Beiträge zur Optik trüber Medien, speziell kolloidaler Metallösungen. *Ann. Phys.* **330,** 377–445 (1908).

39. Anonymous. Proceedings of the American Physical Society. *Phys. Rev.* **69,** 674–674 (1946).

40. Weitz, D. A., Garoff, S., Gersten, J. I. & Nitzan, A. The enhancement of Raman scattering, resonance Raman scattering, and fluorescence from molecules adsorbed on a rough silver surface. *J. Chem. Phys.* **78,** 5324–5338 (1983).

41. Gersten, J. & Nitzan, A. Electromagnetic theory of enhanced Raman scattering by molecules adsorbed on rough surfaces. *J. Chem. Phys.* **73,** 3023–3037 (1980).

42. Barnes, W. L. Fluorescence near interfaces: The role of photonic mode density. *J. Mod. Opt.* **45,** 661–699 (1998).

43. Drexhage, K. H. Influence of a dielectric interface on fluorescence decay time. *J. Lumin.* **1–2,** 693–701 (1970).

44. Maier, S. *Plasmonics: Fundamentals and Applications*. (Springer US, 2007). doi:10.1007/0-387-37825-1

45. Amos, R. M. & Barnes, W. L. Modification of the spontaneous emission rate of Eu3+ ions close to a thin metal mirror. *Phys. Rev. B* **55,** 7249–7254 (1997).

46. Knobloch, H., Brunner, H., Leitner, A., Aussenegg, F. & Knoll, W. Probing the evanescent field of propagating plasmon surface polaritons by fluorescence and Raman spectroscopies. *J. Chem. Phys.* **98,** 10093–10095 (1993).

47. Pockrand, I., Brillante, A. & Möbius, D. Nonradiative decay of excited molecules near a metal surface. *Chem. Phys. Lett.* **69,** 499–504 (1980).

48. Weber, W. H. & Eagen, C. F. Energy transfer from an excited dye molecule to the surface plasmons of an adjacent metal. *Opt. Lett.* **4,** 236 (1979).

49. Aravind, P. K., Nitzan, A. & Metiu, H. The interaction between electromagnetic resonances and its role in spectroscopic studies of molecules adsorbed on colloidal particles or metal spheres. *Surf. Sci.* **110,** 189–204 (1981).

50. Bethe, H. A. Theory of Diffraction by Small Holes. *Phys. Rev.* **66,** 163–182 (1944).

51. De Abajo, F. J. G. Colloquium: Light scattering by particle and hole arrays. *Rev. Mod. Phys.* **79,** 1267–1290 (2007).

52. Koerkamp, K. J. K., Enoch, S., Segerink, F. B., van Hulst, N. F. & Kuipers, L. Strong Influence of Hole Shape on Extraordinary Transmission through Periodic Arrays of Subwavelength Holes. *Phys. Rev. Lett.* **92,** 183901 (2004).

53. Bravo-Abad, J. *et al.* How light emerges from an illuminated array of subwavelength holes. *Nat. Phys.* **2,** 120–123 (2006).

54. Garcia-Vidal, F. J., Martin-Moreno, L., Ebbesen, T. W. & Kuipers, L. Light passing through subwavelength apertures. *Rev. Mod. Phys.* **82,** 729–787 (2010).

55. García de Abajo, F. J., Gómez-Medina, R. & Sáenz, J. J. Full transmission through perfect-conductor subwavelength hole arrays. *Phys. Rev. E* **72,** 16608 (2005).

56. Genet, C., van Exter, M. . & Woerdman, J. . Fano-type interpretation of red shifts and red

tails in hole array transmission spectra. *Opt. Commun.* **225,** 331–336 (2003).

57. Sarrazin, M., Vigneron, J.-P. & Vigoureux, J.-M. Role of Wood anomalies in optical properties of thin metallic films with a bidimensional array of subwavelength holes. *Phys. Rev. B* **67,** 85415 (2003).

58. Fano, U. Effects of Configuration Interaction on Intensities and Phase Shifts. *Phys. Rev.* **124,** 1866–1878 (1961).

59. Giannini, V., Francescato, Y., Amrania, H., Phillips, C. C. & Maier, S. A. Fano Resonances in Nanoscale Plasmonic Systems: A Parameter-Free Modeling Approach. *Nano Lett.* **11,** 2835–2840 (2011).

60. Rodriguez, S. R. K. *et al.* From weak to strong coupling of localized surface plasmons to guided modes in a luminescent slab. *Phys. Rev. B* **90,** 235406 (2014).

61. Stockman, M. I. Nanoplasmonics: The physics behind the applications. *Phys. Today* **64,** 39–44 (2011).

62. Trügler, A. *Optical Properties of Metallic Nanoparticles*. **232,** (Springer International Publishing, 2016).

63. Asano, S. & Yamamoto, G. Light Scattering by a Spheroidal Particle. *Appl. Opt.* **14,** 29 (1975).

64. Xu, H.-X. A new method by extending Mie theory to calculate local field in outside/inside of aggregates of arbitrary spheres. *Phys. Lett. A* **312,** 411–419 (2003).

65. Novotny, L. & Hecht, B. *Principles of Nano-Optics*. (Cambridge University Press, 2006). doi:10.1017/CBO9780511813535

66. PEREZJUSTE, J., PASTORIZASANTOS, I., LIZMARZAN, L. & MULVANEY, P. Gold nanorods: Synthesis, characterization and applications. *Coord. Chem. Rev.* **249,** 1870–1901 (2005).

67. Wolf, M. Femtosecond dynamics of electronic excitations at metal surfaces. *Surf. Sci.* **377–379,** 343–349 (1997).

68. Sun, C.-K., Vallée, F., Acioli, L. H., Ippen, E. P. & Fujimoto, J. G. Femtosecond-tunable measurement of electron thermalization in gold. *Phys. Rev. B* **50,** 15337–15348 (1994).

69. Lamprecht, B. Ultrafast plasmon dynamics in metal nanoparticles. (Karl-Franzens-Universität Graz, 2000).

70. Kühn, S., Håkanson, U., Rogobete, L. & Sandoghdar, V. Enhancement of Single-Molecule Fluorescence Using a Gold Nanoparticle as an Optical Nanoantenna. *Phys. Rev. Lett.* **97,**

17402 (2006).

71. Anger, P., Bharadwaj, P. & Novotny, L. Enhancement and Quenching of Single-Molecule Fluorescence. *Phys. Rev. Lett.* **96,** 113002 (2006).

72. Farahani, J. N., Pohl, D. W., Eisler, H.-J. & Hecht, B. Single Quantum Dot Coupled to a Scanning Optical Antenna: A Tunable Superemitter. *Phys. Rev. Lett.* **95,** 17402 (2005).

73. Greffet, J.-J. APPLIED PHYSICS: Nanoantennas for Light Emission. *Science (80-.).* **308,** 1561–1563 (2005).

74. Muhlschlegel, P. Resonant Optical Antennas. *Science (80-.).* **308,** 1607–1609 (2005).

75. Novotny, L. & van Hulst, N. Antennas for light. *Nat. Photonics* **5,** 83–90 (2011).

76. Bharadwaj, P., Deutsch, B. & Novotny, L. Optical Antennas. *Adv. Opt. Photonics* **1,** 438 (2009).

77. Coenen, T., Bernal Arango, F., Femius Koenderink, a & Polman, A. Directional emission from a single plasmonic scatterer. *Nat. Commun.* **5,** 3250 (2014).

78. Coenen, T., Vesseur, E. J. R., Polman, A. & Koenderink, A. F. Directional Emission from Plasmonic Yagi–Uda Antennas Probed by Angle-Resolved Cathodoluminescence Spectroscopy. *Nano Lett.* **11,** 3779–3784 (2011).

79. Curto, A. G. *et al.* Unidirectional Emission of a Quantum Dot Coupled to a Nanoantenna. *Science (80-.).* **329,** 930–933 (2010).

80. Taminiau, T. H., Stefani, F. D., Segerink, F. B. & van Hulst, N. F. Optical antennas direct single-molecule emission. *Nat. Photonics* **2,** 234–237 (2008).

81. Mertens, H., Biteen, J. S., Atwater, H. A. & Polman, A. Polarization-Selective Plasmon-Enhanced Silicon Quantum-Dot Luminescence. *Nano Lett.* **6,** 2622–2625 (2006).

82. Ming, T. *et al.* Strong Polarization Dependence of Plasmon-Enhanced Fluorescence on Single Gold Nanorods. *Nano Lett.* **9,** 3896–3903 (2009).

83. Wang, Y., Yang, T., Tuominen, M. T. & Achermann, M. Radiative Rate Enhancements in Ensembles of Hybrid Metal-Semiconductor Nanostructures. *Phys. Rev. Lett.* **102,** 163001 (2009).

84. Muskens, O. L., Giannini, V., Sánchez-Gil, J. A. & Gómez Rivas, J. Strong Enhancement of the Radiative Decay Rate of Emitters by Single Plasmonic Nanoantennas. *Nano Lett.* **7,** 2871–2875 (2007).

85. Ringler, M. *et al.* Shaping Emission Spectra of Fluorescent Molecules with Single

Plasmonic Nanoresonators. *Phys. Rev. Lett.* **100,** 203002 (2008).

86. Biteen, J. S., Lewis, N. S., Atwater, H. A., Mertens, H. & Polman, A. Spectral tuning of plasmon-enhanced silicon quantum dot luminescence. *Appl. Phys. Lett.* **88,** 131109 (2006).

87. Nowy, S. Understanding losses in OLEDs: optical device simulation and electrical characterization using impedance spectroscopy. (Universität Augsburg, 2010).

88. Yariv, A. & Yeh, P. *Photonics: Optical Electronics in Modern Communictions*. (Oxford University Press, 2006).

89. Auguié, B. & Barnes, W. L. Collective resonances in gold nanoparticle arrays. *Phys. Rev. Lett.* **101,** 1–4 (2008).

90. Volakis, J. L., Chatterjee, A. & Kempel, L. C. *Finite Element Method Electromagnetics: Antennas, Microwave Circuits, and Scattering Applications*. (John Wiley & Sons, 1998).

91. Jian-Ming, J. *The Finite Element Method in Electrodynamics*. (John Wiley & Sons, 2015).

92. Draine, B. T. & Flatau, P. J. Discrete-Dipole Approximation For Scattering Calculations. *J. Opt. Soc. Am. A* **11,** 1491 (1994).

93. Draine, B. T. & Goodman, J. Beyond Clausius-Mossotti - Wave propagation on a polarizable point lattice and the discrete dipole approximation. *Astrophys. J.* **405,** 685 (1993).

94. Kottmann, J. P. & Martin, O. J. F. Accurate solution of the volume integral equation for high-permittivity scatterers. *IEEE Trans. Antennas Propag.* **48,** 1719–1726 (2000).

95. Taflove, A. & Hagness, S. C. *Computational Electrodynamics: The Finite-Difference Time-Domain Method*. (Artech House, 2005).

96. Kane Yee. Numerical solution of initial boundary value problems involving maxwell's equations in isotropic media. *IEEE Trans. Antennas Propag.* **14,** 302–307 (1966).

97. FDominec. FDTD Yee grid 2d-3d. *Wikimedia commons* (2015). Available at: https://commons.wikimedia.org/wiki/File:FDTD_Yee_grid_2d-3d.svg. (Accessed: 28th September 2017)

98. Mohammadi, A., Nadgaran, H. & Agio, M. Contour-path effective permittivities for the two-dimensional finite-difference time-domain method. *Opt. Express* **13,** 10367 (2005).

99. Zhao, Y. & Hao, Y. Finite-Difference Time-Domain Study of Guided Modes in Nano-Plasmonic Waveguides. *IEEE Trans. Antennas Propag.* **55,** 3070–3077 (2007).

100. Wenhua Yu & Mittra, R. A conformal finite difference time domain technique for modeling curved dielectric surfaces. *IEEE Microw. Wirel. Components Lett.* **11,** 25–27 (2001).

101. Kittel, C. *Introduction to Solid State Physics*. (John Wiley and Sons Ltd, 2004).

102. Zan, H.-W., Yeh, C.-C., Meng, H.-F., Tsai, C.-C. & Chen, L.-H. Achieving High Field-Effect Mobility in Amorphous Indium-Gallium-Zinc Oxide by Capping a Strong Reduction Layer. *Adv. Mater.* **24,** 3509–3514 (2012).

103. Fortunato, E., Barquinha, P. & Martins, R. Oxide Semiconductor Thin-Film Transistors: A Review of Recent Advances. *Adv. Mater.* **24,** 2945–2986 (2012).

104. Medvedeva, J. E. Combining Optical Transparency with Electrical Conductivity: Challenges and Prospects. in *Transparent Electronics* 1–29 (John Wiley & Sons, Ltd, 2010). doi:10.1002/9780470710609.ch1

105. Sze, S. M. & Ng, K. K. *Physics of Semiconductor Devices*. (Wiley, 2006).

106. Ibaraki, N. a-Si TFT technologies for large-size and high-pixel-density AM-LCDs. *Mater. Chem. Phys.* **43,** 220–226 (1996).

107. Kamiya, T. & Hosono, H. Material characteristics and applications of transparent amorphous oxide semiconductors. *NPG Asia Mater.* **2,** 15–22 (2010).

108. Nomura, K. *et al.* Local coordination structure and electronic structure of the large electron mobility amorphous oxide semiconductor In-Ga-Zn-O: Experiment and ab initio calculations. *Phys. Rev. B* **75,** 35212 (2007).

109. Nomura, K. *et al.* Room-temperature fabrication of transparent flexible thin-film transistors using amorphous oxide semiconductors. *Nature* **432,** 488–492 (2004).

110. Greiner, M. T. *et al.* Universal energy-level alignment of molecules on metal oxides. *Nat. Mater.* **11,** 76–81 (2011).

111. Scanlon, D. O., Morgan, B. J., Watson, G. W. & Walsh, A. Acceptor Levels in p-type CuO2: Rationalizing Theory and Experiment. *Phys. Rev. Lett.* **103,** 96405 (2009).

112. Nolan, M. & Elliott, S. D. The p-type conduction mechanism in Cu2O: a first principles study. *Phys. Chem. Chem. Phys.* **8,** 5350 (2006).

113. Ruiz, E., Alvarez, S., Alemany, P. & Evarestov, R. A. Electronic structure and properties of Cu2O. *Phys. Rev. B* **56,** 7189–7196 (1997).

114. Raebiger, H., Lany, S. & Zunger, A. Origins of the p-type nature and cation deficiency in

Cu2O and related materials. *Phys. Rev. B* **76,** 45209 (2007).

115. Wang, Z., Nayak, P. K., Caraveo-Frescas, J. A. & Alshareef, H. N. Recent Developments in p-Type Oxide Semiconductor Materials and Devices. *Adv. Mater.* **28,** 3831–3892 (2016).

116. Walsh, A. & Watson, G. W. Electronic structures of rocksalt, litharge, and herzenbergite SnO by density functional theory. *Phys. Rev. B* **70,** 235114 (2004).

117. Liang, L. Y. *et al.* Phase and Optical Characterizations of Annealed SnO Thin Films and Their p-Type TFT Application. *J. Electrochem. Soc.* **157,** H598 (2010).

118. Togo, A., Oba, F., Tanaka, I. & Tatsumi, K. First-principles calculations of native defects in tin monoxide. *Phys. Rev. B* **74,** 195128 (2006).

119. Jaffe, J. E. *et al.* Electronic and Defect Structures of CuSCN. *J. Phys. Chem. C* **114,** 9111–9117 (2010).

120. Halliburton, L. E. *et al.* Production of native donors in ZnO by annealing at high temperature in Zn vapor. *Appl. Phys. Lett.* **87,** 172108 (2005).

121. Stjerna, B., Granqvist, C. G., Seidel, A. & Häggström, L. Characterization of rf-sputtered SnO x thin films by electron microscopy, Hall-effect measurement, and Mössbauer spectrometry. *J. Appl. Phys.* **68,** 6241–6245 (1990).

122. De Wit, J. H. W., Van Unen, G. & Lahey, M. Electron concentration and mobility in In2O3. *J. Phys. Chem. Solids* **38,** 819–824 (1977).

123. Anderson, P. W. Absence of Diffusion in Certain Random Lattices. *Phys. Rev.* **109,** 1492–1505 (1958).

124. Baranovski, S. & Rubel, O. Description of Charge Transport in Amorphous Semiconductors. *Charg. Transp. Disord. Solids with Appl. Electron.* 49–96 (2006). doi:10.1002/0470095067.ch2

125. Cohen, M. H., Fritzsche, H. & Ovshinsky, S. R. Simple Band Model for Amorphous Semiconducting Alloys. *Phys. Rev. Lett.* **22,** 1065–1068 (1969).

126. Mott, N. F. Electrons in disordered structures. *Adv. Phys.* **16,** 49–144 (1967).

127. *Charge Transport in Disordered Solids with Applications in Electronics*. (John Wiley & Sons, Ltd, 2006). doi:10.1002/0470095067

128. Shur, M. & Hack, M. Physics of amorphous silicon based alloy field-effect transistors. *J. Appl. Phys.* **55,** 3831–3842 (1984).

129. Tiedje, T. & Rose, A. A physical interpretation of dispersive transport in disordered

semiconductors. *Solid State Commun.* **37,** 49–52 (1981).

130. Lee, C. G., Cobb, B. & Dodabalapur, A. Band transport and mobility edge in amorphous solution-processed zinc tin oxide thin-film transistors. *Appl. Phys. Lett.* **97,** 1–4 (2010).

131. Le Comber, P. G. & Spear, W. E. Electronic Transport in Amorphous Silicon Films. *Phys. Rev. Lett.* **25,** 509–511 (1970).

132. Coropceanu, V. *et al.* Charge transport in organic semiconductors. *Chem. Rev.* **107,** 926–52 (2007).

133. Horowitz, G. Organic Field-Effect Transistors. *Adv. Mater.* **10,** 365–377 (1998).

134. Torricelli, F. *et al.* Transport Physics and Device Modeling of Zinc Oxide Thin-Film Transistors Part I: Long-Channel Devices. *IEEE Trans. Electron Devices* **58,** 2610–2619 (2011).

135. Servati, P., Nathan, A. & Amaratunga, G. A. J. Generalized transport-band field-effect mobility in disordered organic and inorganic semiconductors. *Phys. Rev. B - Condens. Matter Mater. Phys.* **74,** 1–7 (2006).

136. Zheng, H. *et al.* All-solution processed polymer light-emitting diode displays. *Nat. Commun.* **4,** 1971 (2013).

137. Søndergaard, R. R., Hösel, M. & Krebs, F. C. Roll-to-Roll fabrication of large area functional organic materials. *J. Polym. Sci. Part B Polym. Phys.* **51,** 16–34 (2013).

138. Trattnig, R. *et al.* Bright Blue Solution Processed Triple-Layer Polymer Light-Emitting Diodes Realized by Thermal Layer Stabilization and Orthogonal Solvents. *Adv. Funct. Mater.* **23,** 4897–4905 (2013).

139. Kawano, K., Nagayoshi, K., Yamaki, T. & Adachi, C. Fabrication of high-efficiency multilayered organic light-emitting diodes by a film transfer method. *Org. Electron.* (2014). doi:10.1016/j.orgel.2014.04.035

140. Lee, T. W., Chung, Y., Kwon, O. & Park, J. J. Self-organized gradient hole injection to improve the performance of polymer electroluminescent devices. *Adv. Funct. Mater.* **17,** 390–396 (2007).

141. Khodabakhsh, S. *et al.* Using Self-Assembling Dipole Molecules to Improve Hole Injection in Conjugated Polymers. *Adv. Funct. Mater.* **14,** 1205–1210 (2004).

142. Lee, B. R. *et al.* Highly Efficient Polymer Light-Emitting Diodes Using Graphene Oxide as a Hole Transport Layer. *ACS Nano* **6,** 2984–2991 (2012).

143. Huang, F., Cheng, Y.-J., Zhang, Y., Liu, M. S. & Jen, A. K.-Y. Crosslinkable hole-transporting materials for solution processed polymer light-emitting diodes. *J. Mater. Chem.* **18,** 4495 (2008).

144. Pattanasattayavong, P. *et al.* Electric field-induced hole transport in copper(I) thiocyanate (CuSCN) thin-films processed from solution at room temperature. *Chem. Commun. (Camb).* **49,** 4154–6 (2013).

145. Pattanasattayavong, P. *et al.* Hole-transporting transistors and circuits based on the transparent inorganic semiconductor copper(I) thiocyanate (CuSCN) processed from solution at room temperature. *Adv. Mater.* **25,** 1504–1509 (2013).

146. Xu, L.-J., Wang, J.-Y., Zhu, X.-F., Zeng, X.-C. & Chen, Z.-N. Phosphorescent Cationic Au 4 Ag 2 Alkynyl Cluster Complexes for Efficient Solution-Processed Organic Light-Emitting Diodes. *Adv. Funct. Mater.* **25,** 3033–3042 (2015).

147. Auer-Berger, M., Tretnak, V., Wenzl, F., Krenn, J. R. & List-Kratochvil, E. J. W. Aluminum-nanodisc-induced collective lattice resonances: Controlling the light extraction in organic light emitting diodes. *Appl. Phys. Lett.* **111,** 173301 (2017).

148. Auer-Berger, M., Tretnak, V., Wenzl, F.-P. & Krenn, J. R. Adjusting the emission color of organic light-emitting diodes through aluminum nanodisc arrays. *Opt. Eng.* **56,** 1 (2017).

149. Ye, S. *et al.* CuSCN-Based Inverted Planar Perovskite Solar Cell with an Average PCE of 15.6%. *Nano Lett.* **15,** 3723–3728 (2015).

150. Zhao, K. *et al.* Solution-processed inorganic copper(i) thiocyanate (CuSCN) hole transporting layers for efficient p-i-n perovskite solar cells. **3,** 20554–20559 (2015).

151. Qin, P. *et al.* Inorganic hole conductor-based lead halide perovskite solar cells with 12.4% conversion efficiency. **5,** (2014).

152. Gertman, R., Harush, A. & Visoly-Fisher, I. Nanostructured photocathodes for infrared photodetectors and photovoltaics. *J. Phys. Chem. C* **119,** 1683–1689 (2015).

153. Treat, N. D. *et al.* Copper thiocyanate: An attractive hole transport/extraction layer for use in organic photovoltaic cells. *Appl. Phys. Lett.* **107,** 13301 (2015).

154. Ye, S. *et al.* CuSCN-Based Inverted Planar Perovskite Solar Cell with an Average PCE of 15.6%. *Nano Lett.* **15,** 3723–3728 (2015).

155. Zhao, K. *et al.* Solution-processed inorganic copper(i) thiocyanate (CuSCN) hole transporting layers for efficient p-i-n perovskite solar cells. *J. Mater. Chem. A* **3,** 20554–20559 (2015).

156. Qin, P. *et al.* Inorganic hole conductor-based lead halide perovskite solar cells with 12.4% conversion efficiency. *Nat. Commun.* **5,** (2014).

157. O'Regan, B., Schwartz, D. T., Zakeeruddin, S. M. & Grätzel, M. Electrodeposited Nanocomposite n-p Heterojunctions for Solid-State Dye-Sensitized Photovoltaics. *Adv. Mater.* **12,** 1263–1267 (2000).

158. Wu, W., Jin, Z., Hua, Z., Fu, Y. & Qiu, J. Growth mechanisms of CuSCN films electrodeposited on ITO in EDTA-chelated copper(II) and KSCN aqueous solution. *Electrochim. Acta* **50,** 2343–2349 (2005).

159. Selk, Y., Yoshida, T. & Oekermann, T. Variation of the morphology of electrodeposited copper thiocyanate films. *Thin Solid Films* **516,** 7120–7124 (2008).

160. Yoshioka, S., Mishima, T. & Ihara, M. The Effect of TiO2 Microstructure and Introduction of Silver Nanoparticles on Conversion Efficiency of Sb2S3 Sensitized Semiconductor Solar Cells. *ECS Trans.* **50,** 33–44 (2013).

161. Zhang, X., Yoshioka, S., Loew, N. & Ihara, M. Microstructure Control of Absorber Sb2S3 and p-Type Semiconductor CuSCN for Semiconductor-Sensitized Solar Cells (TiO2/Sb2S3/CuSCN). *ECS Trans.* **64,** 1–13 (2014).

162. Srinivasan, K. & Subrahmanya, R. S. Polarographic and redox potential studies on copper(I) and copper(II) and their complexes. *J. Electroanal. Chem. Interfacial Electrochem.* **31,** 233–244 (1971).

163. Wijeyasinghe, N. *et al.* Copper(I) Thiocyanate (CuSCN) Hole-Transport Layers Processed from Aqueous Precursor Solutions and Their Application in Thin-Film Transistors and Highly Efficient Organic and Organometal Halide Perovskite Solar Cells. *Adv. Funct. Mater.* 1701818 (2017). doi:10.1002/adfm.201701818

164. Perumal, A. *et al.* High-Efficiency, Solution-Processed, Multilayer Phosphorescent Organic Light-Emitting Diodes with a Copper Thiocyanate Hole-Injection/Hole-Transport Layer. *Adv. Mater.* **27,** 93–100 (2015).

165. Owens, D. K. & Wendt, R. C. Estimation of the surface free energy of polymers. *J. Appl. Polym. Sci.* **13,** 1741–1747 (1969).

166. Greiner, M. T. & Lu, Z.-H. Thin-film metal oxides in organic semiconductor devices: their electronic structures, work functions and interfaces. *NPG Asia Mater.* **5,** e55 (2013).

167. Meyer, J. *et al.* Transition metal oxides for organic electronics: energetics, device physics and applications. *Adv. Mater.* **24,** 5408–27 (2012).

168. Nau, S. *et al.* Highly efficient color-stable deep-blue multilayer PLEDs: Preventing PEDOT:PSS-induced interface degradation. *Adv. Mater.* **25,** 4420–4424 (2013).

169. Biesinger, M. C. *et al.* Resolving surface chemical states in XPS analysis of first row transition metals, oxides and hydroxides: Cr, Mn, Fe, Co and Ni. *Appl. Surf. Sci.* **257,** 2717–2730 (2011).

170. Vasquez, R. P. CuSO 4 by XPS. *Surf. Sci. Spectra* **5,** 279–284 (1998).

171. Yu, X., Marks, T. J. & Facchetti, A. Metal oxides for optoelectronic applications. *Nat. Mater.* **15,** 383–396 (2016).

172. Sirringhaus, H. 25th anniversary article: Organic field-effect transistors: The path beyond amorphous silicon. *Adv. Mater.* **26,** 1319–1335 (2014).

173. Di Carlo, A., Piacenza, F., Bolognesi, A., Stadlober, B. & Maresch, H. Influence of grain sizes on the mobility of organic thin-film transistors. *Appl. Phys. Lett.* **86,** 263501 (2005).

174. Li, H. H. Refractive index of alkali halides and its wavelength and temperature derivatives. *J. Phys. Chem. Ref. Data* **5,** 329–528 (1976).

175. Rosker, M., Cheng, K. & Tang, C. Practical urea optical parametric oscillator for tunable generation throughout the visible and near-infrared. *IEEE J. Quantum Electron.* **21,** 1600–1606 (1985).

176. Brus, V. V. On impedance spectroscopy analysis of nonideal heterojunctions. *Semicond. Sci. Technol.* **27,** 35024 (2012).

177. Brus, V. V., Kyaw, A. K. K., Maryanchuk, P. D. & Zhang, J. Quantifying interface states and bulk defects in high-efficiency solution-processed small-molecule solar cells by impedance and capacitance characteristics. *Prog. Photovoltaics Res. Appl.* **23,** 1526–1535 (2015).

178. Orazem, M. E. & Tribollet, B. *Electrochemical Impedance Spectroscopy*. (John Wiley & Sons, Inc., 2008). doi:10.1002/9780470381588

179. Pattanasattayavong, P., Mottram, A. D., Yan, F. & Anthopoulos, T. D. Study of the Hole Transport Processes in Solution-Processed Layers of the Wide Bandgap Semiconductor Copper(I) Thiocyanate (CuSCN). *Adv. Funct. Mater.* **25,** 6802–6813 (2015).

180. Naka, S. *et al.* Electrical properties of organic electroluminescent devices with aluminium alloy cathode. *Synth. Met.* **91,** 129–130 (1997).

181. Knotek, M. L., Pollak, M., Donovan, T. M. & Kurtzman, H. Thickness Dependence of Hopping Transport in Amorphous-Ge Films. *Phys. Rev. Lett.* **30,** 853–856 (1973).

182. Chiguvare, Z., Parisi, J. & Dyakonov, V. Current limiting mechanisms in indium-tin-oxide/poly3-hexylthiophene/aluminum thin film devices. *J. Appl. Phys.* **94,** 2440–2448 (2003).

183. Rawcliffe, R., Bradley, D. D. C. & Campbell, A. J. Comparison between bulk and field effect mobility in polyfluorene copolymer field effect transistors. in (ed. Dimitrakopoulos, C. D.) 25 (2003). doi:10.1117/12.506038

184. Jang, Y. *et al.* Influence of the dielectric constant of a polyvinyl phenol insulator on the field-effect mobility of a pentacene-based thin-film transistor. *Appl. Phys. Lett.* **87,** 152105 (2005).

185. Shur, M. & Hack, M. Physics of amorphous silicon based alloy field-effect transistors. *J. Appl. Phys.* **55,** (1984).

186. Fishchuk, I. I., Arkhipov, V. I., Kadashchuk, A., Heremans, P. & Bässler, H. Analytic model of hopping mobility at large charge carrier concentrations in disordered organic semiconductors: Polarons versus bare charge carriers. *Phys. Rev. B* **76,** 45210 (2007).

187. Nepurek, S. & Sworakowski, J. Use of space-charge-limited current measurements to determine the properties of energetic distributions of bulk traps. *J. Appl. Phys.* **51,** 2098–2102 (1980).

188. Sworakowski, J. & Nešpůrek, S. On the determination of the density of states in inhomogeneous samples from steady-state space-charge-limited currents. *J. Appl. Phys.* **65,** 1559 (1989).

189. Kalb, W. L., Haas, S., Krellner, C., Mathis, T. & Batlogg, B. Trap density of states in small-molecule organic semiconductors: A quantitative comparison of thin-film transistors with single crystals. *Phys. Rev. B* **81,** 1–13 (2010).

190. Marshall, J. M. Carrier diffusion in amorphous semiconductors. *Rep. Prog. Phys.* **46,** 1235–1282 (1983).

191. Anderson, P. W. The size of localized States near the mobility edge. *Proc. Natl. Acad. Sci. U. S. A.* **69,** 1097–1099 (1972).

192. Lampert, M. a. Volume-controlled current injection in insulators. *Reports Prog. Phys.* **27,** 329–367 (2002).

193. Kokil, A., Yang, K. & Kumar, J. Techniques for characterization of charge carrier mobility in organic semiconductors. *J. Polym. Sci. Part B Polym. Phys.* **50,** 1130–1144 (2012).

194. Tripathi, D. C., Tripathi, A. K. & Mohapatra, Y. N. Mobility determination using frequency

dependence of imaginary part of impedance (Im Z) for organic and polymeric thin films. *Appl. Phys. Lett.* **98,** 1–4 (2011).

195. Martens, H. C. F., Huiberts, J. N. & Blom, P. W. M. Simultaneous measurement of electron and hole mobilities in polymer light-emitting diodes. *Appl. Phys. Lett.* **77,** 1852 (2000).

196. Martens, H., Pasveer, W., Brom, H., Huiberts, J. & Blom, P. Crossover from space-charge-limited to recombination-limited transport in polymer light-emitting diodes. *Phys. Rev. B* **63,** 1–7 (2001).

197. Martens, H. C. F., Huiberts, J. N. & Blom, P. W. M. Simultaneous measurement of electron and hole mobilities in polymer light-emitting diodes. *Appl. Phys. Lett.* **77,** 1852 (2000).

198. Martens, H. C. F., Brom, H. B. & Blom, P. W. M. Frequency-dependent electrical response of holes in poly (p -phenylene vinylene). *Phys. Rev. B* **60,** R8489–R8492 (1999).

199. Schroeder, H. Poole-Frenkel-effect as dominating current mechanism in thin oxide films—An illusion?! *J. Appl. Phys.* **117,** 215103 (2015).

200. Horowitz, G., Hajlaoui, R., Fichou, D. & El Kassmi, A. Gate voltage dependent mobility of oligothiophene field-effect transistors. *J. Appl. Phys.* **85,** 3202–3206 (1999).

201. Le Comber, P. G., Madan, A. & Spear, W. E. Electronic transport and state distribution in amorphous Si films. *J. Non. Cryst. Solids* **11,** 219–234 (1972).

202. Horowitz, G. & Hajlaoui, M. E. Mobility in Polycrystalline Oligothiophene Field-Effect Transistors Dependent on Grain Size. *Adv. Mater.* **12,** 1046–1050 (2000).

203. Bourguiga, R. *et al.* Charge transport limited by grain boundaries in polycrystalline octithiophene thin film transistors. *Eur. Phys. J. Appl. Phys.* **19,** 117–122 (2002).

204. Davenport, K., Djidjou, T. K., Li, S. & Rogachev, A. Characterization of charge accumulation on multiple interfaces in phosphorescent organic light-emitting diodes. *Org. Electron.* **46,** 166–172 (2017).

205. Zhang, L., Nakanotani, H. & Adachi, C. Capacitance-voltage characteristics of a 4,4???-bis[(N-carbazole) styryl]biphenyl based organic light-emitting diode: Implications for characteristic times and their distribution. *Appl. Phys. Lett.* **103,** (2013).

206. Fu, Q., Chen, J., Shi, C. & Ma, D. Solution-processed small molecules as mixed host for highly efficient blue and white phosphorescent organic light-emitting diodes. *ACS Appl. Mater. Interfaces* **4,** 6579–86 (2012).

207. Kim, S.-Y. *et al.* Organic Light-Emitting Diodes with 30% External Quantum Efficiency Based on a Horizontally Oriented Emitter. *Adv. Funct. Mater.* **23,** 3896–3900 (2013).

208. Wang, Z. B. *et al.* Unlocking the full potential of organic light-emitting diodes on flexible plastic. *Nat. Photonics* **5,** 753–757 (2011).

209. Reineke, S. *et al.* White organic light-emitting diodes with fluorescent tube efficiency. *Nature* **459,** 234–238 (2009).

210. Earmme, T. & Jenekhe, S. a. Solution-Processed, Alkali Metal-Salt-Doped, Electron-Transport Layers for High-Performance Phosphorescent Organic Light-Emitting Diodes. *Adv. Funct. Mater.* **22,** 5126–5136 (2012).

211. Xiao, L., Su, S.-J., Agata, Y., Lan, H. & Kido, J. Nearly 100% Internal Quantum Efficiency in an Organic Blue-Light Electrophosphorescent Device Using a Weak Electron Transporting Material with a Wide Energy Gap. *Adv. Mater.* **21,** 1271–1274 (2009).

212. Auer-Berger, M. *et al.* All-solution-processed multilayer polymer/dendrimer light emitting diodes. *Org. Electron.* **35,** 164–170 (2016).

213. Pevzner, L. *et al.* Controlling Polymer Solubility: Polyfluorenes with Branched Semiperfluorinated Side Chains for Polymer Light-Emitting Diodes. *Isr. J. Chem.* **54,** 736–747 (2014).

214. Zhang, G. *et al.* Core-and-Surface-Functionalized Polyphenylene Dendrimers for Solution-Processed, Pure-Blue Light-Emitting Diodes Through Surface-to-Core Energy Transfer. *Macromol. Rapid Commun.* **35,** 1931–1936 (2014).

215. Petrosino, M., Vacca, P., Licciardo, G. D., Rubino, A. & Bellone, S. The effect of ITO surface energy on OLED electrical properties. in *2007 International Workshop on Physics of Semiconductor Devices* 606–609 (IEEE, 2007). doi:10.1109/IWPSD.2007.4472590

216. Besbes, S. *et al.* Effect of surface treatment and functionalization on the ITO properties for OLEDs. *Mater. Sci. Eng. C* **26,** 505–510 (2006).

217. Cho, Y. C. *et al.* The conversion of wettability in transparent conducting Al-doped ZnO thin film. *Solid State Commun.* **149,** 609–611 (2009).

218. Kinner, L. *et al.* Inkjet-printed embedded Ag-PEDOT:PSS electrodes with improved light out coupling effects for highly efficient ITO-free blue polymer light emitting diodes. *Appl. Phys. Lett.* **110,** 101107 (2017).

219. Volz, D. & Baumann, T. Efficient, deep-blue TADF-emitters for OLED display applications (Conference Presentation). in (eds. So, F., Adachi, C. & Kim, J.-J.) 994102 (2016). doi:10.1117/12.2234624

220. Zhang, Q. *et al.* Efficient blue organic light-emitting diodes employing thermally

activated delayed fluorescence. *Nat. Photonics* 1–7 (2014). doi:10.1038/nphoton.2014.12

221. Youn, W., Lee, J., Xu, M., Singh, R. & So, F. Corrugated Sapphire Substrates for Organic Light-Emitting Diode Light Extraction. *ACS Appl. Mater. Interfaces* **7,** 8974–8978 (2015).

222. Liu, Y.-F. *et al.* Enhanced efficiency of organic light-emitting devices with corrugated nanostructures based on soft nano-imprinting lithography. *Appl. Phys. Lett.* **109,** 193301 (2016).

223. Ziebarth, J. M., Saafir, A. K., Fan, S. & McGehee, M. D. Extracting light from polymer light-emitting diodes using stamped Bragg gratings. *Adv. Funct. Mater.* **14,** 451–456 (2004).

224. Bi, Y. G. *et al.* Broadband light extraction from white organic light-emitting devices by employing corrugated metallic electrodes with dual periodicity. *Adv. Mater.* **25,** 6969–6974 (2013).

225. Jeong, S. M. *et al.* Enhancement of normally directed light outcoupling from organic light-emitting diodes using nanoimprinted low-refractive-index layer. *Appl. Phys. Lett.* **92,** 83307 (2008).

226. Zhang, S., Turnbull, G. A. & Samuel, I. D. W. Enhancing the emission directionality of organic light-emitting diodes by using photonic microstructures. *Appl. Phys. Lett.* **103,** 213302 (2013).

227. Jin, Y. *et al.* Solving efficiency-stability tradeoff in top-emitting organic light-emitting devices by employing periodically corrugated metallic cathode. *Adv. Mater.* **24,** 1187–1191 (2012).

228. Shin, C.-H., Shin, E. Y., Kim, M.-H., Lee, J.-H. & Choi, Y. Nanoparticle scattering layer for improving light extraction efficiency of organic light emitting diodes. *Opt. Express* **23,** A133 (2015).

229. Chang, H. W. *et al.* Nano-particle based scattering layers for optical efficiency enhancement of organic light-emitting diodes and organic solar cells. *J. Appl. Phys.* **113,** (2013).

230. Bi, Y.-G. *et al.* Surface Plasmon-Polariton Mediated Red Emission from Organic Light-Emitting Devices Based on Metallic Electrodes Integrated with Dual-Periodic Corrugation. *Sci. Rep.* **4,** 7108 (2014).

231. Khan, I. *et al.* Multidiffractive Broadband Plasmonic Absorber. *Adv. Opt. Mater.* **4,** 435–443 (2016).

232. Shin, J. Bin *et al.* Efficient Green Organic Light-Emitting Diodes by Plasmonic Silver Nanoparticles. *IEEE Photonics Technol. Lett.* **28,** 371–374 (2016).

233. Mulder, C. L., Celebi, K., Milaninia, K. M. & Baldo, M. A. Saturated and efficient blue phosphorescent organic light emitting devices with Lambertian angular emission. *Appl. Phys. Lett.* **90,** (2007).

234. Fitzgerald, J. M., Azadi, S. & Giannini, V. Quantum plasmonic nanoantennas. *Phys. Rev. B* **95,** 235414 (2017).

235. Kinkhabwala, A. *et al.* Large single-molecule fluorescence enhancements produced by a bowtie nanoantenna. *Nat. Photonics* **3,** 654–657 (2009).

236. Hohenberger, E., Freitag, N., Rosenmann, D. & Korampally, V. A facile route towards large area self-assembled nanoscale silver film morphologies and their applications towards metal enhanced fluorescence. *Sensors Actuators B Chem.* **249,** 549–557 (2017).

237. Wei, Q. *et al.* Plasmonics Enhanced Smartphone Fluorescence Microscopy. *Sci. Rep.* **7,** 2124 (2017).

238. Donkers, R. L., Maran, F., Wayner, D. D. M. & Workentin, M. S. Kinetics of the Reduction of Dialkyl Peroxides. New Insights into the Dynamics of Dissociative Electron Transfer 1. *J. Am. Chem. Soc.* **121,** 7239–7248 (1999).

239. Park, Q.-H. Optical antennas and plasmonics. *Contemp. Phys.* **50,** 407–423 (2009).

240. Zhang, J. Z. & Noguez, C. Plasmonic Optical Properties and Applications of Metal Nanostructures. *Plasmonics* **3,** 127–150 (2008).

241. Zoriniants, G. & Barnes, W. L. Fluorescence enhancement through modified dye molecule absorption associated with the localized surface plasmon resonances of metallic dimers. *New J. Phys.* **10,** 105002 (2008).

242. Mohammadi, A., Sandoghdar, V. & Agio, M. Gold nanorods and nanospheroids for enhancing spontaneous emission. *New J. Phys.* **10,** 105015 (2008).

243. Zhang, J. & Lakowicz, J. R. Metal-enhanced fluorescence of an organic fluorophore using gold particles. *Opt. Express* **15,** 2598 (2007).

244. Lakowicz, J. R. Radiative decay engineering 3. Surface plasmon-coupled directional emission. *Anal. Biochem.* **324,** 153–169 (2004).

245. Nie, S. Probing Single Molecules and Single Nanoparticles by Surface-Enhanced Raman Scattering. *Science (80-.).* **275,** 1102–1106 (1997).

246. Kneipp, K. *et al.* Single Molecule Detection Using Surface-Enhanced Raman Scattering (SERS). *Phys. Rev. Lett.* **78,** 1667–1670 (1997).

247. Wustholz, K. L. *et al.* Structure–Activity Relationships in Gold Nanoparticle Dimers and Trimers for Surface-Enhanced Raman Spectroscopy. *J. Am. Chem. Soc.* **132,** 10903–10910 (2010).

248. Giannini, V., Rodríguez-Oliveros, R. & Sánchez-Gil, J. A. Surface Plasmon Resonances of Metallic Nanostars/Nanoflowers for Surface-Enhanced Raman Scattering. *Plasmonics* **5,** 99–104 (2010).

249. Montgomery, J. M., Imre, A., Welp, U., Vlasko-Vlasov, V. & Gray, S. K. SERS enhancements via periodic arrays of gold nanoparticles on silver film structures. *Opt. Express* **17,** 8669 (2009).

250. Bardhan, R. *et al.* Nanoshells with Targeted Simultaneous Enhancement of Magnetic and Optical Imaging and Photothermal Therapeutic Response. *Adv. Funct. Mater.* **19,** 3901–3909 (2009).

251. Montgomery, J. M., Imre, A., Welp, U., Vlasko-Vlasov, V. & Gray, S. K. SERS enhancements via periodic arrays of gold nanoparticles on silver film structures. *Opt. Express* **17,** 8669 (2009).

252. Spuch-Calvar, M., Rodríguez-Lorenzo, L., Morales, M. P., Álvarez-Puebla, R. A. & Liz-Marzán, L. M. Bifunctional Nanocomposites with Long-Term Stability as SERS Optical Accumulators for Ultrasensitive Analysis. *J. Phys. Chem. C* **113,** 3373–3377 (2009).

253. Xie, J., Zhang, Q., Lee, J. Y. & Wang, D. I. C. The Synthesis of SERS-Active Gold Nanoflower Tags for In Vivo Applications. *ACS Nano* **2,** 2473–2480 (2008).

254. Etchegoin, P. G. & Le Ru, E. C. A perspective on single molecule SERS: current status and future challenges. *Phys. Chem. Chem. Phys.* **10,** 6079 (2008).

255. Jain, P. K., Huang, X., El-Sayed, I. H. & El-Sayed, M. A. Review of Some Interesting Surface Plasmon Resonance-enhanced Properties of Noble Metal Nanoparticles and Their Applications to Biosystems. *Plasmonics* **2,** 107–118 (2007).

256. Le Ru, E. C., Etchegoin, P. G. & Meyer, M. Enhancement factor distribution around a single surface-enhanced Raman scattering hot spot and its relation to single molecule detection. *J. Chem. Phys.* **125,** 204701 (2006).

257. Xu, H., Aizpurua, J., Käll, M. & Apell, P. Electromagnetic contributions to single-molecule sensitivity in surface-enhanced Raman scattering. *Phys. Rev. E* **62,** 4318–4324 (2000).

258. Zeman, E. J. & Schatz, G. C. An accurate electromagnetic theory study of surface enhancement factors for silver, gold, copper, lithium, sodium, aluminum, gallium, indium, zinc, and cadmium. *J. Phys. Chem.* **91,** 634–643 (1987).

259. Hrelescu, C., Sau, T. K., Rogach, A. L., Jäckel, F. & Feldmann, J. Single gold nanostars enhance Raman scattering. *Appl. Phys. Lett.* **94,** 153113 (2009).

260. Xiao, Y. *et al.* Surface plasmon-enhanced electroluminescence in organic light-emitting diodes incorporating Au nanoparticles. *Appl. Phys. Lett.* **100,** 13308 (2012).

261. Choi, H. *et al.* Versatile surface plasmon resonance of carbon-dot-supported silver nanoparticles in polymer optoelectronic devices. *Nat. Photonics* **7,** 732–738 (2013).

262. Qiu, T. *et al.* Tailoring light emission properties of organic emitter by coupling to resonance-tuned silver nanoantenna arrays. *Appl. Phys. Lett.* **95,** 213104 (2009).

263. Tanaka, T. *et al.* Enhanced Red-Light Emission by Local Plasmon Coupling of Au Nanorods in an Organic Light-Emitting Diode. *Appl. Phys. Express* **4,** 32105 (2011).

264. Sung, H. *et al.* Controlled positioning of metal nanoparticles in an organic light-emitting device for enhanced quantum efficiency. *Org. Electron.* **15,** 491–499 (2014).

265. Fujiki, A. *et al.* Enhanced fluorescence by surface plasmon coupling of Au nanoparticles in an organic electroluminescence diode. *Appl. Phys. Lett.* **96,** 43307 (2010).

266. Gu, X., Qiu, T., Zhang, W. & Chu, P. K. Light-emitting diodes enhanced by localized surface plasmon resonance. *Nanoscale Res. Lett.* **6,** 199 (2011).

267. Gu, Y. *et al.* Light extraction enhancement in organic light-emitting diodes based on localized surface plasmon and light scattering double-effect. *J. Mater. Chem. C* **1,** 4319 (2013).

268. Kim, S. H. *et al.* Effects of Gold-Nanoparticle Surface and Vertical Coverage by Conducting Polymer between Indium Tin Oxide and the Hole Transport Layer on Organic Light-Emitting Diodes. *ACS Appl. Mater. Interfaces* **7,** 15031–15041 (2015).

269. Kalhor, D., Mohajerani, E. & Hashemi Pour, O. The effect of Indium metal nanoparticles on the electronic properties of organic light emitting diodes (OLEDs). *J. Lumin.* **167,** 376–380 (2015).

270. Gao, C.-Y., Chen, Y.-C., Chen, K.-L. & Huang, C.-J. Double surface plasmon enhanced organic light-emitting diodes by gold nanoparticles and silver nanoclusters. *Appl. Surf. Sci.* **359,** 749–753 (2015).

271. Kim, Y. Y. *et al.* Enhanced performance of blue polymer light-emitting diodes by

incorporation of Ag nanoparticles through the ligand-exchange process. *J. Mater. Chem. C* **4,** 10445–10452 (2016).

272. Shih, H.-C., Chiou, B.-R. & Su, H.-C. Plasmonic enhancement in electroluminescence from light-emitting electrochemical cells incorporating gold nanourchins. *J. Mater. Chem. C* **4,** 5610–5616 (2016).

273. Gao, C.-Y., Chen, K.-L., Sze, P.-W., Chen, Y.-C. & Huang, C.-J. Enhancement and Reduction of Nonradiative Decay Process in Organic Light-Emitting Diodes by Gold Nanoparticles. *Appl. Sci.* **6,** 441 (2016).

274. Peng, J., Tang, F., Xu, X., Jia, M. & Li, L. Doping core–shell nanoparticles into a solution-processed electron transporting layer for polymer light-emitting diodes. *RSC Adv.* **6,** 38148–38152 (2016).

275. Zhao, Y. *et al.* Efficiency roll-off suppression in organic light-emitting diodes at high current densities using gold bowtie nanoantennas. *Appl. Phys. Express* **9,** 22101 (2016).

276. Munkhbat, B. *et al.* Performance Boost of Organic Light-Emitting Diodes with Plasmonic Nanostars. *Adv. Opt. Mater.* **4,** 772–781 (2016).

277. Kim, D. H. & Kim, T. W. Enhancement of the current efficiency of organic light-emitting devices due to the surface plasmonic resonance effect of dodecanethilol-functionalized Au nanoparticles. *Org. Electron.* **34,** 262–266 (2016).

278. Chen, S.-H. *et al.* Light enhancement of plasmonic nano-structure for PLEDs at RGB wavelengths. *Org. Electron.* **38,** 337–343 (2016).

279. Sun, G., Khurgin, J. B. & Soref, R. A. Practical enhancement of photoluminescence by metal nanoparticles. *Appl. Phys. Lett.* **94,** 101103 (2009).

280. Rogobete, L., Kaminski, F., Agio, M. & Sandoghdar, V. Design of plasmonic nanoantennae for enhancing spontaneous emission. *Opt. Lett.* **32,** 1623 (2007).

281. Greffet, J.-J., Laroche, M. & Marquier, F. Impedance of a Nanoantenna and a Single Quantum Emitter. *Phys. Rev. Lett.* **105,** 117701 (2010).

282. Lozano, G. *et al.* Plasmonics for solid-state lighting: enhanced excitation and directional emission of highly efficient light sources. *Light Sci. Appl.* **2,** e66 (2013).

283. Murai, S. *et al.* Hybrid plasmonic-photonic modes in diffractive arrays of nanoparticles coupled to light-emitting optical waveguides. *Opt. Express* **21,** 4250–62 (2013).

284. Abass, A., Rodriguez, S. R., Gómez Rivas, J. & Maes, B. Tailoring Dispersion and Eigenfield Profiles of Plasmonic Surface Lattice Resonances. *ACS Photonics* **1,** 61–68 (2014).

285. Garcia, R. F. *et al.* Enhanced electroluminescence of an organic light-emitting diode by localized surface plasmon using Al periodic structure. *J. Opt. Soc. Am. B* **33,** 246 (2016).

286. Linden, S., Kuhl, J. & Giessen, H. Controlling the interaction between light and gold nanoparticles: Selective suppression of extinction. *Phys. Rev. Lett.* **86,** 4688–4691 (2001).

287. Christ, A., Tikhodeev, S. G., Gippius, N. A., Kuhl, J. & Giessen, H. Waveguide-Plasmon Polaritons: Strong Coupling of Photonic and Electronic Resonances in a Metallic Photonic Crystal Slab. *Phys. Rev. Lett.* **91,** 183901 (2003).

288. Ramezani, M., Lozano, G., Verschuuren, M. A. & Gómez-Rivas, J. Modified emission of extended light emitting layers by selective coupling to collective lattice resonances. *Phys. Rev. B* **94,** 125406 (2016).

289. Luk'yanchuk, B. *et al.* The Fano resonance in plasmonic nanostructures and metamaterials. *Nat. Mater.* **9,** 707–715 (2010).

290. Zhang, J. *et al.* Observation of ultra-narrow band plasmon induced transparency based on large-area hybrid plasmon-waveguide systems. *Appl. Phys. Lett. Appl. Phys. Lett.* **99,** (2011).

291. Boller, K.-J., Imamoğlu, A. & Harris, S. E. Observation of electromagnetically induced transparency. *Phys. Rev. Lett.* **66,** 2593–2596 (1991).

292. Rodriguez, S. R. K., Murai, S., Verschuuren, M. A. & Rivas, J. G. G. Light-emitting waveguide-plasmon polaritons. *Phys. Rev. Lett.* **109,** 1–5 (2012).

293. Nikitin, A., Remezani, M. & Gómez Rivas, J. Luminescent metamaterials for solid state lighting. *ECS J. Solid State Sci. Technol.* **5,** R3164–R3169 (2016).

294. Jou, J.-H., Kumar, S., Agrawal, A., Li, T.-H. & Sahoo, S. Approaches for fabricating high efficiency organic light emitting diodes. *J. Mater. Chem. C* **3,** 2974–3002 (2015).

295. Flidj, N. *et al.* Grating-induced plasmon mode in gold nanoparticle arrays. *J. Chem. Phys.* **123,** (2005).

296. Palik, E. D. *Handbook of Optical Constants of Solids*. (Elsevier B.V, 1998).

297. Bulović, V. *et al.* Weak microcavity effects in organic light-emitting devices. *Phys. Rev. B* **58,** 3730–3740 (1998).

298. Furno, M., Meerheim, R., Hofmann, S., Lüssem, B. & Leo, K. Efficiency and rate of spontaneous emission in organic electroluminescent devices. *Phys. Rev. B* **85,** 115205 (2012).

299. Ou, Q. D. *et al.* Simultaneously Enhancing Color Spatial Uniformity and Operational Stability with Deterministic Quasi-periodic Nanocone Arrays for Tandem Organic Light-Emitting Diodes. *Adv. Opt. Mater.* **3,** 87–94 (2015).

300. Lee, J. *et al.* Color temperature tuning of white organic light-emitting diodes via spatial control of micro-cavity effects based on thin metal strips. *Org. Electron.* **26,** 334–339 (2015).

301. Al-Attar, H. a. & Monkman, A. P. Solution processed multilayer polymer light-emitting diodes based on different molecular weight host. *J. Appl. Phys.* **109,** 74516 (2011).

302. Langhammer, C., Schwind, M., Kasemo, B. & Zorić, I. Localized Surface Plasmon Resonances in Aluminum Nanodisks. *Nano Lett.* **8,** 1461–1471 (2008).

303. Mayer, K. M. & Hafner, J. H. Localized Surface Plasmon Resonance Sensors. *Chem. Rev.* **111,** 3828–3857 (2011).

304. Petryayeva, E. & Krull, U. J. Localized surface plasmon resonance: Nanostructures, bioassays and biosensing—A review. *Anal. Chim. Acta* **706,** 8–24 (2011).

305. Hicks, E. M. *et al.* Controlling plasmon line shapes through diffractive coupling in linear arrays of cylindrical nanoparticles fabricated by electron beam lithography. *Nano Lett.* **5,** 1065–1070 (2005).

306. Humphrey, A. D. & Barnes, W. L. Plasmonic surface lattice resonances on arrays of different lattice symmetry. *Phys. Rev. B - Condens. Matter Mater. Phys.* **90,** 1–8 (2014).

307. Zou, S. & Schatz, G. C. Narrow plasmonic/photonic extinction and scattering line shapes for one and two dimensional silver nanoparticle arrays. *J. Chem. Phys.* **121,** 12606 (2004).

308. Verschuuren, M. *Substrate Conformal Imprint Lithography for Nanophotonics*. (2009).

309. Schuller, J. a. *et al.* Plasmonics for extreme light concentration and manipulation. *Nat. Mater.* **9,** 193–204 (2010).

310. Ramezani, M. *et al.* Plasmon-exciton-polariton lasing. *Optica* **4,** 31 (2017).

311. Zhao, D., Loebl, H.-P. & Van Elsbergen, V. Transient luminescence in organic light-emitting diodes explained by trap-assisted recombination of stored charges. *Org. Electron.* **14,** 3117–3122 (2013).

312. Kajii, H., Takahota, N., Wang, Y. & Ohmori, Y. Current Density Dependence of Transient Electroluminescence in Phosphorescent Organic Light-Emitting Diodes. *MRS Proc.* **1286,** mrsf10-1286-e03-12 (2011).

313. Lee, J.-H., Lee, S., Yoo, S.-J., Kim, K.-H. & Kim, J.-J. Langevin and Trap-Assisted Recombination in Phosphorescent Organic Light Emitting Diodes. *Adv. Funct. Mater.* **24,** 4681–4688 (2014).

314. Wang, Q. *et al.* Exciton and polaron quenching in doping-free phosphorescent organic light-emitting diodes from a Pt(II)-based fast phosphor. *Adv. Funct. Mater.* **23,** 5420–5428 (2013).

315. Erickson, N. C. & Holmes, R. J. Engineering Efficiency Roll-Off in Organic Light-Emitting Devices. *Adv. Funct. Mater.* **24,** 6074–6080 (2014).

316. Xiang, C. *et al.* Efficiency Roll-Off in Blue Emitting Phosphorescent Organic Light Emitting Diodes with Carbazole Host Materials. *Adv. Funct. Mater.* **26,** 1463–1469 (2016).

317. Zakharko, Y. *et al.* Surface Lattice Resonances for Enhanced and Directional Electroluminescence at High Current Densities. *ACS Photonics* **3,** 2225–2230 (2016).

318. Auguié, B., Bendaña, X. M., Barnes, W. L. & García De Abajo, F. J. Diffractive arrays of gold nanoparticles near an interface: Critical role of the substrate. *Phys. Rev. B - Condens. Matter Mater. Phys.* **82,** 1–7 (2010).

319. Kahn, A., Koch, N. & Gao, W. Electronic structure and electrical properties of interfaces between metals and ?-conjugated molecular films. *J. Polym. Sci. Part B Polym. Phys.* **41,** 2529–2548 (2003).

320. Koch, N. Electronic structure of interfaces with conjugated organic materials. *Phys. status solidi - Rapid Res. Lett.* **6,** 277–293 (2012).

321. Lee, C. W. & Lee, J. Y. Above 30% external quantum efficiency in blue phosphorescent organic light-emitting diodes using pyrido[2,3-b]indole derivatives as host materials. *Adv. Mater.* **25,** 5450–4 (2013).

322. *Colorimetry: Understanding the CIE System*. (John Wiley & Sons, Inc., 2007). doi:10.1002/9780470175637

323. Reineke, S., Schwartz, G., Walzer, K. & Leo, K. Reduced efficiency roll-off in phosphorescent organic light emitting diodes by suppression of triplet-triplet annihilation. *Appl. Phys. Lett.* **91,** 123508 (2007).

324. Xiao, L. *et al.* Recent Progresses on Materials for Electrophosphorescent Organic Light-Emitting Devices. *Adv. Mater.* **23,** 926–952 (2011).

325. Vasquez, R. P. Cu 2 O by XPS. *Surf. Sci. Spectra* **5,** 257–261 (1998).

326. Vasquez, R. P. CuO by XPS. *Surf. Sci. Spectra* **5,** 262–266 (1998).